Influence of nanostructuring on thermoelectric properties of p-type bulk materials based on (Bi, Sb, Te)

Viktoriia Ohorodniichuk

UNIVERSITE DE LORRAINE
École doctorale N°409 : Énergie, Mécanique et Matériaux (EMMA)
Institut Jean Lamour (Nancy) – EDF R&D
CONVENTION CIFRE N° 2011/1329

Thèse présentée pour l'obtention du
grade de docteur de l'Université de Lorraine

par
Viktoriia Ohorodniichuk
le 18 décembre 2014

Influence de la nanostructuration sur les propriétés thermoélectriques de matériaux massifs de type p à base de (Bi,Sb,Te)

Membres du jury :

Mme Sylvie HEBERT	*Rapporteur*	Directrice de recherche au CRISMAT, ENSICAEN, France
M. Jiří HEJTMANEK	*Rapporteur*	Directeur de recherche à Institute of Physics ASCR, République Tchèque
M. Pascal DALICIEUX	*Examinateur*	Ingénieur à ENERBAT, EDF R&D, France
M. Franck GASCOIN	*Examinateur*	Maître de Conférences au CRISMAT, ENSICAEN, France
Mme Anne DAUSCHER	*Co-directeur de thèse*	Chargée de Recherche au CNRS - Institut Jean Lamour, France
M. Bertrand LENOIR	*Directeur de thèse*	Professeur à l'Université de Lorraine - Institut Jean Lamour, France
M. Mehdi AIT-AMEUR	*Invité*	Ingénieur à ACOME, France
M. Philippe BARANEK	*Invité*	Directeur de recherche à MMC, EDF R&D, France
M. Paul GARRET	*Invité*	Ingénieur à ENERBAT, EDF R&D, France

Acknowledgments

The work presented in this thesis was performed at the Department of Chemistry and Physics of Solids and Surfaces of Institut Jean Lamour (Nancy, France) within the group of Thermoelectric Materials. I want to thank Dr Eric Gaffet, head of the laboratory, for welcoming me in his lab.

It was a big honor for me that Dr Sylvie Hebert, research director at CRISMAT, ENSICAEN, accepted to become the President of the Jury. I also want to present my deep gratitude to Dr Hebert and Dr Jiří Hejtmanek, research director at Institute of Physics of Praha (Czech Republic), for their reviews on this work that raised important questions and gave wise suggestions. This thesis developed a lot from their hard work.

I strongly appreciate the constant interest of Dr Franck Gascoin, Associate Professor at CRISMAT, ENSICAEN, to this project and his meaningful suggestions and I want to thank him for his willing to become the examiner during my defense.

I would like to greatly thank Mr Pascal Dalicieux and Dr Philippe Baranek (EDF R&D) to give me the opportunity to join this project, and further for their judicious advices and help all along the project as well as for their assistance to the defence. I hardly acknowledge the support of EDF R&D through a CIFRE convention, and their support for the numerous possibilities I get to present our work to the international scientific society.

Mr Paul Garret, engineer at EDF R&D, and Mr Mehdi Ait-Ameur, engineer at ACOME, gave me an important example of the contribution of a laboratory study to the practical goals. Thank you for your kind advices and constant interest.

Beyond I will continue to mention those, who guided, taught, supported and provided help all these three years of the PhD study. This thesis includes the efforts of numerous persons and could not be finished without them.

These three years were filled by situations and tasks that I faced for the first time in my life: living by myself in a foreign country, first experience in laboratory work with complex facilities, discovering the scientific world from inside. In all this aspects and many others, I was constantly guided by two amazing people and passionate professionals with whom I had an

honour to collaborate these years: Pr Bertrand Lenoir and Dr Anne Dauscher. Somehow all my words about these persons and their role in my life can sound too pretentious despite being truthful. I would like to thank Bertrand for being wisdom mentor and an example of passionate scientist I will keep for life. I really appreciate our long talks and miss them a lot. Thank you, Anne, for our discussions during the lunch-time and French lessons with the cup of tea. You showed me the beauty of micro-scale world and helped to not get lost in it. I also would like to prize your hospitability for the annual laboratory Christmas meetings that made us feel close and share the joy and delicious food. I just hope you both know how much I appreciate your support, patience and believe in me.

I also want to mention all those kind, intelligent and active scientists who created the powerful team and became my family for these years. First of all, I want to thank the persons who were the closest all these three years, sharing the same office, creating working atmosphere and willingly helping – Dr Christophe Candolfi and Mr Philippe Masschelein. Philippe, thank you for your teaching skills, cheerful mood and for being near every time something went wrong. I want also to say my best wishes for the long and prominent scientific future to Dr Jean-Baptiste Vaney, who shared with me the destiny of being PhD student, provided many measurements and inspired the life in laboratory. Thank you, Dr Iurii Kogut, Dr Driss Kenfaui, Dr Quentin Recour, Yohan Bouyrie, Malika Colin and Selma Sassi for being nice and supportive friends. I sincerely wish you good luck and send all my best regards to all of you.

An important part of this work was based on the TEM images that were provided by Ms Sylvie Migot-Choux and Dr Jaafar Ghanbaja. They performed not an easy task and I would like to send my gratitude to them. The quality of images depends strongly on the quality of the thin samples, so I also want to thank to Dr Laurent Legras (EDF R&D, Les Renardières) and Dr Flavio Soldera (Material Engineering Center Saarland) for their contribution.

I also want to mention Mr John G. Stockholm for his kind support, wise advices and constant interest to this project.

And finally I want to thank my dear mother, loving sister and all the family, who constantly supported me and stayed strong despite the circumstances. I wish I could protect you and share with you all your joys and misfortunes. Hope better times will come soon.

CONTENTS

CHAPTER III: Synthesis of $Sb_{2-x}Bi_xTe_3$ based compounds. Microstructural characterizations.

CHAPTER IV: Measurement techniques for thermal, electrical and galvanomagnetic properties

CHAPTER V: Results and Discussions

INTRODUCTION

Producing new buildings that use 80 percent less energy than today's average buildings is a new target in the fight against global climate change. If such a building's remaining energy consumption is supplied by clean, carbon-neutral renewable energy, it would be responsible for little or no greenhouse gas emissions.

The building sector is, among all economic sectors, the most energy consumer in France (42.5% of total final energy). It is also responsible for about 23 % of greenhouse gas emissions (40 % worldwide). In order to answer to the recommendations of 'Grenelle de l'Environnement', introduced in France in 2007 for contributing to the development of sustainable, eco-friendly and less energy consuming housings, the label 'Bâtiments Basse Consommation' (BBC) has been introduced. The new Thermal Regulation (RT2012), applied from January, 2013, fixes the maximum consumption level to 50 and 80 kWh_{pe}/m^2/year (h_{pe} : hour of primary energy) for new and renovated BBCs, respectively. It can range from 40 kWh/m² to 65 kWh/m² depending on the climatic area and altitude (new BBCs). This value has been divided by 3 with regard to RT2005, and emphasises the arrival of positive energy buildings at 2020. Taken into account is the consumption of the so-called conventional primary energy: heating, cooling, ventilation, auxiliaries, production of domestic hot water and lighting facilities.

Of particular interest for decreasing the greenhouse gas emissions is the use of heat pumps. For instance, 1 kWh of heat produced by a heat pump generates 3 to 4 times less CO_2 than 1 kWh of heat produced by a boiler using fossil energy (fuel or coal), and avoids the emission of certain pollutants (SO_2, NO_x). A heat pump concentrates the heat stored outside in the air, ground or water to restore it in a warm water network connected to radiators, underground floor heating or a boiler. Some systems are also reversible and can produce cooling through extracting heat and ejecting it to the immediate surroundings.

Heat pumps need conventional energy, in particular, electricity to function. In the heating mode, a coefficient of performance (COP) has been defined as being the ratio of heat output to electricity input for a specified source and output temperature. The system is all the more performant and less energy consuming than the COP is high. It is measured in laboratories with more or less accuracy according to European norms. A seasonal coefficient of performance (SCOP) has also been designed and is the coefficient of performance averaged over the length of the heating season for the heat pump system at a specified

location. In the cooling mode, the energy efficiency ratio (EER) is the ratio of cold output to electricity input for a specified source and output temperature. To get the eco-friendly label, according to the type of electric heat pump (heat source/heat sink: air/air, air/water, water/water, water/air) and to the inlet and outlet temperatures, the COP should be comprised between 2.6 (air/water) and 5.1 (water/water).

The conventional heat pumps developed considerably since 2005, but have come to a screeching halt over the last few years. What can bring thermoelectricity? Heat pumps with electrically driven compressors are relatively expensive, three to four times more expensive than a traditional boiler. These traditional heat pumps use a closed circuit in which a refrigerant (hydrofluorocarbons) undergoes a cycle of compression/expansion between a condenser and an evaporator. A thermoelectric heat pump (THP) would have several advantages with regard to conventional heat pumps: less noise and maintenance (more reliable) due to the absence of moving parts, more space-saving, less expensive (less than one kg of thermoelectric material should be needed) and more environmentally friendly. A THP is equipped with Peltier modules, based on thermoelectric effects, that can transfer heat from a cold side to a hot side when an electrical DC current is passed between the two sides. By simply reversing the direction of the current flow, the heat flow can be reversed. A THP is thus fully reversible, acting either for heating or cooling the housing spaces. Cooling of BCCs is all the more important as heating.

Even if the development of THP is interesting and tested in laboratories, commercial issues are lacking. It arises in part from the low theoretical COPs that can be achieved (less than 2 compared to 4 for conventional heat pumps) and to the fact that the COP depends on the variations of the external temperature according to the season. The SCOP has thus to be taken into account. The COP that the THP should reach would be ideally 2.5, to be in direct concurrence with gas boilers, to produce about 3-4 kW of heating power, enough for flats of several rooms or individual houses. With BBCs, the heating needs will decrease (except domestic water) and a value of only 2 kW is expected. The temperature to take into consideration are -10°C outside and 30°C to be produced.

The COP of a thermoelectric heat pump depends on the material transport properties through the so-called dimensionless figure of merit *ZT*. *ZT* depends both on electrical and thermal properties and a high *ZT* value is required to reach a high COP. Regarding the application using TE technology for heat pumps, a *ZT* around 1.6 would be needed to reach

the COP target of 2.5. If such a *ZT* value was well above the maximum to reach in most of the conventional material during many years (*ZT* ~ 1), there are real hopes now thanks to the recent progress realized through the nanostructuration of bulk TE materials. Actually, this approach proved to be very efficient for improving the performance of n- and p- type thermoelectric materials constituting the Peltier modules. Several groups claimed that *ZT* much over unity can be reached in advanced or conventional TE materials including the solid solutions Sb_2Te_3-Bi_2Te_3 and Bi_2Te_3-Bi_2Se_3. These two alloys constitute the p and n-type legs of commercial Peltier modules used for applications near room temperatures.

The objective of this PhD thesis is thus to improve the thermoelectric performance by nanostructuring bismuth-antimony telluride materials that are the most efficient p-type materials for the range of temperature sought in THPs. This work has been supported by EDF R&D through a CIFRE-ANRT convention. It is part of a more complete program aiming at fabricating performant thermoelectric Peltier modules for an integration in THPs. The counterpart n-type material, made of bismuth telluride-selenide alloys, has been the topic of the PhD thesis of Quentin Lognoné from CRISMAT (Caen), supported by the society ACOME. It was defended in September, 2014. A previous study dealing on a numerical and experimental innovative THP was performed in the frame of the PhD of Yeweon Kim, defended in 2013 and also supported by EDF.

This manuscript is divided into five chapters.

Chapter 1 introduces some brief theoretical aspects concerning the thermoelectric effects enabling to understand how the thermoelectric figure of merit *ZT* can be improved and optimised by tuning the electrical and thermal properties. Criteria for selecting thermoelectric materials will be described. We will finish by a detailed but non exhaustive review in the progress realised with state-of-the-art and advanced thermoelectric materials, including bulk and nano-structured materials.

Chapter 2 provides a literature-based review of the structural, chemical, electronic and transport properties of the material at the heart of this PhD, i.e. the solid solution $Sb_{2-x}Bi_xTe_{3+z}$. We will see in particular how the lamellar structure introduces anisotropy in the physical properties and how deviation from stoichiometry, nano-microstructuring and/or doping can influence the thermoelectric performance.

Chapter 3 deals with the preparation of the various bulk nano-structured and reference samples. Particular emphasis is devoted to a new technique used in the team for introducing nanoparticles in a bulk matrix, i.e. melt-spinning. A brief description of the principle and set-up used for characterizing the chemical composition (electron dispersion spectroscopy) and structure (x-ray diffraction, scanning and transmission electron microscopy) is given. Results and analyses of these microstructural studies are presented and will be a base of discussion of the variation in the transport properties.

Chapter 4 describes the different methods and techniques used to characterize the thermoelectric and galvanomagnetic properties of the various samples we prepared. The principle, the mounting of the samples, and the apparatus used will be given for measurements performed on one hand at low temperature (2-300 K) and on the other hand at higher temperature (300-460 K). Particular care is devoted to the preparation of the samples in order to guarantee reliable measurements.

Finally, chapter 5 is devoted to the presentation and discussion of all our results concerning the thermoelectric and galvanomagnetic properties in the wide range of temperature studied. This chapter include the two series of samples $Sb_{2-x}Bi_xTe_3$ and $Sb_{2-x}Bi_xTe_{3.1}$. We will show that in each of this family, the content of Bi, *x*, the anisotropy, and the synthesis route play an important role on the transport properties. The doping of these two series of samples by Sn will also be discussed in the light of resonant impurities. Finally, we will state on the effectiveness of nanostructuring for improving the dimensionless figure of merit ZT with regard to literature.

In complement to this presentation, three appendixes will be provided. The first one will concern the influence of melt-spinning parameters like speed of the wheel and diameter of the nozzle on the transport properties. The second will deal with the transport Boltzmann equation while the last one will be devoted to modelling the thermoelectric performance of a thermoelectric heat pump. This model, developed on Comsol Multiphysics, will be based on the thermoelectric properties found in the frame of this work for the p-type leg and those obtained by Dr Quentin Lognoné (CRISMAT) on the counterpart n-type leg.

Chapter I

Introduction to thermoelectricity. Survey of state-of-the-art materials

INTRODUCTION

Over the years, thermoelectricity has been recognized as an enabling technology to dissipate heat or to generate electrical power. Thermoelectric devices exhibit several advantages such as compactness, quietness (no moving parts), localized heating or cooling, as well as the advantage of being "environmentally friendly". Thermoelectric refrigerators and generators were used in specialized applications in which their desirable features outweigh their relatively high cost and low performance. For example, thermoelectric refrigeration has been successful in domestic food refrigerators, air conditioning, and cooling of CCD's (charge coupled devices) infrared detectors. Since 1961, Radioisotope Thermoelectric Generators (RTGs) have been successfully built for powering NASA's spacecrafts or deep space probes over extended periods of time: the lifetime of RTGs, favored by the absence of mechanical motions and low maintenance needs, exceeds 37 years for Voyager 1 and 2 (launched in 1977) for example. Thermoelectric generators are more recently of interest for the generation of electrical power using low–level waste heat sources. Intensive research programs in the automotive industry were initiated these last years to recover waste heat from exhaust gases with an overall objective to achieve a 7-10% improvement in fuel economy.

The essence of a good thermoelectric material is captured in the material's dimensionless figure of merit, *ZT*, defined by:

$$ZT = \frac{S^2}{\rho\kappa}T \qquad \text{(I-1)}$$

where S is the Seebeck coefficient or thermopower, T is the absolute temperature, ρ is the electrical resistivity and κ is the total thermal conductivity. The S^2/ρ ratio is called the power factor. High *ZT* values are an essential ingredient in achieving highly-efficient thermoelectric devices. The challenge lies then in achieving simultaneously high S, low ρ and low κ for a given thermoelectric material at the operating temperature T. The three transport properties are linked to the details of the electronic structure and to the scattering of charge carriers (electrons and holes) and thus are not independent.

Heavily doped semiconductors and/or alloys based on heavy elements of the periodic table were found to be the most suitable materials for thermoelectric energy conversion.

$(Bi_{1-x}Sb_x)_2(Te_{1-y}Se_y)_3$ and $Bi_{1-x}Sb_x$ alloys are considered as state-of-the art materials for thermoelectric refrigeration for near room-temperature and low-temperature applications, respectively. Materials for high-temperature applications (power generation) include PbTe and $Si_{1-x}Ge_x$ alloys. For all state-of-the art materials and despite important research effort

between 1950 and 1990, the maximum *ZT* was found to be nearly equal to unity in a given range of temperature, which gives a thermoelectric performance at least twice lower than that of conventional refrigerators. It is conceivable that, if materials with *ZT* ~ 2-3 could be developed, a more widespread use of this technology would occur.

A renewed interest in thermoelectrics began in the mid-1990s driven by the needs to make a more efficient use of the non-sustainable resources (fossil fuels) left in the world, and to develop alternative energy technologies. In this context, new ideas and concepts were proposed with the aim to identify and develop new thermoelectric materials that would break the *ZT* ~ 1 barrier. Two directions of intensive research were simultaneously pursued for developing the next generation of thermoelectric materials. One has been devoted to the exploration of new families of bulk materials such as semiconductors with complex and/or open crystal structures while the second direction focused on low-dimensional systems (as occurring in quantum wells (2D), quantum wires (1D) or quantum dots (0D)) and later on nanostructured bulk materials.

After introducing the basic principles of thermoelectric energy conversion, some criteria that guided the selection of good state-of-the-art and advanced thermoelectric materials recently investigated will be presented. Then, a brief summary of the properties of state-of-the-art thermoelectric materials will be given. Finally, the most recent developments in thermoelectric material research including bulk materials and low dimensional structures will be highlighted and briefly discussed. For detailed aspects of thermoelectricity (including theory, materials, measurements and applications), the reader is invited to read some excellent textbooks / GOL86, IOF57a, ROW12a, ROW12b, ROW83, ROW95, TRI01, URE61/.

I) BASIC PRINCIPLES

I-1) Thermoelectric effects

In the early 1800s, Thomas Seebeck /SEE23/ showed that if a small temperature difference (*dT*) is applied between the ends of a material (under the condition that the circuit is open) an electric field *E* or a voltage difference (*dV*) develops (Fig. I-1). This voltage is proportional to the temperature difference (*dT*):

$$dV = S\, dT \tag{I-2}$$

The Seebeck coefficient S, which can be negative (electron conduction) or positive (hole transport), is an intrinsic property of the material, like the electrical resistivity or the thermal conductivity. The local form of equation I-2 is:

$$\vec{E} = S\, d\vec{T} \tag{I-3}$$

The thermopower is very low for metals (only a few $\mu V.K^{-1}$) and much larger for semiconductors (typically a few hundreds $\mu V.K^{-1}$).

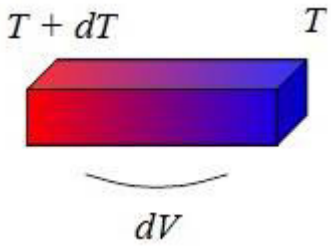

Figure I-1: When a small temperature difference *dT* is applied between the ends of a material (under the condition that the circuit is open), a voltage difference *dV* appears: this is how the Seebeck effect manifest.

A related effect (the Peltier effect) was discovered a few years later by the watchmaker Jean-Charles Athanase Peltier /PEL34/, who showed that if a material is subjected to an electrical current *I* (or current density $\vec{j}$) under isothermal conditions (see Fig. I-2), a heat flux $\vec{q}$ develops such that:

$$\vec{q} = \pi\, \vec{j} \tag{I-4}$$

where π is called the Peltier coefficient. A direct consequence of equation I-4 is that if an electrical current *I* is passed through the junction of two dissimilar materials a and b, heat will be either absorbed or rejected at the junction depending on the direction of the current. Indeed, as each material possesses its own Peltier coefficient, there will be a discontinuity of

the heat at the junction. The rate at which heat, Q, is liberated or rejected at the junction is given by:

$$Q = (\pi_a - \pi_b)\, I \tag{I-5}$$

It is in fact under this form that the Peltier effect was discovered.

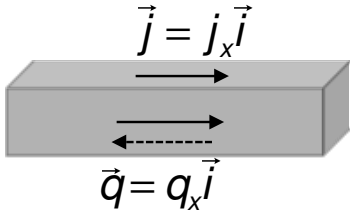

Figure I-2: When a current density $\vec{j}$ passes in a material kept under isothermal conditions, a heat flux $\vec{q}$ appears: this is how the Peltier effect manifest.

The third thermoelectric effect was predicted (1851) and confirmed experimentally by William Thompson /THO51/ (later Lord Kelvin). He demonstrated that a material exchanges heat with the environment when subjected simultaneously to a temperature gradient and an electrical current I. The elementary rate at which heat, dQ, is emitted or absorbed by a layer (Fig. I-3) between T and $T+dT$ is given by:

$$dQ = -\tau\, I\, dT \tag{I-6}$$

where τ is the Thompson coefficient which can be either positive or negative. Thompson also showed that the Seebeck, Peltier and Thompson coefficients are related together according to:

$$\pi = S\, T \tag{I-7}$$

$$\tau = T\ dS/dt \tag{I-8}$$

These two relations forms what is called the Kelvin's relations now.

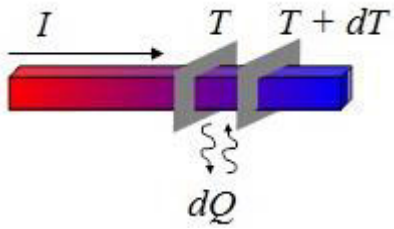

Figure I-3: When a current I passes through a material subjected to a temperature difference, heat is absorbed or emitted.

I-2) Thermoelectric modules and performance

The Seebeck and Peltier effects are the basis for many modern thermoelectric refrigeration and thermoelectric power generation devices, respectively. The versatility of thermoelectric materials is illustrated in Fig. I-4, which shows a diagram of a thermoelectric couple composed of an n-type (negative thermopower *i.e.* electron carriers) and a p-type (positive thermopower *i.e.* hole carriers) semiconducting materials connected through metallic electrical contact pads. Both refrigeration and power generation may be accomplished using the same module as shown in Fig. I-4. A thermoelectric module or device is built up of an array of these couples, which are arranged electrically in series and thermally in parallel.

Thermoelectric energy conversion utilizes the heat generated (as a result of the Peltier effect) when an electrical current is passed through a thermoelectric material to yield a temperature difference with heat being absorbed on the cold side and rejected at the sink, thus providing a refrigeration or heat pump capability (Fig. I-4a). Similarly, an imposed temperature difference applied on the material will result in a voltage (as a result of the Seebeck effect) or current, that is, power generation on a small scale (Fig. I-4b).

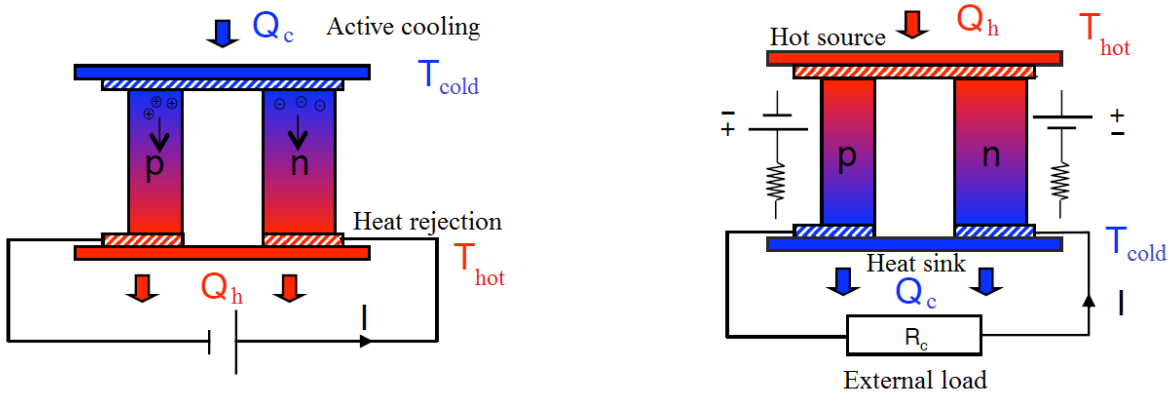

(a) (b)

Figure I-4: Schematic diagram of a single thermocouple configured for refrigeration (a) or power generation (b). The thermoelectric couple consists of a p- and a n- type semiconducting branch. Actual thermoelectric devices are typically composed of a plurality of such thermoelectric couples connected electrically in series and thermally in parallel to form a module. When an electrical current is passed through the module, heat is absorbed at one side (cold side) of the module and rejected at the other side (hot side) and the device operates as a cooler. Conversely, if an external temperature difference is applied to the module, electrical power will be delivered to an external load and the device operates as a power generator.

Qualitatively, it is easily seen that a good thermoelectric material should have a high Seebeck (or Peltier) coefficient to obtain a sizeable thermoelectric effect, a low electrical resistivity to minimize Joule heating losses and a low thermal conductivity κ to maintain a

large temperature difference. Altenkirch /ALT09, ALT11/ was the first to express these considerations in a quantitative form. He showed that the performance of a well-designed thermocouple can be expressed in terms of the temperature of the hot, T_h, and cold, T_c, junctions, and a quantity known as the figure of merit Z_{np} defined by:

$$Z_{np} = \frac{(S_p - S_n)^2}{\left[(\rho_p \kappa_p)^{1/2} + (\rho_n \kappa_n)^{1/2}\right]^2} \tag{I-9}$$

where the subscripts *p* and *n* refer to the positive and negative branches, respectively.

The $Z_{np}T_m$, where $T_m = (T_c + T_h)/2$ is the average temperature of the thermocouple over which the device operates, is not a fixed quantity for the couple and can depend on the relative dimensions of the branches. $Z_{np}T_m$ is maximized when the product *RK* is minimized, where *R* is the total couple resistance and *K* is the couple's thermal conductance. This is accomplished when:

$$\frac{L_n A_p}{L_p A_n} = \sqrt{\frac{\rho_p \kappa_n}{\rho_n \kappa_p}} \tag{I-10}$$

where *L* is the height of the branch, *A* – the cross-section of the branch. The figure of merit for the couple is given by equation I-9.

Figure I-5 shows the coefficient of performance (ratio of the heat absorbed at the cold side to the electrical power consumption) of a cooling device and the efficiency (ratio of the electrical power output to the thermal power input to the hot side) of a thermoelectric generator as a function of T_c/T_h for various $Z_{np}T_m$ values. It is apparent from this figure that a Peltier refrigerator can operate under an appreciable temperature difference for high $Z_{np}T_m$ values (values greater than unity are highly desirable). Similarly, to reach a high efficiency, high $Z_{np}T_m$ values are needed combined with high temperature differences (to boost the Carnot efficiency).

Equation I-9 refers to a couple, while in the materials-development problem it is more convenient to have a criterion describing the quality of a single material. For this reason, the figure of merit of a single material is defined by analogy as in equation I-1. For two materials whose individual *ZT* are similar and whose Seebeck coefficients are opposite in sign but similar in magnitude, the resulting *ZT* of the couple is approximately equal to the average of the individual *ZTs*.

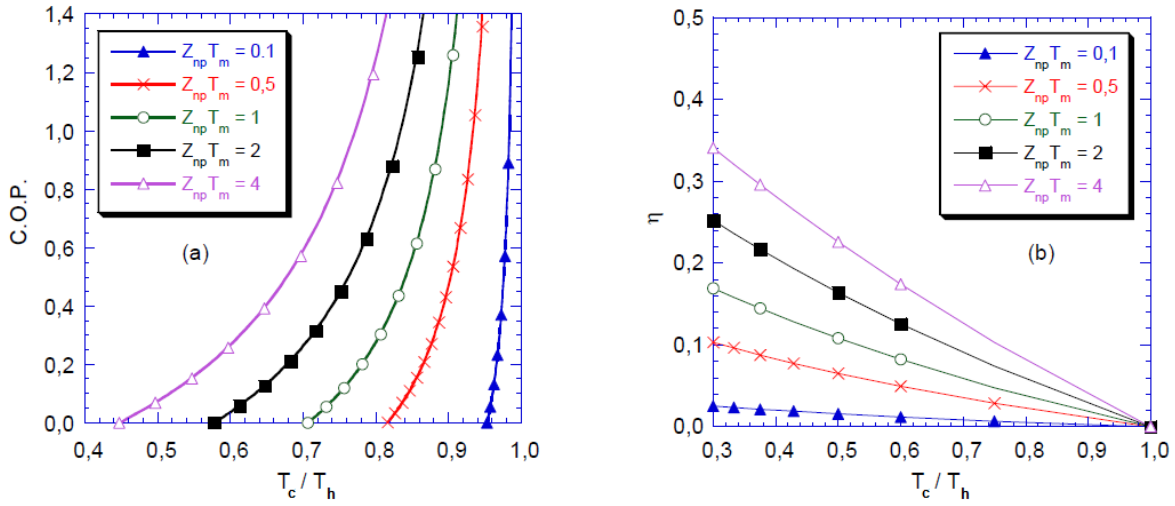

Figure I-5: Coefficient of performance, C.O.P., (a) and efficiency η (b) versus the ratio of cold to hot junction temperature for thermoelectric refrigerators and generators for various values of $Z_{np}T_m$.

I-3) Selection criteria

From the above considerations, it is clear that the selection of materials for thermoelectric applications involves the search for materials with high *ZT* values, able to operate over the widest possible range of temperatures. In addition, the material should have good mechanical, metallurgical and thermal characteristics that allow its use in practical thermoelectric devices. It is also usually desirable to obtain positive and negative branches with closely matched properties and composition to minimize unbalanced geometry for the branches (see equation I-10) and to ease mechanical stress associated with module/device fabrication.

The three transport parameters included in equation I-1 are mutually interdependent, each being related to some extent to the carrier concentration, usually expressed in terms of the reduced Fermi energy (*i.e.* Fermi energy divided by k_BT, the thermal energy where k_B is the Boltzmann constant). When considering electrical conduction phenomena, materials can be divided into four main groups: insulators, semiconductors, semimetals, and metals. The dependence of each of the parameters on carrier concentration is shown qualitatively in Fig. I-6. The total thermal conductivity consists mainly of two components, a contribution due to the lattice vibration κ_L and a contribution due to the charge carriers κ_E:

$$\kappa = \kappa_L + \kappa_E \qquad \text{(I-11)}$$

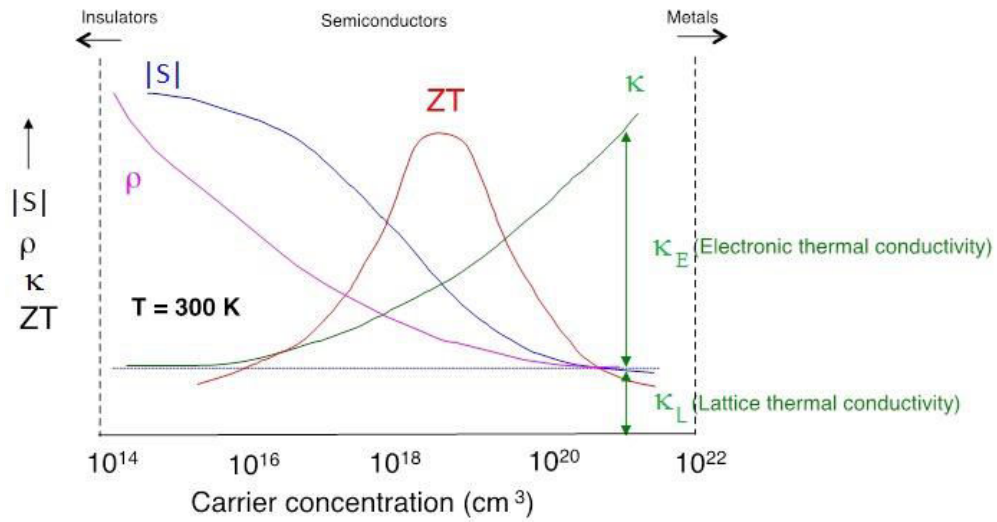

Figure I-6: Schematic representation of the Seebeck coefficient (S), the electrical resistivity (ρ), the total thermal conductivity (κ), and the figure of merit (ZT) as a function of electron concentration n at room temperature. The lattice thermal conductivity (κ_L) is essentially independent of n.

The lattice thermal conductivity is essentially independent on the carrier concentration, while the electronic component is directly related to the electrical resistivity through the Wiedemann-Franz law:

$$\kappa_E = LT/\rho \tag{I-12}$$

where L is the Lorenz number. This factor depends both on the Fermi level and the scattering mechanisms. For a degenerated gas of electrons, $L = 2.44\ 10^{-8}$ W.Ω.K^{-2}.

The value of the Seebeck coefficient decreases as the carrier concentration increases. It is therefore immediately apparent why "normal" metallic conductors are unsuitable for thermoelectric applications, their Seebeck coefficient being too small. For insulators, on the other hand, the Seebeck coefficient can reach high values but the electrical resistivity is prohibitively too high. As Ioffe /IOF57a/ has shown, the figure of merit reaches its maximum value in the region where the carrier concentration is of the order of 10^{18} to 10^{21} carriers per cm^3 at 300 K. This is the region of heavily-doped semiconductors and of semimetals.

A general mathematical analysis of the dependence of ZT on the temperature and carrier density is fairly complex since it requires, for a material, a detailed description of both phonon and electron energy spectra as well as an accurate knowledge of their scattering mechanisms. However, qualitative information can be obtained from the simple approach based on conventional theory for a single band semiconductor /IOF57a/. This theory shows that the maximum ZT value, reached for an optimum doping level (or charge carrier

concentration) depends both on the carrier scattering mechanisms and the properties of the material through a so-called material parameter β:

$$\beta \propto \left(\frac{m^*}{m_0}\right)^{\frac{3}{2}} \frac{\mu}{\kappa_L} \tag{I-13}$$

where m^* is the effective mass of electrons (in the case of n-type materials) or holes (p-type materials), m_0 – the free electron mass and μ – the intrinsic carrier mobility.

A large value of β is typically an indicator of the potential for high *ZT* values. This indicates that semiconductors with a large effective mass, a high mobility and a small lattice thermal conductivity are desirable. Even though these requirements tend to be mutually incompatible (a high mobility is usually linked to a low effective mass for example), empirical guidelines to the selection of desirable thermoelectric materials can be obtained by examining trends for given classes of materials. Useful rules for conventional semiconductors have been established in the past by Ioffe /IOF57a/, Goodman /GOO58/, Goldsmid and Douglas /GOL54/ and more recently by Slack /SLA74, SLA95/. The main desirable attributes for achieving high *ZTs* are:

1. Compounds with heavy atoms, many elements and large unit cell size in order to achieve low lattice thermal conductivity,
2. Small electronegativity differences between the constituting elements resulting in high carrier mobility,
3. Fermi levels close to the edge of the conduction band (valence band) for n-type materials (p-type materials) to have a large Seebeck coefficient,
4. Multi-valley band structures to maximize $(m^*/m_0)^{3/2}\mu$,
5. Energy band gap, E_g, falling in the range 5 $k_BT \leq E_g \leq$10 k_BT at projected operation temperature.

The lower limit is set by the requirement that thermal excitation of minority carriers degrades the thermoelectric performance. The contributions to the Seebeck and Peltier effects from electrons and holes are opposite in sign so that the simultaneous presence of both types of carrier leads to compensation effects. Moreover, electron-hole pairs in a mixed or intrinsic semiconductor carry their ionisation energy down a temperature gradient thereby increasing the thermal conductivity (this is the so-called ambipolar contribution).

The importance of a low lattice thermal conductivity has already been mentioned. Attention has therefore been given to different strategies to achieving low lattice thermal conductivity without affecting the electrical properties. Higher values of the thermoelectric

figure of merit can be achieved by forming solid solutions due to an increase in μ/κ_L. The stronger scattering rate of phonons, compared with electrons, is due to the difference between their wavelengths as predicted by Ioffe et al. /IOF56/; it forms the basis of one of the major optimization schemes for increasing the efficiency of thermoelectric materials. All state-of-the-art materials (Bi-Sb, Si-Ge, Bi_2Te_3, and PbTe based alloys) use enhanced phonon scattering rates due to mass fluctuations to achieve low thermal conductivity. However, no chemistry variation is possible for Bi-Sb and Si-Ge alloys. A large family of isostructural compounds is thus more attractive as the optimization process of the figure of merit offers a larger number of possibilities to change the type of conductivity, the carrier concentration, the lattice thermal conductivity, and possibly the temperature range of applications.

Other ways to minimize the lattice thermal conductivity such as phonon scattering by grain boundaries and particle inclusions have also been considered /BAN95/ with more or less success. These ideas, initiated as early as 1974 by Rowe /ROW74/, are at the heart of the recent developments on nanomaterials (as we shall see later in the paragraph dealing with nanostructured materials).

II) SURVEY OF STATE-OF-THE ART MATERIALS

A great number of materials have been examined in the last century for thermoelectric applications. Bismuth-antimony alloys, bismuth and lead telluride families, together with silicon-germanium alloys form the main part of the most established materials. Each of them operates over a particular range of temperature as illustrated in Fig. I-7. Most of the above-mentioned in §I-3 desirable features are common to all of established thermoelectric materials and the traditional semiconducting theory can generally be used to describe the transport properties.

Preparation is usually carried out by growth of single crystalline samples or by powder metallurgy techniques. Single crystals are preferable when performance is the crucial criterion, especially when the transport properties show a significant degree of anisotropy. On the other hand, mechanical strength is usually enhanced in polycrystalline materials and one also may expect lower lattice thermal conductivity values due to phonon scattering at grain boundaries. In addition, powder metallurgy is attractive in that it facilitates device fabrication and can be easily scaled up.

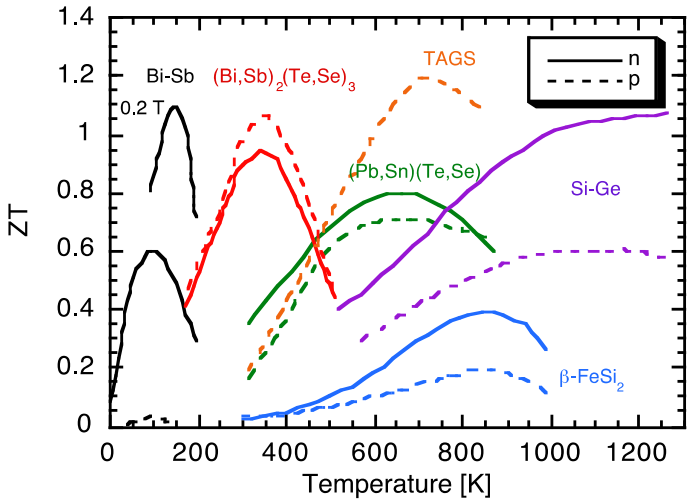

Figure I-7: Schematic representation of the typical temperature dependence of the dimensionless figure of merit *ZT* as a function of temperature for several n- and p- type established materials.

The figure of merit *Z* can be either determined by measuring individually the three transport coefficients (α, ρ and κ) on the same sample (see chapter IV) or estimated directly using the Harman method /GOL86, ROW95/. In the next paragraphs, a summary of the main properties of conventional thermoelectric materials is reported. For a comprehensive discussion, reviews are available in the literature /GOL86, RAV70, ROW83, ROW95, TRI01, URE61 and references therein/.

Below room temperature, interesting results were observed near liquid nitrogen temperature in n-type Bi-rich $Bi_{1-x}Sb_x$ alloys properly orientated, with *ZT* ~ 0.6 /LEN96, LEN98/. However, the use of $Bi_{1-x}Sb_x$ alloys in thermoelectric cooling devices has been constrained both by the absence of a good p-type material with a figure of merit comparable to that of the n-type below 150 K and by the relative brittleness of the material when used in its optimal configuration. The former can be solved by using high-*Tc* superconductors as passive branches in conjunction with n-type Bi-Sb thermoelements /GOL88/, while the latter can be overcome by employing polycrystalline samples produced by sintering, hot-pressing or extruding powdered materials. For instance, Martin-Lopez et al. have shown that the mechanical strength of an extruded polycrystalline $Bi_{0.85}Sb_{0.15}$ alloy is enhanced by one order of magnitude at 77 K as compared to a single crystal grown by the Czochralski method /MAR98/. However, the thermoelectric performance of the disordered structures is affected as a result of the random orientation of the grains and the presence of defects that strongly influence the transport at low temperatures.

The performance of Bi-Sb single crystals is even more important in the presence of a transverse magnetic field, as first pointed out by Wolfe and Smith /WOL62/ for a $Bi_{0.88}Sb_{0.12}$ single crystal. They reported a dimensionless figure of merit *ZT* greater than unity between 125 and 275 K by applying an optimum magnetic field. These values are at least twice the zero-field values. The reason for this large improvement is the presence of transverse thermomagnetic effects. The magnitude of these effects is particularly high for Bi-rich Bi-Sb alloys, making them very attractive materials for Ettingshausen cooling devices /CUF63, HOR80, JAN94/.

Near room temperature, the best materials are the $(Bi,Sb)_2(Te,Se)_3$ alloys. They constitute the most well-established materials used nowadays in thermoelectric devices for cooling applications. As these materials are at the heart of this thesis, a review of their salient properties, including their thermoelectric properties, will be presented in detail in the next chapter. Apart from cooling applications, bismuth-telluride-based alloys can be also used for power generation applications. However, the existence of a small energy gap as well as chemical stability problems limits their use for power generation up to around 500 K. At higher temperature, materials with superior thermoelectric properties are used.

Applications of materials in power generators require chemical stability at high temperature and appropriate band gaps in order to achieve reasonable Seebeck coefficients in the extrinsic regime of conduction. Alloys based on lead telluride, PbTe, satisfy these requirements and are the most suited materials to operate in the 500-800 K temperature range. They were employed in Radioisotope Thermoelectric Generators (RTGs) for space applications during fourteen years covering the period 1961-1975.

PbTe and its related compounds crystallize in a rock-salt structure and exhibit isotropic transport properties. Their electronic band structure is multi-valley with a direct band gap of 0.32 eV at 300 K. Both n- and p-type electrical conduction can be achieved in PbTe as a result of deviations from stoichiometry. Excess Pb with respect to the stoichiometric ratio results in n-type conduction while excess Te yields a p-type material. However, the maximum carrier concentration that can be achieved through these deviations is not sufficient to attain optimal electrical properties at elevated temperatures. Doping is therefore essential and can be realized upon using alkali metals (acceptors) and/or halogens (donors) /BAS80, RAV70/. A maximal *ZT* of about 0.8 is achieved around 700 K for both materials at optimal doping (see Fig. I-7). Recently, these materials were revisited and improved thermoelectric properties were obtained (100% increase!) in both n- and p-type materials /LAL11, PEI11/. The results

were consistent with prior reports though the thermal conductivity has been found to be historically overestimated according to the authors. Another impressive result was obtained by Heremans et al. /HER08/ in PbTe doped by Tl (p-type). Thallium impurities play a specific role by adding additional electronic states in the valence band. This causes a distortion of the density of states that can be used to boost the thermopower. Such band structure engineering resulted in a twofold increase in *ZT* that reaches 1.5 at 773 K.

Likewise the Bi_2Te_3 system, the figure of merit of PbTe can be improved by the formation of solid solutions. A study of the PbTe-SnTe alloys showed that one of the most promising composition for n-type is $Pb_{0.75}Sn_{0.25}Te$ /ROS61/. Due to oxidation and evaporation of Te, the usefulness of PbTe and PbSnTe solid solutions for power generation is limited to temperatures up to 800 K. More complex compounds, formed by alloying $AgSbTe_2$ with GeTe, and referred to as TAGS compounds, have been proven to be more efficient p-type materials than PbTe alloys /SKR95/.

In this same temperature range (Fig. I-7), iron disilicide (β-$FeSi_2$), though possessing modest *ZT* values, is a useful material for power generation applications and effort are currently underway to build terrestrial power generators incorporating this material. It is often preferred to other materials because of the following advantages:

- its stability with respect to oxidation, sublimation, evaporation and diffusion,
- its non-toxic elements,
- its low-cost,
- the possibility to use powder technology for its synthesis.

This material has been widely investigated by Birkholz and co-workers /BIR89, BIR95/.

At even higher temperatures, the most commonly used materials are Si-Ge alloys. This can be somewhat unexpected since both Si and Ge have rather high lattice thermal conductivities (κ_L = 113 and 63 $W.m^{-1}.K^{-1}$ at 300 K, respectively), resulting in very modest thermoelectric properties. However, the lattice thermal conductivity of the Si-Ge mixed crystals is much lower (about 10 $W.m^{-1}.K^{-1}$ at 300 K) while the carrier mobility is only slightly decreased by alloying. Si-Ge devices can operate with minimal performance degradation up to about 1300 K and have been the exclusive choice for NASA's RTGs since 1976 /WOO88/. Similarly to the Bi-Sb system, silicon and germanium form a solid solution in the whole range of composition. Dopants such as P or B are used to obtain n- or p-type materials, respectively. Since the band gap of Si is 1.15 eV, and that of Ge is 0.65 eV, it is more beneficial to use Si-rich alloys (70-90 at.% Si). The cost is even lower. The $Si_{0.7}Ge_{0.3}$

composition possesses good thermoelectric performances /DIS64/. Optimum *ZT* values are reached near 1100-1200 K for both n- and p-doped Si-Ge alloys (Z_nT ~ 0.6 and Z_pT ~ 1.0 at 1200 K, respectively).

III) NEW THERMOELECTRIC MATERIALS

It becomes evident from the previous sections that, in order to develop higher efficiency devices and systems, new thermoelectric materials with $ZT > 1$ must be identified. The limit for current materials over a wide range of temperature is of the order of unity raising the question about limits on *ZT* values. This question has been addressed theoretically and thermodynamic laws do not put any limits on *ZT* /MAH98c/. For bulk materials, physical models have been developed to describe the transport coefficients involved in the figure of merit in terms of valence and conduction band parameters. Using upper physical limits for some of these parameters, the limit was estimated to fall between 2 and 10.

Slack /SLA95/ has revisited the upper bound for *ZT* in bulk materials. As described in section I, a good thermoelectric material must combine a low lattice thermal conductivity with good electronic properties. It is therefore of interest to identify materials that possess lattice thermal conductivity comparable to amorphous materials. Slack suggested that the minimum thermal conductivity could be obtained when phonons have a mean free path equal to their wavelength. The minimum lattice thermal conductivity estimated based on this assumption is about 0.2 W/mK. Slack further suggested that crystals with complex structures containing loosely-bounded atoms or molecules should possess low lattice thermal conductivity. Of course, the challenge is, once one has identified a crystalline material with a lattice thermal conductivity approaching the minimum theoretical value, to be able to optimize the electronic properties of this material in order to achieve large power factors. This is essentially linked to the maximization of the parameter β introduced earlier. Slack called the ideal material combining a glass-like thermal conductivity and good electronic properties a phonon-glass electron-crystal (PGEC) /SLA95/. While several materials are known to either have a glass-like thermal conductivity or excellent electronic properties such as Bi, the challenge is to identify materials in which the electronic and thermal properties can be decoupled and optimized separately. Slack listed several candidate materials that could potentially be PGEC materials. Considering a hypothetical material, which would have the transport properties of Bi and a lattice thermal conductivity of 0.2 W/m.K, Slack estimated a maximum dimensionless figure of merit of about 4 based on a band structure model. Although it might

be quite difficult to develop such a material, this model shows that *ZT* values on the order of 2 to 3 may not be unrealistic.

Research efforts in the last 25 years have focused on two types of materials: bulk materials and nanostructured materials (including low dimensional systems and nanostructured bulk materials). Many new bulk materials under investigation have complex crystal structures, which often contain loosely-bounded atoms that could be used as efficient phonon scattering centers (referred in literature as "rattlers"). Several new promising families of materials have been identified and encouraging results have been obtained. In nanostructured materials, several approaches for increasing *ZT* have been proposed, including quantum size effects to increase the power factor values or to utilize the increased phonon scattering at interfaces to decrease the lattice thermal conductivity without degrading the electronic properties. In the next parts, we briefly review some of the past developments for bulk and nanostructured materials.

III-1) Moderated and high temperature bulk materials

III-1-1) Skutterudites

Among materials that were suggested originally to show attributes for the realization of a PGEC material are skutterudite compounds. The name of skutterudite is derived from a naturally occurring mineral with $CoAs_3$ structure, which was discovered in Skutterud (Norway). The general formula of skutterudite compounds is MX_3, where M is one of the group 9 transition metals such as Co, Rh, or Ir and X is a pnictogen atom such as P, As, or Sb. These compounds exhibit a body-centered-cubic structure that contains 32 atoms in the unit cell described within the space group Im3. The most important point of the skutterudite structure is that there are two voids in the unit cell that can be occupied by loosely-bound atoms that are known as "rattlers". This generates a so-called filled or partially filled skutterudite $R_xM_4X_{12}$, where R stands for the filler atom and x (< 1) indicates the fractional occupancy on the available void site. Figure I-8 presents the crystal structure of skutterudites.

Among binary skutterudites, $CoSb_3$ has attracted the greatest interest in electrical generation applications due to its reasonable band gap of ~ 0.2 eV, high carrier mobility, and the fact that it is composed of inexpensive and environmentally benign constituent elements as compared to other skutterudites such as $CoAs_3$. However, the lattice thermal conductivity of $CoSb_3$ is too high (κ_L ~ 10 W/m.K at 300 K) to result in high *ZT* values. By filling the cage

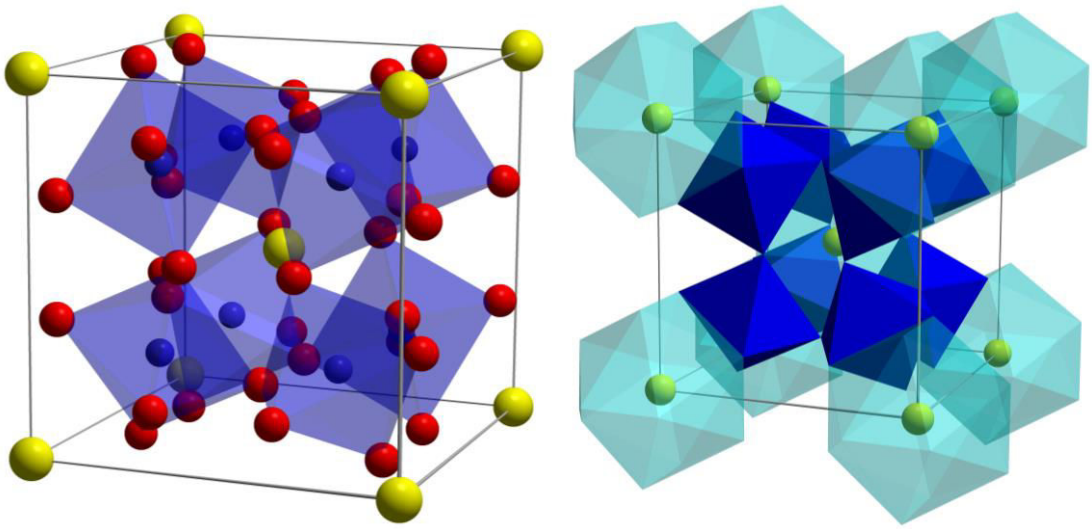

Figure I-8: $R_xM_4X_{12}$ filled skutterudite unit cell. The filler atoms R are in yellow while the M and X atoms are in blue and red. The left figure shows the octahedra formed by X atoms in which are centered the M atoms. The right figure shows the X dodecahedra in which are located the R atoms.

of the structure, it was possible to decrease significantly the thermal conductivity and thus to reach high *ZT* values. It has been reported that a large variety of guest atoms can be inserted, such as rare earth elements /KUZ03, MOR97, NOL98b, NOL00a, PEI08/, alkaline earth elements /CHE01b, PUY04, ZHA06b/, alkali metals /PEI06, PEI09/, or others /FUKU10, HAM10, NOL00b, NOL04, SAL00 /. The filling atoms are loosely-bound to the other atoms in the cages, leading to strong phonon scattering and significant reduction of the thermal conductivity /KEP98, HER03/. Adding filler atoms into the void of the $R_xCo_4X_{12}$ skutterudite structure introduces also extra electrons resulting in n-type semiconductors. In order to create a p-type material, an element with fewer electrons should substitute for Co. This can be realized by using for instance Fe, which provides holes. The resultant chemical formula of p-type skutterudites is usually written in the form $R_yFe_xCo_{4-x}Sb_{12}$. The range for *y* and *x* (in both n and p-type) is determined by the electronegativity, charge states, and structural stability of the filler atoms. In addition to the single-filled system, double-filled or triple-filled compounds show great promise. Introducing two or three filler elements from different chemical groups into the cages of $CoSb_3$ leads to two or three distinctive filler vibrational frequencies that impact a broader range of phonons, leading to a further reduction in the lattice thermal conductivity /SHI08, YAN07/. As a result, the maximum *ZT* values were improved to 1.3–1.5 (at 800 K) in double-filled n-type skutterudites /SHI08/. The p-type skutterudites show maximum *ZT* values around 0.8 – 0.9 at 800 K. While these values are lower than those of n-type analogues, they are high enough to develop modules based only on

skutterudite legs. Coupled with their good mechanical properties, skutterudies materials are so far among the best candidate materials for power generation in the temperature range 500 – 800 K, which cover a large amount of wasted heat generated in industrial processes including transportation.

III-1-1) Clathrates

Among other materials of interest as potential new thermoelectric materials are clathrates. Several comprehensive reviews of these materials can be found in the literature / CHR10, KOV04, NOL01/. Clathrates (or equivalently clathrate compounds) consist in a framework of atoms or molecules, which form a regular cage-like structure in which guest atoms or molecules are entrapped. Mainly five different clathrate structures are known and are usually referred as Type-I, Type-II, Type-III, Type-VIII and Type-IX. The crystal structure of these sub-families of clathrates is composed of cages of various size and geometry (Figure I-9). So far, only the first two groups have focused the efforts in the search for efficient thermoelectric materials. In particular, due to the numerous compositions, structural, and filling variations, a large variety of electronic properties ranging from semimetallic to semiconducting can be obtained.

Nolas et al. /NOL98a/ have measured the thermal conductivity of semiconducting $Sr_8Ga_{16}Ge_{30}$ polycrystalline samples and observed a T^2 temperature dependence typical of amorphous material. Though this behavior was first attributed to the scattering of low frequency phonons by the Sr atoms (the so-called “rattling” effect), further studies revealed the off-center position of these atoms. These atoms are distributed over four positions with an associated fractional occupancy of one quarter on each position. This distribution leads to tunneling of these atoms between the different positions thereby resulting in additional tunneling states responsible for the T^2 dependence at low temperatures. The strong coupling of the phonon modes associated with these atoms and those of the cages help to lower the thermal conductivity values. These results have triggered extensive theoretical and experimental research efforts to synthesize several of these materials and further understand their peculiar transport properties. Switching the metallic behavior into semiconducting properties can be achieved by varying the chemical composition. Both n- and p-type clathrates can be obtained by the same process, even though the latter type of conduction remains rare. To date, the best *ZT* values obtained for n-type clathrate compounds is about 0.9 /ZHA11a/ and 1.2 /SHI10/ at 680 K and 1000 K in $Ba_8Au_{5.3}Ge_{40.7}$ and

$Ba_8Ni_{0.31}Zn_{0.52}Ga_{13.06}Ge_{32.2}$, respectively. For p-type materials, the maximum *ZT* achieved so far amounts to 0.61 at 760 K in $Ba_8Ga_{16}Al_3Ge_{27}$ /DEN08/. While these values are attractive, it is unlikely that these materials will be implemented into a thermoelectric module due to their poor mechanical properties. The ability of engineering clathrates compounds with glass-like thermal conductivity combined with their relatively good electronic properties has nevertheless classified clathrates as another example of PGEC materials.

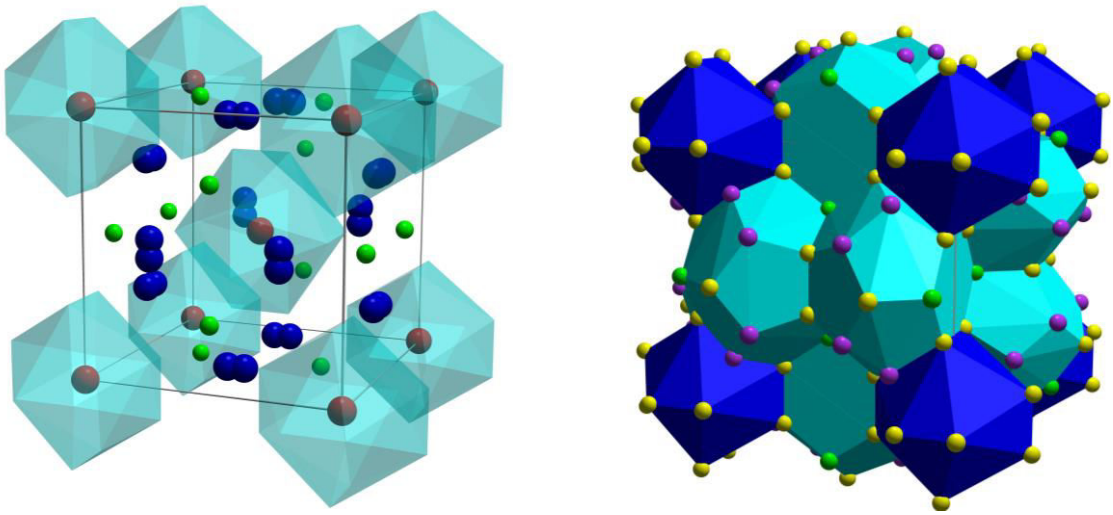

Figure I-9: Crystallographic structure of the ternary type I clathrate $A_8B_{16}E_{30}$. Atoms A (in red and blue on the left image) are located in the center of the two polyedra constituted by atoms B and E (represented in green, violet and yellow on the right image).

III-1-3) Zn_4Sb_3

Another material re-investigated for thermoelectric power generation is β-Zn_4Sb_3 with a hexagonal rhombohedric crystal structure (space group *R*3*C*). Caillat et al. /CAI97a/ have measured the thermal conductivity of polycrystalline β-Zn_4Sb_3 samples. The lattice thermal conductivity was found to be nearly temperature independent between 300 and 650 K with a room temperature value of 0.65 W/mK, nearly twice lower than that of Bi_2Te_3 alloys. This remarkable low value and unusual temperature dependence (a *1/T* temperature dependence is usually observed) can be attributed to the relative complex crystal structure as well as the presence of vacancies in the lattice. The electronic transport properties are typical of a semimetal with low electrical resistivity increasing with increasing temperature. The Seebeck coefficient also increases with temperature and peaks at 675 K with a value of about 200 µV/K. This high thermopower value for a metal is due to fairly large effective masses /CAI97a/. The best *ZT* obtained to date on polycrystalline samples is about 1.4 at 675 K (Fig.

I-12) /CAI97a/. Above 765 K, β-Zn_4Sb_3 transforms into γ-Zn_4Sb_3 that has poorer thermoelectric properties. Band structure calculations /KIM98/ predict a metallic behavior with improved thermoelectric performance for lower doping levels. Little success has however been obtained experimentally in optimizing the doping level of this compound. β-Zn_4Sb_3 forms a full solid solution with the isostructural compound Cd_4Sb_3. Low-temperature thermal conductivity measurements on $Zn_{4-x}Cd_xSb_3$ mixed crystals showed a nearly temperature independent variation of the thermal conductivity. The measured values are even lower than for β-Zn_4Sb_3 /CAI97b/ due to additional point defect scattering. Though a maximum *ZT* of 1.4 at about 400 K was obtained, this solid solution appears to be less stable than β-Zn_4Sb_3 itself. Efforts to incorporate β-Zn_4Sb_3 into advanced, highly-efficient thermoelectric unicouples were undertaken /CAI99/. Further optimization of the thermoelectric properties of these compounds is limited because of the difficulties to dope them and the restricted compositional variations possible.

III-1-4) Half-Heusler

Half-Heusler intermetallic compounds based on MNiSn or MCoSb (M = Zr, Hf, Ti) have also attracted considerable interest as potential new thermoelectric materials. These compounds possess the MgAgAs structure (Fig. I-10) and are closely related to the full Heusler MNi_2Sn which are metals. Replacing one Ni atom by an ordered lattice of vacancies leads to a gap formation in the density of states and to a semiconducting character with band gap values of the order of 0.1 to 0.2 eV. As a result of large electron effective masses in these materials, high Seebeck coefficients are typically obtained above 300 K. Effective masses of 2-3 m_0 were estimated by Uher et al. /UHE99/ for ZrNiSn and Seebeck coefficients as high as –300 µV/K were measured at 300 K in this material. It was originally suggested by Cook et al. that these materials might be good thermoelectrics /COO96/ considering the combination of low electrical resistivity and large Seebeck coefficients. Large power factors of up to 25-30 $\mu W/cm.K^2$ have been experimentally obtained for several of these materials, such as ZrNiSn or HfNiSn. While the power factors are promising, the thermal conductivity of the ternary compounds is rather high. The total thermal conductivity (which is essentially the lattice thermal conductivity for these materials) exceeds 5 W/m.K at 300 K. Efforts were devoted to reduce the lattice thermal conductivity of these materials using mass-defect scattering on the various sublattices leading to some success. So far, *ZT* values around 0.8 at 1000 K in n-type are common /CUL06/. However, p-type doping in MNiSn has not been very successful at

high temperatures, because undoped MNiSn itself is a very strong n-type material. Interestingly, although intrinsically MCoSb is also a n-type semimetal at room temperature, partially substituting Fe for Co, or replacing Sb by Ge or Sn leads to p-type conduction. Currently, Sn doped MCoSb is the most widely studied p-type half-Heusler with a maximum *ZT* value of 0.5 at 1000 K /CUL08/.

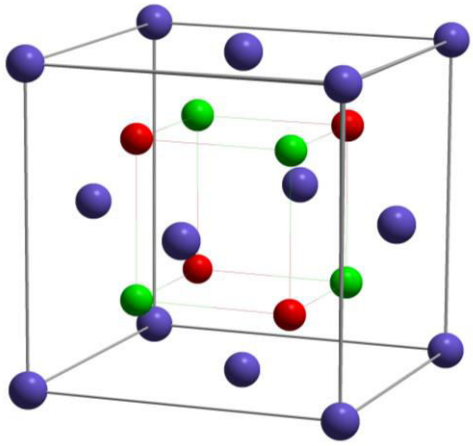

Figure I-10: Crystallographic structure of MNiSn half-Heusler (with M = Zr, Hf or Ti). M atoms are in blue, Ni in red and Sn in green.

III-1-5) Mg_2Si

The intermetallic compounds Mg_2X (X = Si, Ge, Sn) are another class of compounds of considerable interest as potential thermoelectric materials for mid temperature range /DAS11, GAO11, LIU10, MAR09, ZAI06, ZHA08b/. In 1961, Nikitin *et al.* /NIK61/ already underlined that the inherent properties of these compounds could provide a basis for the development of new efficient thermoelectrics. But it is only in 2006 that the thermoelectric potential of these silicides was demonstrated /ZAI06/. The Mg_2X compounds crystallize in the cubic system (Fm3m) and possess the antifluorite structure. Compared with other thermoelectric materials operating in the same temperature range such as PbTe, Mg_2Si-based compounds have the advantages of being non-toxic and composed of elements that are abundant in the earth's crust.

In recent years, progress has been made towards high *ZT* values using doped (Bi, Sb,…) or undoped $Mg_2Si_{1-x}Sn_x$ solid solutions /DAS11, GAO11, LIU10, LIU12a, MAR09, ZAI06, ZHA08a, ZHA08b/. In optimized compositions, a *ZT* above unity has been reached /LIU10, LIU12a, ZHA08b/. The incorporation of Mg_2Sn significantly reduces the thermal conductivity of Mg_2Si. While it is also possible to tune the electrical properties of the Mg_2Si-based compounds by appropriate dopants to get p-type materials, the thermoelectric properties

remain much lower (ZT ~ 0.4 – 0.5 at 600 – 700 K /MAR09/) with respect to those of the n-type analogues and efforts in this direction should be pursued.

III-1-6) Zintl phase $Yb_{14}MnSb_{11}$

$Yb_{14}MnSb_{11}$ has recently emerged as a promising thermoelectric material at very high temperatures. The compound belongs to the Zintl family, $A_{14}MPn_{11}$, where A is an alkaline-earth or rare-earth metal, M is a transition or main-group metal, and Pn is a pnictogen. The Yb analogue appears to be an excellent p-type thermoelectric material. Figure I-11 shows the crystal structure of $Yb_{14}MnSb_{11}$, which crystallizes in the cubic $Ca_{14}AlSb_{11}$ structure type. $Yb_{14}MnSb_{11}$ is considered to be a valence precise semiconductor based on the classical Zintl concept in which the strongly electropositive Yb atoms donate electrons to Sb atoms in the structure. In reality, the material exhibits weakly metallic or semimetallic behavior as a function of temperature.

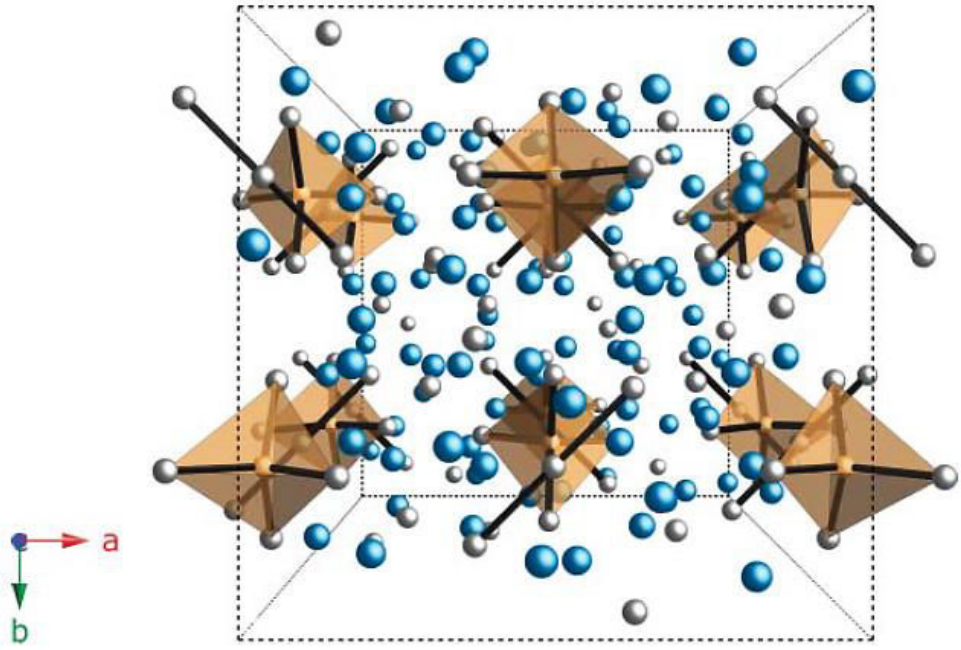

Figure I-11: View of the crystal structure for $Yb_{14}MnSb_{11}$. Yb_2^+ cations, Sb and Mn atoms are shown in blue, grey and brown, respectively.

Polycrystalline $Yb_{14}MnSb_{11}$ demonstrated quite low power factor (6 $mW.cm^{-1}.K^{-2}$) at 1200 K. However, the significantly low thermal conductivity ranging between 0.7 and 0.9 W/mK in the 200 – 1275 K temperature range gives rise to the remarkable ZT value of approximately 1.0 at 1200 K /BRO06/. The low thermal conductivity is primarily attributed to

the large unit cell, the structural complexity, and to the ionic character of the lattice bonding. $Yb_{14}MnSb_{11}$ has nearly twice the *ZT* at high temperatures (975–1275 K) than the p-type SiGe based material (maximum *ZT* of 0.65 at 873 K) /VIN91a, VIN91b/. Hence, it is possible that $Yb_{14}MnSb_{11}$ and its alloys may replace p-type Si-Ge alloys in future NASA space missions.

A variety of substitutions in $Yb_{14}MnSb_{11}$ with other alkaline-earth and rare-earth metals as well as transition/main-group metals has been achieved for further optimization of the thermoelectric performance /FIS00, KAU07/.

III-1-7) Oxides and oxychalcogenides

Numerous oxides with metal atoms in their common oxidation states are stable at elevated temperatures and show electrical properties ranging from insulating to superconducting. Nevertheless, oxides have received very little attention for TE applications because of their strong ionic character: they have narrow conduction bandwidths arising from weak orbital overlap, which leads to localized electrons with low carrier mobilities. This situation changed in 1997 with the unexpected discovery of good p-type thermoelectric properties in a strongly correlated layered oxide, $NaCo_2O_4$ /TER97, TER02/, where a *ZT* ~ 0.7–0.8 at 1000 K was obtained in single crystals. Inspired by this striking thermoelectric performance, intensive efforts were made later on Co-based layered oxides such as $Ca_3Co_4O_9$ and $Bi_2Sr_3Co_2O_y$ that crystallize in misfit-layered structures /DIE10, KEN12/. However, the results obtained on polycrystalline samples proved to be quite disappointing with maximum *ZTs* around 0.2-0.3 at 900 K /DIE10/. Among the n-type oxides, Al-doped ZnO ($Al_{0.02}Zn_{0.98}O$) exhibits reasonably good TE performance (*ZT* ~ 0.3 at 1000 K and under nitrogen) /OHT96/ but its performance is highly dependent of the oxygen stoichiometry, which depends on the measurement atmosphere (under air for example, the *ZT* drops to only 0.1) /BER10/.

Oxyselenides deserve also great interest /LI12b, SUI13, ZHA14a/. These materials, originally investigated for their superconducting properties, are at the interface between oxides and intermetallics. These materials exhibit a layered structure and one of the member of this family based on BiCuSeO has been found to exhibit promising p-type thermoelectric properties with *ZT* ~1.4 at 923 K /SUI13/. The reader interested by this new family of compounds may read a recent dedicated review /ZHA14a/.

Before turning to the materials for low-temperature applications, it is worth mentioning the recent work on SnSe single crystals where a record *ZT* of 2.6 at 923 K was claimed by

Zhao et al. /ZHA14b/ due to an extremely low thermal conductivity. However, this astonishing result should be taken with care because three reports suggested, few weeks later, that the thermal conductivity was underestimated /SAS14, CHE14, CAR14/.

III-2) Low and room temperature bulk materials

While several materials with $ZT > 1$ have been identified above room temperature, there is a severe need for new thermoelectric materials with $ZT > 1$ for cooling applications. At and below room temperature, only two materials, which have been known for many years, have decent thermoelectric properties: Bi-Sb and Bi_2Te_3 alloys. According to the 10 k_BT rule, if one looks for new low-temperature semiconducting thermoelectric materials, one should investigate narrow band gap materials /MAH98/.

III-2-1) Chalcogenides

An extensive effort at Michigan State University has focused on a number of new chalcogenides composed mostly of heavy elements. They have identified a number of potential new materials for low-temperature thermoelectric applications. A comprehensive review of these materials can be found in the literature /KAN01/. A number of complex phases have been prepared preferably by a flux technique and several new compounds have been identified. Among the materials investigated are the sulfides $KBi_{6.33}S_{10}$ and $K_2Bi_8S_{13}$, the selenides β-$K_2Bi_8Se_{13}$ and $K_{2.5}Bi_{8.5}Se_{14}$, $A_{1+x}Pb_{4-2x}Bi_{7+x}Se_{15}$ (A = K, Rb) compounds, and the tellurides A/Bi/Te and A/Pb/Bi/Te. A common feature of most of these materials is their low thermal conductivity, comparable or even lower than that of Bi_2Te_3 alloys. Many of these compounds show very anisotropic transport properties. Perhaps the most promising compound identified to date is $CsBi_4Te_6$. This compound has a layered anisotropic structure with Cs ions between Bi_4Te_6 layers. The atomic displacement parameters (ADPs) of the Cs ions are 1.6 times larger than those of the Bi and Te atoms. Crystals of $CsBi_4Te_6$ grow with a needle-like morphology and are stable in air and water. The crystals are amenable to doping and SbI_3, BiI_3 or In_2Te_3 have been successfully used to optimize the carrier concentration of this material. The power factor can be maximized through doping and a maximum power factor of about 50 $\mu W/cm.K^2$ was obtained at 185 K in the p-type material /KAN01/. The total thermal conductivity along the growth axis is about 1.5 W/m.K at 300 K and is essentially constant down to 100 K. This atypical temperature dependence suggests again that

the "rattling" Cs ions significantly contribute to phonon scattering in this compound. The best *ZT* to date obtained along the needle direction is 0.82 for the p-type material (see Fig. I-12), slightly better than p-type Bi_2Te_3 at this temperature. The In_2Te_3 "doped" n-type material has poorer thermoelectric properties. Nevertheless, p-type $CsBi_4Te_6$ is the first compound identified in the low temperature range to match or even outperform Bi_2Te_3 alloys. Whether or not this compound can be further optimized through doping and/or alloying will need to be determined in the future as well as its mechanical stability to envisage its practical use in devices.

III-2-2) Pentatellurides

Pentatelluride materials such as $HfTe_5$ and $ZrTe_5$ /LIT98/ and their alloys have been considered as promising new thermoelectric materials at low temperatures because of their relatively large thermopower values at low temperatures which, combined with relatively low electrical resistivity values, result in large power factors. Electronic properties can be tuned through alloying and doping but the challenge is clearly to reduce the lattice thermal conductivity. Thermal conductivity values range between 2 and 5.5 W/mK. Another challenge lies in the very anisotropic nature of these materials, which requires the growth of large single crystals for their characterization. Single crystalline whiskers were obtained by a vapor transport technique but measurements on these small crystals are a great challenge. Further investigations will be required to determine whether or not the transport properties of these materials can be further optimized and if thermal conductivity values close to those of state-of-the-art thermoelectric materials can be obtained without significantly degrading the electronic properties.

III-2-3) Organic materials

Organic polymeric materials constitute a recent growing topic in thermoelectricity thanks to their easier process of preparation with respect to that of inorganic materials, their low cost in some cases, their high flexibility, and the easiness to tune their properties by simply changing their molecular structures. Besides, they are considered environmentally friendly. The organic polymers, however, exhibit an important drawback *i.e.* their lack of thermal stability at high temperatures confining them to near-room-temperature applications. Among the ever-growing number of organic polymers studied nowadays, the one that present the most suitable properties for thermoelectric applications is the poly (3,4-

ethylenedioxythiofene), known as PEDOT, which has also been widely investigated for a number of other applications, such as photovoltaics /YAN11b/, sensors /LAT09/, bioelectronics /XIA04/ or electroluminescent devices /GAR99/. When PEDOT is doped with tosylate (Tos), the resulting films of PEDOT:Tos exhibit a Seebeck coefficient of ~210 µV/K and an electrical conductivity of ~70 S cm^{-1}, that combined with the low value of the thermal conductivity of 0.33 W/m K yields a *ZT* value of 0.25 at room temperature /BUB11/. This result, while still moderate compared to state-of-the-art materials, could be an alternative in the future provided higher *ZT* values are obtained and good n-type polymers are also discovered. So there is still a long way to go!

To summarize this non-exhaustive list of materials showing an interest for thermoelectric energy conversion, figure I-12 represents the temperature dependence of *ZT* of the advanced n- and p-type materials presented.

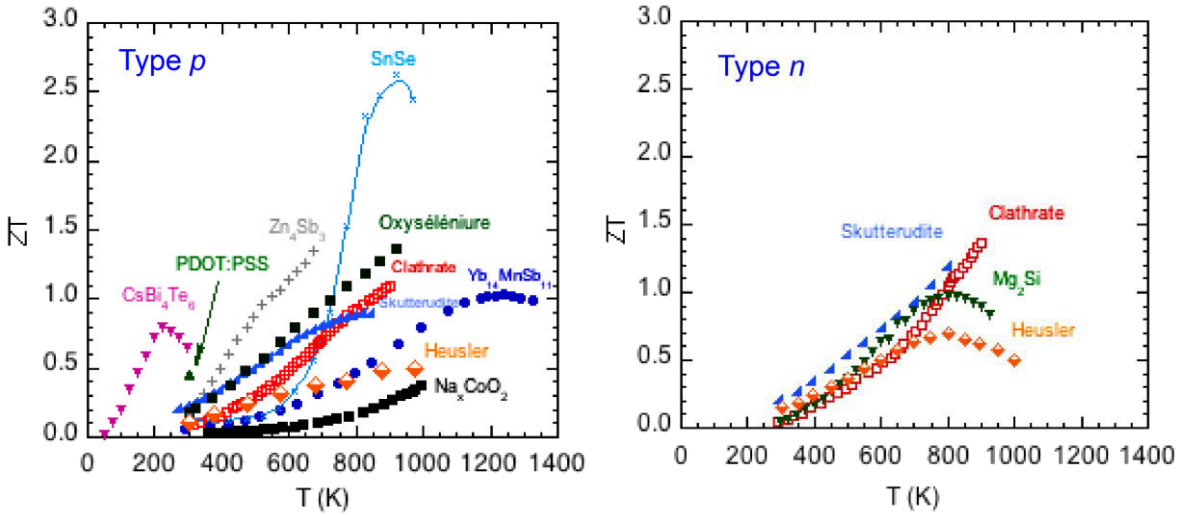

Figure I-12: Temperature dependence of *ZT* for some n and p-type advanced thermoelectric materials (see text for references).

III-2) Low-dimensional structures and nanostructured bulk materials

During the last two decades, there has been a considerable interest in studying both theoretically and experimentally the thermoelectric properties of low-dimensional structures and nanostructured bulk materials. Exciting and encouraging results have been obtained in these materials. It should be first remembered that nanomaterials, or nanostructured materials refer to a material containing "building blocks" with at least one dimension in size less than 100 nm.

The idea of selectively modifying material properties using lower dimensional structures was first introduced by Hicks and Dresselhaus in 1993 /HIC93a/. They theoretically showed that by using two-, one-, or even zero-dimensional structures made of conventional thermoelectric materials one could obtain a significant increase in the thermoelectric properties (ZT ~ 2-6!), far beyond what was believed possible in bulk thermoelectric materials. There are basically two mechanisms through which ZT can be improved in low-dimensional systems. The first one is linked to size-quantization effects that can increase the thermopower while unaffecting the density of charge carriers and thus the electrical conductivity /HIC93a/.

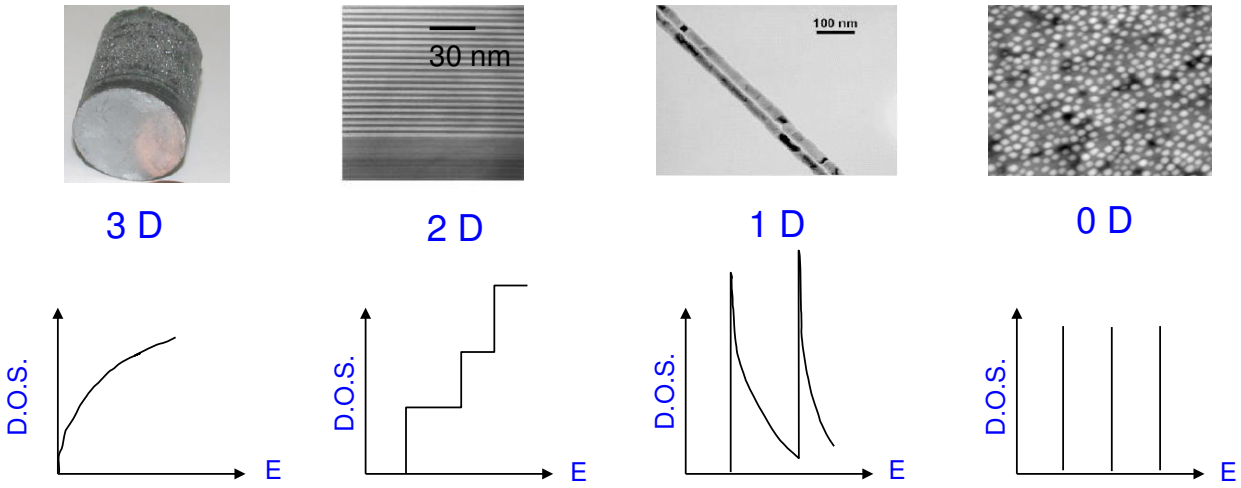

Figure I-13: Electronic density of states (D.O.S) as a function of energy E for a bulk 3D material (3D), a 2 D material, or quantum well, a 1 D material or quantum wire and a 0 D material or quantum dot. As can be seen, the density of states is a strong function of the dimensionality of the system.

Considering that nanostructures confine the electron wave function in zero, one or two dimensions, the electronic density of states $g(E)$ (the number of quantum states available to electrons at energies between E and $E + dE$) at the quantization energies becomes a strong function of the electron energy as shown in Fig. I-13. For low-dimensional systems, $g(E)$ has a sharp maximum at the quantization energy. In solids, where the electron distribution is metal-like, α is proportional to $\propto g(E_F)/n$, where E_F is the Fermi level and n is given by the integral under the $g(E)$ curve from $E = 0$ to $E = E_F$ /HER12/. The sharper a function of energy $g(E)$ is, the higher the ratio $g(E_F)/n$ is, provided that E_F falls near a maximum in $g(E)$. When E_F is tuned to fall at an energy where $g(E_F)$ is maximal in nanostructures, a strong enhancement in the product S^2n occurs. The second mechanism lies on the expectation of a reduction in the lattice thermal conductivity due to modified phonon dispersion relations and

interfacial effects such as acoustic mismatch, defects and dislocations, and roughness /CAH03, HOC08/.

The basic ideas proposed by Hicks and Dresselhaus /HIC93a, HIC93b/ has ignited intense theoretical and experimental researches. Advanced elaboration techniques have been used to fabricate nanostructures such as superlattices (2D structures), nanowires (1D structures), and quantum dots (0D structures) for which the thermoelectric properties could be measured. Increases in *ZT* in superlattices, such as Bi_2Te_3/Sb_2Te_3 /VEN01/, PbTe/Te /HAR99/, PbTe/PbSe /HAR00/, $PbTe/Pb_{1-x}Eu_xTe$ /HAR02, HAR96, HIC96, KOG99a/ and $SrTiO_3/SrTi_{0.8}Nb_{0.2}O_3$ /OHT08, VIN08/ have been reported. Some of these authors claimed record values with *ZT* exceeding 2 or 3 but in at least in two cases /HAR99, HAR00/ the apparent increase was erroneous due to inaccurate carrier concentration measurement, and subsequently corrected measurements confirmed that no *ZT* enhancement due to quantum confinement was observed /VIN08/. Even if quantum confinement of electronic carriers has yet to be proved, the reduction of the phonon thermal conductivity due to more efficient phonon scattering than electron scattering at the interfaces has been clearly established (in superlattices but also in nanowires /BOU08, HAR02, HAR96, HAR99, HAR00, HIC96, HOC08, KOG99a, OHT08, VEN01/ and other systems /KIM06/) and is considered as the main reason of the improvement in *ZT* in the artificial structures.

Although a high *ZT* has been reported in low-dimensional materials, many of these artificial structures are not practical for large-scale commercial use owing to the synthesis techniques used. They are indeed fabricated by atomic layer deposition processes such as molecular beam epitaxy, making them slow and expensive to develop, thereby restricting the amount of material that can be produced. Fortunately, theoretical results obtained by studying superlattices provided a solution to this dilemma. Modeling of phonon transport in superlattices indicated that the primary benefit from nanostructures, a reduced lattice thermal conductivity, does not require an atomically perfect interface or an exact geometry /CHE01a/. All what is required is a material with a high density of interfaces, which can be present in any geometry /JEN08/. This discovery led naturally to the idea that bulk nanostructured materials might be a fertile playground for such effects. These materials retain the high density of interfaces but do not have a special geometry or structure, significantly simplifying the fabrication process and enabling a scale-up of the materials production /YAN05/.

Nanostructured bulk materials have been the subject of significant research over the last years and many excellent reviews are available /BUX10, KAN09, LAN10, LIU12b, MAR13, MED09, MIN09, VAQ10, VIN10/. Instead of doing a detailed review, we shall focus shortly in the next paragraphs on the different types of nanostructuration that can be met in a bulk thermoelectric material, on the preparation methods and on the most salient results obtained to date.

Nanostructured bulk thermoelectric materials exhibit different micro/nano-structures depending on the strategy used to synthesise them. There are four main types of nanostructuration that can be identified as illustrated schematically in Fig. I-14. The first type (Fig. I-14a) refers to a polycrystal made of nanograins of the same composition (or same phase). Type 2 (Fig. I-14b) consists in embedded nanoparticles inside the lattice while type 3 (Fig. I-14c) refers to multi-layered grains. The last type, type 4 (Fig. I-14d), is a polycrystalline material with nano-inclusions at the grains boundaries or with grains coated with another material. In the types 2, 3 and 4, structures may be formed from two or more materials and these structures are usually called nanocomposites. Experimentally, a nano bulk thermoelectric material may have a structure similar to any of these types or a combination of them.

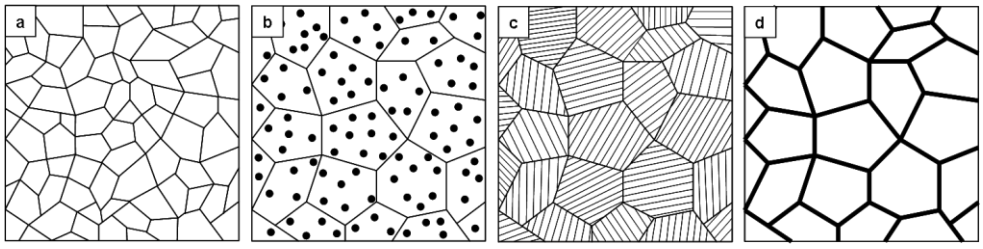

Figure I-14: Different nanostructured bulk materials: (a) refer to structures consisting on one material with a polycrystalline nano-structure. (b), (c) and (d) refer to structures formed by two or more materials, being (b) grains with nanometric inclusions, (c) multi-layered grains, and (d) grains coated with another material or materials with nanoinclusions at the grain boundaries.

There are basically two major approaches, via top-down and bottom-up methods (see Fig. I-15), to fabricate nanostructured bulk thermoelectrics and each of them can be divided into several branches. In addition, a combination of the two approaches is also possible. The top-down methods start from a bulk material and the corresponding nanostructured features are obtained by structural deformations. There are four techniques used which are based on: sever plastic deformation /KOU13/, laser fracture in a liquid media /CHU11/, high energy ball milling, and thermal processing, the last two being the more used. The technique of high-

energy ball milling has attracted much attention in the synthesis of nanostructured thermoelectric materials /BUX09, DRE07, POU08, WAN08/ because of its fully scalability from a few grams to kilogram quantities in hour-time scales. In this method, elemental powders or intermetallic compounds are inserted into a milling vial with some ball bearings / HAR95, SUR01/. The vial is then loaded into a high-energy ball mill. The constant agitation of the ball mill causes the powders to be subjected to a series of impact collisions between the powder and ball bearings. As a result, the powders are constantly cold-welded and fractured, leading to the formation of nanostructured domains (type 1).

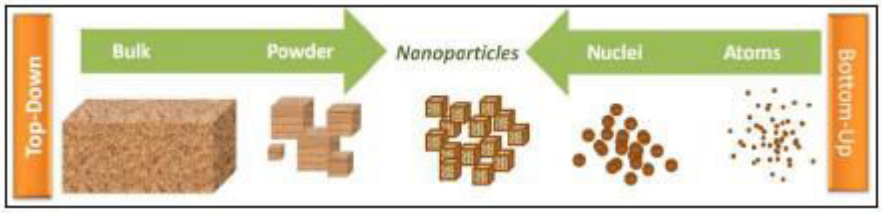

Figure I-15: Scheme of top-down and bottom-up approaches.

Thermal processing techniques have also been widely applied to introduce nanoscale precipitates or domains in a bulk material /AND07, AND11, BIS11, BIS12, GIR10, HE10, HE11, HSU04, IKE07, JOH11, KAN09, LI08a, LI09, SOO06, SOO09, XIE09a, XIE09b, XIE10a/. These techniques include the nanoprecipitation and the melt-spinning techniques. The nanoprecipitation technique is an effective solid-state approach for preparing bulk materials containing nanoinclusions. PbTe-based nanocomposites including $AgPb_mSbTe_{2+m}$ (also known as LAST-m), $AgPb_mSn_nSbTe_{2+m+n}$ (LASTT-m), $NaPb_mSbTe_{2+m}$ (SALT-m), and KPb_mSbTe_{2+m} (PLAT-m) family of compounds can be easily fabricated by this method /AND07, AND11, BIS11, BIS12, GIR10, HE10, HE11, HSU04, JOH11, KAN09, SOO06, SOO09/. During the cooling process of the molten material, nanoinclusions are produced within the matrix by phase segregation or spinodal decomposition; however, it is difficult to control the carrier concentration from batch to batch due to the complex nature of the materials system and the phase diagram. Thus, accurate temperature control is a key aspect of this synthesis. A nanoscale lamellae structure can also be formed by this technique /IKE07/. The advantage of this technique is that it is a one-step technique in which nanoscale inclusions or lamellae are formed by a simple thermal treatment. Moreover, this process can provide coherent or semi-coherent interfaces favorable for electronic transport. This is a promising method of making thermoelectric nanocomposites *in situ*. Melt-spinning is another interesting approach where nanostructured domains are also prepared in-situ /BOE08, EBL09,

LI08a, LI09a, SAL13, TAN13, XIE09a, XIE09b, XIE10a/. The idea is to rapidly cool a liquid melt to room temperature or below to prevent grain growth and favor the glassy state. From a practical point, the melt-spinning method uses a rotating wheel cooled internally, usually by water or liquid nitrogen, and rotated. A thin stream of melt then falls onto the wheel and is cooled, in an inert atmosphere, causing rapid solidification. More details about this technique will be provided in chapter III since this method was intensively used in this work.

The bottom–up approach consists in the production of the nanostructured materials starting from atoms, molecules or ions. This approach includes, obviously, high vacuum techniques, like molecular beam epitaxy (MBE) or physical or chemical vapor deposition (PVD or CVD) to produce nanostructured films (2D systems). In these cases, the building blocks that will constitute the thin film are the atoms. Another particularly interesting bottom-up approach is to use soft chemistry processing where the building blocks will be ions in solution. Examples of these methods include hydrothermal/solvothermal synthesis /LI08b/, synthesis in organic medium /SON09/ and decomposition of organometallic complexes /FAN14, URB06/. These methods are usually easy to perform and they offer a low cost alternative to produce nanostructured materials due to the low reaction temperatures and low processing times. Although the chemical methods can provide excellent control over morphology and particle size distribution, they have some important drawbacks: 1) it can be difficult to control accurately the stoichiometry; 2) it can be very challenging to remove completely external agents (as solvants, surfactants, ligands…) and to obtain dense materials; 3) it can be quite difficult to get phase pure materials. All these issues can be problematic for practical thermoelectric applications as the lack of stoichiometry and low density can adversely affect the electrical transport properties of the materials and degrade significantly the *ZT* values.

Regardless of the approach used, bottom-up or top-down, the starting materials are often powders, and in this form, they cannot be used to perform transport measurements. So the next step is to consolidate the powders by a sintering process. This step is also critical if the goal is to keep the nano-features. Usually uniaxial hot press (HP) is more effective to get higher dense bulk samples than conventional cold-pressing. Although HP is widely used for compacting the initial powders prepared by the methods described previously, it may not be the most effective densification technique because the time of sintering is quite long (several hours) and this can promote grain growth. For this reason, Spark Plasma Sintering (SPS) offers several advantages. In little more than a decade, it has become an established

consolidation method for the fabrication of dense polycrystalline specimens /OMO00, TOK93/. The SPS process is similar to conventional HP, however, instead of heating the die and powder inductively or resistively, a direct electrical current, or a pulse of electric current, is applied to the graphite punch-and-die set which passes through the specimen so that it is heated both from the inside and from the outside. This process generates internal localized heating thus allowing for the rapid, low-temperature, densification of fine-grained powders. SPS minimizes the temperature gradients inside the specimen by guarantying electrical contacts between all parts. Since only the surface temperature of the nanopowders rises rapidly by self-heating, grain growth is controlled. A sintered compact is densified in a much shorter time as compared to HP (several minutes instead of several hours). The general speed of the process, therefore, avoids grain growth.

Let's now turn to a brief review of the more salient thermoelectric results obtained to date with nanostructured bulk materials. Several reports show that conventional materials such as Bi_2Te_3 based materials /POU08, FAN10, TAN07, XIE09a, XIE09b, XIE10a/, PbTe /SOO08, AND07, GEL10/, and SiGe /JOS08, WAN09/ alloys benefit markedly from their nano bulk structured forms as shown in Fig. I-16. The improved thermoelectric performance in all these nanostructured state-of-the-art materials was attributed to a significant drop in lattice thermal conductivity compared to non nanostructured materials over a wide range of temperatures. The progresses made specifically on Bi_2Te_3 based solid solutions will be reviewed in detail in the next chapter. As already mentioned, the nanoprecipitation technique was found to be an effective method for improving the thermoelectric properties of n-type PbTe-based materials. A *ZT* of 1.4 at 673 K was obtained in PbTe containing nanoinclusions of Sn and Pb /HSU04/ while using the spinodal decomposition in the PbTe/PbS system, a *ZT* of 1.5 was reached at 642 K /AND07/. Regarding Si-Ge alloys, it is through a ball-milling and hot-pressing combination that a significant increase in *ZT* was achieved in *p*-type SiGe nanocomposites, reaching a peak value of about 0.95 at 1173–1270 K /JOS08/. The *ZT* improvement was about 50% over the previous highest record (0.65) /VIN91a, VIN91b/. A peak *ZT* of about 1.3 at 1173 K was also achieved in *n*-type SiGe nanocomposites using the same synthesis process /WAN09/.

Besides the above conventional nanostructured bulk materials, the technique has also been applied to other materials systems, including skutterudites /JIE13, LI09b, TAN13, YAN09, ZHA06a/, half-Heuslers /JOS11, XIE10b, YAN11a/, silicides (Mg_2Si) /BUX11, ZHA08a/… Among them, interesting results were obtained in both n- and p-type half Heusler

materials prepared by ball milling to produce nanopowders and then hot pressing. This combination resulted in a simultaneous increase in the thermopower and a significant decrease in the thermal conductivity, which led to a 60% increase in the peak *ZT* from 0.5 to 0.8 at 973 K /YAN11a/ and 25% for n-type (*ZT* = 1) /JOS11/. Since *ZT* ~ 1 (the benchmark for device applications) has been achieved in half-Heusler's, module fabrication has been catching more and more attention.

Before concluding this chapter, it is also important to underline the impressive results obtained in the LAST-18 /HSU04/, LASTT /AND06/, SALT-20 /POU06/ and PLAT-20 /POU09/ materials by the group of Kanatzidis using the nanoprecipitation technique. As shown in Fig. I-17, *ZT* values exceeding 1.5 and even 2 at high temperatures have been reported for all these lead chalcogenide compounds.

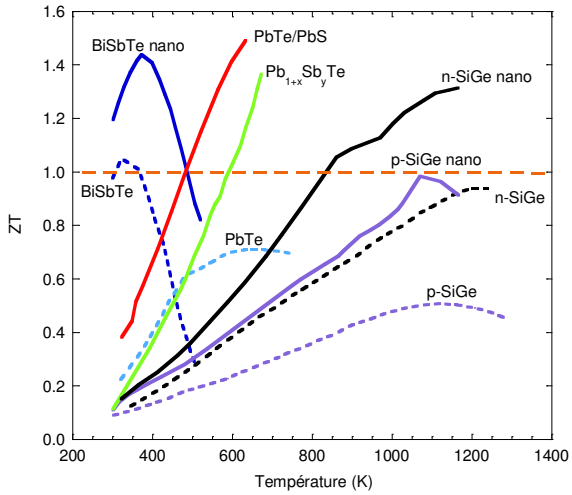

Figure I-16: Temperature dependance of *ZT* for conventional bulk materials (discontinuous curves) and nanostructured bulk materials (continuous curves). The benefic impact of the nanostructuration on the thermoelectric properties is quite clear and impressive. [BiSbTe /POU08/, PbTe/PbS /AND06/; $Pb_{1+x}Sb_yTe$ /SOO08/; n-SiGe /WAN08/; p-SiGe /JOS08/]

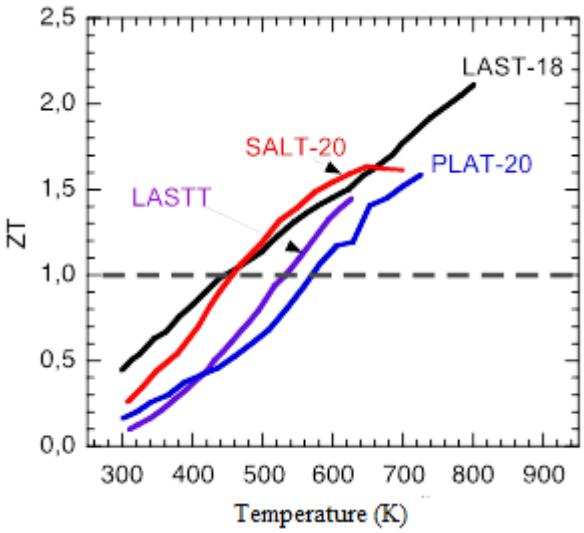

Figure I-17: Temperature dependance of ZT for new lead chalcogenide compounds. [LAST-18 /HSU04/, SALT-20 /POU06/, LASTT /AND06/, PLAT-20 /POU09/]

CONCLUSION

Several topics were covered in this chapter including basic thermoelectric phenomena and materials development. It was shown that a resurgence of interest in thermoelectricity took place in the beginning of the 1990s due to the proposal of new concepts (PGEC) and new directions of research (low-dimensional systems, open and/or complex crystal structures). Intensive theoretical and experimental works led to an increase of the dimensionless figure of merit *ZT* for low, room or high temperature applications as it is demonstrated in figure I-18. The recent development of nanostructured bulk materials shows great promise, and among the progress made, the case of bismuth telluride related compounds should be underlined. As already mentioned, these materials play an important role in commercial modules for cooling or air conditioning near room temperature. Any increase in the performances of these materials will be beneficial in enlarging their field of applications. However, bismuth telluride and their solid solutions cannot be classified as “simple or normal materials” because of their physical and structural peculiarities making their thermoelectric optimization extremely challenging, as we shall see in the Chapter II.

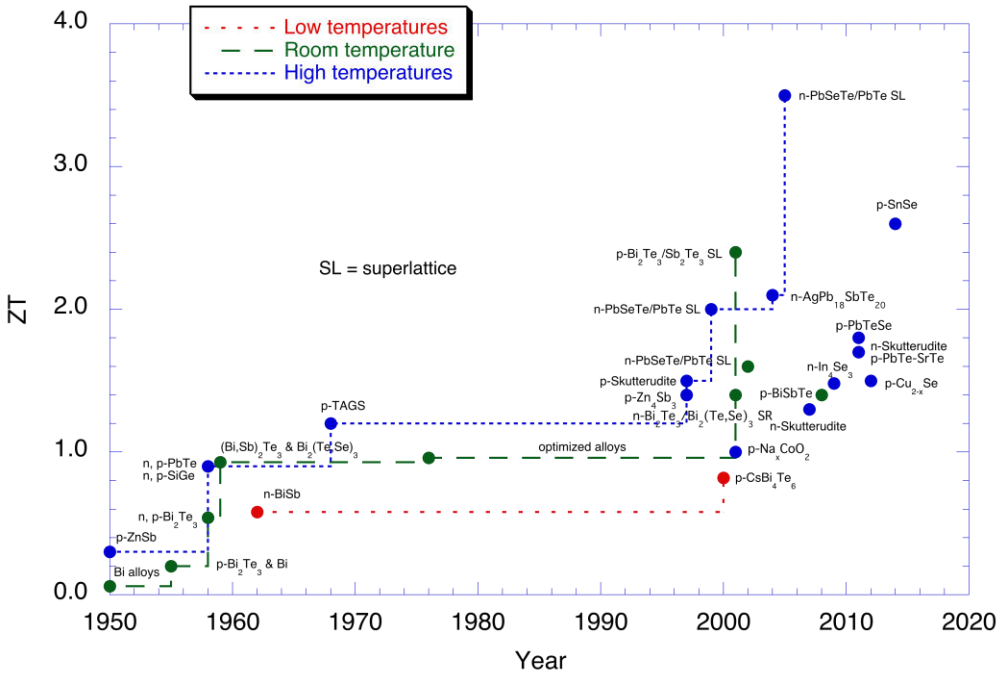

Figure I-18: Evolution of *ZT* over the years. Two distinct breakthroughs can be evidenced from this figure: the first one (just before 1960) is due to the emergence of semiconductors while the second one (after 1990) is linked to the development of new families of materials and nanomaterials.

Chapter II

$Sb_{2-x}Bi_xTe_3$ solid solutions: general properties and state-of-the-art

INTRODUCTION

Studies and measurements of the electrical properties of bismuth telluride Bi_2Te_3 and other compounds in the series $A_2^{V}B_3^{VI}$ (A = Bi or Sb and B = Te, Se) were done as early as 1910 /HAK10/. Some decades later, Goldsmid and Douglas /GOL54/ reported for the first time that Bi_2Te_3 is an effective thermoelectric material. A thermocouple made from a p-type sample of this compound connected to a negative thermoelement made from bismuth was found to yield a cooling effect of 26 K below ambient temperature. Beyond this promising result, this experiment established also the fact that semiconducting thermoelements are superior to metals. Thus, by 1955, after n-type bismuth telluride had been obtained by doping with iodine, it was found that a couple made from both types gave a Peltier cooling effect of 40 K below room temperature or equivalently a *ZT* of 0.35 /GOL55/. During the next couple of years, efforts were made to optimize the electrical properties of the n and p- Bi_2Te_3 thermocouple. The best result led to a *ZT* of about 0.6 /GOL58/.

It was not long after the establishment of bismuth telluride as a thermoelectric material that the ideas of Ioffe et al. /IOF57b/ on semiconducting solid solutions became known. The basic idea was to modify an already promising compound by introducing point defects through the synthesis of isostructural solid solutions. Actually, the solid solutions provide an environment of atomic mass fluctuation throughout the crystal lattice (i.e. disorder) which induces strong phonon scattering while electrons, that possess much higher wavelengths than phonons, will have little affected mobilities. As a result, the lattice thermal conductivity is expected to be much more reduced than the electrical properties leading to a larger *ZT* value. The beneficial effect on the thermal conductivity wad proved first on PbTe, on alloying it with PbSe or SnTe and was duplicated later on alloying Bi_2Te_3 with isomorphous compounds such as Sb_2Te_3 and Bi_2Se_3. Several groups / BIR58, GOL68, ROS59/ demonstrated that solid solutions exhibit lower lattice conductivities than pure bismuth telluride (Fig. II-1) while the electrical properties were kept at a good level. Thus, the best thermoelectric properties were found to be for the p-type Sb_2Te_3-rich $Sb_{2-x}Bi_xTe_3$ solid solutions with $x \sim 0.2$ - 0.25 ($ZT \sim 0.9 - 1$) and for the n-type Bi_2Te_3-rich $Bi_2(Te_{1-y}Se_y)_3$ solid solutions with $y \sim 0.1$ ($ZT \sim 0.8 - 0.9$). During more than sixty years and despite intense effort research, quasi none improvement of *ZT* was observed in these compounds as illustrated in Fig. I-18.

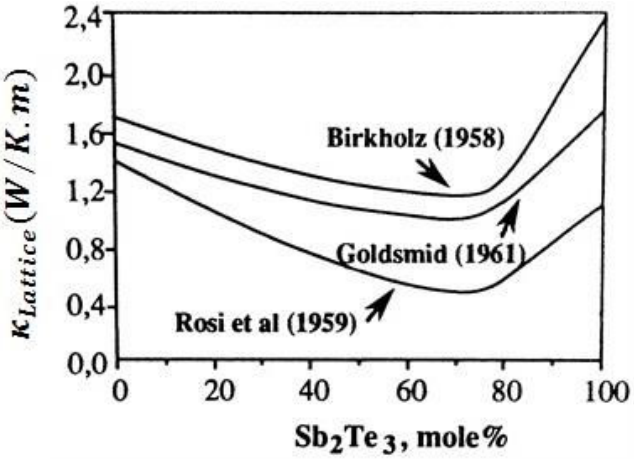

Figure II-1: Lattice thermal conductivity at 300 K plotted versus concentration of Sb_2Te_3 in $Sb_{2-x}Bi_xTe_3$ solid solutions (based on the data of Rosi et al., Birkolz and Goldsmid /BIR58, GOL68, ROS59/). The difference between the results is attributed to the different methods for estimating the electronic thermal conductivity.

As already discussed in the first chapter, the situation changed at the beginning of the 1990's with the advancements in nanostructured materials including both low dimensional systems and bulk materials. To test the new concepts, state-of-the-art materials, including solid solutions based on Bi_2Te_3 were re-investigated. Briefly, the first remarkable results were obtained in superlattices using thin layers (of the order of 100 nm) of Bi_2Te_3 and Sb_2Te_3 (p-type) and Bi_2Te_3 and $Bi_2Te_{2.83}Se_{0.17}$ (n-type). In p-type, *ZT* at 300 K was found as high as 2.4 while the n-type yielded a value for *ZT* of 1.4 /VEN01/ due to a severe reduction of the lattice thermal conductivity. These results are so far the highest reported for the family of (Bi,Sb,Te,Se) materials but, unfortunately, despite numerous attempts, these works were never reproduced by other groups, maybe due to the extremely complex process of sample preparation (MOCVD). On the other hand, the scale-up of this method for commercial scale production would be challenging.

Some years later after the discovery of Venkatasubranian et al. /VEN01/, significant improvements were also claimed in bulk nanostructured materials with *ZT* greater than 1.4 at 300 K /POU08, XIE09, FAN10/ in p-type $Sb_{2-x}Bi_xTe_3$ using bottom-up or top-down methods.

In this chapter we will give an overview of the general properties of $Sb_{2-x}Bi_xTe_3$ solid solutions including crystal structure, electronic structure, phase diagrams and defects responsible for deviation from stoichiometry. Then we will present a brief review of past results on the

thermoelectric properties obtained in single crystals and polycrystalline compounds. Finally, we will summarize the main advances obtained in nanostructured bulk $Sb_{2-x}Bi_xTe_3$ solid solutions. Interesting reviews covering part of this topic can be found in the literature /GOL09, GOL73, ROS68, ROW95, …/. It is interesting to note that the p-type solid solutions are still referred in the literature as bismuth telluride alloys or even, loosely, as bismuth telluride, in spite of the fact that they are composed mostly of Sb_2Te_3. It is for this reason, that all chemical formulae are written differently in this manuscript from what is generally admitted in the literature.

I) GENERAL PROPERTIES OF $Sb_{2-x}Bi_xTe_3$ SOLID SOLUTIONS

I-1) Crystal structure

$Sb_{2-x}Bi_xTe_3$ solid solutions crystallize in a rhombohedral system (Fig. II-2) with the space group D_{3d}^5 (Schoenflies nomenclature) or $R\bar{3}m$ (short international Hermann-Mauguin nomenclature). Sb and/or Bi atoms are located on one site while Te atoms have two different atomic positions. The unit cell contains 5 atoms and the main symmetry elements are:

1) a single threefold (trigonal) rotation axis (in a direction of the longest main diagonal of the rhombohedral cell),

2) three twofold axes normal to three reflection planes containing the trigonal axis,

3) a center of inversion.

It is usually easier to consider the hexagonal rather than the rhombohedral representation (Fig. II-2). Using this representation, the $Sb_{2-x}Bi_xTe_3$ elementary cell can be described as the set of complex layers – quintets – that are perpendicular to the trigonal symmetry axis. In the hexagonal unit cell, three quintets exist (the number of atoms is equal to 15). Each quintet consists of five primitive layers (Figs II-2 and II-3).

The lattice parameters a, b and c, of the hexagonal cell for the end members of this family at 300 K are:

a = b = 4.275 Å, c = 30.490 Å for Sb_2Te_3 (x = 0), /SMI62a/,

a = b = 4.3835 Å, c = 30.487 Å for Bi_2Te_3 (x = 1), /LAN39/,

while for x = 0.50 ($Sb_{1.5}Bi_{0.5}Te_3$) :

a = b = 4.295 Å, c = 30.35 Å /SMI62b/,

a = b = 4.275 Å, c = 30.45 Å /GOL73/.

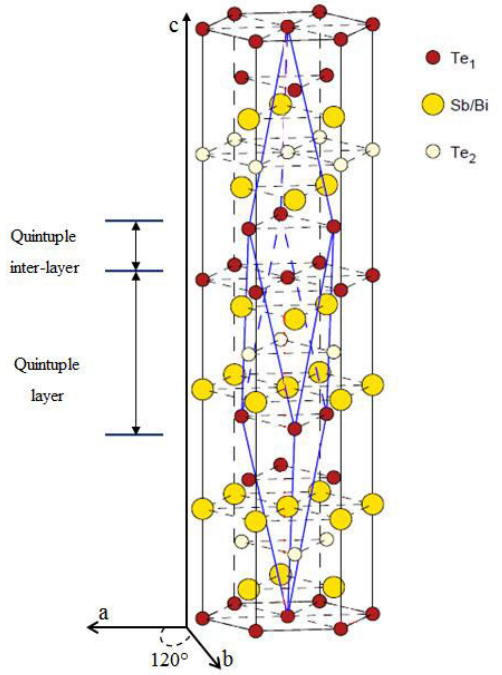

Figure II-2: Crystallographic structure of $Sb_{2-x}Bi_xTe_3$. Blue lines show the rhombohedral elementary cell.

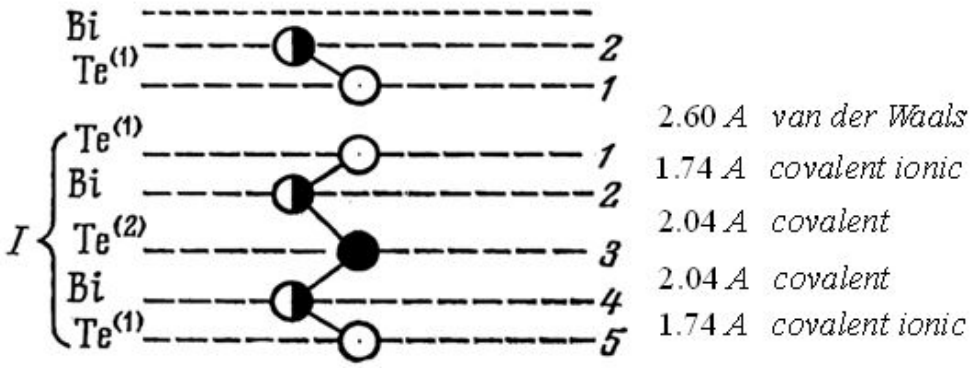

Figure II-3: Atomic arrangement in the lattice quintet of Bi_2Te_3

Atoms within one layer are identical for the binaries and form a hexagonal lattice in plane. A quintet is formed by the sequence – $Te^{(1)}$ – Sb – $Te^{(2)}$ – Sb – $Te^{(1)}$ –. The atoms of each subsequent layer are located above the centers of the triangles formed by the atoms of the previous layer (the hexagonal close packing). Atoms of bismuth replace atoms of antimony in the ternary compounds. $Te^{(2)}$ atoms have six atoms of Sb (or Bi) as closest neighbors (three from each adjoining simple layer), $Te^{(1)}$ atoms are linked with three atoms of Sb and three other atoms of $Te^{(1)}$. Thus, there are two significant different positions for the tellurium atoms in the lattice

structure (Fig. II-2): $Te^{(1)}$ with coordinates (0, 0, 0) and $Te^{(2)}$ with coordinates (0, 0, z). The atoms within this sequence are subject to mixed valence-ionic binding, while the quintets are linked by weak van der Waals bonds, accounting for the very ease of cleavage perpendicularly to the trigonal axis (i.e. along the basal planes) (Fig. II-3). The strong anisotropy resulting from this crystalline structure will be reflected in all physical and mechanical properties of these compounds. The electrical and thermal properties will be described by a tensor having two independent coefficients a_{ii}: one along the basal planes (noted $a_{11} = a_{22}$) and one along the trigonal axis (a_{33}). The dimensionless figure of merit is higher in p-ternary compounds when the current flows parallel to the cleavage planes rather than perpendicular (it is also true for n-type materials): $Z_{11}T > Z_{33}T$ /EBL07, YAN10/.

Note that the density, d, of $Sb_{2-x}Bi_xTe_3$ solid solutions varies linearly from $x = 0$ ($d = 6.505$ g/cm^3) to $x = 2$ ($d = 7.860$ g/cm^3) /TES61/. For $x = 0.5$, the theoretical density is 6.892 g/cm^3.

I-2) Electronic band structure

The first Brillouin zone of $Sb_{2-x}Bi_xTe_3$ solid solutions is represented in Fig. II-4. Due to the large c/a ratio, the Brillouin zone is highly compressed in the direction of the trigonal axis (ΓZ direction). It is well know that $Sb_{2-x}Bi_xTe_3$ compounds are small band gap semiconductors. Depending on x, its indirect energy gap, E_g, ranges from 140 meV for Bi_2Te_3 to 290 meV for Sb_2Te_3 /BLA57, OLE85, SEH62, TOG70/.

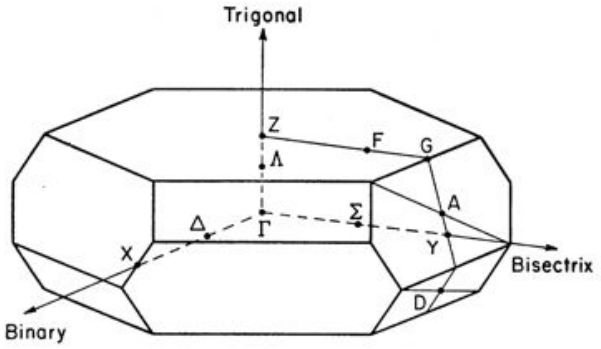

Figure II-4: First Brillouin zone of $Sb_{2-x}Bi_xTe_3$ for the rhombohedral cell. Also shown are the high symmetry points where Γ denotes the center of the first Brillouin zone. The scale of the drawing has been exaggerated along ΓZ for purposes of clarity.

According to experiments probing the Fermi surface (de Haas-Van Halphen or Shubnikov-de Haas techniques), /KOH76, KUL99, KUL00, MAL68/ supported further by some modern ab-initio theoretical calculations /LAR00, WAN07, YOU01/, it is accepted that the electronic band structure of the two binary compounds Sb_2Te_3 and Bi_2Te_3 has six equivalent electron pockets (lower light conduction band – LCB) and six equivalent hole pockets (upper light valence band – UVB). Additionally to these bands, a lower heavy valence band (LVB) and an upper heavy conduction band (UCB) are located closer in energy to UVB and LCB, respectively. Thus, the electronic structure near the band gap can be depicted as a first approach as in Fig. II-5. For a more detailed description, one can, for example, refer to the calculations of Wang et al. /WAN07/ made with the full-potential linearized augmented plane-wave (FLAPW) that are reported in Fig. II-6 for Bi_2Te_3 and Sb_2Te_3. From first principle calculations, we learn that the bang gap comes from an hybridization of the *p* orbitals of the semimetal and the chalcogen and that the spin-orbit coupling plays an important role. However, the key question with the band structures of the two binary compounds is the position of the valence-bands maxima and the conduction-bands minima. There is not yet satisfactory agreement except that UCB and UVB lie in the trigonal-bissectrix plane of the first Brillouin zone.

Quantitative information about the electronic band structure of ternary $Sb_{2-x}Bi_xTe_3$ compounds is rather limited but it is usually assumed that the scheme, represented in Fig. II-5, still applies. For our purpose, the structure of the valence bands is more relevant for us as samples with $x < 0.5$ exhibit a strong *p*-type character. From optical and transport measurements performed on single crystals with $0 \leq x \leq 1$, Stördeur et al. /STO81, STO88/ derived microscopic data for the valence band at 300 K assuming a six valleys non parabolic band model. For the compositions $x = 0.40$ and $x = 0.50$, which are of interest for us, the energy band gap was estimated to be $E_g = 210$ meV and the density of state effective masses are 1.01 m_0 and 0.94 m_0 (where m_0 is the free electron mass), respectively. Caillat. et al. /CAI92b/, using a single parabolic band model, determined the density of state effective masses of holes by fitting their transport properties on single crystals. They found 1.2 and 1.3 m_0 for $x = 0.40$ and 0.50, respectively. Regarding the energy gap between LVH and UVB (noted DE_v in Fig. II-5), the Shubnikov-de-Haas experiments of Köhler and Freudenberger /KOH77/ suggest that $DE_v = 20.5$ meV for $0.4 \leq x \leq 1$. To the best of our knowledge, no information about the temperature dependence of the valence band parameters is available.

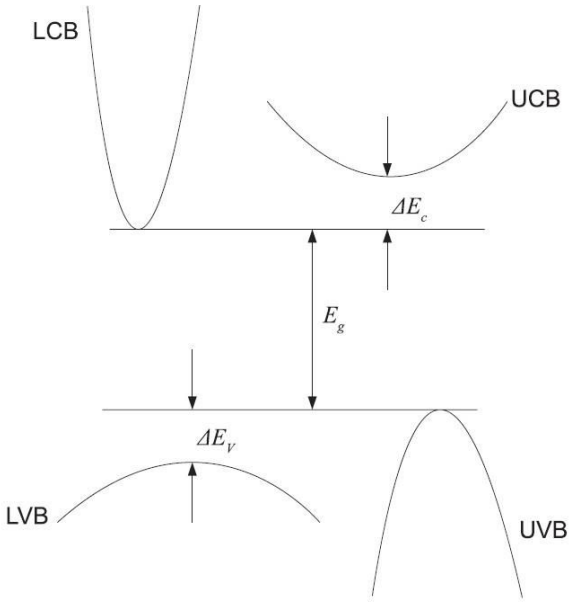

Figure II-5: Schematic band structure for Bi_2Te_3 and Sb_2Te_3 near the gap (*Eg*). Depending on the electron (hole) concentration, one or two conduction (valence) bands should be taken into account: a lower (upper) light conduction (valence) band and an upper (lower) heavy conduction (valence) band. DE_c (DE_V) is the distance in energy between the bottom (top) of UCB (UVB) and LCB (LVB).

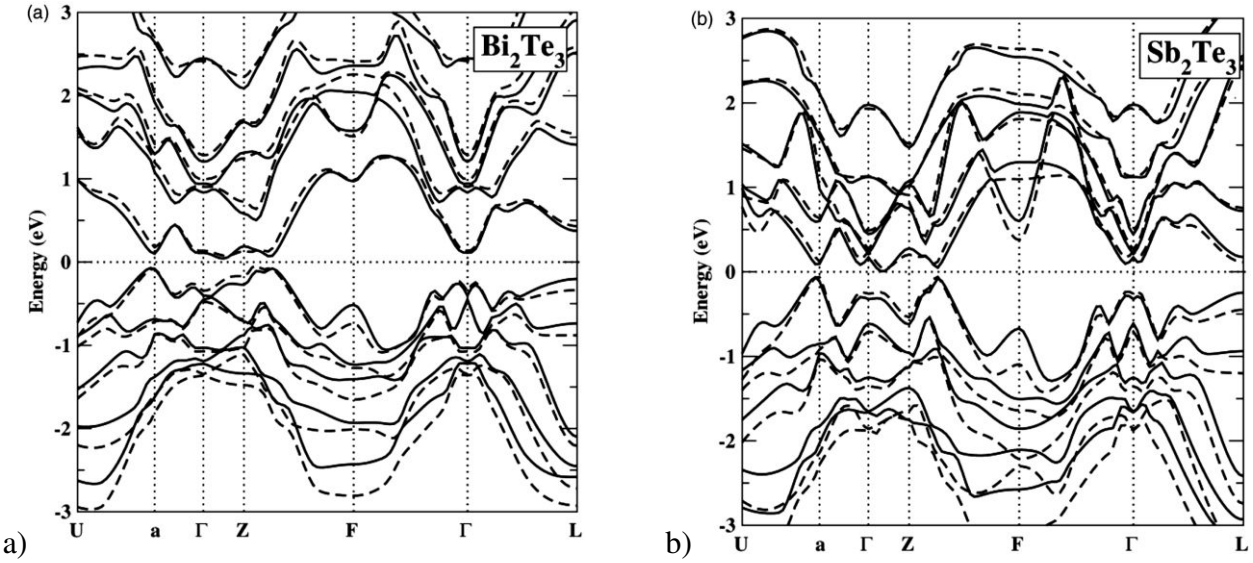

a) b)

Figure II-6: Electronic band structures of (a) Bi_2Te_3 and (b) Sb_2Te_3 along the high-symmetry lines from FLAPW calculation and with spin-orbit interaction /WAN07/. The solid lines show the calculation results for the crystals with the optimized lattice parameters, while the dashed line gives the results for the crystals with the experimental lattice parameters. We can note that these calculations, as most DFT approaches, are not able to predict correctly the value of the band gap (here the results are underestimated for the two binary compounds).

I-3) Phase diagram and defects in $Sb_{2-x}Bi_xTe_3$ solid solutions

The binary system (Sb, Te)/(Bi, Te) has been studied in fair detail by many authors /ABR77, ABR83, BRE69, GLA65, HAN58/. The Sb-Bi-Te ternary phase diagram in the Te-rich area has been determined by Caillat et al. /CAI92b/. The binary phase diagrams of Sb_2Te_3 and Bi_2Te_3 are reported in Fig. II-7. A first common feature is that both binary and ternary compounds are non-stoichiometric as it is illustrated schematically in Fig. II-7. The region of homogeneity of Sb_2Te_3 (surface (a, b, c) in Fig. II-7) is outside the stoichiometric composition and located on the antimony rich side /CAS79/. For Bi_2Te_3, the region of homogeneity is at the stoichiometric composition (surface (a', b', c')), expanding from the Te-rich side and the Bi-rich side when the temperature decreases /FLE88/. Volume (a, b, c, a', b', c') represents the boundaries of the whole solid solutions formed by antimony telluride and bismuth telluride. The boundary of the tellurium-rich solidus corresponds to the shaded region. As the bismuth telluride content increases in the solid solutions, the strong deviation from stoichiometry observed for the Sb_2Te_3 compound decreases. Moreover, a tellurium retrograde solubility is observed for lower temperatures as the bismuth telluride content in the solid solutions of the antimony telluride rich area increases /CAI91,GAI90/.

The reason why $Sb_{2-x}Bi_xTe_3$ compounds deviate from stoichiometry is intimately linked to intrinsic native defects that are formed during the synthesis (either via a liquid or solid state route). Defects in $A^V{}_2B^{VI}{}_3$ compounds have been studied experimentally as well as from a theoretical point of view /CHI95, HOR86, HOR88, HOR95, MAI02, MIL65, PEC94/. It was shown that the main defects in these V-VI compounds are point defects such as vacancies of atoms A or B (noted V_A and V_B) and antisite (or antistructure) defects of A atoms in B-sites (noted A_B) or vice-versa (noted B_A) /HAR55, SAT57/. The concentration of defects, *N*, which depends both on temperature (*T*) and on their formation energy (E_f), can be given, in accordance with statistical physics, by the expression:

$$N = k_1 exp\left[-\frac{E_f}{k_B T}\right] \qquad \text{(II-1)}$$

where k_B is the Boltzmann constant and k_1 is a constant characteristic for a given material. This relation states simply that a high concentration *N* is expected for defects having a low energy formation and that increasing the temperature helps also to promote the concentration of defects.

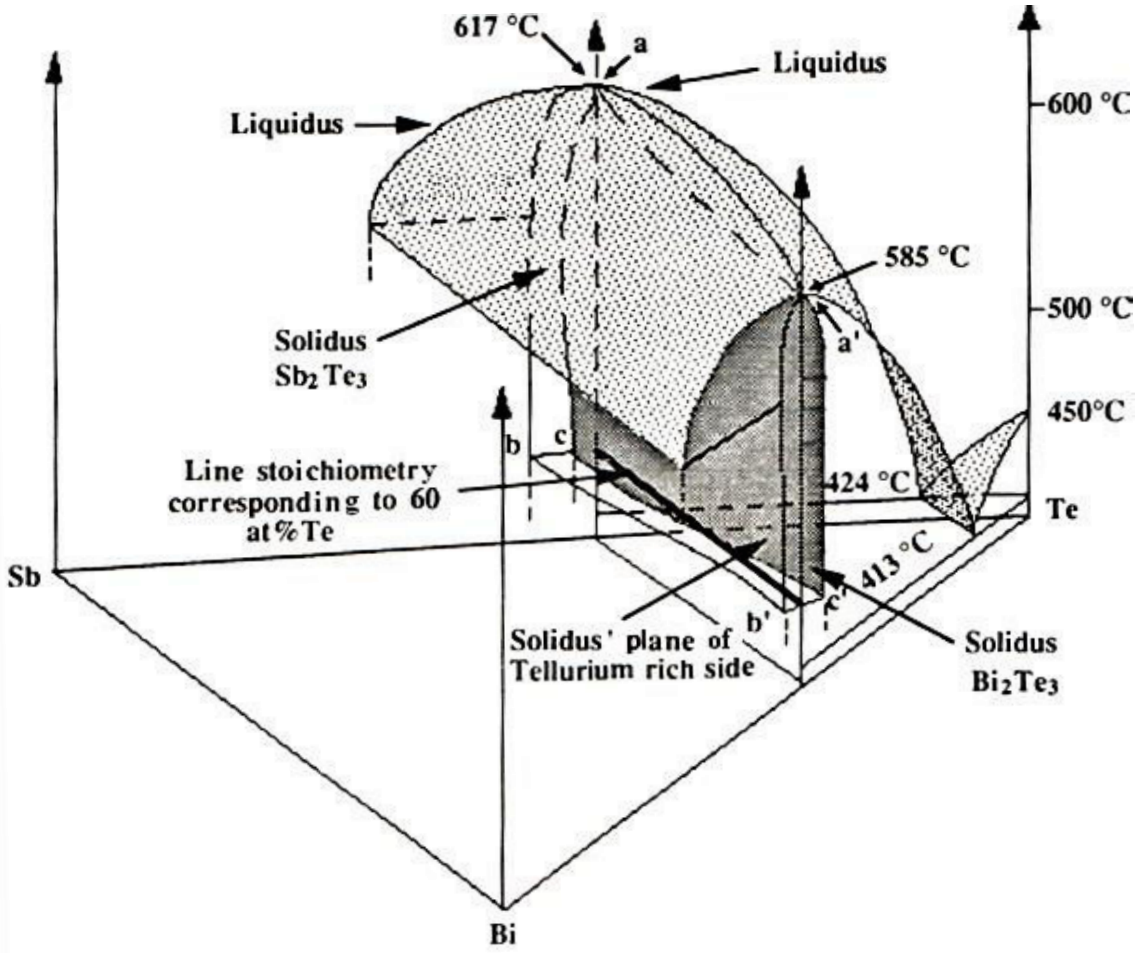

Figure II-7: Phase diagram in perspective of the ternary system Bi-Sb-Te for the Te rich area and for temperatures above 400°C according to Caillat et al. /CAI92a/ This diagram has been drawn with respect for temperatures but the true atomic scale was not conserved in order to enhance the boundaries of the solid solutions formed by Sb_2Te_3 and Bi_2Te_3.

From accurate density measurements performed on Bi_2Te_3 single crystals, Miller et al. /MIL65/ suggested that antistructure defects Bi_{Te} appear to be the main type of defects on the Bi-rich side. However, it was much more difficult to conclude on the Te-rich side and to choose between bismuth vacancies V_{Bi} or antisites Te_{Bi}. The lower energy formation of Te_{Bi}, compared to V_{Bi} (E_f (Te_{Bi}) = 0.42 eV and E_f (V_{Bi}) = 1.65 eV /HAS11/) suggests that antisite defects are dominant. The concentration of antisite defects in Bi_2Te_3 is about 10^{19} cm^{-3} /BRE69/. In Sb_2Te_3, the predominant defects have been identified as being antisite defects Sb_{Te} at concentrations of about 10^{20} cm^{-3}. Their existence was revealed indirectly from the relation between an excess of antimony and the physical properties of the crystals /HOR76/. The energy formation of Sb_{Te} was

estimated to be E_f = 0.32 - 0.35 eV by Horak et al. /HOR86, HOR95/ depending on the model used.

Another important point regarding vacancies and antisite defects in V-VI binary compounds is that they are electrically active. Using a tight binding model, Pecheur and Toussaint /PEC94/ have shown that in Bi_2Te_3, V_{Te} behaves as a triple acceptor, V_{Sb} as a double donor, Bi_{Te} as a single acceptor and Te_{Bi} as a single donor. Due to the similarities between Sb_2Te_3 and Bi_2Te_3, we expect that Sb_{Te} will behave also as a single acceptor. From a chemical point of view, it is formally possible to write relations between non-stoichiometry and the formation of point defects. For example, the formation of antisite Sb_{Te} in Sb_2Te_3 can be described as:

$$2Sb + 3Te \leftrightarrows 2Sb_{Te}^{-} + \frac{3}{2}Te_2(g) + 2h^{+} \qquad \text{(II-2)}$$

where indices (-) or (+) indicates the electrical charge, (g) means that it is in the gas state and h^+ is the produced hole. A similar equation can be written for vacancies.

According to Horak et al. /HOR90/, the formation of antisite defects in Sb_2Te_3 and Bi_2Te_3 crystals is caused by the low polarity of the Sb-Te and Bi-Te bonds, respectively. The low polarity is associated with a small difference in the Pauling's electronegativity (P_E) values of Bi (P_E = 2.02), Sb (P_E = 2.05) and Te (P_E = 2.10). A decrease in the difference of electronegativity of the A and B atoms forming the $A^V{}_2B^{VI}{}_3$ compounds will be favorable for an increase in the ability to form antisite defects.

From the last paragraph, we learn that even if the samples are intentionally undoped, the concentration of native defects that are responsible for the deviation from stoichiometry will make binary $A^V{}_2B^{VI}{}_3$ extrinsic semiconductors with a n or p-type character. For Sb_2Te_3, the material can be only p-type (always excess of Sb) while for Bi_2Te_3, n or p-types can be observed depending on the excess of Bi or Te present in the materials. Controlling the native defects and thus the carrier concentration can then be a route to optimize this family of compounds.

What about Sb_2Te_3 – Bi_2Te_3 solid solutions now? Starting from Sb_2Te_3, it is expected that when replacing Bi for Sb, Sb_{Te} and Bi_{Te} antisite defects will probably also be formed in the mixed Sb_2Te_3 rich crystals. Stördeur /STO86/ showed that the incorporation of Bi atoms into the Sb_2Te_3 lattice leads to a decrease of holes and thus, in view of the relation between holes and defects, to a decrease of the antisite defects. Horak et al. /HOR88/ proposed to correlate these observations to the bond polarity and the energy formation of antistructure defects. Their model shows that by

substituting Bi for Sb, the concentration of Sb_{Te} defects decreases partly because the increase of bond polarity results in an increase in the energy required for the formation of antisites and partly because of the decreasing concentration of Sb atoms in the mixed crystals.

For the compositions of interest for thermoelectric applications (x ~ 0.4 – 0.5) keep in mind that the ternary $Sb_{2-x}Bi_xTe_3$ solid solutions are outside the stoichiometric composition and on the Sb-rich side. Thus, these materials are always p-type. N-type behavior is possible, but higher Bi content (x > 1) is necessary.

II) SOME PAST RESULTS ON SINGLE CRYSTALS AND POLYCRYSTALLINE SAMPLES

A great amount of works has been published on $Sb_{2-x}Bi_xTe_3$ ternary solid solutions since the 1950's, either in the single crystal or polycrystalline form /ABR78, ABR79a, ABR79b, ABR80, ABR81, ABR82a, ABR82b, BAR76, ROS59, SUS76, VOL74, YIM72/. The most studied compound corresponds to the composition x = 0.5. The vertical Bridgman method, the Czochralski technique and zone melting were the most frequently used techniques to prepare the samples in the single crystalline form / ABR78, ABR79a, ABR79b, ABR82a, ROS59, YIM72/. Doping has been extensively used to optimize the carrier concentration /ABR78, ABR79a, ABR80, ABR81, ABR82a, ABR82b, YIM72/. Although *ZT* values of about 0.9 - 1 at 300 K were obtained using this approach, a large scale production of such materials with reproducible thermoelectric properties is hard due to the difficulty to control the stoichiometry deviations especially during the initial growth process. Indeed, the isoconcentration lines are complex so that the direction of the tie-lines is changing as the temperature decreases /CAI92a/. Thus, crystals grown out of the melts cannot have the same composition along the whole ingot because of the change in the initial melt composition. Another limitation is the strong difficulty to control the distribution of the doping agent along the ingot.

It was shown that stoichiometry deviations can be controlled for crystals grown by the Traveling Heater Method (T.H.M.) provided that the phase diagram is accurately known /CAI92b, GAI89/. Using this approach, an original annealing saturation technique was used to explore the solidus line of Sb_2Te_3 on the Te and Sb-rich sides and the solidus line of the three solid solutions with x = 0.4; 0.45 and 0.5 on the Te rich-side only /CAI92b, GAI89/. For each saturation temperature, the

transport properties along and perpendicular to the trigonal axis have been measured at 300 K. This study, dedicated to probe the maximum stoichiometric deviations, unveiled several interesting points. In particular, it was found that the hole concentration, deduced from Hall measurements, depends strongly on the saturation temperature as shown in Fig. II-8. For $x = 0$ (Sb_2Te_3), the hole concentration ranges from 10^{20} to 10^{21} cm^{-3} and for a same saturation temperature, the hole concentration is higher on the Sb-rich side than on the Te-rich side. It is also important to note that near the melting temperature (617°C), the hole carrier concentration can vary drastically (by a factor of 5 due to the flatness of the solidus curve). For the solid solutions, the hole density ranged from $4.8x10^{19}$ to $2x10^{20}$ cm^{-3} for $x = 0.4$ and from 2.8 to $5x10^{19}$ cm^{-3} for $x = 0.5$. This rapid decrease of hole carrier concentration with the increasing mole contents of Bi_2Te_3 is mainly related to the decrease of Sb_{Te} antisite defects as already discussed. Also the retrograde solubility of Sb_2Te_3 becomes less important for $x = 0.4$ and disappears for $x = 0.5$. Note that even if the solidus on the Sb-rich side has not been investigated in the ternary compounds, it is likely that the full solidus line will be more or less the same as for Sb_2Te_3 but shifted to lower hole concentration. From Fig. II-8, we can thus anticipate a strategy to reduce the hole concentration either by adding an excess of Te in the initial composition or by varying the Bi content.

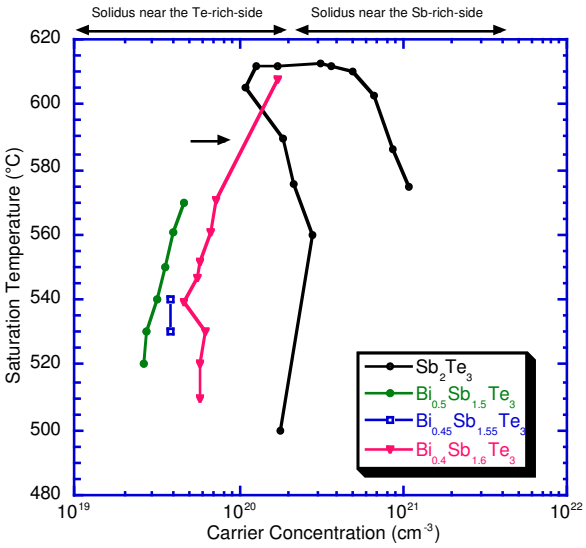

Figure II-8: Hole concentration as a function of the saturation temperature for $Sb_{2-x}Bi_xTe_3$ solid solutions with $x = 0$; 0.4; 0.45 and 0.5 according to Gaillard and Caillat et al. /CAI92b, GAI89/. Te and Sb-rich sides of the solidus line have been explored for $x = 0$, while only the Te-rich side has been studied for the other compositions.

The works of Gaillard /GAI89/ and Caillat et al. /CAI92b/ on well controlled thermodynamic samples have also revealed that the electrical and thermal properties of $Sb_{2-x}Bi_xTe_3$ single crystals are anisotropic and that the anisotropy depends both on the Bi content (with a trend that it decreases with increasing x) and for a fixed x value, on the hole carrier concentration through deviation from stoichiometry. Whatever x is, the electrical resistivity, ρ, is greater in the basal planes than in the trigonal plane: $\rho_{33} > \rho_{11}$ (with ρ_{33}/ρ_{11} ~ 1.5 - 4). For the thermal conductivity, κ, the situation is reversed: $\kappa_{11} > \kappa_{33}$ (with κ_{11}/κ_{33} ~ 2.5-8). These two results can be understood quite easily if we refer to the layered structure and the nature of the chemical bonds. The thermopower, α, exhibits a more complex behavior since depending on x, the anisotropy is more or less marked. For x = 0 and 0.4, it is observed that $\alpha_{11} \leq \alpha_{33}$ (with α_{33}/α_{11} ~ 1-1.5) while for x = 0.5, $\alpha_{11} \sim \alpha_{33}$. Finally, if for Sb_2Te_3, $Z_{11}T < Z_{33}T$, the situation is reversed in the ternary compounds with $Z_{11}T \geq Z_{33}T$. Due to an excess of hole concentration, Sb_2Te_3 has a low ZT and is not a good candidate for thermoelectric applications but by alloying it with Bi_2Te_3, the concomitant decrease of the hole density and of the thermal conductivity boost the ZT. Finally, the maximum $Z_{11}T$ values obtained for x = 0.4 and x = 0.5 are close to 0.9 at 300 K for carrier concentrations of 4.8×10^{19} and 3.4×10^{19} cm^{-3}, respectively as represented in Fig. II-9. A value, a little bit higher, has been reached for x = 0.45 ($Z_{11}T$ = 0.96). Note also from Fig. II-9 that a small deviation from the optimized carrier concentration results inevitably in a drop of ZT.

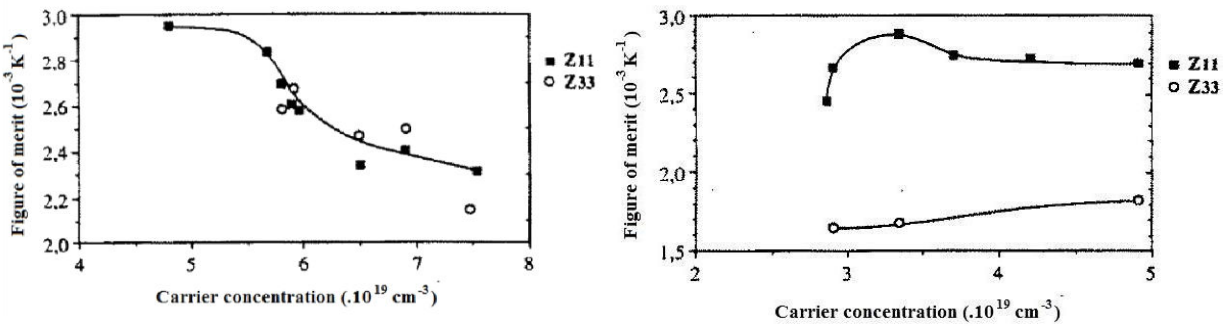

Figure II-9: Figure of merit (Z) versus hole concentration along (Z_{11}) and perpendicular (Z_{33}) to the trigonal direction for x = 0.4 (a) and for x = 0.5 (b). The anisotropy depends both on x and on the carrier concentration. For x = 0.4, $Z_{11} \approx Z_{33}$. The data are from Caillat et al. /CAI92b/.

If these studies performed on single crystals grown by the THM demonstrated that ZT close to 1 can be obtained in a reproducible way under specific thermodynamic conditions, the scaling-up of such an approach is clearly not viable from an industrial point of view. Moreover, melt-

grown materials are fragile and often cleave easily due to the weakness of the bonds between the quintets. For this reason, powder metallurgical methods have been used to prepare materials with improved mechanical strength. Numerous papers have been published on the subject with plenty of techniques applied including cold pressing + annealing /YAM03, IVA13…/, hot pressing /FAN10, HYU01, KIM04, NAV96, YAN01/ and mechanical alloying /FAN06, VAS10, YAN06…/ to rapidly produce at low cost p-type ternary compounds. These studies demonstrated that it is possible to produce polycrystalline samples without any drastic decrease of their thermoelectric performance compared to single crystals. They have also underlined the strong impact of the elaboration and sintering conditions on the thermoelectric properties and the difficulty (again) to control the defects that are responsible of the electrical properties. A situation, finally, reminiscent to what is observed for single crystals.

III) PROMISING RESULTS ON NANOSTRUCTURING OF $Sb_{2-x}Bi_xTe_3$

As it was already mentioned in Chapter I, nanostructuration gained popularity during the last 15 years as a method to fulfill the requirements for a good thermoelectric material: low electrical resistivity to minimize Joule heating, low thermal conductivity to prevent thermal shorting and a high thermopower to maximize energy conversion. Recent research in this field revealed that the nanostructuring approach can either reduce the lattice thermal conductivity or enhance the power factor and then lead to a possible enhancement of the thermoelectric performance. We will give below a brief overview of the most promising results obtained by nanostructuring bulk Sb_2Te_3-based materials. Table II-1 summarizes the elaboration methods (top-down or bottom-up) of a few of the numerous reported p-Sb_2Te_3 based bulk nanostructured that led to outstanding *ZT* values compared to the state-of-the-art (*ZT* ~ 1).

Among the top-down methods of nanostructuration, that where briefly presented in chapter I, the high-energy ball milling combined to hot pressing was announced by Poudel et al. /POU08/ as one that can improve significantly the thermoelectric properties of $Sb_{1.5}Bi_{0.5}Te_3$ alloys. They reported that the *ZT* of their nanograined bulks was increased by 30-40% as compared to an ingot prepared through zone melting (with a peak *ZT* = 1.4 at 373 K as shown in Fig. II-10). It is worth to mention that *ZT* demonstrated surprisingly nearly isotropic behavior when comparing the results obtained perpendicular and parallel to the pressing direction of the samples. The test of

unicouple cooling device made from the obtained nano-structured material was performed as well, and its performance was significantly better than the performance of a commercial one.

The method of mechanical alloying was applied by Ma et al. /MA08/, using elemental chunks as starting materials contrarily to Poudel et al. /POU08/ who performed ball milling of alloyed crystalline ingots. The samples of $Sb_{2-x}Bi_xTe_3$ (exact composition was not marked) were found to be isotropic. The results turned to be less efficient with a *ZT* peak of around 1.25 in the temperature range 348 – 375 K. On the other hand, this process is significantly simplified for scaling-up.

Rather than sintering the powders obtained after mechanical alloying or ball milling process, Vasilevskii et al. /VAS10/ proposed to use a hot extrusion process to strongly texture the $Bi_{0.4}Sb_{1.6}Te_3$ compounds. Hot extrusion is a hot working process where material is pushed through a die of the desired cross-section at temperatures over the material's recrystallization temperature. Extruded samples possessed a highly textured structure with some nanosized subgrains within the much larger crystallites. Thanks to this process, a peak *ZT* value of 1.1 at 373 K was obtained. The experiments on the thermoelectric performance of a two-leg thermocouple produced from extruded materials gave similar results to those obtained by Poudel et al. /POU08/.

Table II-1: The most salient results obtained for the $Sb_{2-x}Bi_xTe_3$ family of materials. Hot pressing marked as HP, spark plasma sintering as SPS.

Composition	***Preparation Method***	***ZT***	***Thermal conductivity (W/m.K)***	***References***
$x = 0.5$	Ball Milling + HP	1.4 at 373 K	1 ($\kappa_L \sim 0.4$)	/POU08/
$x = 0.52$	Melt-spinning + SPS	1.56 at 300 K	0.67 ($\kappa_L \sim 0.26$)	/XIE09/
$x = 0.4$	Melt-spinning + Ball milling + HP	1.8 at 323 K	0.65 ($\kappa_L \sim 0.2$)	/FAN10/
$x = 0.5$	Spark erosion + SPS	1.36 at 360 K	0.9 ($\kappa_L \sim 0.37$)	/NGU12/
Bi_2Te_3/Sb_2Te_3	Chemical method + sintering	1.47 at 450 K	1.18	/CAO08/

The melt-spinning technique proved to be also a powerful process to increase the thermoelectric performance of the mixed Sb_2Te_3-Bi_2Te_3 crystals. This method, that has been widely used for the rapid cooling of liquids to prepare non-equilibrium phases and supersaturated phases of many amorphous alloys since the early 1960s, will be described in detail in chapter III. From the end of the1980's the melt-spinning technique was applied on conventional thermoelectric materials like $Sb_{2-x}Bi_xTe_3$ by Soviet Union and Russian scientists /GLA86, GLA95, GOG88, GOG91, IVA13/. More recently, several papers using the melt-spinning technique and spark plasma sintering were published by one group to prepare p-$Sb_{2-x}Bi_xTe_3$ ($0 < x < 0.6$) solid solutions /XIE09a, XIE09b, XIE10a, XIE11, XIE13/. Melt-spinning leads to the production of ribbons made partly of amorphous domains in which nano-sized crystals (5-15 nm) are embedded in. As a result, a remarkably high *ZT* of 1.56 at 360 K was observed in $Sb_{1.48}Bi_{0.52}Te_3$ in the further bulk samples produced by spark plasma sintering, as it is illustrated in Fig. II-10. It was reported that the presence of the small nano-crystalline regions, kept during the sintering process, contributes to these high *ZT* values by lowering the lattice thermal conductivity /XIE09a, XIE09b, XIE10a/.

Following, these outstanding results, Fan et al. /FAN10/ reported also impressive results on nanocomposites prepared by a mixture of melt-spun and grinded $Bi_{0.4}Sb_{1.6}Te_3$ compounds that was then hot pressed. They claimed that such materials exhibit a *ZT* peak of 1.8 at 323 K (Fig. II-10) due to the wide variety of microsized/nanosized particles that scatter phonons on a wide spectrum of wavelengths. An important point that is however not clear in the study of Fan et al. /FAN10/ is how the transport properties have been measured (same direction?).

A spark erosion method was proposed by Nguyen et al. /NGU12/ to produce a combination of nanoparticles (20-30 nm in size) and micro-sized particles (0.1-10 μm) of $Bi_{0.5}Sb_{1.5}Te_3$ compounds with a remarkably high synthesis rate. By sintering these particles by SPS, the resulting nanocomposites show high *ZT* values with a peak of 1.36 at 360 K (Fig. II-10). The stronger phonon scattering at nanograin interfaces was claimed to be, as in the previously mentioned works on nanostructuration, the main reason of the enhanced thermoelectric performance.

It is worth to mention here the most promising up-to-date results obtained by applying hydrothermal routes (bottom-up approach). Generally, chemical methods of nanostructuration

alongside with the high grain size reduction and rate of nano-scale material production have some issues like complexity in further densification, cleaning of resulting material from chemical agents and high grain growth rate during any thermal treatment as it was mentioned in chapter I. Despite these problems, successful results were obtained by Cao et al. /CAO08/. Nanosized binary Bi_2Te_3 and Sb_2Te_3 powders, synthesized by a hydrothermal route, were mixed in different ratios and hot pressed. Samples prepared with the ratio 1:1 demonstrated high values of *ZT* around 1.5 peaked at 450 K. Despite the room temperature value of these samples is quite moderated (*ZT* ~ 0.55), the strong enhancement of the thermopower with increasing temperature and a concomitant decrease of the electrical resistivity contribute to enhance *ZT*.

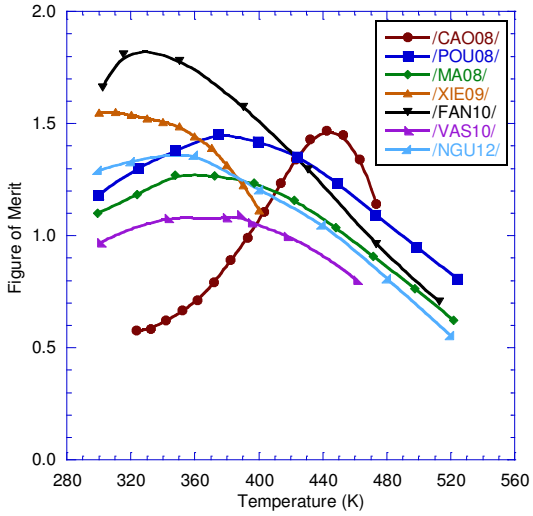

Figure II-10: Temperature dependence of figures of merit *ZT* obtained by the different approaches mentioned in this paragraph. Data were taken from the publications marked in the legend.

CONCLUSION

This chapter, focused on p-type $Sb_{2-x}Bi_xTe_3$, showed that these materials exhibit unique physical properties: small band gap semiconductors, strong anisotropy and deviations from stoichiometry due to their native defects. Interesting p-type thermoelectric properties are found near 300 K for Bi content *x* of about 0.4 – 0.5, which, combined with their counterpart based on (Bi,Te,Se), make them suitable for cooling mainly in niche applications (opto-electronic applications for example). The numerous past studies on either single crystals or polycrystals demonstrated that the optimization of their figure of merit *ZT*, through the hole concentration, is a

challenging task. This fact is attributed to the small bang gap and the difficulty to control the carrier concentration in a reproducible way.

During more than 60 years after their discovery, the evolution of *ZT* over years in p- $Sb_{2-x}Bi_xTe_3$ compounds stayed nearly constant with only some incremental increases leading to a peak around 0.9-1 at 300 K. A spectacular jump (increase of 50 to 80 % !!) was observed these last years with the contribution of the nanostructuration. Nanostructures are believed to scatter more effectively phonons than electron making more flexible the optimization of the thermoelectric properties. Processing technologies were developed to prepare materials in their bulk form so as to preserve the advantages of nanostructuration. Among them, the melt-spinning method proved to be particularly promising for improving the thermoelectric properties of p- $Sb_{2-x}Bi_xTe_3$ in the temperature range useful for our application. The next chapter will introduce in a more detailed way this method and its specificity.

Chapter III

Synthesis of $Sb_{2-x}Bi_xTe_3$ based compounds. Microstructural characterizations.

INTRODUCTION

Nanostructuring of thermoelectric materials has proven to be an efficient way to enhance the thermoelectric performance of materials by lowering the thermal conductivity as it has been shown in chapter I. It has been applied to numerous materials. Remarkable results had been achieved with bismuth-antimony telluride materials with *ZT* enhancements of about 20 to 50%, depending on the authors /FAN10, POU08, TAN07, XIE09a, XIE09b, XIE10a/. Such improvements could benefit largely to many applications and make more viable new technologies such as thermoelectric heat pumps. Among the various techniques proposed to prepare bulk nanostructured bismuth telluride compounds, melt-spinning followed by a sintering process was proved to be particularly efficient /FAN10, XIE09a, XIE09b, XIE10a/. For this reason, we decided to use this method for the preparation of our nanomaterials.

In this chapter, we will first describe the preparation process used to synthetize our materials: preparation of the initial compositions, melt-spinning and spark plasma sintering. The various aspects of this rather unusual method that is melt-spinning will be developed and we will insist in particular on the study to adjust the experimental parameters that are specific to the nature of the desired nanoparticles.

Then we will introduce the different methods we have used to characterize the structure, the chemical composition and homogeneity, and the morphology of the various samples we have prepared: x-ray diffraction, energy dispersive X-ray spectroscopy, scanning and transmission electron microscopy.

The results of the different characterizations of the materials we synthesized will be given in a third part of this chapter.

I) ELABORATION OF MATERIALS

I-1) Parameters studied and prepared samples

Several p-type $Sb_{2-x}Bi_xTe_{3+z}$ ($0.4 \leq x \leq 0.52$ and $z = 0$ or 0.1) solid solutions have been prepared during this study with the aim to probe the influence of the composition (Bi and Te content, x and z, respectively) on the structural, physical properties, and thermoelectric performance of these materials. Other directions of research were also explored on specific compositions in order to enhance the thermoelectric performance. Influence of melt-spinning parameters (diameter of nozzle, gap between the nozzle and the wheel, wheel speed, over pressure, …), influence of the densification method (spark plasma sintering (SPS) - electric field assisted sintering technique and cold pressing – process with no thermal or electrical influence on the sample), and influence of anisotropy have been investigated. The additional structuration expected to be obtained by a double-SPS process was also among our fields of interest as it was stated having a favorable influence on the thermoelectric performance of analogous n-type compounds /BHA13, LOG14/. Influence of annealing, as it can relax strain, has also been tested.

Another important part of our study was concentrated on the doping. Numerous attempts of doping and composition variation for the ternary $Sb_{2-x}Bi_xTe_3$ compounds are reviewed in the literature. We opted for Sn because Sn can potentially increase the power factor of $Sb_{2-x}Bi_xTe_{3+z}$ compounds through a distortion of the band structure as observed in analogous Bi_2Te_3 compounds /HER12/.

A list of part of the samples we prepared is given in table III-1, showing the nominal composition, the way they were prepared, and their relative density.

I-2) Preparation of the initial alloys

The starting point of all our experiments is the preparation of initial ingots of given nominal composition according to the focus we want to follow (base material, doping, …). This ingot will be used in two ways: either to serve as a reference sample in which no influence of nanostructuring is expected, or as the material that will be used for the melt-spinning process, giving rise to expected introduction of some nanoparticles.

Basic elements of high purity (bismuth (CERAC, 99.999%), antimony (5N +, 99.999%)

Table III-1: List of some samples prepared in frame of this work: nominal compositions, elaboration methods (WQ – water quenching, MS – melt-spinning, SPS – spark plasma sintering, CP – cold pressing) and relative densities.

Composition	***Elaboration method***	***Relative density***
$Sb_{1.6}Bi_{0.4}Te_3$	WQ + SPS	98%
$Sb_{1.6}Bi_{0.4}Te_3$	WQ + MS + SPS	95%
$Sb_{1.52}Bi_{0.48}Te_3$	WQ + SPS (2 samples)	96%
$Sb_{1.52}Bi_{0.48}Te_3$	WQ + MS + SPS (2 samples)	96%
$Sb_{1.52}Bi_{0.48}Te_3$	WQ + MS + SPS (aligned)	94%
$Sb_{1.52}Bi_{0.48}Te_3$	WQ + MS + CP	93%
$Sb_{1.52}Bi_{0.48}Te_3$	WQ + MS + SPS + annealing	96%
$Sb_{1.6}Bi_{0.4}Te_{3.1}$	WQ + SPS (2 samples)	96%
$Sb_{1.6}Bi_{0.4}Te_{3.1}$	WQ + MS + SPS	98%
$Sb_{1.55}Bi_{0.45}Te_{3.1}$	WQ + SPS	96%
$Sb_{1.55}Bi_{0.45}Te_{3.1}$	WQ + MS + SPS	95%
$Sb_{1.52}Bi_{0.48}Te_{3.1}$	WQ + SPS	97%
$Sb_{1.5}Bi_{0.5}Te_{3.1}$	WQ + SPS	97%
$Sb_{1.5}Bi_{0.5}Te_{3.1}$	WQ + MS + SPS (2 samples)	97%
$Sb_{1.5}Bi_{0.5}Te_{3.1}$	WQ + MS + double SPS	97%
$Sb_{1.5}Bi_{0.5}Te_{3.1}$	WQ + MS + CP	93%
$Sb_{1.5}Bi_{0.5}Te_{3.1}$	WQ + MS + SPS + annealing	97%
$Sb_{1.48}Bi_{0.52}Te_{3.1}$	WQ + SPS	98%
$Sb_{1.48}Bi_{0.52}Te_{3.1}$	WQ + MS + SPS	98%
$(Sb_{1.52}Bi_{0.48})_{0.85}Sn_{0.15}Te_3$	WQ + SPS	97%
$(Sb_{1.52}Bi_{0.48})_{0.85}Sn_{0.15}Te_3$	WQ + MS + SPS	96%
$(Sb_{1.52}Bi_{0.48})_{0.97}Sn_{0.03}Te_3$	WQ + SPS	96%

$(Sb_{1.52}Bi_{0.48})_{0.994}Sn_{0.006}Te_3$	WQ + SPS	98%
$(Sb_{1.52}Bi_{0.48})_{0.994}Sn_{0.006}Te_3$	WQ + MS + SPS	95%
$(Sb_{1.52}Bi_{0.48})_{0.994}Sn_{0.006}Te_{3.1}$	WQ + SPS	98%
$(Sb_{1.52}Bi_{0.48})_{0.994}Sn_{0.006}Te_{3.1}$	WQ + MS + SPS	97%
$(Sb_{1.52}Bi_{0.48})_{0.997}Sn_{0.003}Te_{3.1}$	WQ + SPS	97%
$(Sb_{1.52}Bi_{0.48})_{0.997}Sn_{0.003}Te_{3.1}$	WQ + MS + SPS	95%
$(Sb_{1.52}Bi_{0.48})_{0.999}Sn_{0.001}Te_{3.1}$	WQ + SPS	98%
$(Sb_{1.52}Bi_{0.48})_{0.999}Sn_{0.001}Te_{3.1}$	WQ + MS + SPS	95%

and tellurium (5N +, 99.999%)) were used in the form of granules. Weighting of the elements in stoichiometric amounts (for total weights of about 20, 30 or 50 g) was performed in a glove box under a controlled atmosphere of argon. The elements were then placed inside a quartz tube of 12-14 mm in diameter, according to the amount of material (Fig. III-1). All quartz tubes used had previously undergone cleaning treatments in successive baths of hydrofluoric acid and nitric acid, followed by thorough rinsing with distilled water. The tubes are then stored in ethanol until undergoing a degassing for 6 hours at 900°C just before their use.

Once the materials inside the tube, a short quartz tube of diameter just smaller than the main tube, is placed at the open extremity of the tube. It will serve as a sealing cap. The whole is then quickly installed on a pumping device equipped with a primary pump and a diffusion oil pump to achieve a vacuum of 10^{-6} mbar. After degassing under primary vacuum for about five minutes, the mixture is maintained under secondary vacuum for three hours. Before sealing the tube at the level of the cap with the help of a torch, a reducing gas mixture H_2/He (5/95) is introduced into the tube under slight depression (~ 400 mbar).

The sealed quartz tube with the mixture of elements is then placed in a vertical oscillating furnace and heated up to 710°C at a temperature rise of 8°C/min. At this temperature, all the elements are in the liquid state and slowly react creating the ternary compound. After 5 hours at 710°C, the liquid mixture is quickly quenched at room temperature in a water bath. The obtained ingot is shown in figure III-2.

Figure III-1: A quartz tube with the total amount of pure elements (about 50 g) inside the glove box.

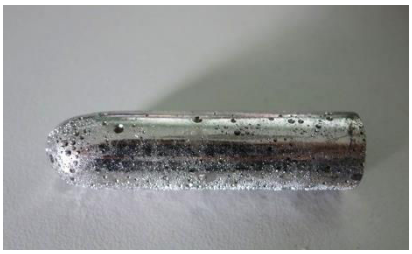

Figure III-2: Image of the initial ingot obtained after quenching in water (WQ in table III-1).

I-3) Nanostructuration by melt-spinning

Melt-spinning (MS) is a rapid solidification technique that, compared with conventional solidification methods, produces microstructures with refined grain sizes, increased solubility of alloying elements and impurities, reduced levels of segregation, and in some cases the formation of metastable crystalline and amorphous phases /CAN78, COC88, MAS82, STE85/. These effects may lead to beneficial improvements in mechanical, magnetic, electrical, and other properties in many alloy systems. Rapid solidification processing is therefore being used increasingly to manufacture metallurgical materials which take advantage of these improved properties in a variety of applications /CAN78, COC88, MAS82, STE85/. Quite recently, MS was applied to the production of thermoelectric materials with improved thermoelectric

performance (BiSbTe, skutterudites, …) /FAN10, LI09, SAL13, TAN13, XIE09a, XIE09b, XIE10a/.

In all rapid solidification techniques, a mass of liquid metal or alloy is manipulated so as to be thin in at least one dimension, and at the same time in good thermal contact with an efficient heat sink. Under these conditions, heat is extracted quickly from the liquid mass, which then cools and solidifies rapidly. Typical liquid thicknesses are in the range 10 to 100 μm with corresponding cooling rates of 10^4 to 10^7 K/s, so that cooling and solidification is complete within a few milliseconds.

I-3-1) Principle of melt-spinning

From 1908, Strange and Pim /STR08/ patented a form of melt-spinning instrument for the rapid solidification of liquid alloys, using a metal wheel to extract heat (Fig. III-3). The drawings on Figure III-3 describe this prototype of up-to-date melt-spinners, where number (1) represents the receptacle in which the material is kept molten, for example by a Bunsen burner (2). The molten material passes out by the outlet (3), in proximity to which is mounted a disk (4) with longitudinally straight and smooth periphery and fixed in any suitable support with means for rapidly rotating the disk /STR08/.

Various melt spinning instruments have been developed over the past 30 years and have been widely used, particularly at bench-scale for the production of metallic glasses. Commercial scale-up has however been limited, primarily because of the difficulty in maintaining good product quality. Much of the instruments have thus been developed for specific needs by the metallurgical community.

The principle of the planar-flow melt-spinning (PFMS, also known as single-roll melt-spinning or planar-flow spin casting), technique we used (the twin-roll melt-spinning technology is another possible configuration), is shown schematically in Figure III-4.

The process feeds molten metal from a crucible (due to imposed overpressure ΔP) through a nozzle of size B and into a narrow gap region between the nozzle and the chill wheel (or substrate). Because of the small gap height, G, the nozzle interferes with the flow, and a puddle held by surface tension is formed. ΔP is held constant during a cast and G adds hydrodynamic resistance to the flow rate. The close proximity of the nozzle to the substrate tends to stabilize the

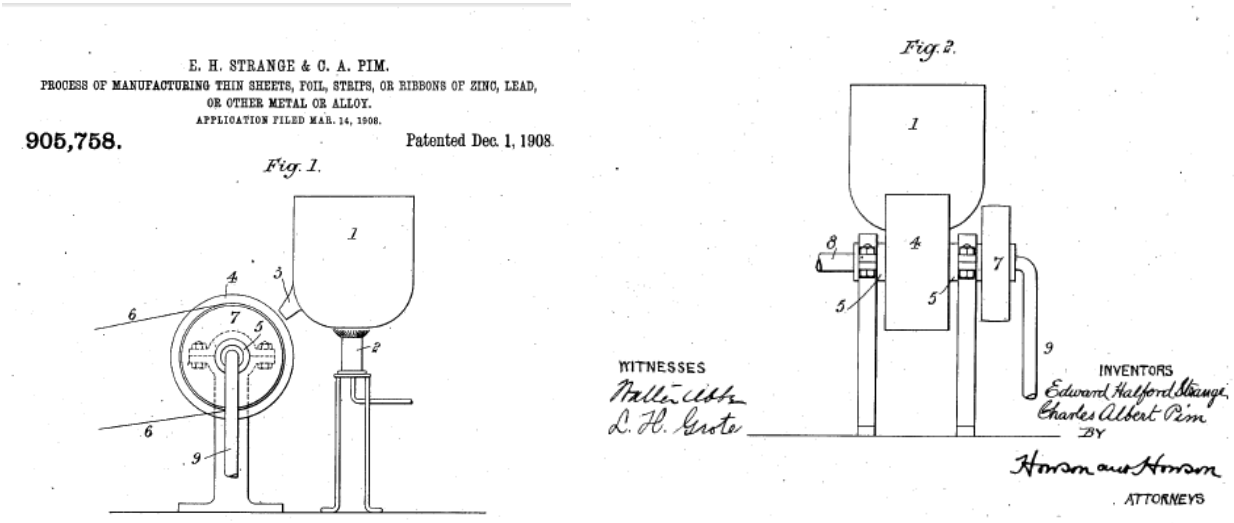
E. H. STRANGE & C. A. PIM.
PROCESS OF MANUFACTURING THIN SHEETS, FOIL, STRIPS, OR RIBBONS OF ZINC, LEAD, OR OTHER METAL OR ALLOY.
APPLICATION FILED MAR. 14, 1908.
905,758. Patented Dec. 1, 1908.
Fig. 1.
Fig. 2.
WITNESSES
INVENTORS
Edward Halford Strange,
Charles Albert Pim
BY
ATTORNEYS

Figure III-3: The title page of the patent signed by E.H.Strange and C.A.Pim in 1908. The drawings represent the first prototype of current melt-spinners.

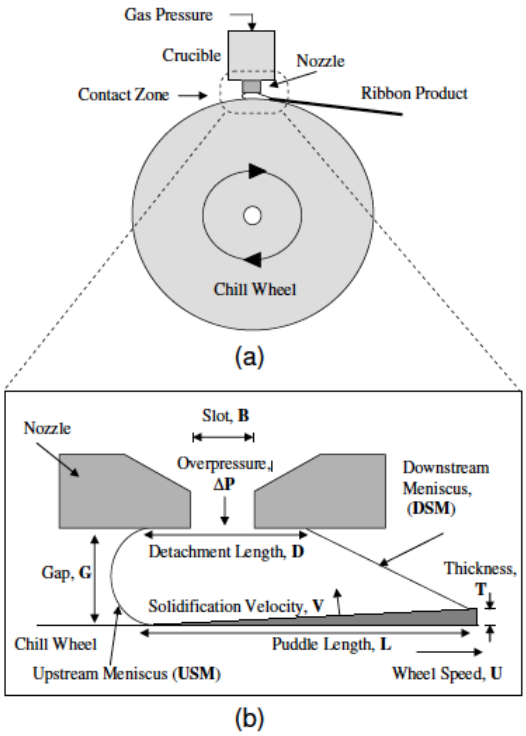

Figure III-4: (a) Schematic of the MS apparatus /BYR06/. Molten metal flows from the crucible through a nozzle onto the spinning substrate or chill wheel, where it forms a puddle. Solidification occurs and a continuous ribbon is 'spun' from the puddle and released from the substrate. (b) Blow-up of the contact zone or puddle region. Note that the horizontal length scale has been compressed for clarity.

puddle. The contact between the wheel and the molten puddle is such that enough heat is removed from the melt for solidification to occur. A solidification front grows from the wheel as it translates and a ribbon is eventually pulled of the puddle and spun from the wheel a short time later. The wheel continually removes the solidified product from the casting zone.

The complicated interaction between fluid flow, heat transfer, solidification are still subject to active research. Some typical parameters that may play a role are: the nozzle geometry (nozzle-wheel gap G, nozzle slot breath B, nozzle slot width W), the process variables (ribbon thickness R, puddle length L, linear wheel speed U, overpressure ΔP, solidification rate V, superheat temperature T_{sh}, nominal quench temperature (293 K) T_q), and the materials properties (densities of solid and liquid d_s and d_l, respectively, viscosity η, surface tension σ, liquidus temperature T_l, solidus temperature T_s). It has been shown that the fluid flow and heat transfer in PFMS can be decoupled, based on the orthogonality of fluid flow and heat transfer /CAR97/. Fluid flow is essentially left-to-right in Figure III-4 while heat is extracted vertically into the substrate. The variance from this orthogonality is measured by the ratio G/L and $G/L<<1$ indicates decoupling is possible. With this assumption, the fluid flow can be analyzed separate from the heat transfer. As our work was not to study these phenomena, we will not enter in the details of the numerous studies that are available on this topic, either from an experimental, or from a theoretical point of view. Details can be found for instance in the article reviews of Chen et al. /CHE80/, Steen and Karcher /STE97/, Wang and Prasar /WAN00/ and the book of Kamal and Mohammad /KAM12/.

I-3-2) Instrument description and samples preparation

On Figure III-5 is displayed the device used in this work (Edmond Bühler) where, even if still recognizable, we can see the upgrade of the initial system of Stange and Pin /STA08/ done during the last century. It is equipped with a cupper wheel (3) of 198 mm in diameter that is cleaned with a polishing paste in between each two experiments. Quartz crucibles (1) of inner diameter and thickness of 12 or 10 and 2 mm, respectively and 8-10 cm in height were used. The end of the quartz tubes is V-shaped and nozzles of 0.5, 0.7 or 1.0 in diameter have been drilled by us by ultrasonic drilling in the V. It gives the possibility to use up to 10 *g* of material per process.

Several ways of introducing the material into the quartz crucible were investigated. In the case of powders (the initial ingot has been ground to powders), the melting process cannot be

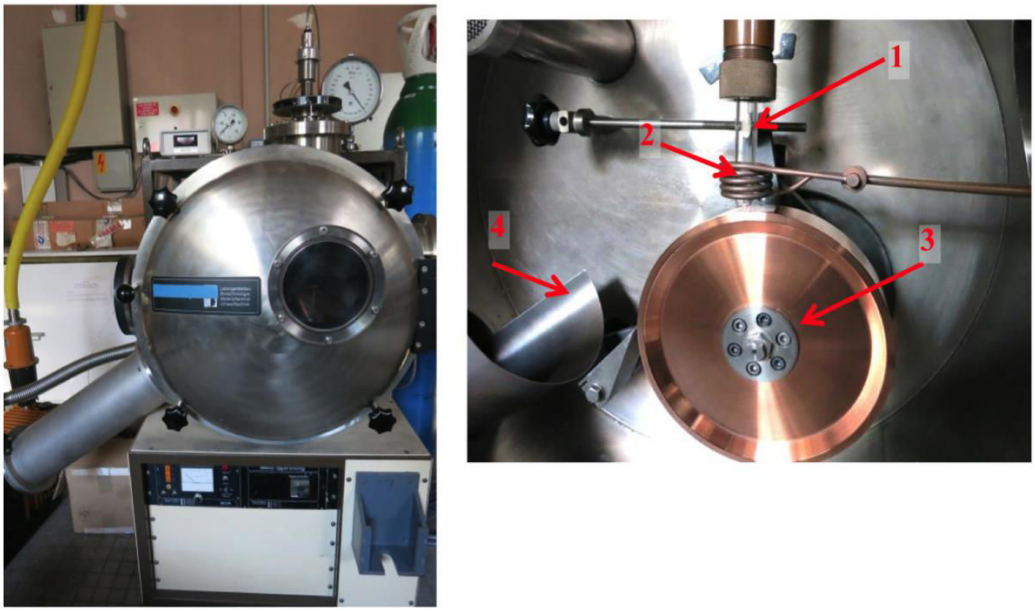

Figure III-5: Edmund Bühler melt-spinner located in IJL. Left: general view; right: inner chamber design, where 1 – crucible, 2 – induction coil, 3 – cupper wheel, 4 – material collector.

well controlled so that very high melting speed can occur resulting sometimes in overheating and high rates of Te evaporation. Another possibility examined was to cut the initial ingot into sectors along the crystallization direction with a diamond wire-saw and to use the obtained elongated pieces in the melt-spinner. This method gave quite satisfying results in terms of Te loss, but the heating time and speed were not well reproducible from operation to operation. It is likely due to the weak heat coupling between pieces of irregular shape (with high dispersion in material size inside) and the induction coil (2) that serves to the melting purpose. The last and most satisfying method that gave reproducible melting processes and low Te evaporation is the use of well-defined size pre cold-pressed cylinders (pellets) prepared from the grinded initial ingots. Thus we improved a lot the melting process due to the regular shape of the pellets that fit to the crucible. The description of the cold-pressing process can be found in paragraph II-4 of this chapter.

After the material has been put in the crucible, the latter is fixed in the chamber and moved to such a position that the gap between the nozzle and the wheel is of the order of the nozzle diameter. The chamber is pumped down to 10^{-3} mbar (primary vacuum) during 10 min and filled with argon atmosphere up to 0.6 bar. Two gas cartridges are filled with argon as well up to 1.2 bar, thus an overpressure of 0.8 bar can be reached allowing pushing the molten material onto the wheel. Several variants of the pressure to overpressure rate have been tried during the first

attempts. Due to the relatively low viscosity of the $Sb_{2-x}Bi_xTe_3$-based compounds and the high volatility of Te, the values mentioned above were empirically chosen. After the chamber is prepared, the wheel starts to turn with a speed varied between 1000 and 6000 rpm (10-50 m/s linear). Finally, the electrical supply of the conduction coil is turned on to melt the material inside the crucible. The temperature inside the crucible is constantly checked by a MAURER digital infrared pyrometer. When it rises above 620°C (the melting temperature of ternary compounds is about 615°C), the overpressure is applied by opening a valve and the melt goes down through the nozzle onto the rotating cupper wheel. The melt cooled on the wheel forms melt-spun "ribbons" or "flakes" of typical dimensions 3-5 mm in length, 0.5-3 mm in width, and 5-15 µm in thickness (Fig. III-6) that are mostly gathered in the material collecting tube (4) with some amount spread in the chamber. The overall duration of the ribbons production is about 1-2 minutes with crucibles charged at maximum.

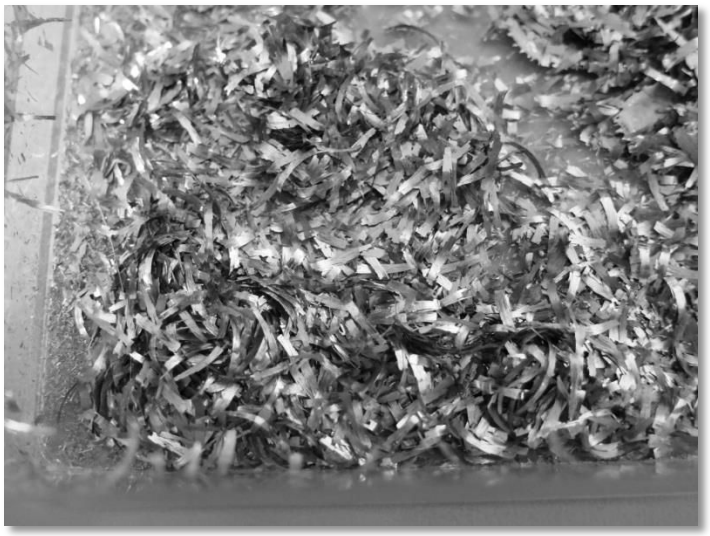

Figure III-6: Collected melt-spun ribbons.

The process has been visualized through an ultra high-speed video system (Photron SA5) using frame rate 12000 fps. The captured video has been transferred to a computer by Video Studio 8 software (v. 8.5 Pinnacle Systems). Photron FASTCAM Viewer software was used for the data analyses. Figure III-7 displays some images taken at different stages of the process. A sufficient lighting is a crucial point to allow imaging of smaller scale motions of the melt-spun material. The camera needs to be focused on the edge of the puddle before casting. Ensuring the focus is correct is the most important part of this procedure, given that that the depth of focus is

typically only a couple of millimeters. Focusing on a small piece of wire placed in the gap at the edge of the nozzle slot is an easy way to focus the camera. Ensuring that the camera is looking straight through the gap region is also difficult but important. The puddle length *L*, estimated from these images, is 1 mm. This measurement has a large uncertainty due to the difficulty in locating the downstream air-liquid-ribbon tri-junction. One can then define an average residence time $\tau = L/U$ (*U*: wheel speed) of the liquid in the puddle, defined as the amount of time it takes for a point on the wheel surface to rotate through the length of the puddle. This is the average time that a packet of material spends within the puddle region. For our process with the average speed *U* about 35 m/s the average residence time can be roughly estimated as $29 \cdot 10^{-6}$ s. It was shown by Huang et al. /HUA85/ that the residence time could be correlated with ribbon thickness (*R*), such that $R \sim \tau^{1/2} \cdot 10^{-3} \mathrm{m \cdot s^{-1/2}}$. Taking into account the previous estimation, the thickness of the obtained ribbons should vary in the range of 5 – 10 µm. These results are in a good agreement with the thickness observed on scanning or transmission electron microscopy images from ribbons cross-sections, as we will see later in this chapter.

Figure III-7: Images taken by a high-speed camera before the melt ejection (left) and during the melt-spinning process (right).

Fedotov et al. /FED14/ estimated the cooling rate using the following equation:

$$K = \frac{\alpha \cdot \theta}{Cp \cdot d \cdot R} \qquad \text{(III-1)}$$

where *a* is the heat convection coefficient, θ is the excessive temperature of the melt, *Cp* is the specific heat capacity of the melt (~ 0.19 J/g.K), *d* is the $Sb_{2-x}Bi_xTe_3$ density (~ 6.83-6.90 g/cm^3 depending on the composition). Heat convection coefficient for a polished copper surface can be estimated as $(1–2) \cdot 10^5$ W/(m^2·K) /BOE93/. Excessive temperature of the melt was about 20 K.

Taking into account the *a* value for copper, and also θ, *Cp* and *d* for $Bi_xSb_{2-x}Te_3$, the cooling rate is estimated to be in order of 10^4 K/s for thicknesses of 5-20 µm. Similar values were reported by other researchers for similar experiments /BOE93, SAL60/.

I-4) Densification of the materials

I-4-1) Spark Plasma Sintering (SPS)

1) Principle

Spark Plasma Sintering (SPS), contrarily to more conventional sintering methods (hot pressing, for example) in which the powders are heated through convection and radiation, uses Joule effect for the densification. Sintering of powders from an electrical current is not a new technique, since the first studies are dated from 1930 (concept proposed by Taylor /TAY33/. However, the current SPS process has only been developed from 1960 by the group of Inoue /HON64/. Due to the joint actions of uniaxial pressure and pulsed electrical current, the process takes only few minutes (time may however vary up to one hour depending on the material) while several hours are required with hot pressing, to obtain a material of similar density, making this process unique in terms of time-saving. Moreover, the very short sintering time offers the opportunity to retain very fine microstructures and to prevent grain growth, rendering this technique essential for the preparation of nano-structured materials /KAT07, KUO09, LI06, LIU07, REC07, ZHA04/. The technique has also other advantages like: easiness of use, little prior experience necessary, appropriate for many materials, excellent reproducibility and reliability, precise control of the applied energy, high rate of densification leading to enhanced mechanical and physical properties. The application of SPS gave rise to numerous improvements in material science, especially for the elaboration of new materials sensitive to deformation.

The SPS sintering process was previously explained by phenomena that occur during electrical discharges, i.e. the creation of plasmas around the particles (Fig. III-8). According to this theory, the plasma created at the contact between two particles would lead to the formation of bridges improving diffusion phenomena. When a spark discharge appears in a gap or at the contact point between the particles of a material, a local high temperature-state (discharge column) of several thousands of degrees centigrade is generated in a moment. This causes

evaporation and melting on the surface of the powder particles leading to the formation of "necks" around the area of contact between particles /TOK99/. Other authors also assume that these plasmas would eliminate surface impurities, promoting densification /CHE05, GRO03/. The existence of these micro-plasmas has however still not been clearly demonstrated and is still currently the object of numerous debates.

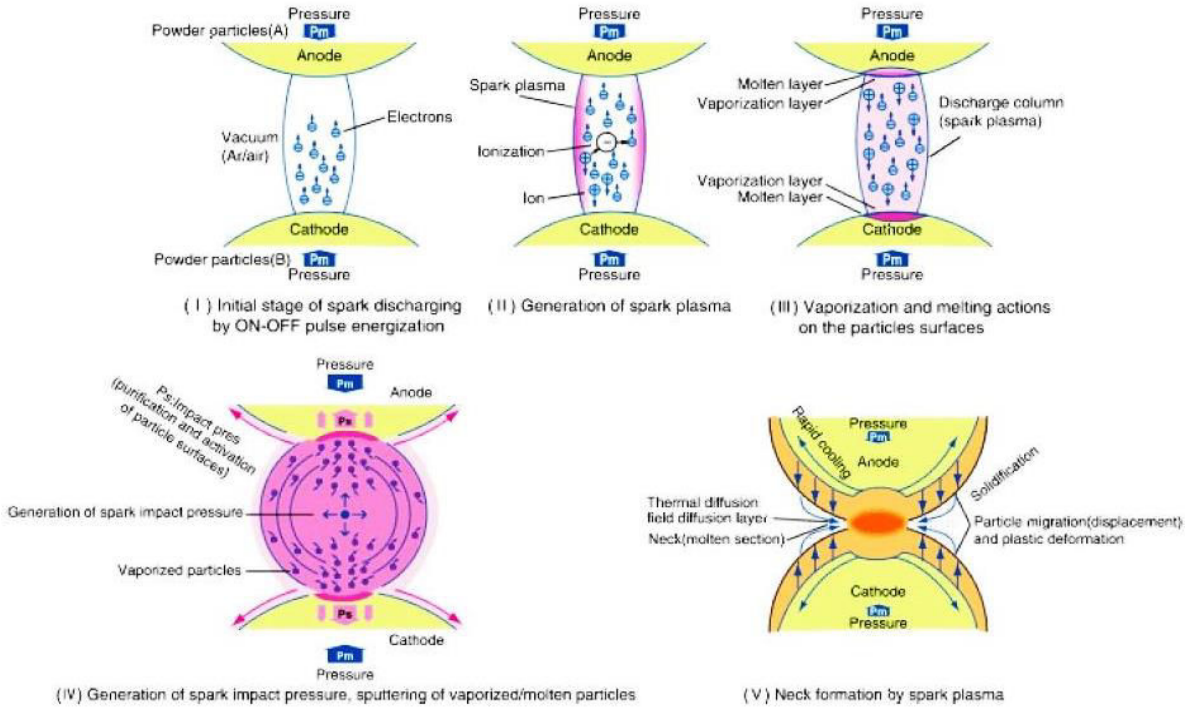

Figure III-8: Creation of a plasma at the contact between two particles after /TOK99/.

2) Apparatus description

The SPS densification of our materials was perfomed according to an established protocol using a Dr Sinter 515S SPS model marketed by SPS Syntex Inc (Figure III-9). The machine delivers a maximum current of 1500 A and a maximum force of 50 kN. Experiments can be conducted under primary vacuum, secondary vacuum or under an argon atmosphere.

Graphite dies (Fig. III-10a) supporting a pressure of 90 MPa of different inner diameters (10.4, 12.4 or 15.4 mm) and graphite punches (10, 12, or 15 mm in diameter, respectively) have been used according to the objective of our work. First, the hole of the die was covered with a graphite paper (0.2 mm in thickness) adjusted to the size of the die hole in order to facilitate

Figure III-9: Dr Sinter 515S SPS Syntex Inc. installed at IJL.

removal of the fabricated ingot. The lower punch, one graphite disc, the powder to be sintered, a second graphite disc and the upper piston were then introduced into the die successively. The whole was then placed in the SPS chamber as shown in Figure III-10b and the thermocouple for the temperature control was positioned in a lateral hole in the matrix. Primary vacuum was then done in the chamber, followed by the densification process.

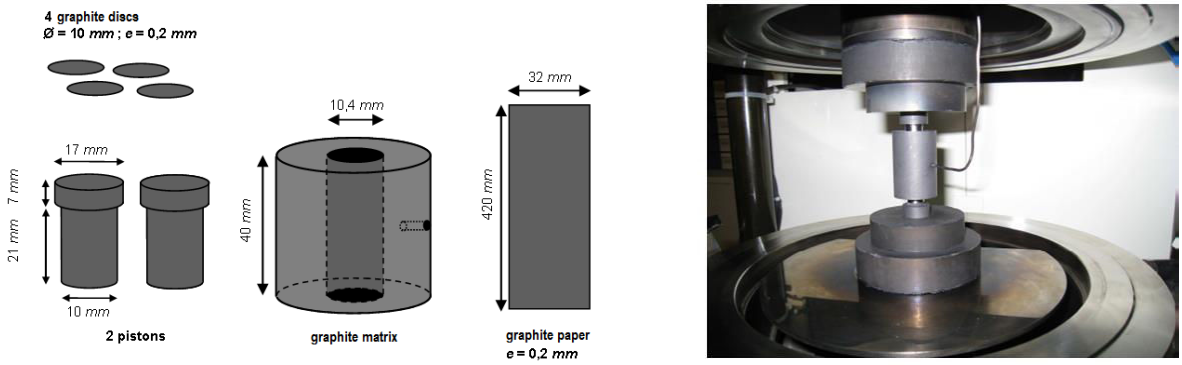

(a) (b)

Figure III-10: (a) Scheme of dies, punches and graphite foils used and their dimensions illustrated for an inner hole diameter of die of 10.4 mm, (b) photograph of the matrix installed in the sintering chamber. The thermocouple is inserted into the side hole for controlling the temperature the closest to the powder.

3) Preparation of the samples

The powders were obtained from crushing in an agate mortar either the initial ingot or the melt-spun ribbons. After SPS, the former bulk material will serve as the reference material to

check the influence of melt-spinning on the transport properties. A particular sample was prepared in which we aligned the melt-spun ribbons in the graphite die.

All compounds were densified at a pressure of 30 MPa. During the experiment, it is possible to follow the evolution of densification through the change of the displacement Δz. The heating rate from room temperature up to 500 °C was about 2°C/s. After heating, the sample was stabilized at this temperature during 1 min. The overall sintering process did not exceed 5 min as suggested in some publications /XIE11/. An example of temperature rising and corresponding Δz rising during the sintering can be found on Figure III-11.

The idea of checking the influence of an additional structuration on the thermoelectric properties of materials was successfully realized by Kenfaui et al. /KEN12/ for cobaltite oxides. Repeating the SPS process another time improved the texture of the sample and oriented the grains in a preferable way, increasing thus by two times the *ZT* values. It was further applied with some promising results to p-type BiSbTe and n-type BiSeTe based compounds /BHA13, LOG14/. In our work, we performed two cycles of SPS densification with the same heating ratio and pressure applied, replacing the 12 mm in diameter pellet obtained after the first SPS in a die of 15 mm in diameter for the second process.

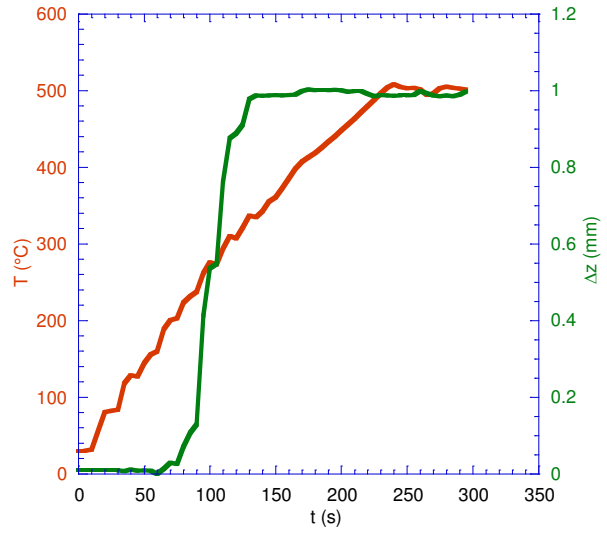

Figure III-11: Common behavior of Δz for the chosen temperature program during the SPS process for $Sb_{2-x}Bi_xTe_3$ samples. The densification starts at about 200°C and stabilizes above 350°C.

The density, d, of all prepared samples was evaluated from their dry mass and their geometrical dimensions. The values were compared to the theoretical density, d_{th}, of $Sb_{2-x}Bi_xTe_3$. The values vary from 6.79 to 6.90 g/cm^3 depending on the stoichiometry. The relative densities, d_r, ($d_r = d/d_{th}$), are as high as 93-98% for the different samples we prepared (see Table III-1).

I-4-2) Cold-pressing

Cold pressing was used for some samples (Table III-1) as an alternative method to SPS in order to see if absence of heating (even if low heating times are required) could have any influence on the transport properties. More precisely, we were interested if there is a possibility to access to the intrinsic transport properties of melt-spun ribbons themselves through this experiment.

The process was performed in a hydraulic press Specac (Fig. III-12a). Fine powders of the materials (melt-spun samples) were placed in between punches in a stainless steel die (Fig. III-12b) with a hole diameter of 10 mm. The whole was placed in the press and connected to the primary pump. The total pressure applied was 5 tons (that corresponds to 49 kN or 625MPa). The scheme of the hydraulic pressing is presented on Figure III-13. The obtained samples were in the form of cylinders with a diameter of 10 mm and a height of about 5 mm. With this simple approach a relative density as high as 93% was reached for the cold pressed samples.

a) 

b) 

Figure III-12: Cold-pressing: a) hydraulic press; b) the stainless steel die with connection to the primary pump and the punches.

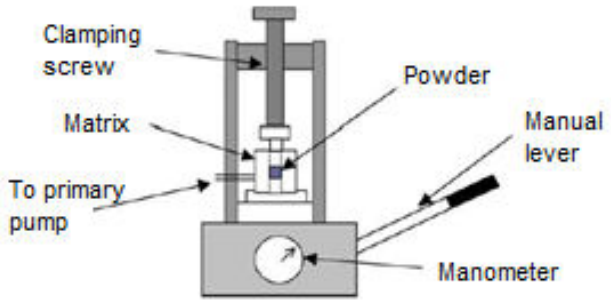

Figure III-13: Principle of the hydraulic press operation.

II) CHARACTERIZATION TECHNIQUES

II-1) X-ray diffraction (XRD)

X-ray diffraction was used both to determine the samples structure and as a mean of verifying the synthesis products at each state of the preparation. Interaction between X-rays and the electrons of a material cause X-rays to diffract. When the paths of two diffracted X-rays differ by an integral value of their wavelength, they are in phase and constructive interference is observed. Formally, the condition for such constructive interference is described by Bragg's law,

$$2d_{hkl}\sin\theta = n\lambda \qquad \text{(III-2)}$$

where n is an integer representing the order of the diffraction peak, λ is the wavelength of X-ray radiation, d_{hkl} is the interplanar distance for the given (hkl) set of lattice planes and θ the angle between incident rays and scattering planes. Scanning the sample through a range of angles (2θ) allows reaching all possible diffraction directions of the lattice, due to the random orientation of the powdered material.

X-ray diffraction patterns were recorded on a Bruker D8 Advance diffractometer in Bragg-Brentano geometry (Fig. III-13) using Cu $K_{\alpha 1}$ radiation (λ_{Cu} = 1.54056 Å). The primary monochromator (Vario 1) is a (111) oriented crystal of germanium allowing to separate ray $K_{\alpha 1}$ from ray $K_{\alpha 2}$. Two detectors are available:

- a LynxEye detector of linear localization, equipped with Soller slits (2.5 and 1.5°) and blocks of anti-diffusion slits. This detector can work in two modes: 1D-mode for very fast θ/2θ measurements and 0D-mode for direct beam alignment;

- a SolX detector, equipped with different motorized blocks for anti-diffusion slits controlled by computer.

Data were generally collected in the following conditions: $20° \leq 2\theta \leq 120°$ with step size 0.02894°.

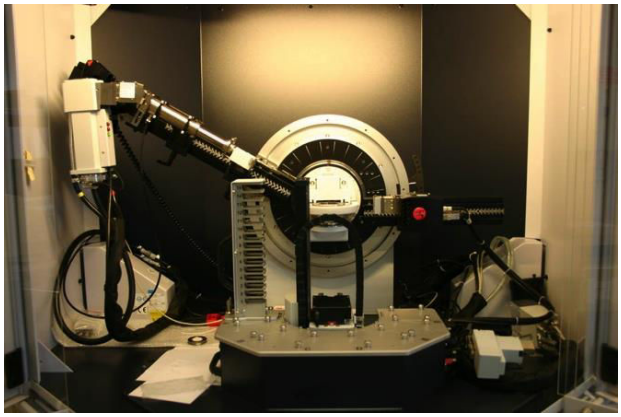

Figure II-13: Bruker D8 Advance diffractometer.

According to the nature of the samples (powders, ribbons, bulk), different ways of fixing the samples to the sample holder have been adopted:

- fine crushed powders are uniformly dispersed on a plane sample holder with a few drops of cyclohexane,
- ribbons are attached to the sample holder with double face scotch or with a few drops of cyclohexane,
- bulk samples, previously polished, are fixed by modeling clay in a cavity of the sample holder with the polished face arising on the surface of the cavity.

The plane sample is set in an automatic sample changer (2 X 15 positions) positioning the sample in the center of the goniometer in a unique position. It can be driven in a rotational motion perpendicular to the scattering plane. The source is fixed, the sample is rotating at an angle θ, while the detector is driven by a rotation of 2θ.

All the diffraction patterns were analyzed using EVA software.

II-2) Scanning Electron Microscopy (SEM)

The principle of scanning electron microscopy is based on the electrons-matter interactions. A material emits several types of radiations under the action of primary electrons. The main signals generated are secondary electrons (SE), backscattered electrons (BSE), and furthermore X-rays, according to the energy of the primary electrons, revealing information about surface morphology, phase contrast, and chemical composition, respectively.

The secondary electrons are emitted from atoms that are located at the upper surface of the sample (between 1 and 10 nm in depth) and give a topological contrast of the surface. The obtained micrographs reproduce an easily interpretable image of the surface. The brightness change of the cathode ray tube as a function of the angle of incidence of the electrons gives the contrast in the obtained image, resulting in the production of a topographical image of the surface. A high-resolution image can be obtained due to the small diameter of the primary electron beam.

The backscattered electrons are electrons of the primary beam that are backscattered or reflected in an elastic way by the atoms in the sample. The compositional contrast in the generated image arises from the difference in atomic number of the sample elements. The signal is brighter for regions of a higher middle atomic number in the investigated area. The image thus shows the distribution of the different chemical phases present in the sample. Since these electrons are emitted from a certain depth in the sample (between 1 and 200 nm in depth), the image resolution is not as good as for secondary electrons.

The interaction of the primary beam with atoms leads also to ionization processes of their inner shells giving rise to the emission of X-rays whose energy is characteristic of the parent element. Scanning electron microscopes equipped with energy dispersive X-ray spectrometry (EDS, EDX) allows performing an elemental analysis of the elements in presence. EDS can provide a rapid qualitative analysis or, using standard reference samples or inner software, a quantitative analysis of the elementary composition at a depth of about 1-2 microns. X-ray mapping provides images of elemental distributions in a sample. The information that X-ray maps provide can be readily assimilated and, in many cases, a problem can be solved by knowing the distribution of a particular element without requiring quantitative point analysis. While BSE images can show variations in composition in a sample, X-ray maps can show which elements are responsible for the variation. Elemental X-ray maps are produced by recording the number of

X-ray photons of a specified energy generated from each point over a fixed counting time, while the electron beam is scanned over a rectangular area.

a)  b) 

Figure III-14: Scanning electron microscopy facilities available at IJL: a) Philips/FEI XL30 FEG; b) FEI Quanta 600 FEG.

In this work, we used two different field emission gun (FEG) scanning electron microscopes. The first one is a Philips/FEI (SEM-FEG XL30) (Figure II-14a) equipped with a high resolution TLD detector allowing working at low voltage and an EDS spectrometer (EDAX system, Eloïse, EDAX Genesis software, Si(Li) detector, optimal working conditions: 1000 counts, working distance of 5.3 mm). The second one is a FEI (Quanta 600 FEG) (Figure II-14b), equipped with an EDS spectrometer (Quantax, Bruker AXS, Esprit software, SDD detector, optimal working conditions: 10000 counts, working distance of 11 mm).

Observation of bulk materials has been carried out either on a small broken piece of an ingot or on a mirror-polished piece. Ribbons have been observed on both faces (free surface or surface in contact with the wheel). Some images have been taken directly from the cross section.

II-3) Transmission electron microscopy (TEM)

Transmission electron microscopy has been used to complete on a more nanometric scale our morphological, chemical and structural studies undertaken with the previous instruments (MEB, EDS, XRD). A high energy electron beam is transmitted through a very thin sample to image and analyze the microstructure of materials with atomic scale resolution. The electrons are focused with electromagnetic lenses and the image is observed on a fluorescent screen or recorded with a digital camera.

II-3-1) Description

The TEM image of a sample is formed either from the transmitted electron beam (bright field image) or from one of the diffracted beams (dark field image). In bright field images, the contrast has two origins: the contrast of absorption and the contrast of diffraction. The contrast of absorption comes from the absorption of the incident electrons when they cross the sample. Absorption is all the more intense and the image all the more dark that the sample is thick and made of heavy elements. The diffraction contrast depends on the orientation of the crystal or of the local defects in the structure with regard to the incident beam. When the diffracting element is in a Bragg position, the intensity of the transmitted beam is decreased by the formation of diffracted beams. The image is thus darker. The bright field image appears thus as a shadow of the specimen. Dark field images are formed by selecting a diffracted beam with the use of a diaphragm. Only regions that are in the Bragg position are diffracting strongly into the objective aperture giving rise to bright contrast in the image. This technique allows distinguishing the diffracting parts. This kind of imaging is useful in studying crystal defects, and for the imaging of specific crystallographic phases.

Transmission electron microscopy studies can also give information about the structure, in particular the crystalline nature, of the samples under investigation. When the electron beam passes through the thin crystalline sample, it is diffracted by the atomic planes in the sample when the Bragg condition is satisfied. These waves interact constructively and are brought to focus at the back focal plane of the objective lens to form the diffraction pattern. The appearance of the diffraction pattern reflects the nature of the crystalline phases in the specimen. When the electron beam interacts with the sample that is oriented with a zone axis pattern parallel to the electron beam, the diffraction pattern formed is a regular array of reflections (bright spots)

organized in a predictable manner based on the crystal structure of the sample. Instead of intensity spots, the electron diffraction pattern can be composed of concentric rings. Diffuse ring diffraction patterns with no discrete reflections and one or possibly two diffuse rings of maximum intensity are produced with amorphous materials, e.g. polymers and metallic glasses, that contain no long-range order in the atomic lattice produce. Individual reflections can be seen within the rings if the material is a collection of a large number of crystals, with different orientations.

High resolution transmission electron microscopy (HRTEM) images are images that have the symmetry and the aspect of the projected crystallographic structure. The images in HRTEM are based upon the interference between the direct beam and at least one of the diffracted (hkl) beam. The distance between the interference rings is directly proportional to the distance between the (hkl) type planes. The imaging of the atomic lattice requires its orientation in such a way that the atomic columns of this lattice are oriented parallel to the incident electron beam. The main difference between conventional TEM and HRTEM is that HRTEM creates an image based on several beams, while conventional TEM produces an image from only one electron beam. The HRTEM images will be simply analyzed by the mean of the Digital Micrograph software allowing creating a pseudo-diffraction pattern via Fast Fourier Transform (FFT).

Scanning Transmission Electron Microscopy (STEM) is a TEM technique in which a focused electron beam is scanned over the sample. The signal is recovered at each point. We have only used the STEM mode for the chemical analysis of our samples. This configuration allows delivering high probe current, even for probe sizes less than one nanometer, while keeping good spatial and energetic resolutions.

II-3-2) Preparation of the samples

The preparation of the samples is of prime importance to obtain good images. As our material contains quite heavy elements that are absorbing a lot, very thin slices must be achieved (less than 60 nm in thickness) to get highly contrasted images.

Two methods of sample preparation have been tested during our work:

1) Micro-cleavage, consisting in scratching with a diamond pen the surface of the sample and to recover the powder on a carbon covered cupper grid, hoping some particles will be thin enough.

2) Cutting a slice using the dual beam Focused Ion Beam – Scanning Electron Microscopy (FIB-SEM) technique in a zone of interest. It gives the possibility to cut the slices from the starting material in any orientation. In the FIB technique, the projection of Ga^+ ions (accelerated between 0.5 and 30 keV) enables precise local sputtering of a material. The ionic beam is a mean to either machine the slice or to have a ionic image of the sample (likewise an electronic image in the SEM). In the dual beam technique, the FIB column is mounted on a scanning electron microscope. In this instrumental configuration, electronic images of the slice can be obtained during the ionic machining, allowing following in live the thinning of the sample. The ionic column makes an angle of 52° with regard to the electronic column. A protective layer of platinum or carbon is generally deposed on the surface that will be machined thanks to an evaporation source included in the machine. The instrument is also equipped with a micromanipulator to in-situ extract the slice and to weld it to a support adapted for TEM observations. The so-called lift-out technique is used to produce the thin slices /THO07/.

Thin slices of melt-spun ribbons (top and cross-sections) and bulk materials have been prepared by the dual FIB-SEM technique thanks to Dr Laurent Legras (EDF R&D, Les Renardières) and Dr Flavio Soldera (Material Engineering Center Saarland). In both cases, the machine used is a Helios Nanolab 600 (FEI). Two FIB-SEM providers (FEI and JEOL) have also contributed to the providing of thin slices. Many attempts have been performed before good quality slices of $Sb_{2-x}Bi_xTe_3$ could be achieved.

II-3-3) Microscopes

Three different microscopes have been used to observe the various samples we have prepared. The observations were performed with Mrs Sylvie Migot and/or Dr Jaafar Ganbahja at Institut Jean Lamour either on a Philips CM-200 microscope (Figure III-15b) operating at 200 keV to check the quality of the slice and to perform imaging, diffraction, and analyses or on a Jeol ARM200F cold FEG (Figure III-15a) corrected in beam when the quality of the sample was recognized (mainly what concerns the thickness of the slices that must be thin enough to transmit the electron beam) to perform HRTEM and STEM coupled with chemical analyses (resolution of 0.08 nm at 200 kV with a STEM Cs corrector incorporated as standard, Jeol SDD detector, Analysis Station software). One slice was observed at EDF R&D Les Renardières with Dr Laurent Legras on a Titan (FEI) microscope.

a) 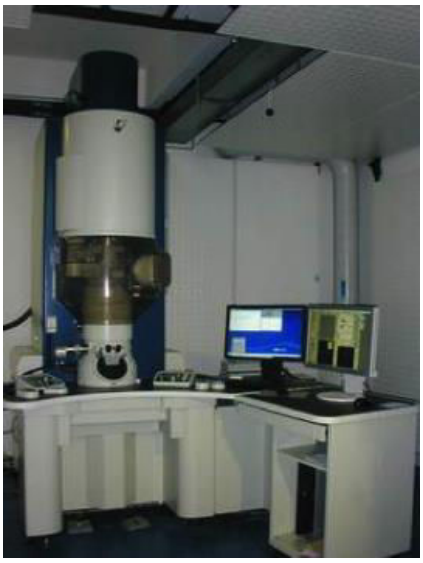 b) 

Figure III-15: Transmission electron microscope facilities available at IJL: a) Jeol ARM200F cold FEG; b) Philips CM-200.

III) PHYSICO-CHEMICAL CHARACTERISATIONS OF THE MATERIALS

Different samples have been characterized by the several techniques described before. Systematic studies have not been carried out, but specific analyses have been performed to provide any information on the influence of some preparation parameters on the micro-nanostructure that could help to interpret the transport properties.

III-1) Structural investigations by X-ray diffraction (XRD)

III-1-1) Melt-spun ribbons

In order to investigate if the temperature gradient (and thus the cooling rate) occurring during the solidification of the ribbons has an influence on their crystallographic orientation, few uncrushed MS ribbons were fixed on the sample holder of the XRD apparatus.

It seems to be important here to precise the order of magnitude of the penetration depth δ that is probed with XRD as the thickness of the ribbons is quite small according to the estimations made in §I-3-2 of this chapter. According to the M. Birkholz et al. /BIR06/, a

penetration depth for normal incidence that specifies the path length for which the intensity I_0 drops to $1/e$ of its initial value is:

$$\delta_{1/e} = \left(\rho \cdot \sum_i \frac{g_i}{G}(\mu_m)_i\right)^{-1} \quad \text{(III-3)}$$

where ρ – the density of material, g_i – the atomic mass of the element in the compound, G is the mass of the molecular unit and μ_m – the mass absorption coefficient of the element. The values of μ_m are tabulated and for Cu K_α radiation they reach 25.9, 26.7 and 24.4 m^2/kg for Sb, Te and Bi correspondently /CRE99/. So the penetration depth δ can be estimated as several µm depending on the composition and does not exceed our ribbons thickness.

The study, performed separately on the ribbons surface that was and was not in the contact with the copper wheel during melt-spinning ("contact" and "free" surface, respectively), revealed well crystallized structure. The width of the peaks suggests that the size of the grains are above nanoscale range. And, finally, ribbons demonstrate preferential growth orientations according to the analyzed surface. For the free surface, the main peak corresponds essentially to the (015) *hkl* planes, whereas in the case of the contact surface, it is the (110) diffraction peak that is the most intense among the three strong peaks observed (Fig. III-16). None of the (00*l*) diffracting plane, corresponding to the c axis perpendicular to the surface, could be observed. The solidification rate has thus a great influence on the crystallographic orientation, with a strong texturation occurring at the beginning of solidification. It should have been interesting to know at which thickness the change of orientation occurs by changing for instance the angle of the X-rays penetration in the matter.

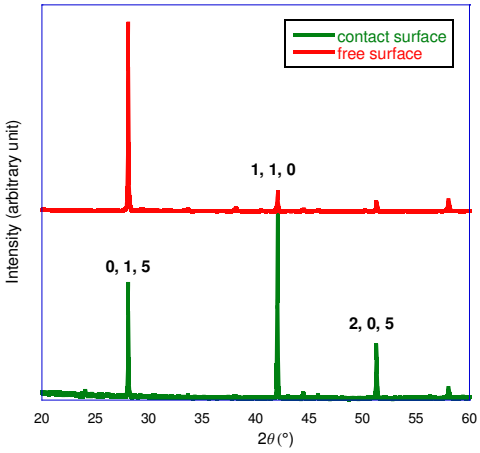

Figure III-16: XRD patterns for the contact and free surfaces of $Sb_{1.52}Bi_{0.48}Te_3$ melt-spun ribbons.

The presence of (110) diffracting planes means that the trigonal (c) axis of the hexagonal representation of the $Sb_{2-x}Bi_xTe_3$ cell is parallel to the surface with grain growing in a random way in the basal planes, whereas the occurrence of (015) diffracting peaks means the c axis makes an angle of 58° with respect to the surface normal (Fig. III-17).

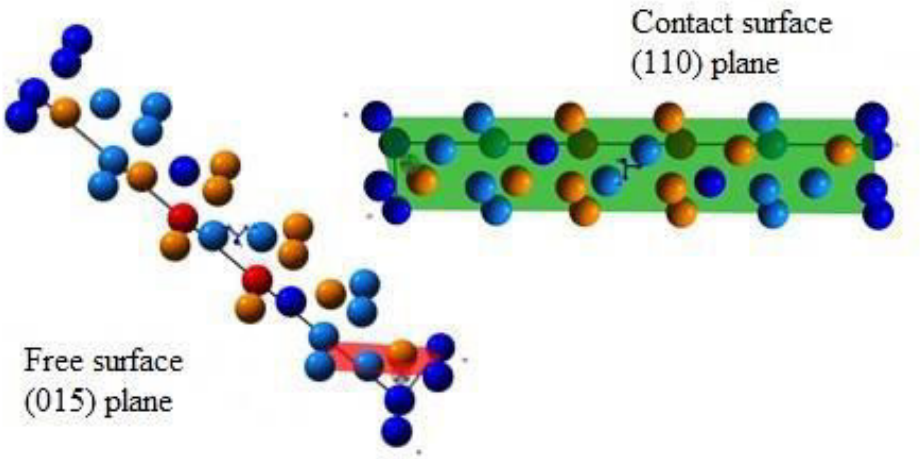

Figure III-17: Scheme of the most pronounced orientations depending on the side of the melt-spun ribbons: free surface (015) planes, wheel contact surface (110) planes.

III-1-2) Initial ingots and densified samples

X-ray diffraction analyses were performed on all bulk samples after each thermal treatment. As the variation of composition was applied in three directions (Bi content, Te content, and Sn content), it was interesting to check the influence of the variant content on the crystallographic structure and the purity.

Let us first have a look on the influence of Te over-stoichiometry. The powder XRD patterns of initial ingots of composition $Sb_{1.6}Bi_{0.4}Te_3$ and $Sb_{1.6}Bi_{0.4}Te_{3.1}$ are displayed in Fig. III-18. The samples are polycrystalline and the right phase has been formed. Both compounds crystallize into the rhombohedral crystal structure (R-3m), the position of the peaks matching well with the reference pattern for $Sb_{1.5}Bi_{0.5}Te_3$ (pattern n°01-080-6663). In the Te-rich compound, an additional peak located at $2\theta = 27.56°$ can be seen, that can be attributed to the hkl (011) peak of pure tellurium.

After the SPS process, the amount of Te decreases in $Sb_{1.55}Bi_{0.45}Te_{3.1}$, as can be seen in Fig. III-19a, where the peak of Te remains just as a shoulder of the (015) peak of the main compound.

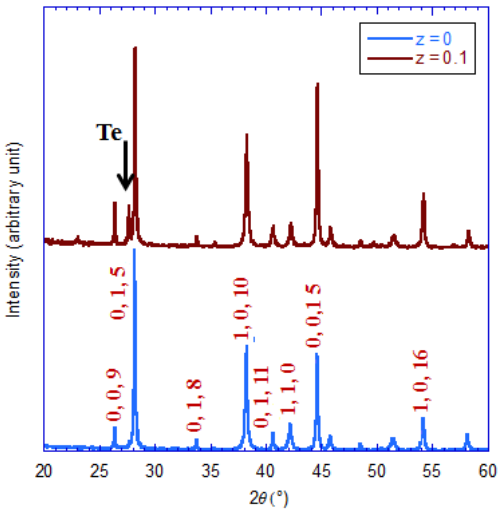

Figure III-18: Powder X-ray diffraction pattern taken at 300 K for the initial ingots of $Sb_{1.6}Bi_{0.4}Te_{3+z}$. The indexation of main peaks (hkl) planes is given.

It is much more evidenced by a zoom in the region of interest (Fig. III-19b). The MS-SPS sample of same composition is pure phase. During both MS and SPS (as it also occurs for the initial ingot, even if not of same Bi content) processes may cause a partial evaporation of Te during heating. It might also be due to its homogeneous assimilation into the crystallographic structure as nano-sized precipitates that are too small to be detected by XRD. The intensity of the (00*l*) peaks is decreased alongside with an increase of intensity of the (110) peak in the MS-SPS sample with regard to the reference sample, meaning a beginning of texture could be introduced leading to more anisotropic properties.

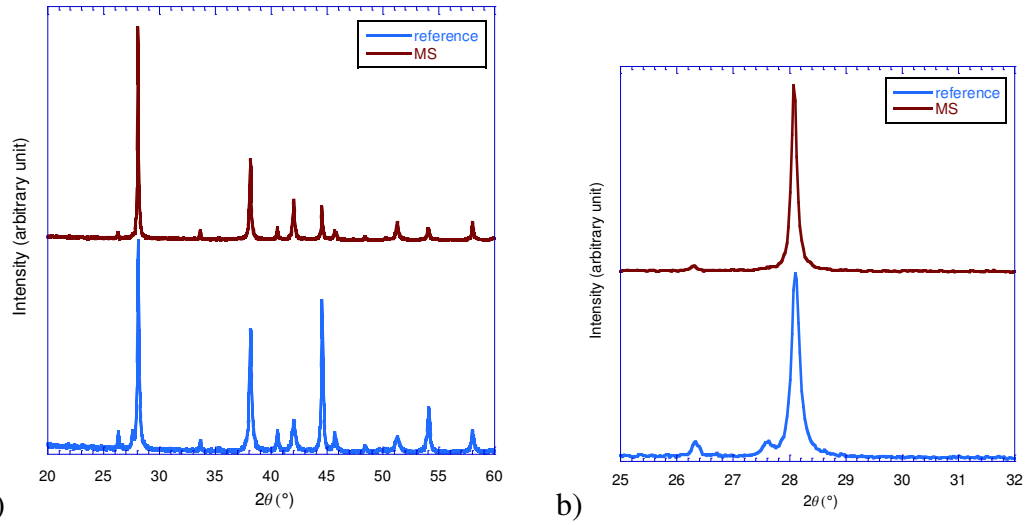

Figure III-19: a) Powder XRD patterns for $Sb_{1.55}Bi_{0.45}Te_{3.1}$ reference and MS-SPS samples; b) zoom in the region of interest 25-32°.

The influence of increasing x in the $Sb_{2-x}Bi_xTe_{3.1}$ manifests by a slight shift of the peaks towards higher 2θ values (Fig. III-20), highlighted for the region of interest of the (015) peak. This cell enlargement could be expected considering the substitution of Sb (of atomic radius = 0.145 nm) for Bi with higher atomic radius (0.155 nm). No Bi phase could be detected.

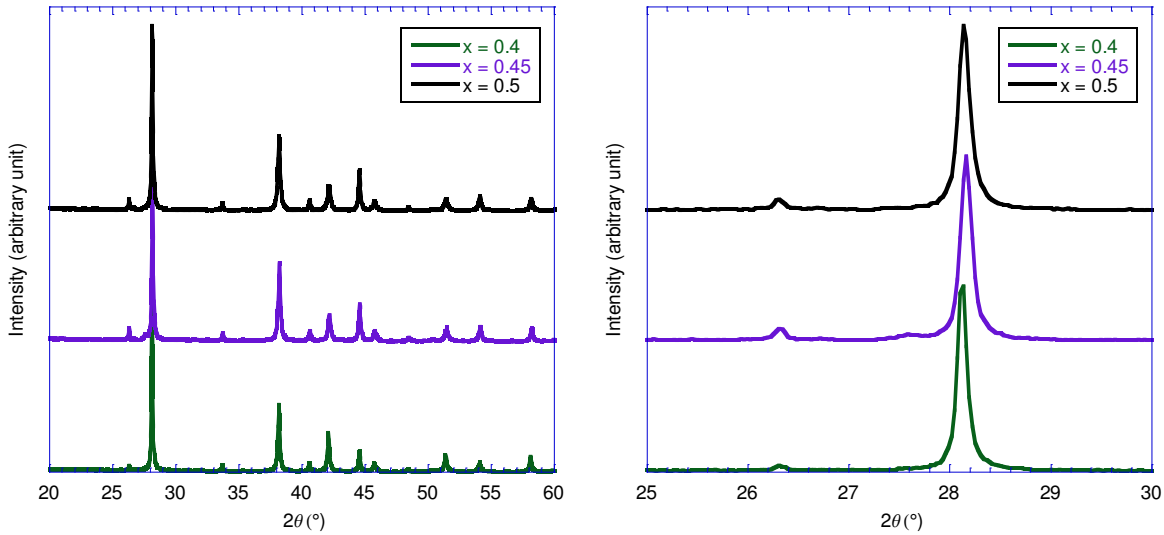

Figure III-20: Influence of x on the XRD patterns of MS-SPS samples of composition $Sb_{2-x}Bi_xTe_{3.1}$. Complete pattern (left) and zoom on the area near the main (105) peak (right).

Influence of doping with Sn on the crystallographic structure is shown for the reference samples of $(Sb_{1.52}Bi_{0.48})_{1-y}Sn_yTe_{3+z}$ family of materials. Enhancing y results in peak shifts towards lower angles (Fig. III-21), that is attributed to the possibility of Sn substitution at Bi/Sb atomic side /SAN11/.

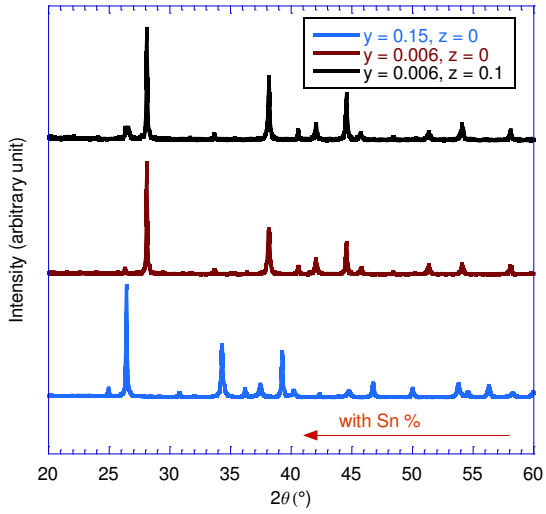

Figure III-21: Powder XRD patterns for reference $(Sb_{1.52}Bi_{0.48})_{1-y}Sn_yTe_{3+z}$ samples

III-2) Microstructure investigations by SEM

Numerous SEM, TEM and HRTEM investigations were performed in the frame of this work to check the structural influence of the melt-spinning process on our samples. The most representative of them will be reproduced in this chapter.

III-2-1) Melt-spun ribbons

Images obtained by SEM proved the complex two-sided crystallographic singularity of the melt-spun ribbons related to the position of the wheel to the ribbon. The surface that was in contact with the Cu wheel (contact surface) does not demonstrate any specific microstructural details except those related to the wheel roughness while the side that did not touch the wheel (free surface) exhibits very clear dendritic microstructures of 0.1-0.5 µm in width and some nanoparticles on them (Fig. III-22). As the thermal conductivity of the $Sb_{2-x}Bi_xTe_3$-based compositions is known to be quite low, a huge difference in the cooling rates between the contact surface and free surface can be expected explaining the gradual microstructure changeover observed. Different nucleation processes occur at different positions within the ribbons. This result is in the perfect agreement with those reported earlier by Xie and collaborators /XIE09a, XIE09b, XIE10a/, and the more recent results of Ivanova et al. /IVA13/. Such global microstructures have been observed whatever the conditions of preparation and the compositions of the alloys were.

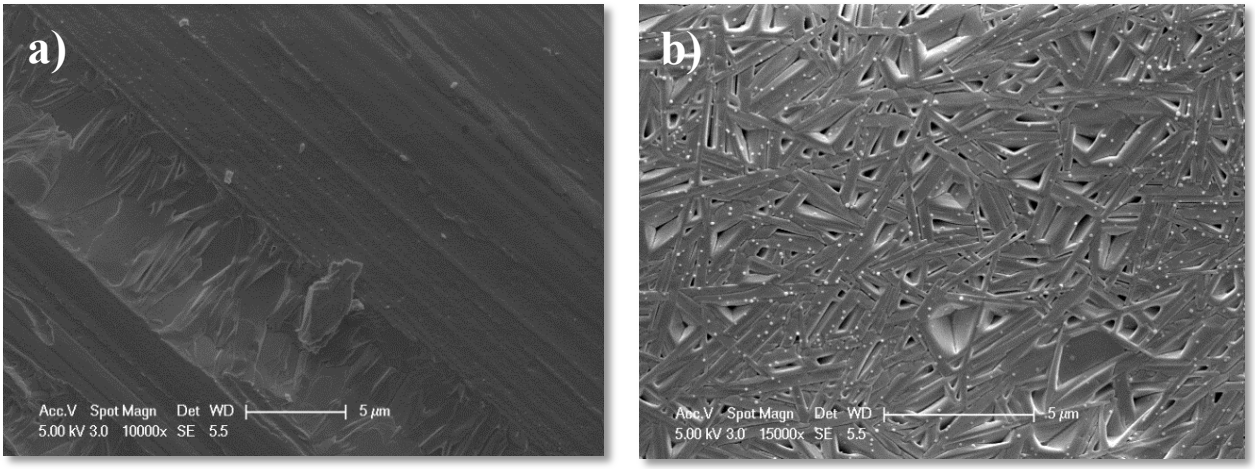

Figure III-22: SEM images of melt-spun ribbons of $Sb_{1.6}Bi_{0.4}Te_{3.1}$: a) contact surface; b) dendritic structure of the free surface decorated with nanoparticles.

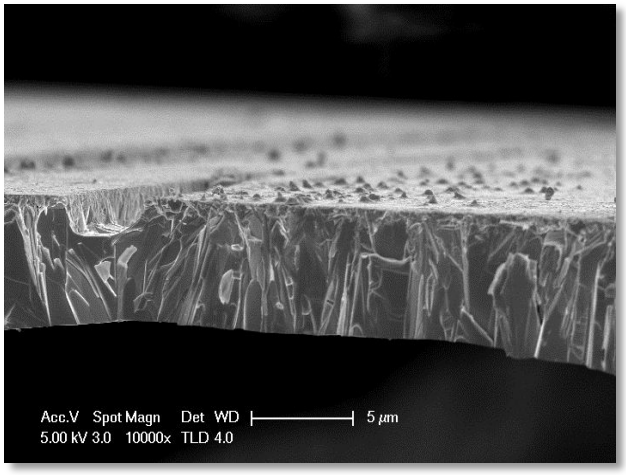

Figure III-23: Cross-section SEM image of a melt-spun ribbon.

From the cross-sectional views of the MS ribbons, a value of the average thickness was found to be in the range of 4-15 µm (Fig. III-23). Like bulk materials, the ribbons grow or solidify according to the c axis more or less parallel to the surface, likely because the thermal conductivity is higher is basal planes than along the trigonal axis to evacuate the heat and then to solidify. This observation is in agreement with the XRD study of the ribbons, leading to the presence of vertical lamellae that can be assimilated to columns (Fig. III-24a). The cleavage

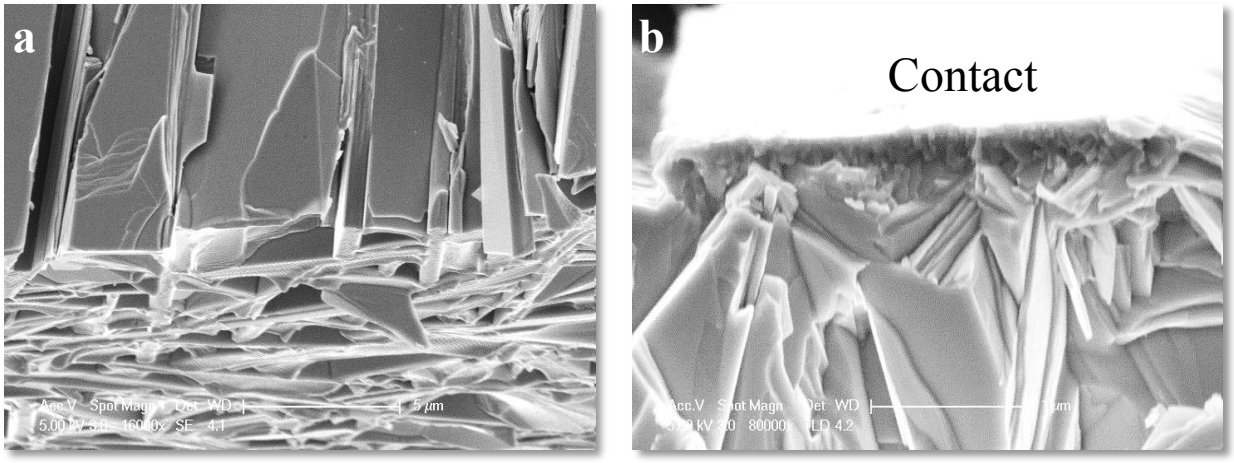

Figure III-24: High magnification SEM images of a cross-section of a ribbon: a) close to the free surface; b) close to the contact surface.

planes appear clearly along the direction perpendicular to the surface. The dendritic appearance of the free surface seems to result from the erratic growth in the basal planes (Fig. III-24a). Close to the contact surface, a mixture of small sized particles up to one micrometer in size was regularly observed (Fig. III-24b). These will serve as seeds for the future growth. This layer is

less than 100 nm in thickness. To have better ideas about the size and concentration of these crystals, HRTEM study was performed (see the following paragraph of this chapter). The free surface is also sometimes recovered with nanoparticles that were likely evacuated in the MS chamber during the material exit from the nozzle and that accumulate on the top of the ribbon.

III-2-2) MS-SPS ingots

After the densification of grinded melt-spun ribbons by SPS, the fracture of the obtained ingot shows that the particles are randomly oriented with an average grain size of about few dozen micrometers (Fig. III-25). The lamellar structure of the bismuth-antimony telluride family of materials can be easily observed. No difference could be observed according to the pressing direction (perpendicular or parallel).

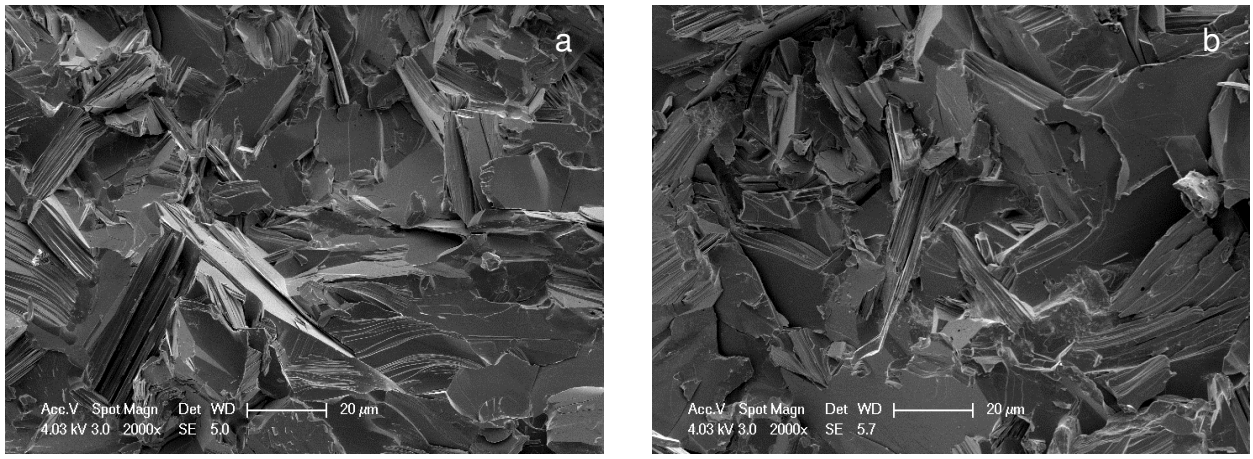

Figure III-25: SEM images of MS-SPS densified $Sb_{1.5}Bi_{0.5}Te_{3.1}$ samples a) along the pressing direction; b) perpendicularly to the pressing direction.

X-ray mappings were performed on two SPS densified series of samples: the series with excess Te and the series with Sn doping using the Quanta 600 FEG microscope.

For the samples with excess of Te, the Bi, Te, and Sb elements are homogeneously dispersed, proving the homogeneity at the microscopic scale of the densified samples. No trace of excess of Te could be found (Fig. III-26a). This can indicate the entrance of Te into the structure through occupation of vacant positions created during the thermal and mechanical treatment of the samples at pre-SPS steps or point out the evaporation of Te during the synthesis process. Te can also exist as nano-precipitates that cannot be detected by this method.

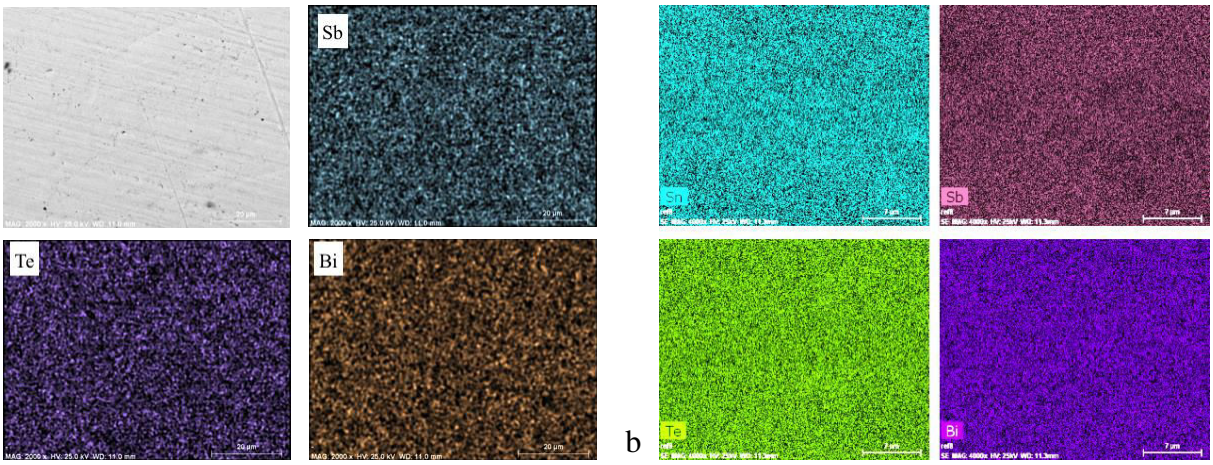

Figure III-26: Back-scattered electron image and X-ray mapping for: a) the $Sb_{1.6}Bi_{0.4}Te_{3.1}$ sample, b) the $Sn_{0.15}(Sb_{1.52}Bi_{0.48})_{1-x}Te_3$ sample.

For the series with Sn doping, even with the highest doping level, no evidence of aggregation of dopant could be observed (Fig. III-26b). All the elements are uniformly dispersed in the sample. We can conclude that these samples are homogeneous at a micron scale.

III-2-3) MS-double SPS ingots

Double SPS has been investigated on the $Sb_{1.6}Bi_{0.4}Te_{3.1}$ series. SEM images (Fig. III-27) taken on ingot fractures performed parallel or perpendicular to the pressing direction show no particular improvement of the orientation of the particles, in particular parallel to the pressing direction, as we could expect from this iterative process and mentioned in previous publications on the parents n-type materials /BHA13, LOG14/.

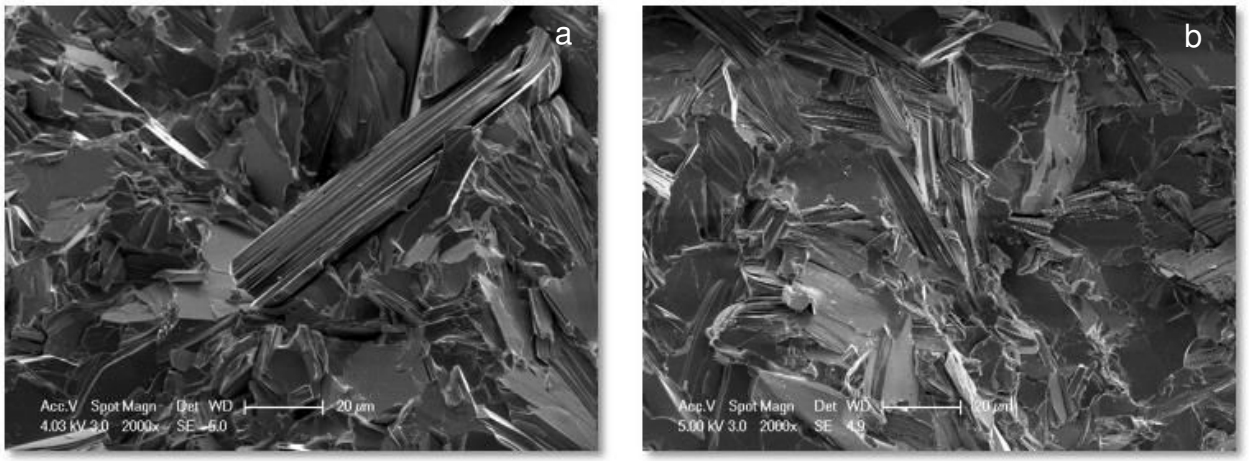

Figure III-27: Images of a) MS–SPS and b) MS-2SPS $Sb_{1.6}Bi_{0.4}Te_{3.1}$ samples taken along the pressing direction of SPS.

III-2-4) MS-aligned ribbons-SPS

On one series of samples, the $Sb_{1.6}Bi_{0.4}Te_{3.1}$ series we have tested if using aligned ribbons rather than grinded ribbons during SPS could provide a particular orientation to the particles, knowing that the ribbons grow in a columnar way, that could further influence the transport properties. In figure III-28 are reported the SEM fracture images obtained on such a sample and compared to an image from grinded MS ribbons-SPS, taken perpendicular to the pressing direction. The overall structure of the aligned ribbons-SPS looks more dense with larger grains, but the lamellar structures are randomly oriented.

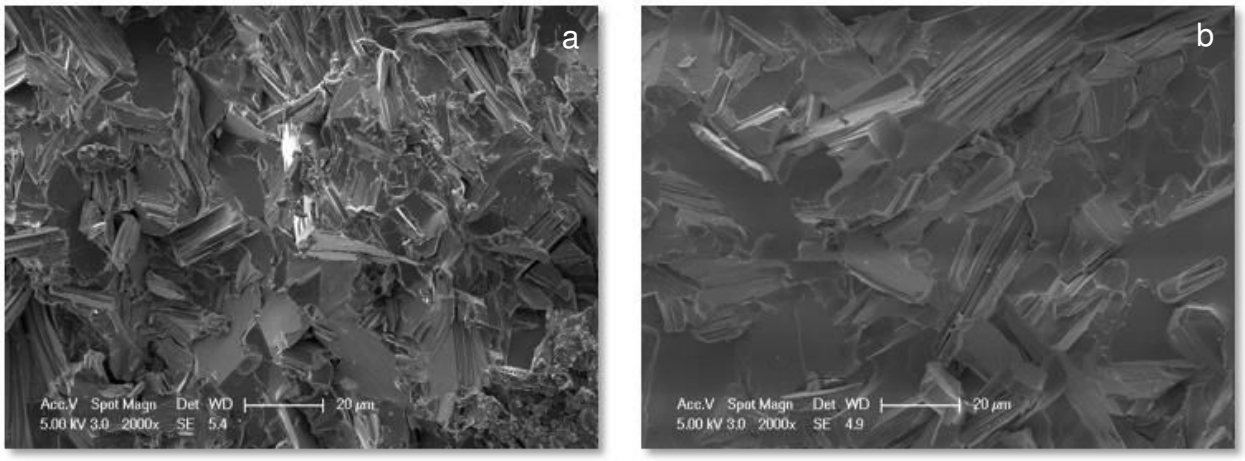

Figure III-28: SEM fracture images of a) grinded MS ribbons-SPS and b) aligned MS ribbons-SPS $Sb_{1.6}Bi_{0.4}Te_{3.1}$ samples taken perpendicular to the pressing direction.

III-3) Microstructural investigations by TEM and HRTEM

As for the other analyses, and even more for the TEM and HRTEM characterizations, we have selected the samples to investigate. Of particular importance for us was to study the nanostructure of the ribbons (do we get nanoparticles, how are they distributed?), the nanostructure of the MS-SPS samples (do we keep some nano-features in the densified samples), the nanostructure of the MS-cold pressed samples (does SPS induce grain growth?), and the location of Te, if any, in the Te-rich series.

III-3-1) MS ribbons of $Sb_{1.6}Bi_{0.4}Te_3$

The first tests have been performed on fragments obtained by scratching MS flakes of $Bi_{0.4}Sb_{1.6}Te_3$ on the wheel surface contact face. These fragments have been recovered on a carbon

covered cupper grid. In figure III-29a is represented a bright field (BF) image of an enough thin fragment to be observed by TEM. Large closely packed grains can be observed (several thousands of nm) but some small features of less than 20 nm seem to be visible. The electron diffraction pattern (Fig. III-29b) is made of diffraction rings exhibiting bright spots, correlated to the number of nanosized particles in the analysed area. A total of 2*N* symmetrical spots on a given diffraction ring is the signature of *N* nanosized particles favourably oriented for the particular diffraction conditions within the analysed area. Indexation of the rings corresponds to the $Bi_{0.4}Sb_{1.6}Te_3$ crystallographic structure and confirms the presence of polycrystalline particles. From selected spots on the diffraction pattern, dark field (DF) images have been taken allowing recognising the diffracting grains. A mix of different particle sizes is illuminated, ranging from about 20-30 (pink arrow, Fig. III-29c, it is difficult to evaluate the size) to less than 10 nm (yellow arrows, Fig. III-29c). So, very small particles can be found that may play a role in the transport properties. We can note that whatever the fragment we could observe, no amorphous zone was found. On another fragment, some dislocations could be observed (Fig. III-30), but as they are on the border, they may arise from the stress induced by the scratching.

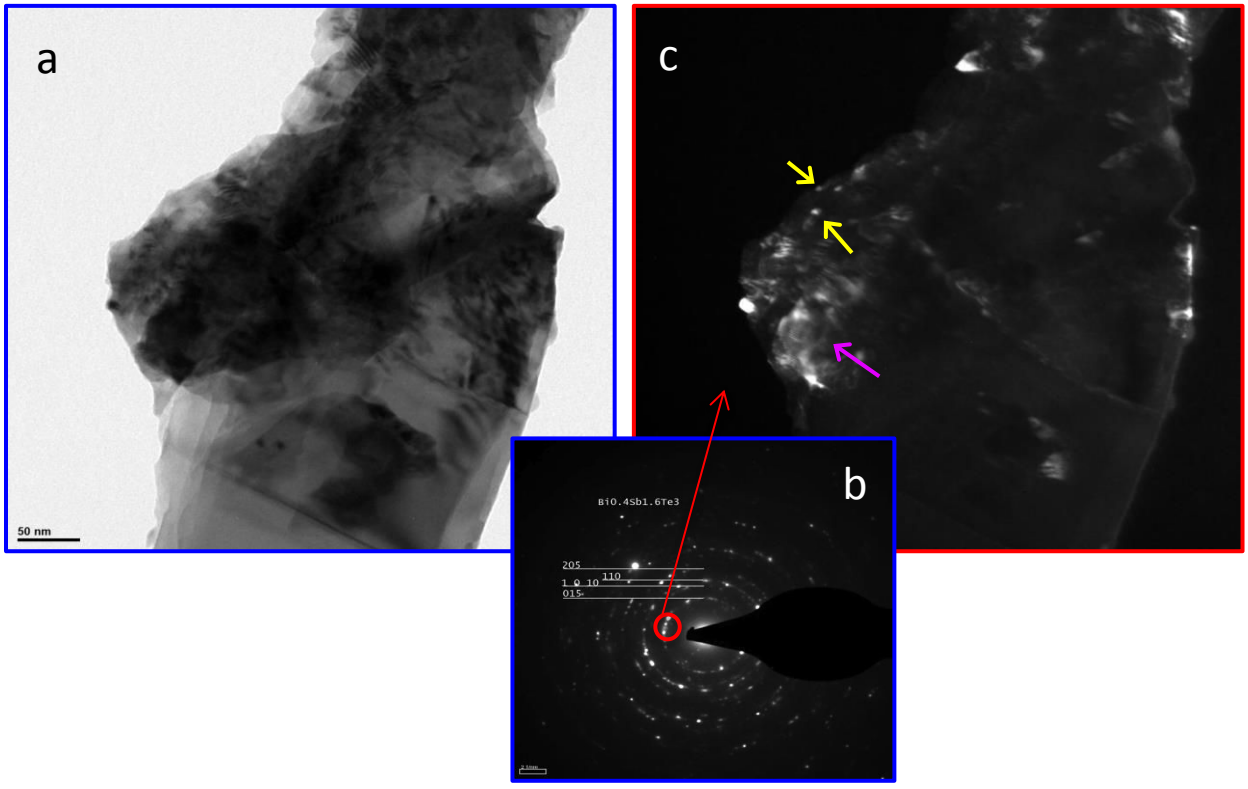

Figure III-29: TEM features (CM200) of a scratched fragment of a MS $Sb_{1.6}Bi_{0.4}Te_3$ contact surface ribbon. a) BF field image, b) indexed SAED pattern corresponding to a, c) DF image corresponding to the selected spots of c.

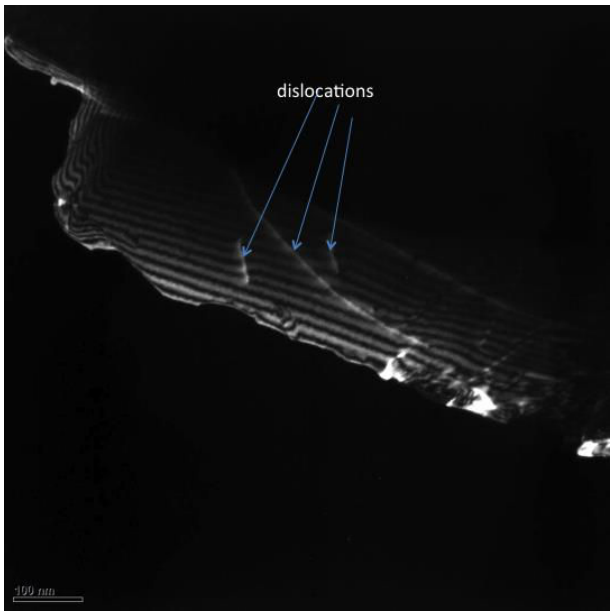

Figure III-30: TEM image (CM200) of a MS $Sb_{1.6}Bi_{0.4}Te_3$ ribbon emphasizing the presence of dislocations.

III-3-2) MS ribbons of $Sb_{1.52}Bi_{0.48}Te_3$

In Figure III-31 are displayed global TEM images of the thin slices we get from different sources for performing the fine morphology and structure analyses by TEM and HRTEM. All are made with MS ribbons of composition $Sb_{1.52}Bi_{0.48}Te_3$ coming from the same batch. As we can see, the quality of these slices is quite different, arising mainly from a problem of thickness. Slice FEI1 (Fig. III-31a) is obviously too thick, while if they are too thin, they are torn and only a little part can be exploited (Figs III-31b, e-h). Figs III-31a-f display thin slices of the overall cross sections of the ribbons. The thickness of the ribbons, *e*, determined from slices FEI1-4, is ranging between 5.0 and 12.5 μm.

As already evidenced from the SEM results, a variety of different microstructures can be observed throughout the overall cross section, owing to the difference in temperature gradient and thus cooling rate along the growth (highest temperature gradient on the contact surface). From these pictures, the most salient features are the columnar solidification structure at the beginning of growth (straight or twinned), quite well visible on slices FEI3 and EDF (Figs III-31c, III-31f) and the presence of dendrites at the free surface. These dendrites are particularly evidenced when the slices have been cut parallel to the free surface (Figs III-31g,h).

Let us now get more insight into the micro and nano structures of these ribbons. Looking to the area of the ribbon in contact with the copper wheel on a cross section, we can see on the TEM images that a thin amorphous layer is formed on a thickness of about 25 nm (Fig. III-32b) at the beginning of the solidification. The nano features seen just beneath the amorphous layer is the electron-deposited protective layer of platinum and deeper the ion-deposited platinum (Fig. III-32a). From the fast Fourier transform (FFT) taken in the different parts on the HRTEM image (Fig. III-33), we can clearly see the amorphous nature of the interface layer (diffuse ring pattern) and the crystallized nature (single crystal pattern) of the further solidified part. On this crystallized part, two different series of perpendicular lattice fringes can be observed, with inter-fringes distances of 0.284 and 0.292 nm (Fig. III-33). It is a quasi square structure, that is unusual for our materials. The value of about 0.29 nm could correspond to the inter-lattice distance for the (107) crystalline plans of the $Sb_{1.52}Bi_{0.48}Te_3$ phase, orientation quite unusual as we will see later. On another place taken close to the amorphous layer, the inter-fringe distance is found to be 0.231 nm, in good agreement with the inter-planar distance (0.236 nm) of the $Sb_{1.52}Bi_{0.48}Te_3$ (1 0 10) crystal.

The amorphous layer thickness represent about 0.3 % of the overall thickness of the ribbon (slice FEI4, Fig. III-31d). Such a layer is generally encountered in MS ribbons due to the high cooling rate that prevents crystallisation. It is however quite thin in our case, compared to the about 500 nm (of an overall thickness of about 3 μm if all the cross-section is shown in their papers) obtained by Xie et al. /XIE10a, XIE13/, in quite similar preparation conditions.

A coherent interface between the amorphous layer and the solidified crystals is observed (Fig. III-32). Here again, we don't observe the area of nanoparticles embedded in an amorphous matrix (thickness of about minimum 1 μm) shown by Xie et al. /XIE10a, XIE13/, comprised between the amorphous layer and the micron-sized crystals solidified afterwards.

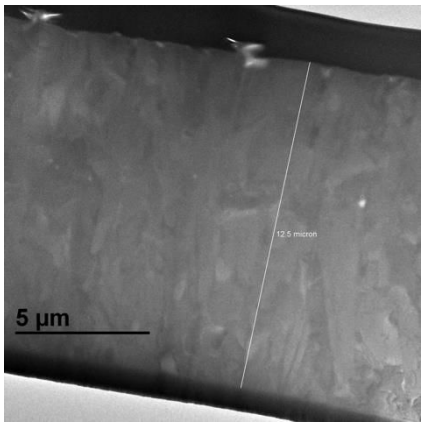

a) FEI1, CS, *e* = 12.5 µm

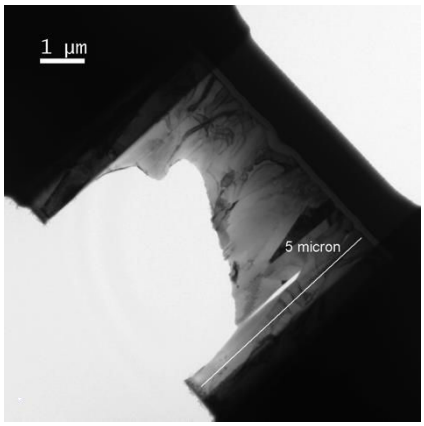

b) FEI2, CS, *e* = 5.0 µm

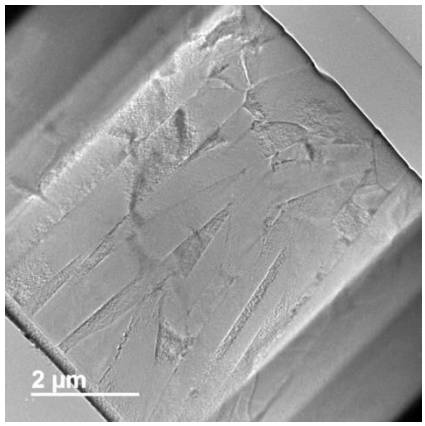

c) FEI3, CS, *e* = 7.1 µm

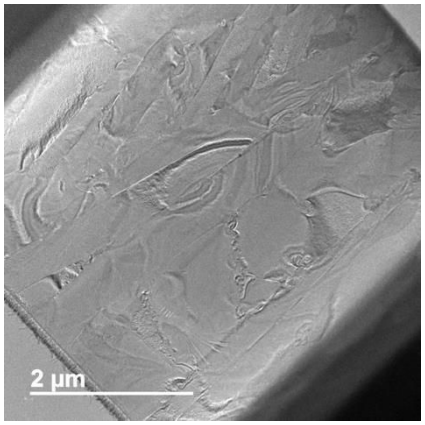

d) FEI4, CS, *e* = 8.1 µm

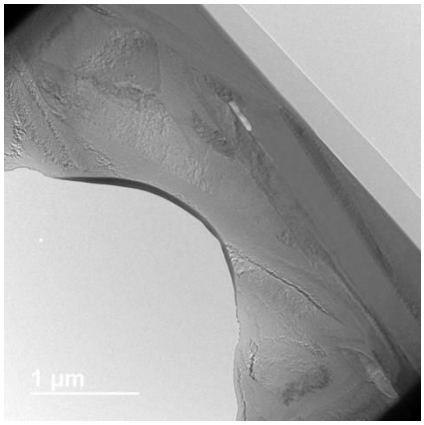

e) JEOL, CS, *e* = ?

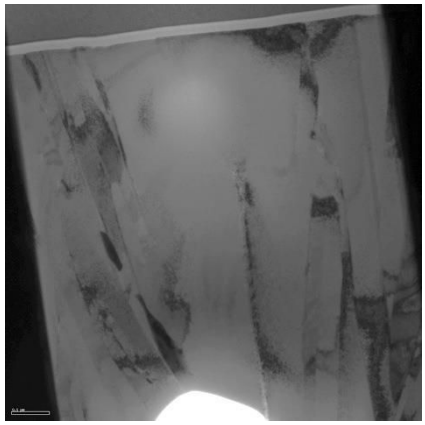

f) EDF, CS, *e* = ?

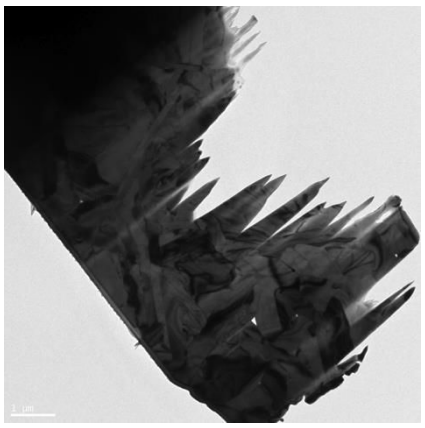

g) FEI5, LS

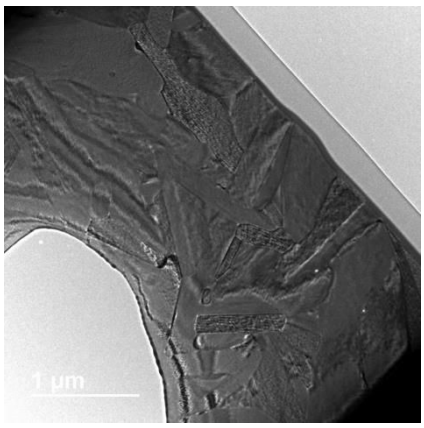

h) JEOL, LS

Figure III-31: TEM images of thin slices of MS ribbons of $Sb_{1.52}Bi_{0.48}Te_3$ prepared by SEM-FIB by different sources, showing the difficulty to get appropriate specimens. a-f: cross-sections (CS) of the ribbons; g,h) cut from the contact surface (LS) (*e* corresponds to the ribbon thickness).

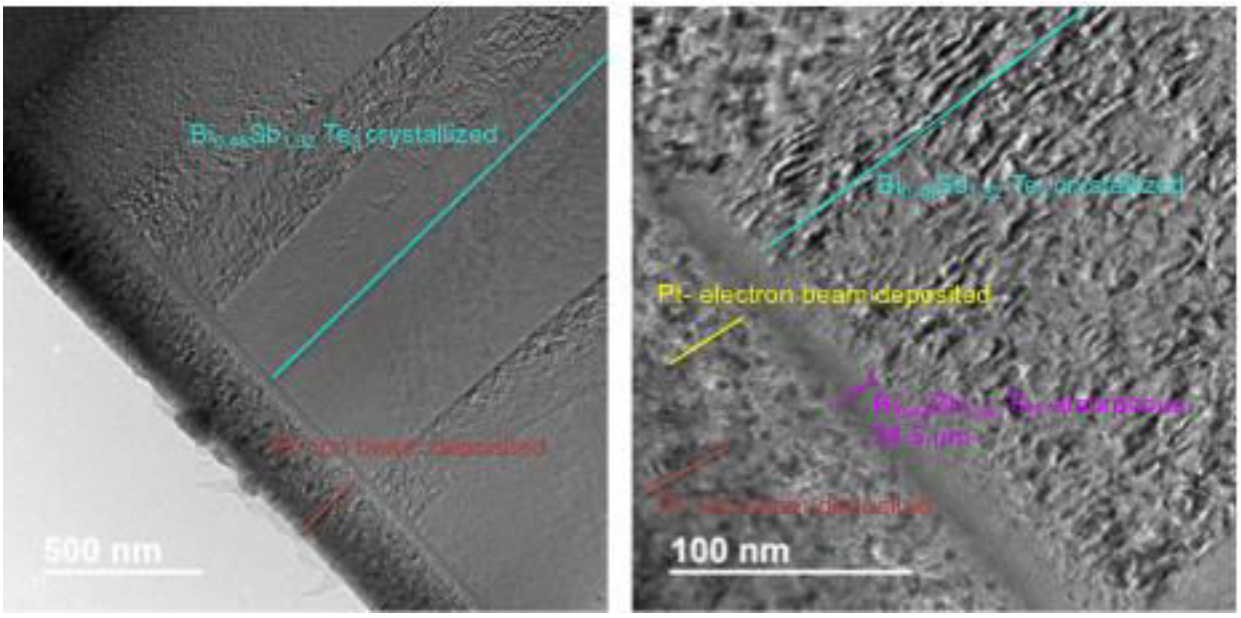

Figure III-32: TEM images of the interface between the contact wheel and the solidified $Sb_{1.52}Bi_{0.48}Te_3$ ribbon at two different scales.

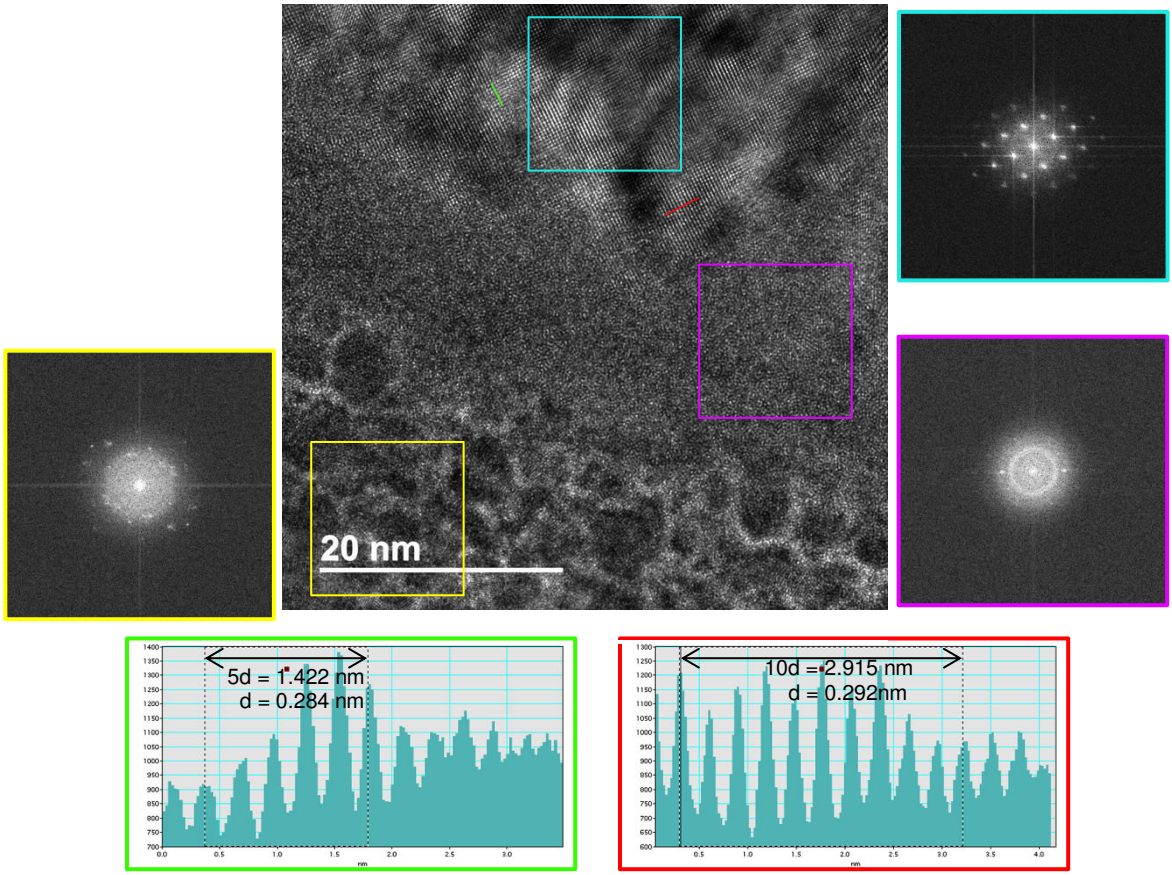

Figure III-33: HRTEM image of the interface between the $Sb_{1.52}Bi_{0.48}Te_3$ amorphous layer and the crystallized solidified grain, corresponding FFT's and line profiles according to the color code.

Let us now look to the structure of the solidified crystals in the middle and dendritic zones taken on the cross section of a $Sb_{1.52}Bi_{0.48}Te_3$ ribbon. In Figure III-34 are displayed two HRTEM images taken in the middle zone: one of an interface between two grains showing the cleanliness of the interfaces and another taken in the centre of a grain. From the FFT, we can see that it is quite well crystallized. The average inter-fringes distances taken along the lines marked in the figure are 0.319 and 0.213 nm, in the main and perpendicular directions, respectively, in good agreement to the inter-planar distances for the (015) (0.317 nm) and (110) (0.215 nm) orientations.

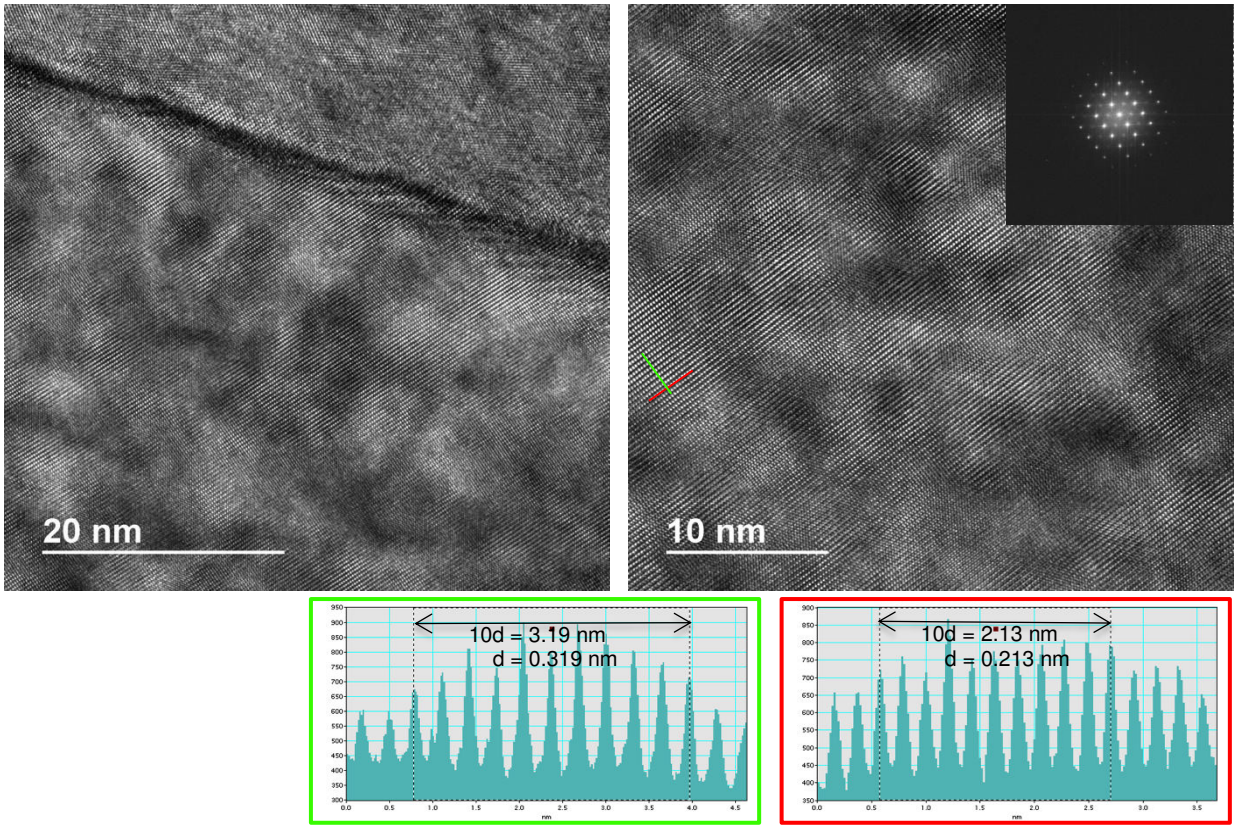

Figure III-34: HRTEM images of an interface between two grains (left) and of a well crystallized grain (right) taken in the middle thickness of a $Bi_{0.48}Sb_{1.52}Te_3$ MS ribbon. Inter-planar fringe distances have been evaluated through the line profiles taken on the rows in the left image (follow the color code).

Figure III-35 shows a grain boundary between four adjacent grains taken in the dendritic zone from a SEM-FIB thin slice cut parallel to the free surface. The triangular-shaped feature of about 70 nm in side, located in between larger grains, is typical of growth with the trigonal axis perpendicular to the surface. It is evidenced by the hexagonal disposition of the spots obtained on

the FFT of this zone. Some of these triangular-shaped structures can be observed all over the thin slice. They exhibit clean interfaces with the surrounding crystals. The dendrites are about 100-200 thick and are twinned. They look as single crystals with random orientations, as it can be seen on Fig. III-35 from the FFT put as inserts. These sub-micron-sized crystallized domains have been observed by all authors having worked on MS ribbons of $Sb_{2-x}Bi_xTe$ /XIE09a, XIE09b, XIE10a, JAC10,XIE13/.

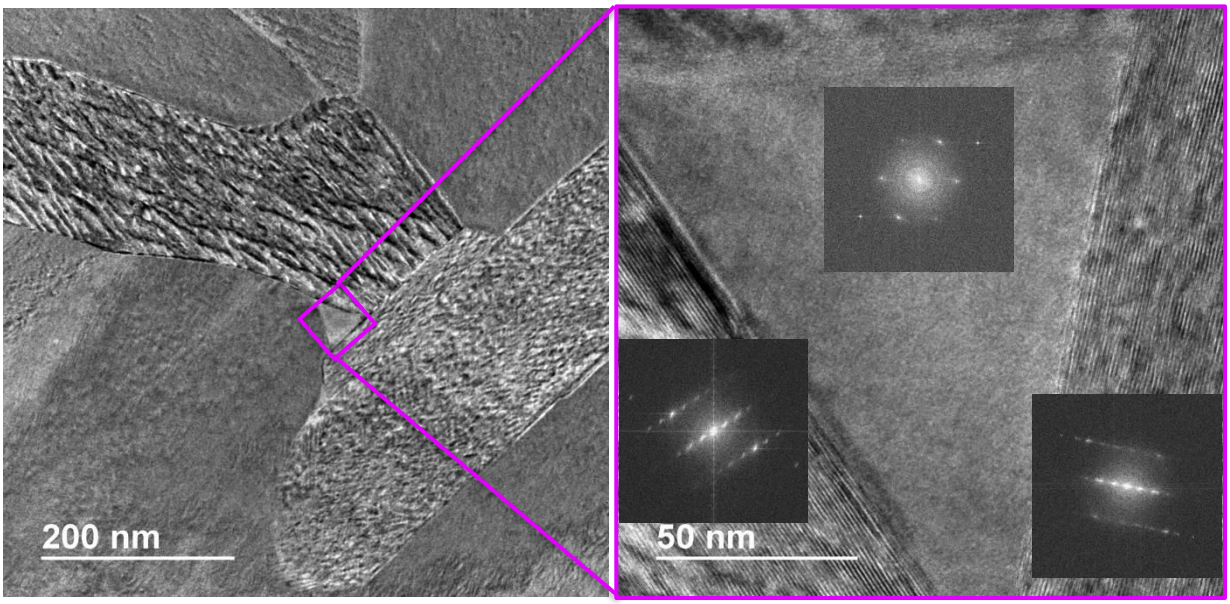

Figure III-35: TEM images of a grain boundary between four adjacent grains (left) and zoom of the highlighted square (right) taken in the dendritic zone of a $Sb_{1.52}Bi_{0.48}Te_3$ MS ribbon.

In some grains, TEM images show lattice stripes of much greater width, having a definite width of about 1 nm (Fig. III-36). A zoom shows that it is formed by series of five bright-doted rows separated with by a more dark-spotted row. It is consistent with the five-layer lamellae structure representing likely the ideal structure of the Sb-Bi tellurides (see chapter II). The width is also in good agreement with the -Te-Bi-Te-Bi-Te- quintet. Quite similar features have already been reported by Lan et al. /LAN09/ and Li et al. /LI13/ in $Sb_{2-x}Bi_xTe$ p-type materials prepared by mechanical alloying-SPS and mechanical alloying-hot pressing, respectively. It is thus not inherent to the fabrication process. The appearance is however little different and they describe it as a series of two rows of extra-bright dots that are separated by four weaker bright dot rows, forming the five layer lamellae.

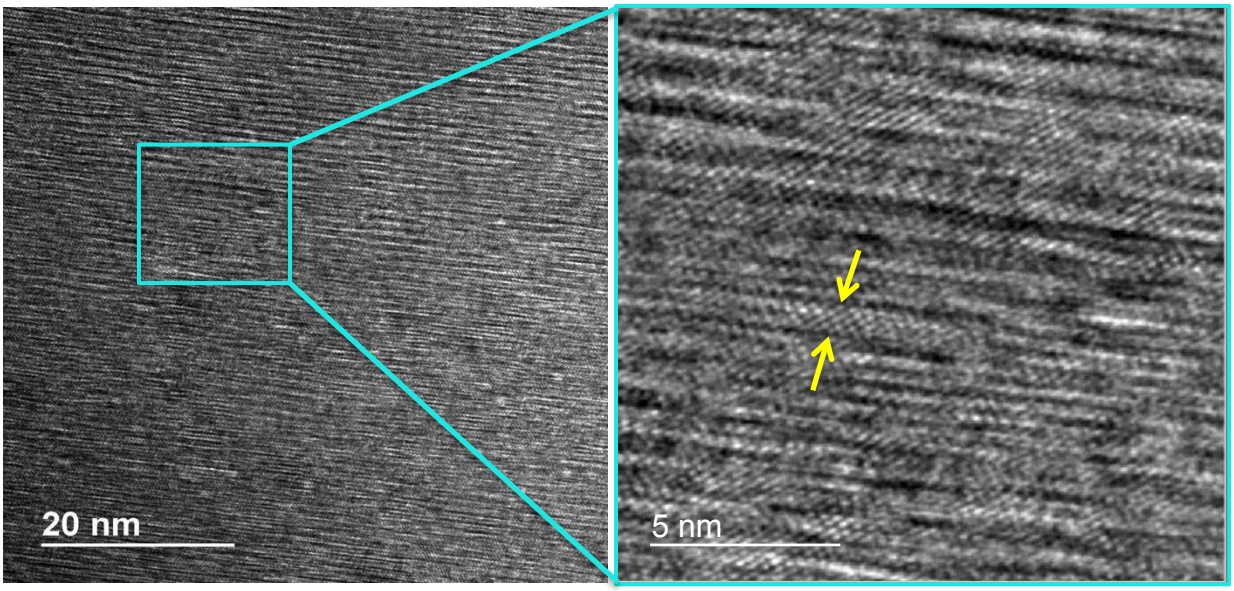

Figure III-36: TEM image showing lattice stripes of about 1 nm in width (left) and zoom of the highlighted square (right) showing in between the arrows the quintet organization of a $Sb_{1.52}Bi_{0.48}Te_3$ grain.

Some other domains show amorphous-like aspects that are in fact constituted, on the base of the FFT's, of amorphous (diffuse rings) and crystallized phases (Fig. III-37). The crystallized phase show a pattern either of a hexagonal lattice or of small crystal grains randomly oriented. The grains are not clearly evidenced on the images. It is strange to observe these amorphous zones on the side of the free surface. We have no explanation until now.

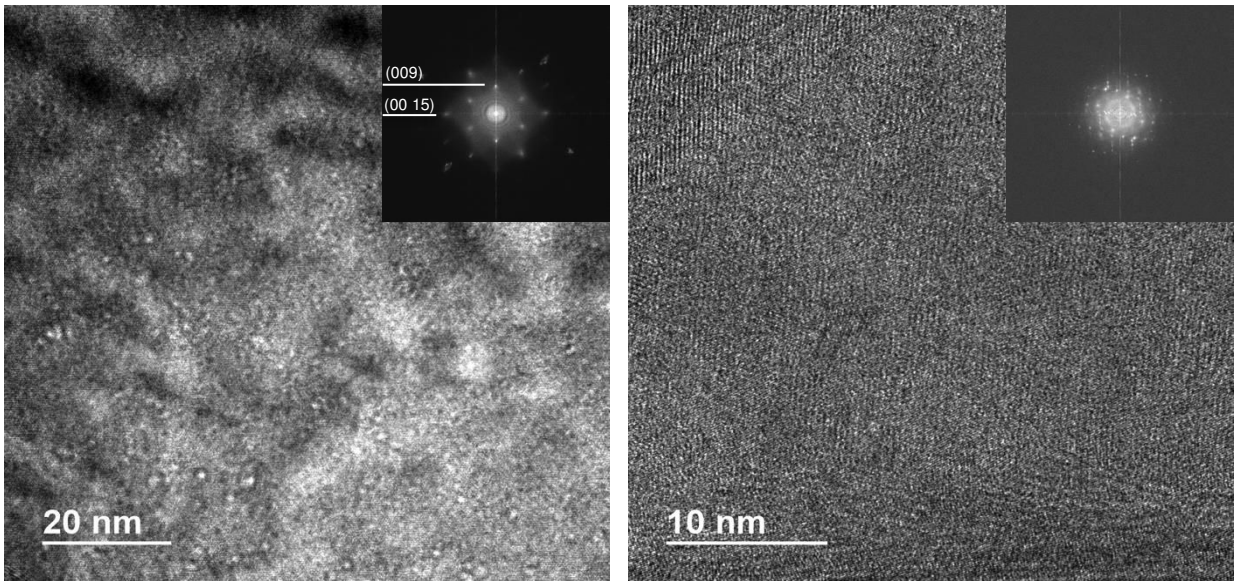

Figure III-37: TEM images showing different domains constituted of amorphous and crystallized phases.

In another thin slice, a needle-like structure containing nano-grains of about 5 to 10 nm in size has been observed (Fig. III-38). These small grains seem to be not closely packed, contrarily to the bigger grains. The needle was located in the middle of the cross section of a ribbon. It is difficult to say in this case if the diffuse halo rings observed in the FFT's are due do the MS process or if they are due to the small amount of amorphized material produced by the impact of high energy Ga ions during the FIB sample thinning.

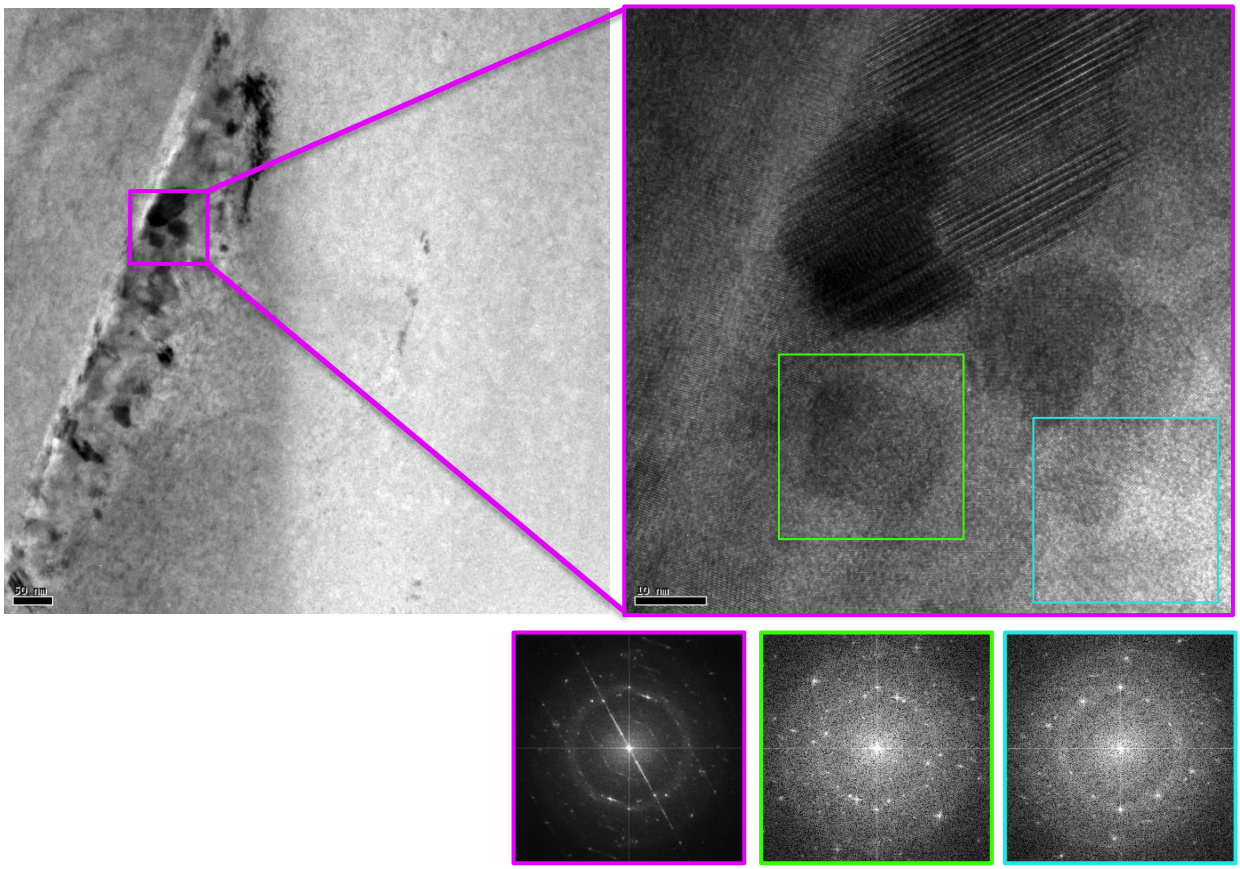

Figure III-38: TEM (left) and HRTEM (right) images of a needle-like structure containing nano-grains of about 5 to 10 nm in size.

All the micro-nano structures observed in this study will of course have an incidence on the transport properties that will be measured. To be really representative, a lot of ribbons should be analysed, because even if the MS process is rapid, difference in structures may be expected from the beginning and end of the process. Thousands of flakes are produced, and we select some randomly, and even after in a ribbon we select a minute amount of material. Many features can thus escape from the observations we performed. For instance, we have never seen the nanostructures appearing as dense striations with spacings of the order of 10 nm observed by

Jacquot et al. /JAC10/ and Lan et al. /LAN08/, previously described by Peranio and Eibl /PER08) for Bi_2Te_3. These features may however arise from the preparation of the thin slices by ion-milling with Ar+ ions, as underlined by Homer and Medlin /HOM12/.

The chemical composition of the ribbons has been analyzed using energy-dispersive X-ray (EDX) spectroscopy inside a high-resolution transmission electron microscope (HR-TEM). No reference materials have been used, and the results will only be compared qualitatively. Quantitative analysis the compounds studied is very trivial and many artifacts can occur so that the quantitative should be taken with great care, as underlined by Peranio and Eibl /PER07/. EDX experiments were performed along five lines from two ribbons as depicted in Fig. III-39. The compositions are roughly the same either they are taken along a columnar grain or in the dendritic zone. An enrichment in Te to the detriment of both Bi and Sb is observed in the sixth point of the pink line at a grain boundary of an hexagonal-shaped grain.

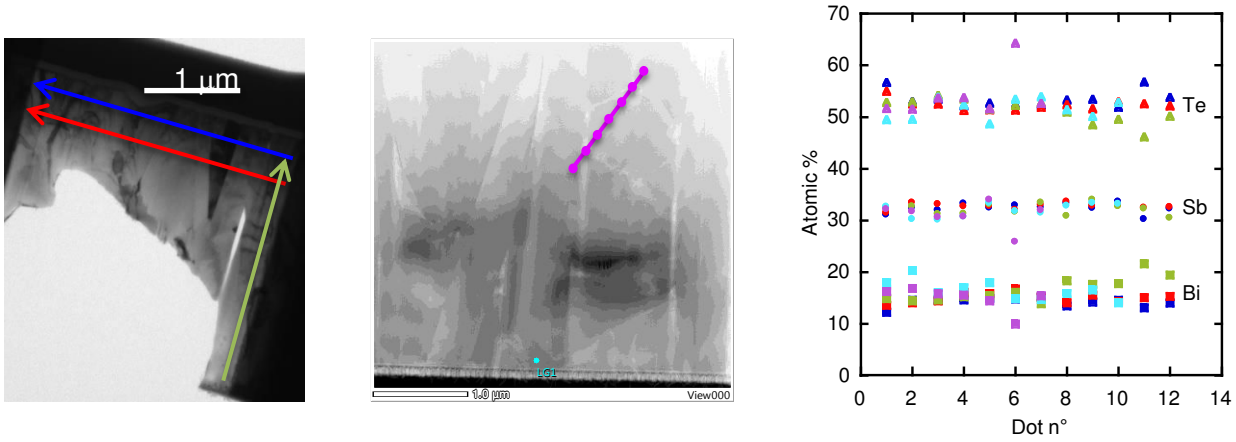

Figure III-39: EDX compositional results for as-grown $Sb_{1.52}Bi_{0.48}Te_3$ ribbons measured along the coloured lines. The results are shown in the graph using the same color code. Two different samples have been tested. The compositions are quite homogeneous in one ribbon and from one ribbon to the other.

X-ray mappings were performed in several zones of one ribbon: dendrites, interface amorphous-crystallised solidified grain, hexagonal grain (Fig. III-40). The elemental distribution shows that the elements are evenly distributed in the dendrites, the columnar structures, and the amorphous layer, without particular composition segregations. A deplation in Sb can however be observed at the grain boundaries of the hexagonal grain mentioned in the EDS analyses, but no Te-rich phase seems to be featured.

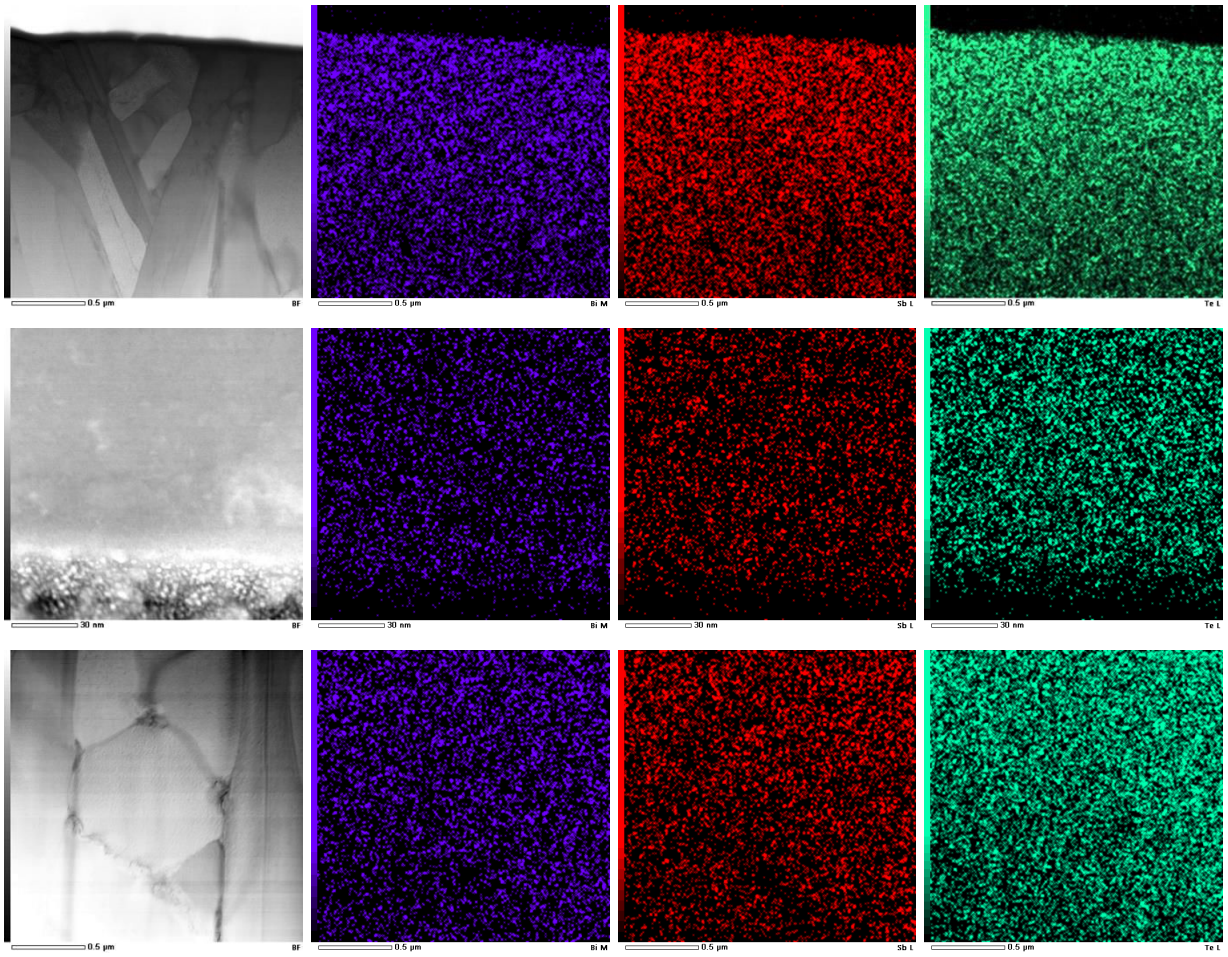

Figure III-40: EDX mapping of an as-grown $Sb_{1.5}Bi_{0.482}Te_3$ ribbon taken at three different places. HAADF image, Bi map (blue), Sb map (red), and Te map (green).

III-3-3) Bulk samples

All the samples tested in this section have been analysed with the CM200 microscope on scratched ribbons or on thin slices prepared by F. Soldera at Saarbrücken. The slices are a little bit to thick to be exploited in a critical way. Thus, only short description will made on what can exploited on some thinner parts of the slices.

In figure III-41 are shown TEM images of a fragment of a MS $Sb_{1.6}Bi_{0.4}Te_3$ sample densified by SPS (scratched sample). Thin enough large parts to see the micron or sub-micron sized particles couldn't be observed. On the other hand, some fragments clearly display features showing closely packed nano-grains, that seems to be aggregated, with none amorphous structure. The electron diffraction pattern exhibits nearly bright continuous diffraction rings that could all

be indexed within the R-3m structure of $Sb_{1.6}Bi_{0.4}Te_3$. By selecting spots on two different rings, the dark field images clearly highlight the presence of the diffracting nanoparticules. Their size is less than 20 nm, suggesting that the SPS treatment do not seem to affect the nanoparticles size. These densely packed nanograins form a great number of grain boundaries that can affect the phonon scattering at the grain boundaries to enhance the thermoelectric figure of merit, but they can also impede the movement of dislocations /LI12a/.

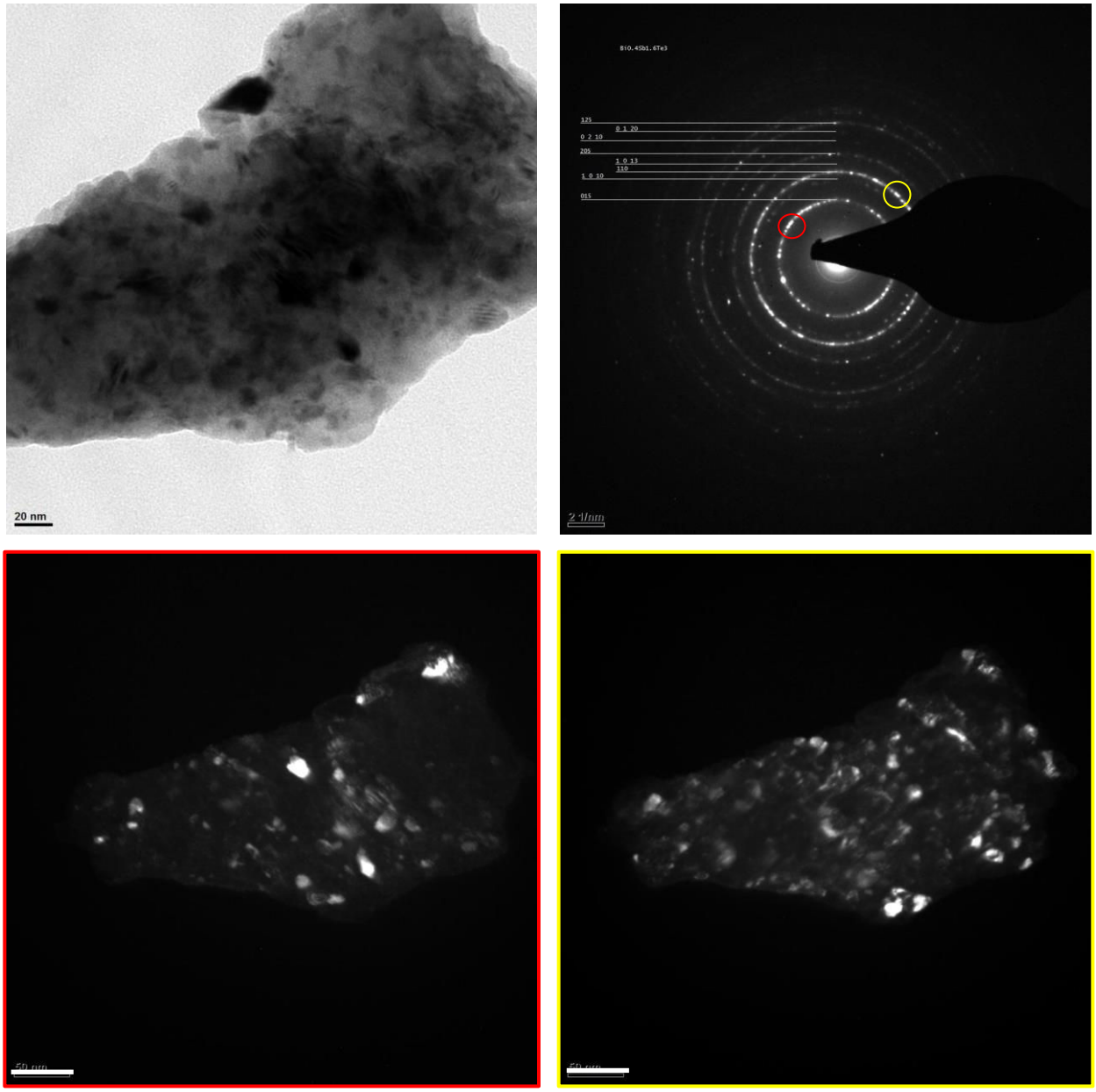

Figure III-41: Bright field image, electron diffraction pattern and dark field images taken on two specific places in the rings of the diffraction pattern (red and yellow circles) of a $Sb_{1.6}Bi_{0.4}Te_3$ MS-SPS sample. Indexation is also shown. Scale bar = 50 nm on DF images.

In order to look the influence of the melt-spinning process on the microstructure, two samples referred one as reference sample (initial ingot+SPS) and the other as MS-SPS sample of composition $Sb_{1.5}Bi_{0.5}Te_{3.1}$ have been selected. The reference sample (Figs III-42a,b) displays a close packed structure of large particles of a few microns in size. No cavity between particles is

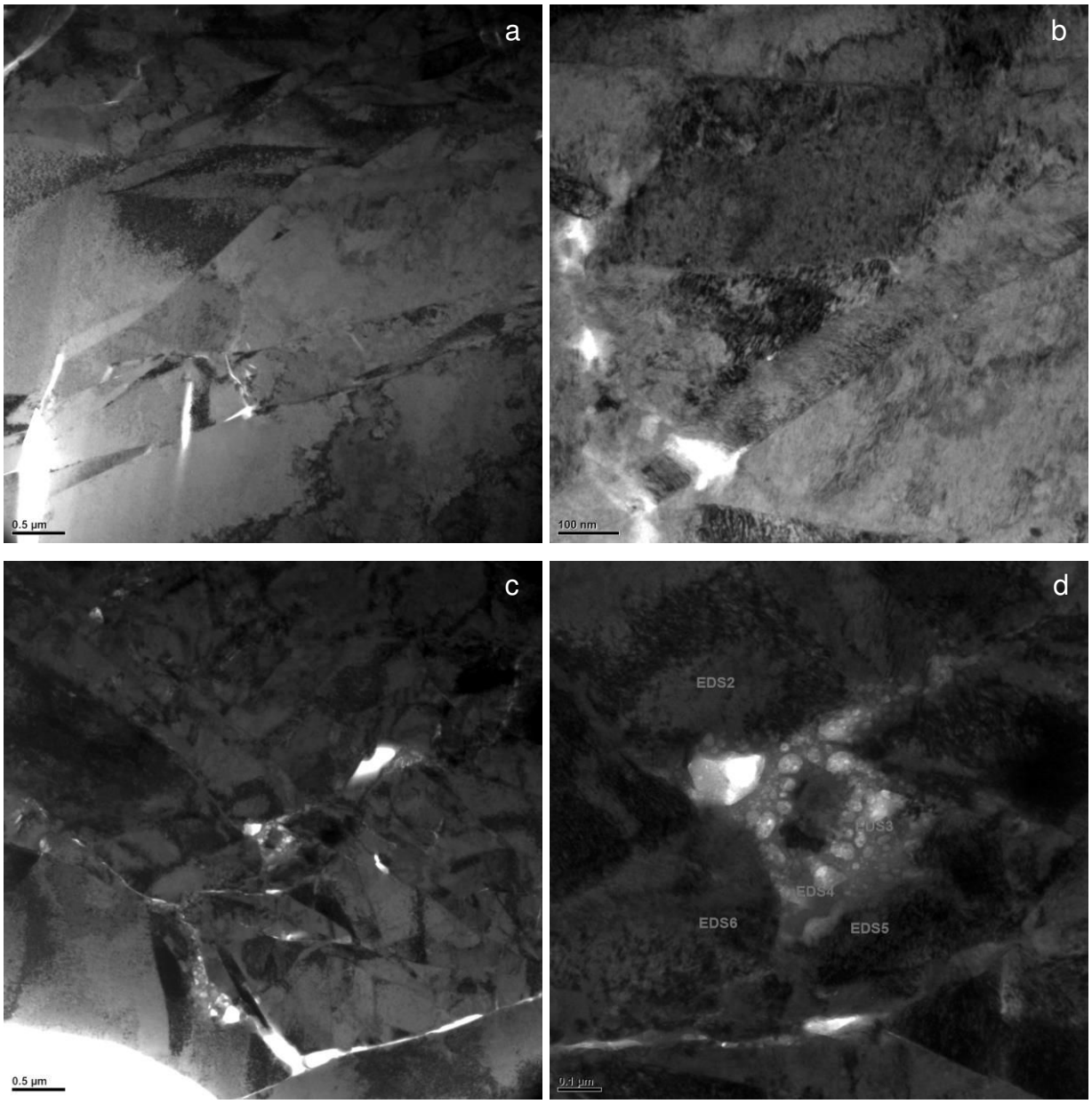

Figure III-42: TEM images of a,b) reference samples and c,d) MS-SPS samples of nominal $Bi_{0.5}Sb_{1.5}Te_{3.1}$ composition.

observed, consistent with the high density achieved. The presence of some small holes can however be seen, but it may be due to the preparation of the thin slice. Some smaller particles of

about 100 nm can also be observed. In the MS-SPS sample, the structure appears constituted of smaller particles (Fig. III-42c).

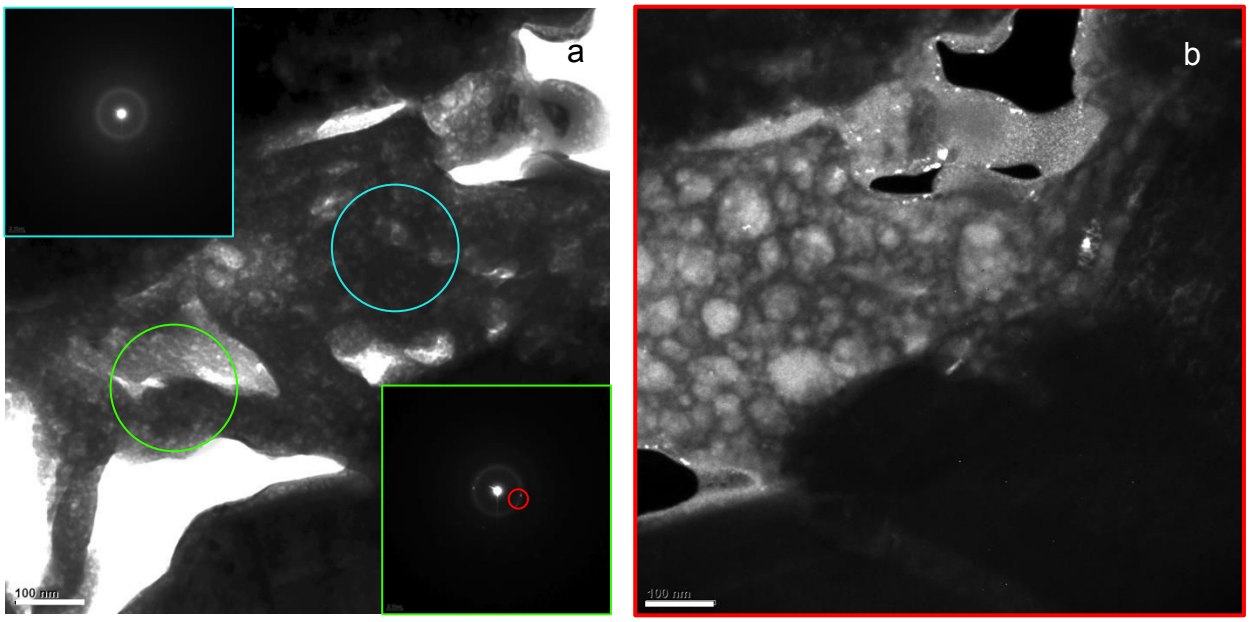

Figure III-43: TEM images the MS-SPS sample of nominal $Sb_{1.5}Bi_{0.5}Te_{3.1}$ composition emphasizing particular features present in this sample. a) BF image and SAED patterns, b) DF image from red spot in a. (bar scale = 100 nm)

In between grain boundaries appear clearly some zones where nano-features can be seen (Fig. III-42d, zoom in the middle part of c). Some greater zones were these features appear are shown in Fig. III-43a. SAED patterns performed on two different zones are displayed in the insets of corresponding color. One zone is completely amorphous while it appears two spots on the other zone. Dark field images taken from the spots illuminate very small grains of less than 10 nm in size (Fig. III-43b).

To get an insight of the influence of the excess of Te on the micro-nano structure, sample of $Sb_{1.52}Bi_{0.48}Te_3$ composition has been analyzed. It was also the composition of the ribbons. The presence of the amorphous phase was not observed in these samples. Even in absence of excess Te, some Te features could be observed either in the form of precipitate (Fig. III-44a) as previously, or in the form of droplets (Fig. III-44b) as if resulting from melting. The composition, around the Te particle, is particularly rich in SbThe excess of Te manifests thus in the MS-SPS (not in the reference sample) sample by the presence of the amorphous Te-rich phase observed in Fig. III-43.

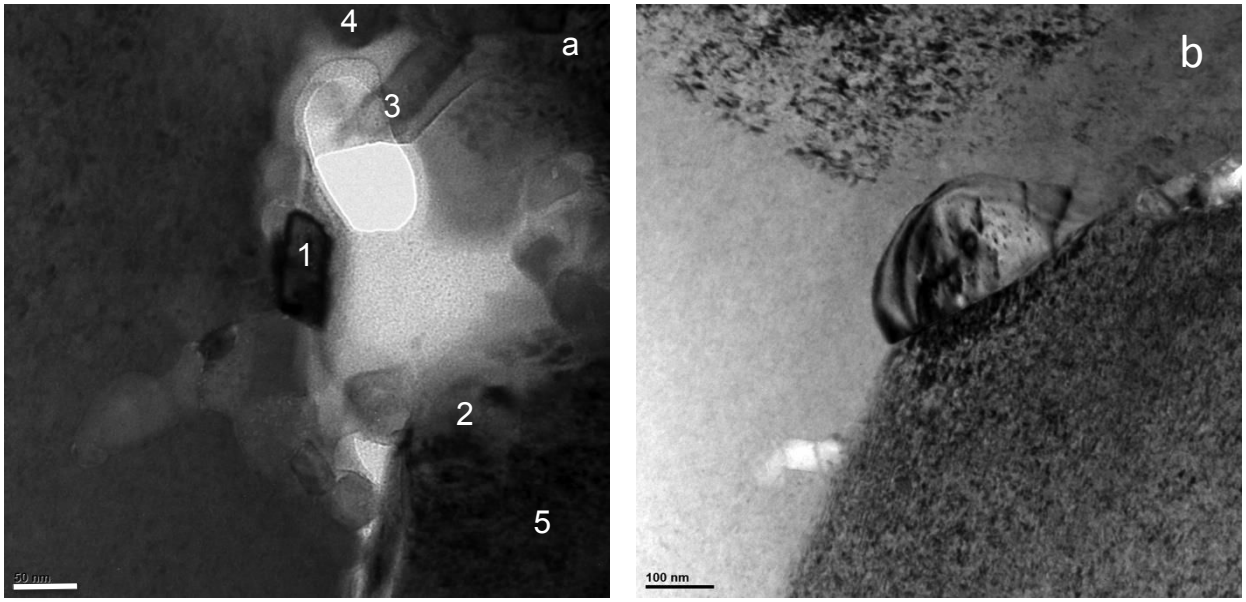

Figure III-44: TEM images of the MS-SPS sample of nominal $Sb_{1.52}Bi_{0.48}Te_3$ composition emphasizing particular Te features present in this sample. (bar scale = 50 nm in a)

Effect of cold pressing, instead of SPS, was undertaken in the sample of same composition $Sb_{1.52}Bi_{0.48}Te_3$. The main difference seems to come from the interfaces between the grains, presenting much more defects than the SPS processed samples (Fig. III-45). It may arise from the higher plastic deformation induced by the higher pressure applied.

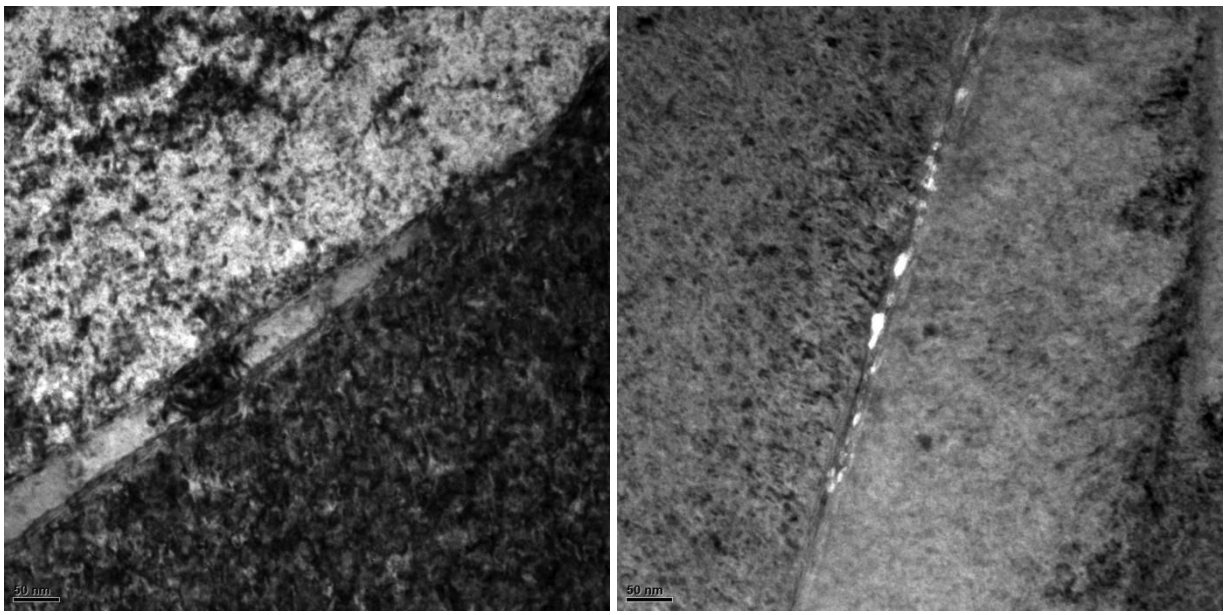

Figure III-45: TEM images of the MS-cold pressed sample of nominal $Sb_{1.52}Bi_{0.48}Te_3$ composition emphasizing the presence of numerous defects at the grain boundaries.

In all the thin slices we have checked, none zone of small grains could be observed, but of course only a very small part of a compacted sample is checked, and if the particles are not distributed in a homogeneous way, they can be missing. Moreover, the quality of the thin slices has to be improved.

CONCLUSION

We have described the new metallurgical route, i.e. melt-spinning, developed in the thermoelectric team to synthesize thermoelectric materials with nano-features included. It was applied for the preparation of $Sb_{2-x}Bi_xTe_3$ solid solutions, with or without excess of Te, with or without Sn doping. Many experimental parameters, either coming from the melt-spinning or from the densification methods or the doping, have been tested in order to change the microstructure and/or the chemical composition to look their further influence on the transport properties, the final objective being to enhance the dimensionless thermoelectric figure of merit. The prepared samples have been characterized by X-ray diffraction. All samples are polycrystalline, with no particular texture induced whatever the preparation method used is. Small amounts of Te could be detected in the Te-rich samples. A careful attention has been taken for the microstructural characterization of the MS-ribbons using TEM and HRTEM. The ribbons, due to the low thermal conductivity of the family of materials studied, undergo a microstructural transformation during their growth due to the temperature gradient between the cooled wheel (contact surface) and the free surface. Only a small thickness is amorphous, in the near contact of the wheel (about 20 nm). Difficulties to get high quality thin slices for TEM and HRTEM have been emphasized.

Nano-sized features are formed in the flakes produced by melt-spinning, whose size is kept during the spark plasma sintering process, as shown from scratched samples. Influence of the presence of these nanoparticles should be observed in the variations of the transport properties. But there are also many other defects detected by the TEM observations that can influence them, i.e., rough interfaces, presence of Te-rich phases creating Bi or Sb antisite defects, structural defects, and surely many others that couldn't be seen in the minute analyses performed with regard to the huge amount of material produced.

Chapter IV

Measurement techniques for thermal, electrical and galvanomagnetic properties

INTRODUCTION

The performance of a thermoelectric material is evaluated from the dimensionless figure of merit *ZT*, which, as was described in the first chapter, is a function of the transport properties of the material, i.e. the thermopower, the electrical resistivity and the total thermal conductivity. Therefore, the estimation of *ZT* naturally involves measurements of these three physical properties[1]. In practice, it is well established that the thermoelectric materials based on Bi_2Te_3 – Sb_2Te_3 develop the most promising performance between 270 and 500 K depending on the composition (see Chapters I and II). However, to make the study more complete and to get a deeper insight about the physical processes governing the electrical and thermal transport in nanostructured bulk chalcogenides, it is also essential to examine the transport properties at low temperature (well below 270 K). For this reason, we probed a broad temperature range (5 – 500 K) including both the low and high temperatures.

Performing a single measurement, whether electrical or thermal, over such a temperature range, poses however insoluble technological problems (choice and maintenance of materials and sensors, compatibility between cryostat and oven, ...). Different techniques and tools adapted to each of the two thermal ranges, low temperatures (2-300 K) and high temperatures (300-500 K), have therefore been employed.

In addition to the thermal and electrical measurements, we have also performed galvanomagnetic measurements in the range 5-400 K. These measurements have enabled us to have valuable information on the nature and the number of charge carriers and also on their mobility.

Each of the experimental techniques used is described in detail in this chapter. Particular attention is also paid to the preparation of the samples that must be done with extreme care for obtaining reliable measurements for the evaluation of *ZT* due to the anisotropy of the samples prepared by SPS. It is important to note that for each of the compositions studied, the same bar was used during the various studies at low temperatures (thermoelectric and galvanomagnetic measurements).

[1] It is possible to determine directly the figure of merit *ZT* by the Harman's method /HAR59/ but it is difficult to implement because of the drastic assumptions on which it is based (adiabatic state for example).

I) THERMOELECTRIC MEASUREMENTS AT LOW TEMPERATURE

I-1) Principle of measurement

I-1-1) Electrical resistivity

The standard configuration of the 4-point probe resistivity method is perfectly adapted for our samples that have quite low electrical resistance (< 0.1 Ω between 2 and 300 K for all the samples investigated in this study). This enables to eliminate any parasitic contact resistance caused by the measurement wires.

In the 4-point probe method, the passage of an electrical current I is provided by two metallic contacts connected to the ends of the sample displayed in the form of a parallelepipedic bar. The resulting voltage ΔV is measured between two other metallic contacts remote from the distance l, as shown at Fig.IV-1.

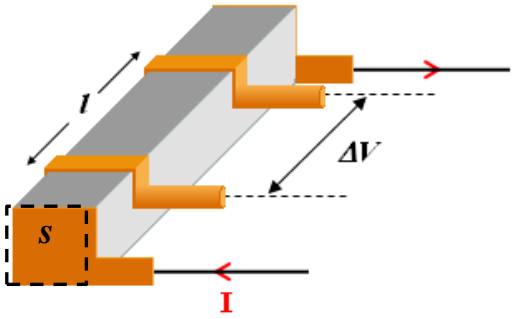

Figure IV-1: Schematic representation of the electrical resistivity measurement principle by the 4-point probe method on a parallelepipedic sample. The current I flows between the external contacts while the internal contacts are used for measuring the voltage ΔV.

Electrical resistivity, ρ, is determined from Ohm's law:

$$\rho = \frac{\Delta V}{I}\frac{s}{l} \qquad \text{(IV-1)}$$

where s is the cross section of the sample.

It is important to remember that the passage of a direct current is accompanied by a temperature gradient established along the bar (manifestation of the Peltier effect) and thereby, an additional voltage generated by the Seebeck effect is superimposed to the Ohmic voltage. To overcome this problem, measurements must be carried out either by using a direct current (DC) of low intensity and short duration or by using an alternating current (AC).

I-1-2) Thermal conductivity and thermopower

The stationary method is the most often implemented technique to determine the thermal conductivity of solid materials at low temperature. It can also be applied to the measurement of the thermoelectric power. To perform these two types of measurement, one end of a bar-shaped sample is maintained at a constant temperature by means of a heat sink while at the other end a small resistive furnace (Fig.IV-2) is connected. Applying an electrical current in this resistor generates an electrical power *P* by Joule effect. As a result, a one dimensional heat flow goes through the sample from the furnace to the heat sink under strict adiabatic conditions.

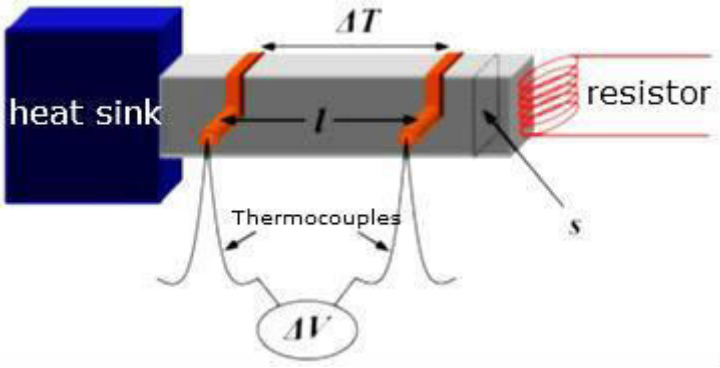

Figure IV-2: Schematic representation of the measurement principle of the thermal conductivity and the thermopower. Knowledge of the temperature ΔT and voltage ΔV differences as well as of the thermopower of the measuring wires permit to derive the thermopower of the bar.

In the stationary mode, the thermal conductivity κ of the material is calculated directly from the applied electrical power *P* and the resulting temperature difference ΔT (obtained for example by using thermocouples) between two points of the sample distant by *l,* by the following equation:

$$\kappa = C\frac{l}{s} = \frac{P}{\Delta T}\frac{l}{s} \qquad \text{(IV-2)}$$

where *C* is the thermal conductance.

The appearance of a temperature gradient will also generate a thermoelectric voltage ΔV due to the Seebeck effect. If the positive terminal of the voltmeter is connected to the hot side of the bar, the thermoelectric power *S* of the sample is given by:

$$S = S_{wires} - \frac{\Delta V}{\Delta T} \qquad \text{(IV-3)}$$

where S_{wires} represents the thermopower of the wires used for the measurement of the voltage. These wires are not insulated, hence their contribution must be taken into account.

It should be remembered that the measurement of the thermal conductivity is a delicate task. Obtaining reliable results requires many experimental precautions, so that the entire thermal power P is transferred from the furnace to the heat sink. Any significant heat losses must be avoided, such as:

- gas conduction and gas convection losses,
- conduction losses in the wires of the furnace feed and the wires connected to the sample for measurement of temperature or potential,
- radiation losses of the furnace and the sample to the cool parts of the measurement system.

Gas conduction and gas convection losses become negligible if the measurement is performed under high vacuum (< 10^{-5} mbar). Losses by the measurement wires can be minimized in case of using metallic alloys (chromel or manganin for example) rather than pure metals. Similarly, wires of small diameter and long length should be preferred to make negligible their conductance relative to the studied material (the geometry of the sample must be optimized as well). Finally, the measuring cell should be protected by a thermal shield to reduce the radiation losses occurring above around 150 K.

I-2) Equipments and experimental protocols

The thermal conductivity, thermoelectric power and electrical resistivity were measured simultaneously in the temperature range 5 - 350 K using a Physical Property Measurement System (PPMS) cryostat. It is a commercial equipment from Quantum Design, equipped with the Thermal Transport Option (TTO) working under secondary vacuum, ensuring the ideal environment for low-temperature heat transport measurements. The TTO sample holder (Fig. IV-3a) is well adapted for measuring bulk samples with good mechanical properties. Indeed, all the connections between the bar and the components (heat sink, furnace, voltage and temperature sensors) of the sample holder are realized with screws (Fig. IV-3b).

The bars (length L ~ 7-10 mm and cross section s ~ 2-3 × 2-3 mm^2) were cut from the cylindrical ingot obtained after densification by SPS using a diamond wire saw. The orientation

of the sample will be discussed later in this chapter. To minimize uncertainty on *L* and *s* (used in the determination of the electrical resistivity and thermal conductivity), particular attention was given to the polishing of each sample to obtain perfectly parallel faces.

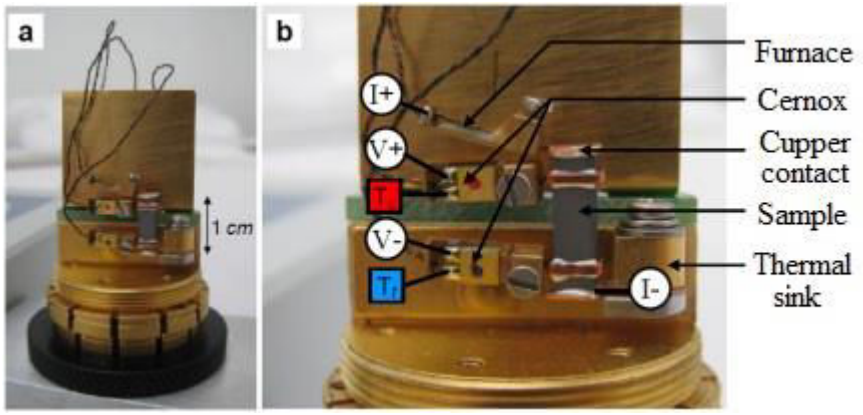

Figure IV-3: a) Photos of the TTO puck and b) zoom of the assembly. The bottom copper strip is clamped to the heat sink with a small screw. The various components (furnace and thermometers) are screwed to the copper contacts. The heat pulse is delivered by a small resistive furnace. The current *I* passes through the sample from the contact of the oven (*I*+) up to the heat sink (*I*-). The resulting voltages (*V*+, *V*-) and the temperature differences (T_c, T_h) are taken at the level of two small copper contacts in between.

As we noted in the previous paragraphs, four contacts on the sample (two on the ends and two on the long face) are required for electrical and thermal measurements. To allow good compatibility with the screw connections implemented in the TTO sample holder, we used copper contacts. These elements, which are initially in the form of wires (Ø 0.5 mm) or plates (thickness 0.4 mm), must be formed (steps of lamination, cutting and bending) to be adapted for the measurement of each sample to guarantee ideal measurement conditions. To ensure good electrical and thermal contacts between the sample and the copper elements, a solder (BiSn) with low melting point (139°C) has been used.

The assembly of the sample on the TTO puck begins first by its connection to the heat sink (Fig. IV-3b), performed by placing the cupper tab located at the end of the sample in a small vice tightened by a screw. The small furnace and the two temperature sensors (Cernox) are then connected. These three elements are glued to a small gold coated copper piece having a cavity (diameter ~ 1 mm) at its end where the copper wire will be placed. The contact is ensured by means of a small screw that blocks the wire. This procedure has to be performed with delicacy

but at the same time the tightening should be sufficient. For an experienced operator, the process of sample installation takes from 10 to 20 minutes. This time can increase exponentially if the sample is fragile.

The highly sensitive Cernox 1050 thermometers, previously calibrated, are then integrated into the temperature/voltage shoe assemblies. The resistive type furnace ($\sim 2\ \mathrm{K\Omega}$ at room temperature) is calibrated as well. Besides wires that provide control of the furnace and the thermometers, additional wires for the current supply and potential outlets are included. They have a small diameter (~ 0.08 mm) and are made of composite alloys (manganin or copper alloy for the current supply) to reduce the losses by thermal conduction along these wires. Two radiation screens (made of gold coated copper) are installed as well. The first screen, in form of a plate, protects the sample from the influence of the electrical connectors and the second, of cylindrical shape, is screwed onto the sample holder and protects against the external environment.

Two modes, stationary or continuous, are available for extracting the thermal conductivity and the thermoelectric power under secondary vacuum ($< 10^{-5}$ mbar). In the first mode, the measurement of ΔT and ΔV is performed at constant temperature after the steady state conditions have been reached, once the furnace was powered. κ and S are then deduced from equations IV-2 and IV-3. The continuous mode is much more sophisticated. In this case, the furnace delivers an electrical power during a short time only (the current is in the form of a square signal, as shown in Fig. IV-4, the period varying from 30 to 1500 s) and the measurement temperature is not constant but follows a ramp preset by the operator. Therefore the stationary state is never reached. It will be simulated, as shown on Fig. IV-4, by the evolution during one period (the period includes the heating and cooling phases) of the temperature difference $\Delta T(t)$ and the voltage $\Delta V(t)$ taken at the internal contacts on the sample. The thermal model used to describe the heat transfer operates with two time constants (model known as "2τ"). It is based on the modeling originally developed by Maldonado /MAL92/ describing the thermal and thermoelectric responses of a sample to a low-frequency square-wave heat pulse and on the experience of Quantum Design for extracting the specific heat (relaxation method).

We choose to perform all our measurements in the continuous mode. Actually, it allows gaining data faster than in the stationary mode, and it is strongly recommended by the developers

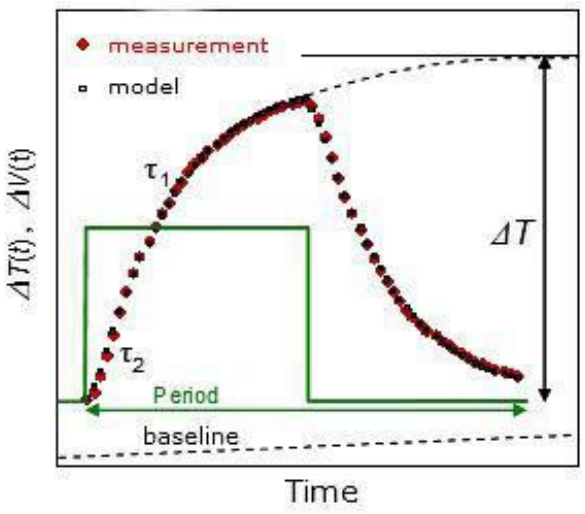

Figure IV-4: Scheme showing how ΔT (or ΔV) is extrapolated in the continuous mode of heating. The green line represents the current profile applied for heating. The measured temperature variation in the sample under the effect of the heat pulse is represented in red and reveals two time constants (τ_1 and τ_2 correspond to the times of heat diffusion into the sample and into the copper pieces, respectively). These values and the curve are adjusted to fit the model and determine the assumed ΔT value if the furnace would remain under heating indefinitely to reach the stationary state. Note that, in our case, the baseline temperature is rising slightly.

of the TTO module. In addition, a sophisticated algorithm allows to control the various measurement parameters and to best adjust the period and the power of the furnace, that is not possible in the stationary mode. The losses by radiation (observable for T > 150 K) are also estimated but it turns out, if one refers to the high temperature data, that it is always under-estimated (3-10%). The lowest the conductance of the sample is, the highest the deviation is. Since our samples have usually low thermal conductivity (about 1 – 1.5 W/mK at 300 K) it is not possible to eliminate completely the radiation even by playing with the geometrical factor.

II) GALVANOMAGNETIC MEASUREMENTS AT LOW TEMPERATURES

II-1) Principle of Hall effect

When a material is subjected to an electrical current and and to a magnetic field B perpendicular to it, the path of the charge carriers is deviated towards the lateral faces of the bar under the effect of the Lorentz force. A transverse electrical field then appears, tending to offset this force. Thus, in a stationary state, a transverse voltage V_H is established. This phenomenon, known as the Hall effect, allows to determine the sign of the dominant charge carriers from the sign of the Hall constant, R_H, defined as:

$$R_H = \frac{V_H\, s}{I\, d\, B} = \frac{\rho_H}{B} \qquad \text{(IV-4)}$$

where d is the transverse dimension of the sample and V_H – the Hall resistivity.

When the material is a metal or a semiconductor with one type of carrier, the Hall constant allows a determination of the density of the charge carriers, electrons (n) or holes (p), according to:

$$n(p) = \pm \frac{1}{e \times R_H} \qquad \text{(IV-5)}$$

where e is the elementary charge.

Also the Hall mobility of the charge carriers μ_H can be established by the following formula:

$$\mu_H = \frac{R_H}{\rho} \qquad \text{(IV-6)}$$

where ρ is the electrical resistivity of the sample. The Hall mobility is a useful parameter in semiconductors. Actually, from the curve describing the dependence of the Hall mobility versus temperature, it is possible to gain some information about the scattering mechanisms of the charge carriers that dominate in the samples.

II-2) Protocol of experiment

The measurements of the Hall coefficient R_H were carried out on the PPMS cryostat cited above using the alternating current transport (ACT) option. The cryostat is provided with a superconducting coil producing a magnetic field ranging from -7 to 7 Tesla. An alternating current, whose frequency can be varied (in our case we use 103 Hz), is applied to characterize the samples. The Hall voltage determination is not always easy. In principle, a 4-contact mounting is sufficient if both contacts 3 and 4 leading to V_H are mounted in a line perfectly perpendicular to the electric field (Fig. IV-5a). From an experimental point of view, this condition cannot be fulfilled rigorously, and the measured voltage V_{meas} is then the sum of the Hall voltage, V_H, and a longitudinal voltage, V_{res}, due to the resistance of the sample (Fig. IV-5a). The resistive component (at the origin of the magnetoresistance) may be higher than the Hall voltage V_H, especially if the concentration and mobility of charge carriers are high. To overcome this problem, a 5-contact (or potentiometric) configuration is generally preferred and used for more accurate measurements of the Hall voltage (Fig. IV-5b). In absence of a magnetic field, a potentiometer (with internal resistance 100 Ω), located between the wires 3 and 4, is adjusted in order to cancel the longitudinal stray voltage. The voltage drop measured between the wires 5 and 6 under a magnetic field gives thus only the result of the Hall voltage. The Hall coefficient R_H is derived from the slope of the Hall resistivity plotted against the magnetic field.

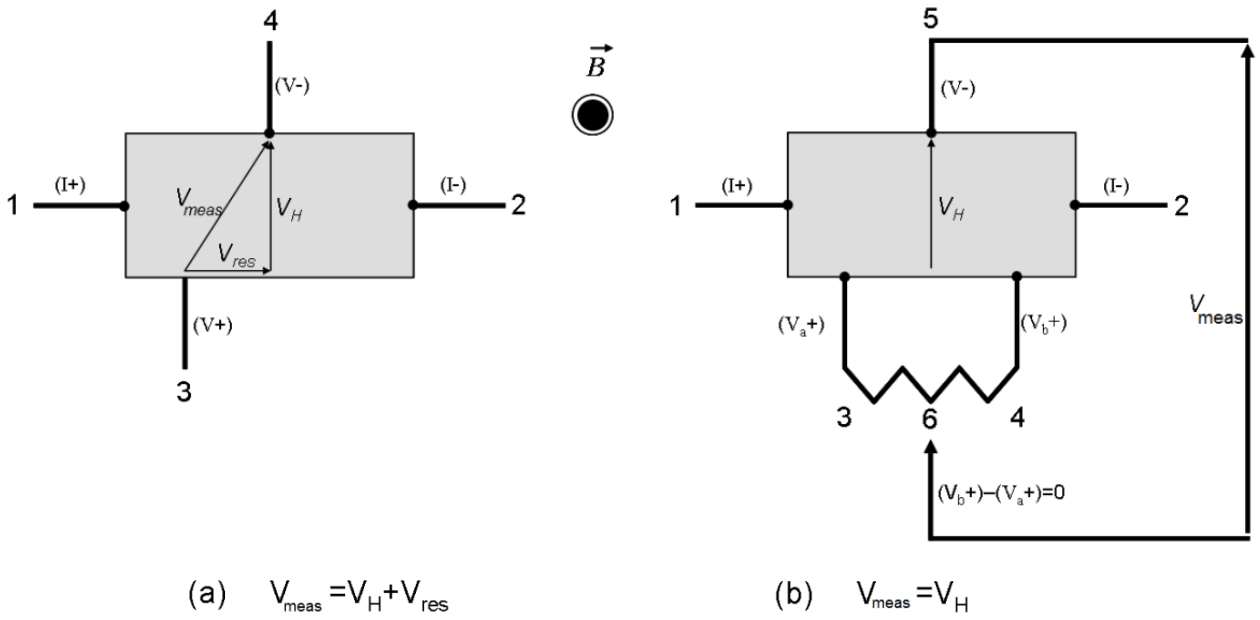

Figure IV-5: Measurement of Hall effect by (a) a 4 contacts and (b) a 5 contacts method.

Two channels are available in each sample holder to perform the Hall effect measurements (Fig. IV-6). The connections are made by tinned copper wires of small diameter (200 µm) that are connected to the bar with a BiSn solder. A thin layer of varnish (GE 7031) is used for thermal anchoring the sample to the support, which has previously been electrically isolated by a Kapton® foil.

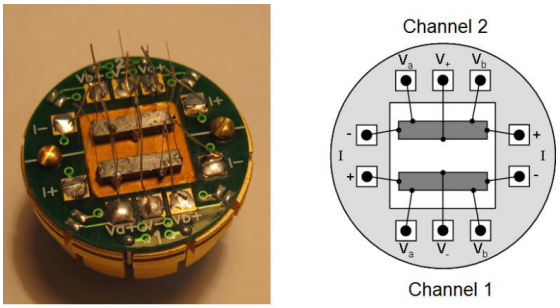

Figure IV-6: Photo and scheme of the sample holder puck that can accommodate two samples, used for galvanomagnetic measurements.

III) HIGH TEMPERATURE THERMOELECTRIC MEASUREMENTS

III-1) Thermal conductivity

III-1-1) Principle of measurement

For temperatures higher than ambient, heat losses by radiation (varying like T^3) are important and seriously limit the use of the stationary method for determining the thermal conductivity. Among the alternative methods, the flash method, originally developed by Parker /PAR61/, is the most commonly indirect measurement method used. The flash method is a dynamic method to determine the thermal diffusivity, $\alpha(T)$, of solid samples, powders or liquids. The thermal conductivity of a material is then determined using the relation:

$$\kappa(T) = \alpha(T)\rho_V(T)C_p(T) \qquad \text{(IV-7)}$$

where $C_p(T)$ is the specific heat at constant pressure and $\rho_V(T)$ – the volumetric mass density. The latter is calculated according to the well-known equation:

$$\rho_V(T) = \frac{m}{V(T)} \qquad \text{(IV-8)}$$

where *m* is the mass of the dry solid and *V(T)* the volume.

The principle of the flash method is to thermally excite by a laser the front surface of a cylindrically-shaped (in general) solid sample of thickness e and radius r_s. It must be opaque at the wavelength of the laser, homogeneous, isotropic and have constant thermophysical properties. Initially placed in isothermal conditions, the excitation is performed by means of a heat pulse of uniform density of energy. The irradiated portion forms a disk of radius $r > r_s$. The sample is subjected to heat losses on its three faces while heating. They are characterized by three exchange coefficients (h_1 on the front face, h_2 on the rear face and h_3 on the lateral face), each one is assumed to be constant in time and uniform on the surface where it occurs.

Determination of diffusivity is made from the temperature evolution with time of the rear face of the material, called thermogram (Fig. IV-7). Several thermal models have been proposed to describe the thermogram issued from a flash experiment.

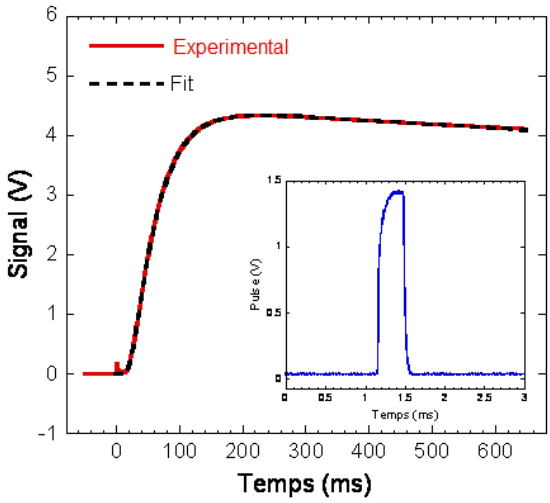

Figure IV-7: Thermogram obtained during one measurement of the thermal diffusivity. The signal is proportional to the temperature of the rear face. The peak which appears at $t = 0$ is an electronic artifact due to the laser impact on the sample. The signal generated by the laser pulse is shown in the insert.

In the ideal case, no heat losses (adiabatic case) and instantaneous laser pulse (temporal Dirac distribution), Parker /PAR61/ showed that the thermal diffusivity is expressed by:

$$\alpha \approx 0.139 \cdot \frac{e^2}{t_{0.5}} \qquad \text{(IV-9)}$$

where $t_{0.5}$ represents the time to reach half of the maximum temperature and e – the thickness of the sample.

The influence of radiative or convective losses and of the width of the energy pulse on the determination of the thermal diffusivity has been studied by several authors /COW61, COW63, CAP63, FAU64, JAM74, CLA75, JOS95, BLU02/. More sophisticated methods, using only the ascending part of the thermogram, were developed by Degiovanni /DEG85/ (method of partial time), Maillet et al. /MAI93/, Balageas /BAL82/, and Degiovanni and Laurent /DEG86/ (method of partial temporal moments). Several models are implemented on the apparatus we used, but, we retained two main models: the model of Cowan /COW61, COW63/ and the revised model of Cape-Lehman /BLU02/. The first model considers unidirectional thermal transfer and takes into account the radiative losses on the front and back sides of the sample ($h_1 = h_2$ and $h_3 = 0$). The second model considers a two-dimensional flow and radiative losses on the three faces ($h_1 = h_2 = h_3$). Both models also incorporate corrections for the finite width of the laser pulse. Cowan's model was used in the majority of cases, our samples having generally a thicknesses of less than 1 mm (thus the heat losses of the sample slice remain negligible). For thicker samples, the Cape-Lehmann model is more appropriate. We do not go deeper into the details of these models here but the reader wishing to have a more complete picture can refer to the mentioned papers.

III-1-2) Protocol of experiment

The diffusivity measurements were performed on a laser flash apparatus (LFA 427, Netzsch) (Fig. IV-8). The scheme of the measuring device is reproduced in Fig. IV-9. The heat pulse is provided by a solid Nd:GGG laser (neodymium: gallium - gadolinium - garnet) operating at a wavelength $\lambda = 1064$ nm and delivering a maximum power of 20 J/pulse. The laser beam is directed to the system by an optical fiber. The temperature rise of the rear face of the material is measured by an infrared detector (InSb with Ge filter) cooled by liquid nitrogen. The alumina sample holder sustaining the material on three legs is introduced into an alumina tubular support, centered in the furnace once the chamber is closed. The whole is designed so as to minimize the contact between the sample holder and the material, thus not only reducing heat losses by conduction but also ensuring a complete and uniform laser irradiation of the front face of the sample. The diameter of the laser beam used is in fact greater than the inner diameter of the sample holder. To avoid damage of the sensor or disturbance of the signal, the part of the laser beam that is not absorbed by the material and not obscured by the sample holder is blocked by a

SiC cap covering the alumina pieces (Fig. IV-9). The first thermocouple, located at the level of the heating elements, is used to regulate the oven temperature. The second one, fixed as close as possible to the sample, provides an accurate measurement of the material's temperature.

Figure IV-8: Photography of the thermal diffusivity measurement system (LFA 427, Netzsch).

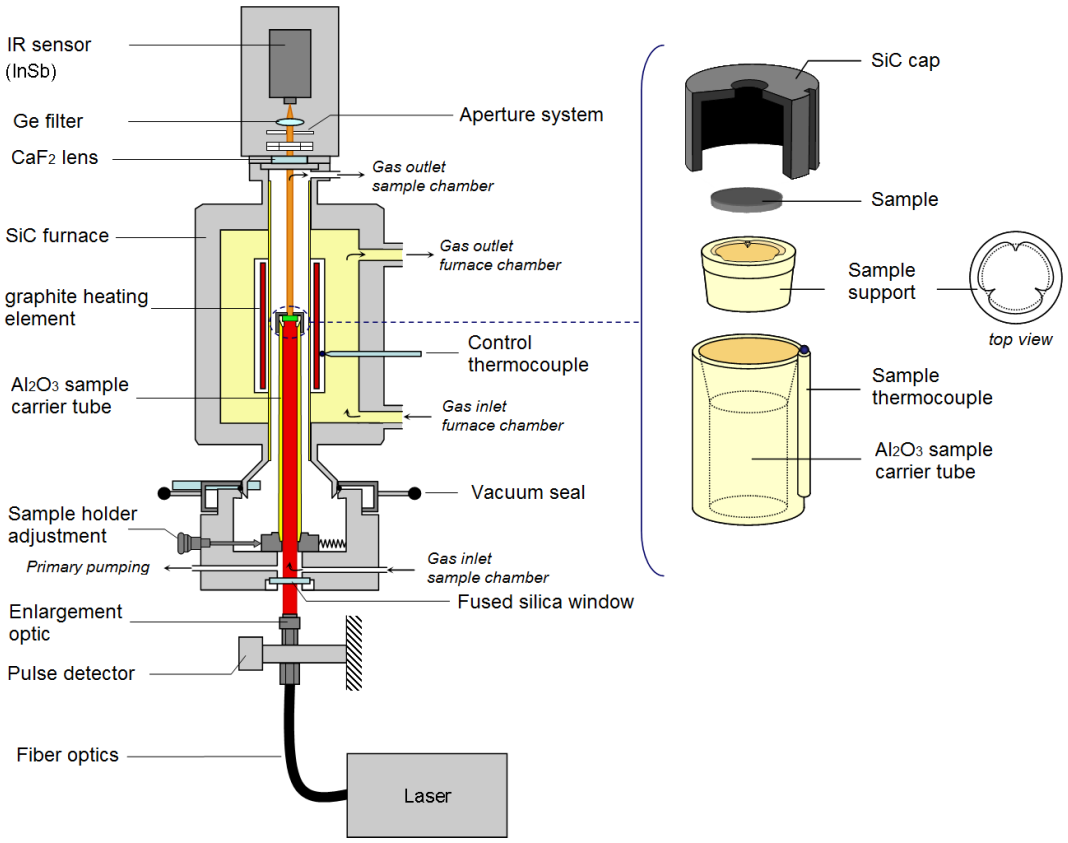

Figure IV-9: Scheme of the thermal diffusivity measurement setup (Netzsch LFA 427).

A circulation of tempered water (1 l/min) on the bottom of the oven helps to prevent overheating. A control interface where the laser and sample parameters can be set, allows making the measurement in two modes: manual or automatic. We usually worked in the automatic mode by entering the adjustable parameters: sample dimensions, temperature steps (25 K), heating ramp (5 K/min), pulse width (0.3 ms), duration in between the pulses (1 min), laser power (420 V). The software automatically manages the different parameters related to the quality of the registrations (gain, diaphragm, acquisition time) and ensures good reproducibility of the measurements by meeting given criteria (stability of the set point T < 1.0 K, stability of the sample temperature T < 0.3 K/30s, stability of the baseline < 1 V/10s). The measurements were carried out under a protective argon atmosphere (flow 75 ml/min) after three successive cycles of pumping – Ar filling, in order to limit the oxygen content.

The preparation of the sample must obviously be performed rigorously to minimize measurement uncertainties due to the operator. Slices of 0.6-0.9 mm in thickness e were cut with a diamond wire saw from the sintered cylindrical ingot either in the form of disks (10 mm in diameter) or squares (6 mm in side) to fit in the different sample holders we have. The orientation of the samples will be discussed later. The surfaces were polished with high accuracy ($\Delta e \leq 0.02$ mm) and the dimensions were verified by caliper at minimum three points. Both sides of the slices were covered with a thin and uniform graphite layer (ideal thickness: 5-10 µm) produced by a graphite spray in order to avoid the effects of reflection due to the metallic shine of our compounds and have a better laser beam absorption and a good emission for the InSb sensor. The introduction of Ar in the chamber has to be done in a gentle manner to avoid the dislodging of the sample from its support. There is nevertheless a risk that an unpredictable slight overpressure contained in the pipes moves the sample or even makes it fall out of the sample holder. In addition, checking the laser beam alignment and cleaning the protection windows (CaF_2 and silica) must be regularly ensured.

The volumetric mass density was determined by estimating the volume V from the geometrical dimensions and the mass (precision: ± 0.02 mg) of the densified sample at room temperature, neglecting any temperature dependence (V constant).

The specific heat measurements were performed on a commercial system (DSC 404 F3 *Pegasus*, Netzsch). Analysis requires a minimum of three experiments carried out all in the same

conditions (same temperature program, same gas flow, same crucibles). First, we have to perform a blank measurement with empty crucibles enabling to further correct the baseline of the DSC signals produced from both crucible and sample. The baseline experiment has to be performed at least two times to verify the stability and the reproducibility of the DSC signal. A standard sample (sapphire) whose C_p is well known and the sample we want to test are then measured, maintaining the product of the mass and specific heat (mC_p) as close as possible between the two analyzes in order to obtain quite similar DSC signals in µV/g near room temperature. We used platinum crucibles recovered with an alumina liner. Experiments were carried out under an argon flow rate of 70 ml/min. The ASTM E 1269 method was used to extract the values of C_p. It requires the presence of an isotherm at the beginning and at the end of the measurement and ensures greater accuracy of drift correction of the baseline. This drift can in fact occur when the measurement system becomes unbalanced (measurement at the end of day, position of the crucible).

As an example, figure IV-10 shows the results obtained on the ternary compound $Bi_{0.4}Sb_{1.6}Te_{3.1}$, one of the compositions synthesized in this thesis. The measurements between 310 and 440 K were performed by the DSC Netzsch. The specific heat is rising slightly in a linear way above 330 K. Below this temperature, a deviation from linearity is observed. This deviation is not intrinsic to the sample but results from a non rigorous matching between the "mC_p" sample and the "mC_p" sapphire (this is a regular artefact difficult to solve near room temperature according to the DSC experts from Netzsch). To try to correct the data in this temperature range, we performed low temperature C_p measurements (2 – 300 K) using the heat specific option of the PPMS.

As seen in Figure IV-10, C_p increases linearly above 150 K and joins nicely the high temperature data above 330 K. A fit of the data between 150-350 K gives the following linear regression:

$$y = 0.16932 + 8.0129e^{-5}x \qquad \text{(IV-10)}$$

It is instructive to note that the C_p data in this temperature range deviates slightly from the specific heat expected using the Dulong and Petit law.

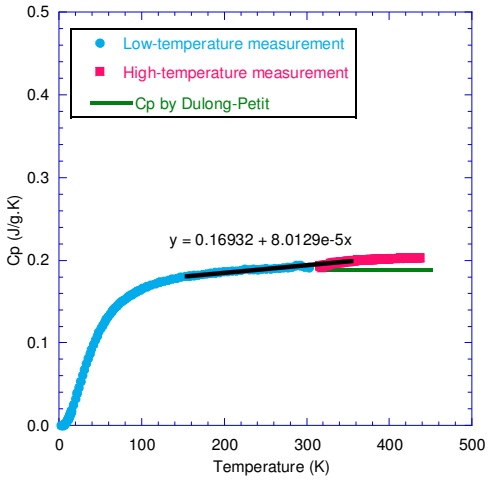

Figure IV-10: Evolution of the specific heat with temperature for $Bi_{0.4}Sb_{1.6}Te_{3.1}$ compound. High and low temperature measurements are in a good correlation. The C_p, calculated by Dulong-Petit law, is also presented in green color.

According to this law, the specific heat for temperatures above the Debye temperature tends to a constant value that is independent of the nature of the atoms according to:

$$C_p(J/g \cdot K) \approx \frac{3nN_A k_B}{M} \qquad \text{(IV-11)}$$

where n is the number of atoms per chemical formula, N_A the Avogadro's number (mol^{-1}), k_B the Boltzmann's constant (J/K) and M the molar mass (g/mol) of the chemical formula. For the composition $Bi_{0.4}Sb_{1.6}Te_{3.1}$ with n = 5.1 atoms and M = 673.97 g/mol, we obtain C_p = 0.19 J/g.K from Eq. (IV-11). The good agreement between the measured values and the value calculated with the Dulong-Petit's law suggests that anharmonicity is low in this family of compounds near room temperature.

We should note that whatever the composition probed in this work, the values of the specific heat measured between 300 and 480 K were very close to that found in Eq (IV-11).

III-2) Thermopower and electrical resistivity

The measurement principles of the thermoelectric power and the electrical resistivity between 300 – 480 K are similar to those described previously for low temperatures. They will not be detailed again in this paragraph (see §I).

The thermoelectric power as well as the electrical resistivity at high temperatures were measured on the ZEM-3 ULVAC-RIKO apparatus (Fig. IV-11).

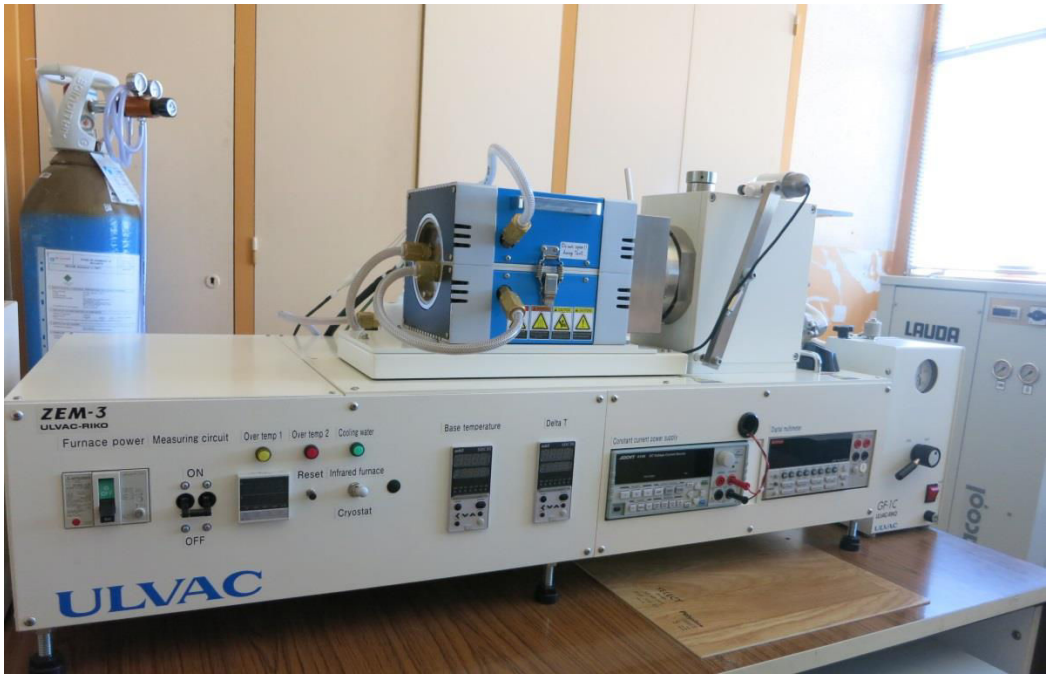

Figure IV-11: Photography of the ZEM-3 measurement system.

This equipment allows measuring simultaneously the two properties in a controlled atmosphere, from room temperature up to 1373 K. The device is configured to accommodate two different sample geometries: cylindrical ($2 < Ø < 4$ mm) or parallelepiped (4 to 16 mm^2 in cross section). Their length can also vary from 5 to 22 mm. In most cases, we used parallelepipedic samples, shaped same as for the low temperature range measurements. In practice, the material to characterize is fixed at each end by a clamp system consisting from a block of alumina and a platinum electrode (Fig. IV-12). The two sections of the sample must be flat and polished to ensure good electrical and thermal contacts. The device contains a halogen oven whose temperature is regulated by controllers (Yamatake SDC30) and whose heating rate is fixed to 50 K/min. They are also used to measure the ΔT.

A reduced helium pressure (100 mbar) was applied to promote heat exchange. The measurements are controlled by a computer program wherein the temperature steps and the number of applied gradients are defined. Typically four temperature differences are imposed between the platinum electrodes (15, 20, 25 and 40 K). These are generated as follows: the bottom alumina block is heated by a set of Pt/Rh wires placed in the center and their temperature is controlled by a thermocouple located at the heart of these wires. The upper block acts as a heat sink. The temperature difference is measured by thermocouples (type K) and is in the range 1.5 – 8 K for our samples (these values depend on the nature of the sample-electrode contact and the conductance of our samples). The Seebeck voltage is obtained in a stationary state from ΔT and ΔV measured by thermocouples in contact with the sample. A linear fit is then used to extract the thermopower (the subtraction of the thermopower of the thermocouple wire is taking into account). A 4-contact method is used to determine the electrical resistivity.

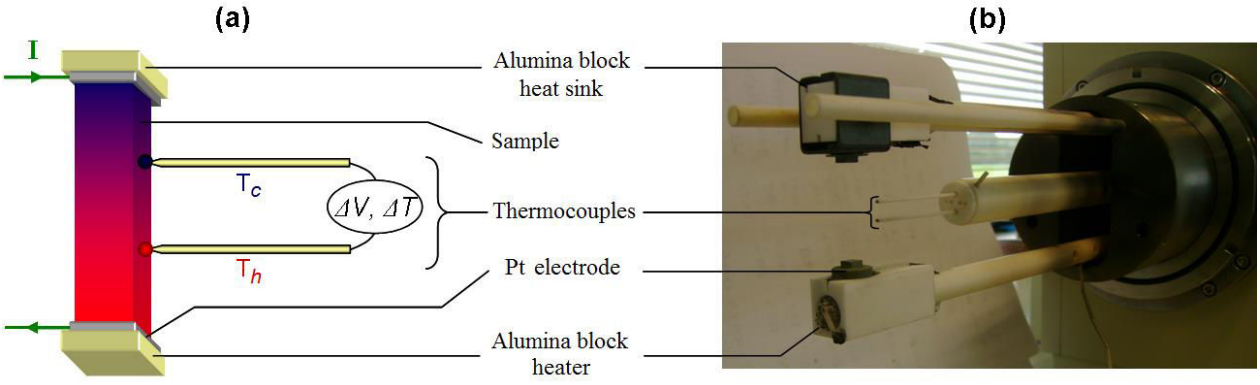

Figure IV-12: (a) Scheme of a sample placed in the clamp system of ZEM3. Thermocouples are put in contact with one side of the bar by simple pressing. (b) Photography of the measurement device

Despite the acquisition speed and ease of implementation, there are some limitations and difficulties on the ZEM3 arising with samples having a resistance higher than 10 Ω.m (due to an intrinsic limitation of potentiometer used in the ZEM-3 package) or a thermoelectric power less than ± 20 µV/K combined with a high thermal conductivity (metallic samples for example). In this later case, good results can nevertheless be obtained by decreasing the conductance of the sample. It means that the sample should have a length of about 20–25 mm and a cross section of about 4 mm^2. The former requirement is sometimes not possible to realize.

IV) GALVANOMAGNETIC MEASUREMENTS AT HIGH TEMPERATURE

We extended, for some samples, the temperature range of the measurements of the Hall coefficient R_H up to 400 K using a home-built measurement system (Fig. IV-13). This set-up allows us also probing the electrical resistivity from a Van-der-Pauw configuration /VAN58/ and then to derive the Hall mobility.

Figure IV-13: High temperature galvanomagnetic properties measurement system.

The measurement method involves applying a current and measuring a voltage using 4 small probes on a flat, square-shaped sample of uniform thickness placed in a magnetic field (Fig. IV-14).

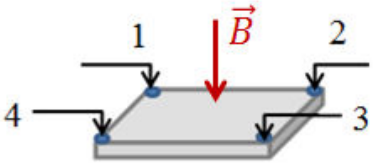

Figure IV-14: Scheme for optimized 4-probes measurement method.

Square-shaped samples of about ~ 5 x 5 mm^2 in size and 0.7 to 1 mm in thickness were cut from the densified cylinders. They were polished with abrasive paper to ensure thickness uniformity. Electrical contacts were made by pressing molybdenum wires on the samples.

Using this measurement setup, the Hall coefficient can be derived from a total of eight measurements that are made around the periphery of the sample with the configuration shown in Fig. IV-15.

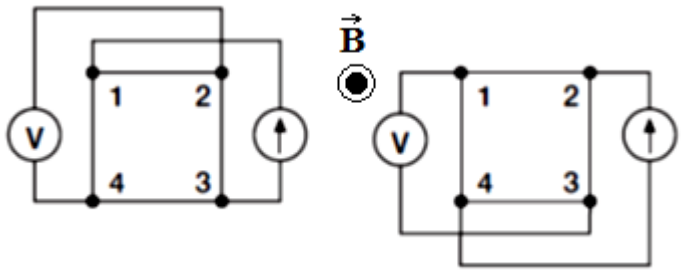

Figure IV-15: Hall voltage measurement configurations.

With a positive magnetic field, *B*, a current is applied between terminals 1 and 3, and the voltage drop $V_{2\text{-}4+}$ between terminals 2 and 4 is measured. After, the current direction was reversed and the voltage drop $V_{4\text{-}2+}$ is measured. The same procedure is made for another pair of terminals, giving us $V_{1\text{-}3+}$ and $V_{3\text{-}1+}$. This procedure was repeated with five different magnetic fields ranging from -0.5 T to 0.5 T with a step 0.25 T. Using a linear regression, the dependence of the obtained Hall voltage with the magnetic field can be built. The slope of this curve gives us the value of R_H. This method offers the opportunity to avoid any influence of asymmetry of probe placing, contact resistance and magnetoresistance effect on the results for highly resistive samples. At each fixed temperature, R_H was measured three times to obtain reliable data.

The electrical resistivity can be determined using the same electrical contact configuration as in Fig.IV-15, following the Van der Pauw method /VAN58, WEB99/. Briefly this method consists in the measurement of two basic resistances $R_{12,34}$ (called horizontal resistance) and $R_{23,41}$ (called vertical resistance) where $R_{ij,kl}$ indicates that the current is injected between the points *ij* while the potential difference is measured between the points *kl*. Knowing these two resistances, the sheet resistance of the sample, R_S, can be extracted from the Van der Pauw formula:

$$e^{-\pi R_{vertical}/R_S} + e^{-\pi R_{horizontal}/R_S} = 1 \qquad \text{(IV-12)}$$

leading then to the resistivity, ρ, of the sample:

$$\rho = R_S \cdot c \tag{IV-13}$$

where *c* is the thickness of the sample.

To improve the accuracy of the measurement, several horizontal and vertical resistances are measured by switching the polarity of the DC current source and taking into account the reciprocity theorem ($R_{ij,kl} = R_{kl,ij}$). When the horizontal and the vertical resistances are equal, the sheet resistance ($R_{12,34} = R_{23,41} = R$) can be extracted easily from Eq. IV-14 :

$$R_S = \frac{\pi R}{ln2} \tag{IV-14}$$

However in most cases, the horizontal and the vertical resistances are not equal and an iterative method should be used to solve the Van der Pauw formula. In our software, such method was implemented.

V) SAMPLE ORIENTATION

It is important, when estimating the dimensionless figure of merit *ZT*, that all three transport properties involved in *ZT* are measured in the same direction to get a reliable *ZT* value. If the sample is fully isotropic (cubic structure for example), this rule can be relaxed since the physical properties are not dependent on the direction. Except this situation, the operator should take care, as in the case of Sb_2Te_3 and related compounds, because of the strong anisotropy of the physical properties as seen in chapter II. Because of the different requirements on the sample geometry, especially for measurements above 300 K, i.e. cylindrical shape for the thermal conductivity and bar shape for the electrical properties, the measurements are often performed in different directions (parallel and perpendicular to the pressing direction for the thermal conductivity and for the electrical properties, respectively), which may lead to questionable validity of the results on *ZT*. The situation in Sb_2Te_3-Bi_2Te_3 solid solutions is particularly dramatic since the thermal properties are usually lower in the parallel direction than in the perpendicular direction while it is the reverse for the electrical properties. Combining such properties will inevitably result in an overestimation of *ZT*.

To probe correctly the *ZT* values, all our bulk ingots obtained after densification (SPS, cold

pressing) had a thickness of about 6-7 mm, allowing cutting samples of good dimensions for measurements to be performed in both directions, perpendicular ("perp") and parallel ("par") to the pressing direction. Figure IV-16 shows how the samples were cut with the diamond wire saw to probe the properties in both directions, with the shape fitted to be optimal and adapted to our experimental set-ups for accurate measurements.

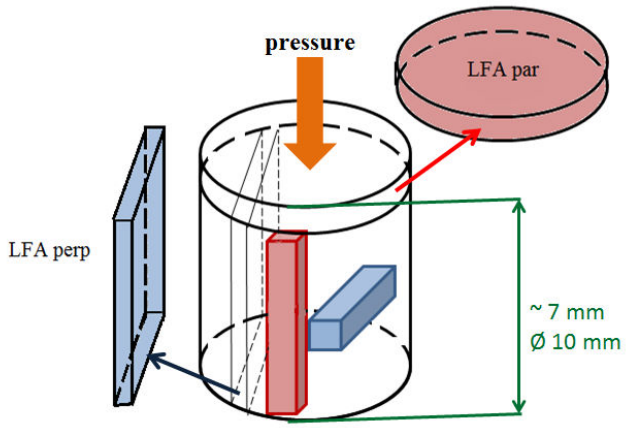

Figure IV-16: Scheme of optimal samples preparation for the measurements in the directions parallel (red color) and perpendicular (blue color) to the pressing direction. Low temperature measurements: bar-shaped samples for both electrical thermal properties cut in "perp" and "par" directions (PPMS, TTO), bar-shaped samples cut in "perp" direction for galvanomagnetic measurements (PPMS, ACT). High temperature measurements: bar-shaped samples for electrical properties (ZEM3); cylindrical ("par") or square ("per") - shaped samples for thermal diffusivity measurements (LFA); square-shaped samples cut from the LFA "par" samples for Van der Pauw resistivity and Hall coefficient measurements in the "perp" direction.

Most of our measurements were made along the direction perpendicular to the pressing direction, because it is in this direction that *ZT* was the highest. The transport properties were however measured in the "par" direction on some samples to investigate the anisotropy.

As the Hall coefficient could also exhibit a small anisotropy, we checked if, in the "perp" direction, probing the Hall voltage along or perpendicular to the pressing direction could lead to different results. Several measurements performed on different samples demonstrated that it is not necessary to take special care about the positions of the Hall voltage contacts (Fig. IV-17).

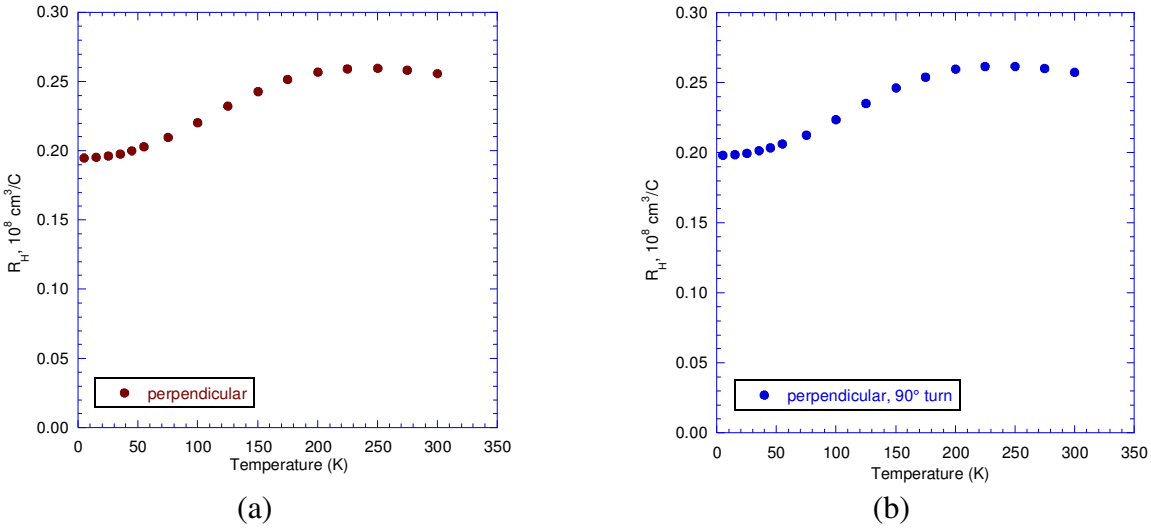

Figure IV-17: Temperature dependence of the Hall coefficient for samples prepared in the "perp" configuration with a Hall voltage placed a) along and b) perpendicularly to the pressing direction. No difference is observed between these two configurations.

VI) CALIBRATION OF THE MEASUREMENTS AND UNCERTAINTY

We carefully and regularly calibrated all the measurements setups we used in this study. The TTO calibration was performed with a nickel standard. For thermal measurements above room temperature, we calibrated our experiments with an inconel alloy and sapphire for diffusivity and specific heat measurements, respectively. For ZEM-3, we verify the calibration of the system with a reference material (constantan) supplied by Ulvac.

The measurement uncertainties given by QD for the PPMS are quite low and consist of 2-3% for electrical resistivity, 4% for thermopower and 5% for thermal conductivity below 200 K (for higher temperatures, uncertainty for thermal conductivity can rise up to 10%). Thus the resulting values of *ZT* below 200 K possess 10-15% uncertainty (rather 10% due to the cancellation of the geometrical factor between the thermal conductivity and the electrical resistivity), while above 200 K, the uncertainty increases due to the uncertainty on the thermal conductivity. Note also that the values of *ZT* above 150 K are systematically underestimated due to the radiations. For ACT measurements, the uncertainty on the Hall coefficient is about 2-3% depending mainly on the geometrical factor.

The physical properties results obtained at temperatures above 300 K are coming from

several measurement systems. In order to get values of thermal conductivity, the density of the sample must be estimated (with uncertainties ~3%), specific heat measurements by DSC performed (~2% of deviation in case of skilled operator) and finally LFA measurements of thermal diffusivity fulfilled (also ~3% of measurement uncertainties). Finally, the error bar for the thermal conductivity is 8-10% at high temperatures. The provider of ZEM3 claims following uncertainties values: 2-3% for electrical resistivity depending on the geometry of the sample and ~ 7% of measurement deviation for the thermopower. So *ZT* values at temperatures above 300 K may demonstrate 15-20% of measurement uncertainty. For Hall measurements and Van der Pauw resistivity, the uncertainty is evaluated to be 2-3%. It is again here the geometrical factor that will play the major role.

In general, we found that the coupling between measurements performed at room temperature and at high temperatures was satisfying. Thus, the gap is less than 5 % for the electrical resistivity and the thermopower and about 10 %, or more sometimes, for the thermal conductivity. It is actually the radiation phenomena in the TTO measurements that appear above 200 K that are responsible for this deviation. A good agreement (few percent difference) was also found in the Hall measurements.

CONCLUSION

Several measurement systems were used during the work to obtain the complete characterization of our $Sb_{2-x}Bi_xTe_3$ samples. We described in detail the experimental procedures and measurement systems we used for the determination of the electrical, thermal, and galvanomagnetic properties in the low range of temperatures (2-300 K) and in the range above room temperature (300-480 K). Particular care has been taken to describe the importance of sample preparation processes and difficulties that could be encountered during the measurements. Some advices on the prevention of main problems and additional uncertainties in data have been given. An overview of the uncertainties given by each facility has been done as well.

Chapter V

Results and Discussions

INTRODUCTION

This chapter is dedicated to the thermal, electrical and galvanomagnetic properties of the materials based on V-VI compounds of general formula $(Sb_{2-x}Bi_x)_{1-y}Sn_yTe_{3+z}$ that were synthetized in this study. All the physical properties were measured in a broad temperature range (5 – 480 K) to probe the basic mechanisms that manifest at low temperatures and are responsible for the electrical and heat transport of charge carriers and phonons. This range covers also the useful temperature range (270 – 310 K) for our application linked to heat pumps. Finally, useful information at "high temperatures" will shed light on the potential of these materials for electrical generation. Most of the measurements presented in this chapter were performed in a direction perpendicular to the pressing direction. However, for selected samples, we shall also present the data collected along the pressing direction to probe the anisotropy.

In order to obtain p-Sb_2Te_3-Bi_2Te_3 solid solutions with improved thermoelectric performances with respect to the state-of-the-art materials and to understand the microscopic processes, a wide range of compositions were prepared by varying the Bi content, *x*, between 0.4 and 0.52. This range was selected because it leads to the best thermoelectric performances (see chapter II). In parallel, we have also investigated the influence of an excess of tellurium ($z = 0.1$) on the transport properties. The idea is to be able to finely tune the carrier concentration, since an excess of Te reduces the deviation from stoichiometry. In addition, this strategy may enable compensating an eventual loss of Te during the synthesis process. In the case where no loss of Te would occur and according to the phase diagram, this (high) excess of Te might lead to the precipitation of Te. Finally, we decided to explore the influence of Sn as a mean to further manipulate the carrier concentration and to determine whether or not Sn acts as a resonant impurity as in Bi_2Te_3 /JAW09/.

The melt-spinning (MS) technique was used as a way of creating nanostructured bulk samples labeled throughout this chapter as "MS". The bulk samples that were prepared from the same initial ingot as the MS-samples were but only densified by SPS will be called hereafter "reference" samples.

The complexity of the $(Sb_{2-x}Bi_x)Te_3$ family of materials in terms of tuning the thermoelectric properties will be discussed. Strong influence of preparation processes on the thermoelectric performance along with structural and energy bond complexity of the studied

materials makes the interpretation of the results obtained in this work quite delicate but efforts to interpret qualitatively and quantitatively the results will be presented.

In this chapter, we start with the $(Sb_{2-x}Bi_x)Te_3$ series and then we discuss the results obtained on samples containing an excess of Te. The influence of different preparation processes including double SPS, cold pressing, annealing and alignment of ribbons as starting materials before SPS will constitute the third part of this chapter. The impacts of other melting parameters such as the influence of the nozzle diameter or the distance between the nozzle and the wheel will be presented separately in Annexe 1. As we shall see below, the physic of the nanostructured and reference $(Sb_{2-x}Bi_x)Te_{3+z}$ samples is similar. The semi-classical approach based on transport Boltzmann equations will be proposed to interpret the common features. Moreover, we shall see that the heat transport, due to phonons, can be treated within the Debye approximation. Finally, the fifth and last part of this chapter will be dedicated to the influence of Sn.

I) TRANSPORT PROPERTIES OF $Sb_{2-x}Bi_xTe_3$ SERIES

I-1) Introduction

In this first part, we present the transport and galvanomagnetic properties of $Sb_{2-x}Bi_xTe_3$ with x = 0.4 and 0.48 on both reference and MS samples measured in the temperature range 5 – 480 K. In addition, we determine how the anisotropy impacts the electrical and thermal transport in these polycrystals. This point is particularly important to evaluate correctly the dimensionless figure of merit ZT and to determine the most favorable direction. The anisotropy has been probed on a reference sample with a Bi content of x = 0.4 and on a MS sample with x = 0.48. Furthermore, we also comment on the reproducibility of our preparation process on the ternary compounds with x = 0.48, both on reference and MS samples.

I-2) Thermoelectric and galvanomagnetic properties of $Sb_{2-x}Bi_xTe_3$ with x = 0.4 and 0.48

The temperature dependence of the electrical resistivity ρ of the reference and MS $Sb_{2-x}Bi_xTe_3$ samples is shown in Figures V-1a and V-1b for x = 0.4 and 0.48, respectively. We also

include in these graphs the partial data collected along the pressing direction for the reference sample with $x = 0.4$ and the MS sample with $x = 0.48$.

The values of the electrical resistivity are constant below $T < 20$ K for the reference samples and increase above this temperature with increasing temperature. Above 200 K, ρ follows a near $T^{1.5}$ law. Taking into account the magnitude of ρ (from 2 to 15 μΩ.m), this behavior is typical of a heavily doped semiconductor. We note that this property is anisotropic for a Bi content of $x = 0.4$ with values significantly higher in the pressing direction than in the perpendicular direction. Further, the anisotropy ratio (ρ_{par}/ρ_{perp}) increases with temperature to reach 1.4 at 300 K. This feature, in line with the results obtained on single crystals (see Chapter II), indicates that the SPS process induces a preferred orientation, which is parallel to the trigonal axis, along the direction of SPS pressure. This is coherent with the SEM fracture images observed along the SPS pressing direction observations that show some large grains with layered structure. We also note that increasing the Bi content from $x = 0.4$ to $x = 0.48$ results in a slight decrease in ρ.

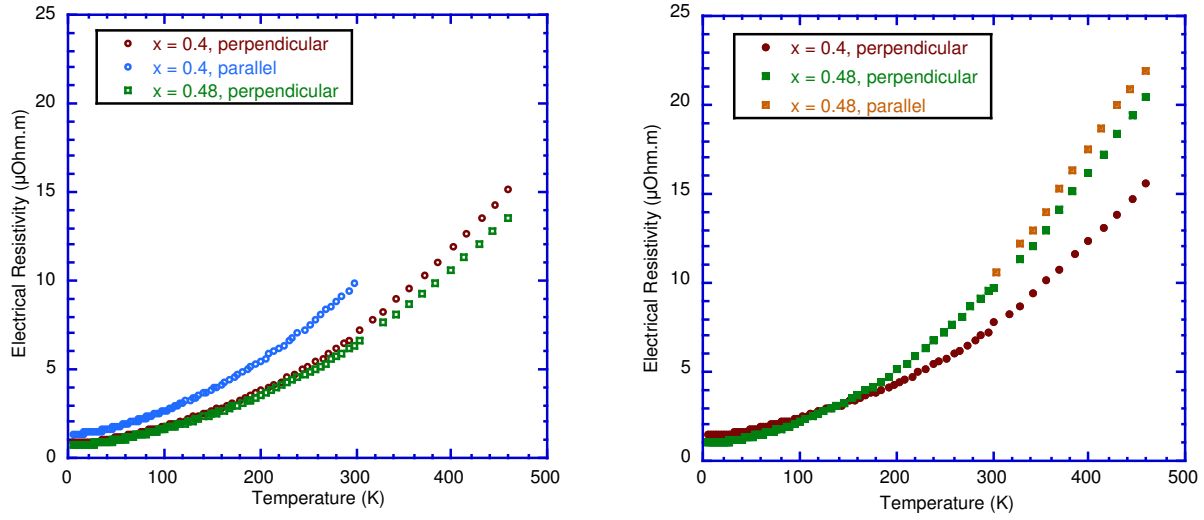

(a) (b)

Figure V-1: Temperature dependence of ρ for (a) reference and (b) MS $Sb_{2-x}Bi_xTe_3$ samples with $x = 0.4$ and 0.48. Partial results obtained along the pressing direction (parallel) are also included.

The MS samples show the same general trend compared to the reference samples regarding their temperature dependence. However, noticeable differences can be noted. Notably, the anisotropy ratio is lower (close to 1 between 300 and 460 K) in the sample with $x = 0.48$.

Moreover, the ρ values of the x = 0.48 specimen are higher than for x = 0.4. A comparison between the ρ values (Figs V-1a and V1b) suggests that the MS samples are more resistive than the reference samples.

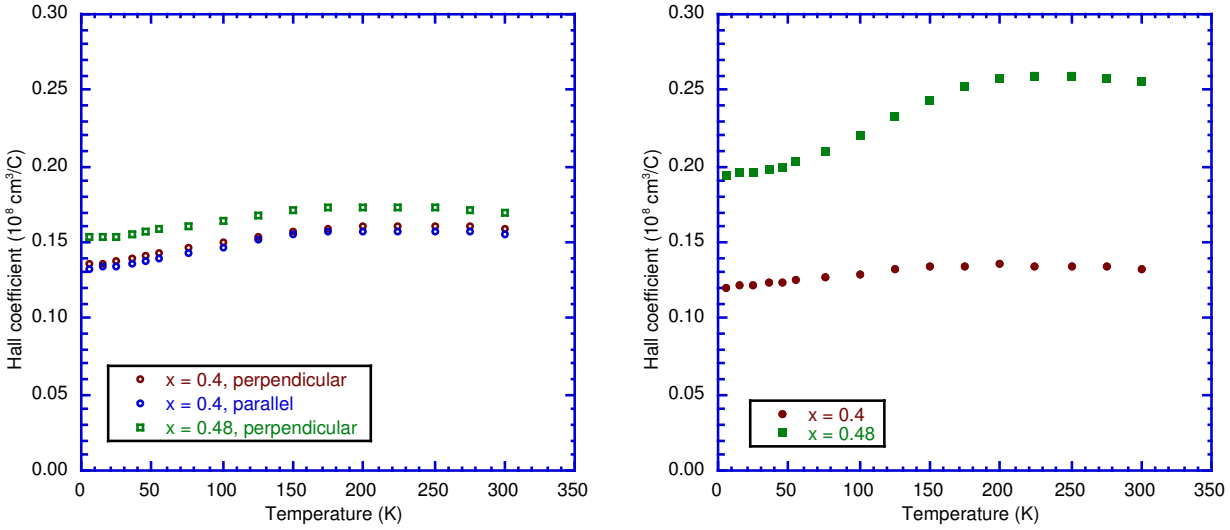

(a) (b)

Figure V-2: Temperature dependence of the Hall coefficient R_H for (a) reference and (b) MS $Sb_{2-x}Bi_xTe_3$ samples with x = 0.4 and 0.48.

The temperature dependence of the Hall coefficient R_H from 5 – 300 K is displayed in Fig. V-2. All the samples show a smooth temperature dependence, with a slight increase on going from low to high temperatures (more marked for MS sample with x = 0.48). This behavior is in good agreement with those obtained on single crystals /CAI93, CHA65, TES61, VOL74/, for which, an increase in the Hall coefficient was explained using a two valence-band model. R_H is always positive indicating that the electrical transport is dominated by holes. We see that the R_H values of the x = 0.4 sample are very close in both directions suggesting that R_H is isotropic. However, we should stress here that it could be anisotropic as reported by Gerovac et al. /GER02/ on polycrystalline samples prepared by mechanical alloying. The reason comes from the fact that two Hall coefficients are present (as a result of the layered crystal structure) in $Sb_{2-x}Bi_xTe_3$ single crystals: R_{123} and R_{231} (in this notation the first index refers to the direction of the electrical field, the second to the direction of the current and the third one to the direction of the magnetic field, and 1,2,3 refers to the binary, bisectrix and trigonal axis, respectively). Stördeur et al. /STO81/ showed that these two coefficients deviate in single crystals in the low field approximation (μB

<< 1 where μ is the carrier mobility and B the magnetic field) due to the peculiarities of the valence band structure. The difference depends on the value of x. For x = 0.4, the difference at 300 K was found to be about 9% but can be as high as 34% for x = 1 /STO81/. Since our reference samples are textured, a difference between the Hall coefficients measured on samples cut in the perpendicular (where roughly $R_{H\text{-}perp} \sim R_{123}$) or parallel (where roughly $R_{H\text{-}par} \sim R_{231}$) direction with respect to the pressing direction is thus possible.

Following several prior investigations we can determine an apparent carrier concentration from the Hall coefficient assuming a single parabolic band. In this approximation, the (apparent) hole carrier, p, is simply defined by:

$$p = \frac{1}{R_H e} \tag{V-1}$$

where e is the elementary charge. In single crystals, it is usual to use the Hall coefficient, $R_H = R_{123}$ (corresponding to a magnetic field along the trigonal axis and the current and Hall field along the basal planes). In polycrystalline samples, the closest orientation to this configuration is when the sample is cut in a direction perpendicular to the pressing direction. For this reason, we shall use $R_{H\text{-}perp}$ in the formula V-1.

Results of the hole densities are shown in Fig. V-3 for the reference and MS samples. p is constant below 20 K and above 200 K. We observe that the hole density in the reference samples is around 4×10^{19} cm^{-3} and 3.7×10^{19} cm^{-3} for x = 0.4 and 0.48, respectively. The melt-spinning process does not strongly impact the hole density event though no clear trend emerges from these data. On one hand, p increases in the sample with x = 0.4 (4.8×10^{19} cm^{-3} at 300 K) and, on the other hand, it decreases when x = 0.48 (2.4×10^{19} cm^{-3} at 300 K). Nevertheless, p is still higher for x = 0.4 than for x = 0.48. We can explain qualitatively this behavior if we assume, as in single crystals, that holes in bulk polycrystals are mainly created by antisite defects which originate from the substitution of Bi or Sb for Te atoms (the driven force to create such defects is the small difference of electronegativity between the atoms – see chapter II). With increasing the Bi_2Te_3 content, fewer antisite defects should be formed due to the larger difference in electronegativity between Bi and Te than between Sb and Te.

From Hall and electrical resistivity measurements, we can calculate the Hall mobility, μ_H, defined by:

$$\mu_H = R_H/\rho \tag{V-2}$$

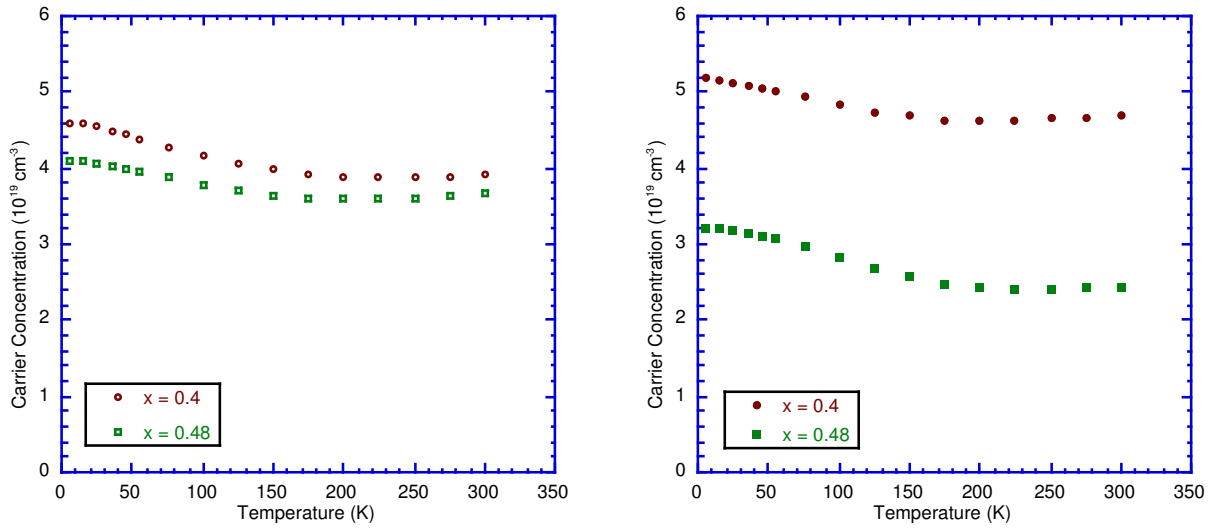

Figure V-3: Temperature dependence of the hole concentration for (a) reference and (b) MS $Sb_{2-x}Bi_xTe_3$ samples with x = 0.4 and 0.48.

and collect useful information about the scattering mechanisms of holes in these samples. The temperature dependences of μ_H are shown in Fig. V-4. Room temperature values are approximately 200 cm^2/V.s for the reference samples, which are high and comparable to those observed in single crystals of the same composition /CAI92a/. From the temperature dependence of μ_H, valuable insights into the carrier scattering mechanisms can be inferred. Near room temperature, μ_H follows a $T^{3/2}$ dependence and saturates to a constant value below about 15 K. This behavior is suggestive of a combination of scattering by acoustic phonons at high temperatures, and ionized and neutral impurities below 15 K. The situation is clearly similar in the MS samples, even though the values, while still important, are somehow degraded by the melt-spining process.

The thermopower (or Seebeck coefficient), S, is displayed as a function of temperature in Fig. V-5. All samples have positive S values, which vary linearly from 5 to 40 K. Then, S increases in magnitude with temperature up to 300 K and presents a constant slope $\partial S/\partial \ln(T)$ ~ 110-140 µV/ln(K) between 200-300 K (see insets Fig. V-5). Above 300 K, the slope of $S(T)$ decreases, vanishes and then becomes negative for some samples. This behavior is attributed to the manifestation of minority carriers (here electrons). As a consequence, the higher the temperature at which minority carriers manifest (within a series of similar compositions) is, the

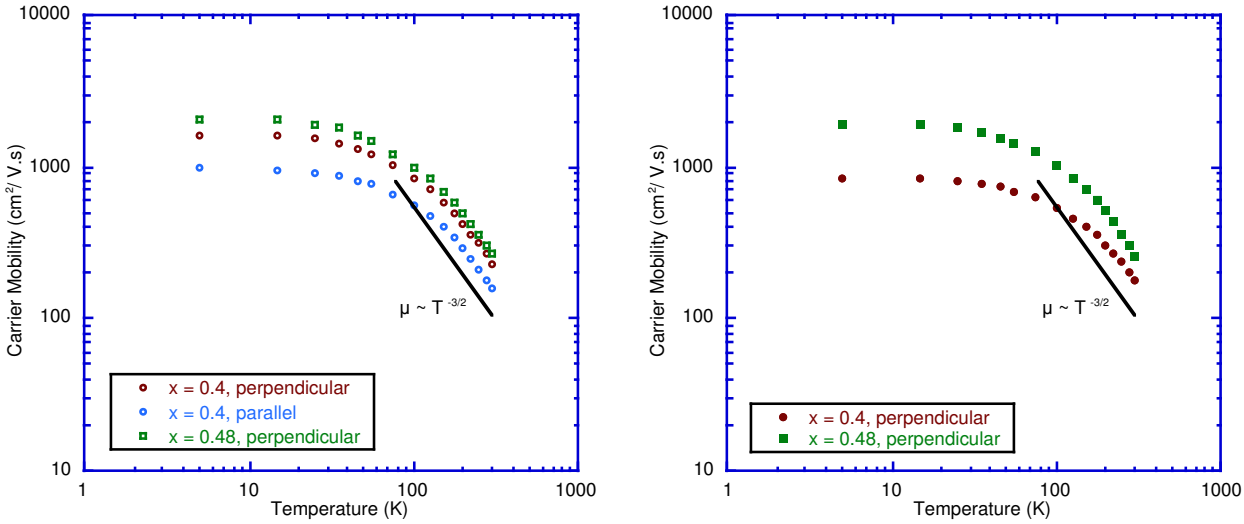

Figure V-4: Temperature dependence of μ_H for (a) reference and (b) MS $Sb_{2-x}Bi_xTe_3$ samples with x = 0.4 and 0.48. The continuous line shows a $T^{-3/2}$ dependence expected from purely acoustic phonon scattering.

higher the carrier concentration is. From this simple picture, we can safely conclude that the MS sample with x = 0.48 has the lowest carrier concentration, in good agreement with Hall measurements. From the position of the maximum S value, the energy band gap of a semiconductor, E_g (in eV), can be estimated from a formula derived by Goldsmid and Sharp /GOL99/:

$$E_g = 2e.S_{max}.T_{max} \qquad \text{(V-3)}$$

where T_{max} is the absolute temperature at which S_{max} occurs. Taking S_{max} = 220 μV/K at T_{max} = 420 K for x_{MS} = 0.48 leads to E_g = 185 meV, in excellent agreement with values reported in the literature using more sophisticated techniques of determination of E_g.

The thermopower is related to the carrier concentration through the chemical potential and to the scattering parameter (see section IV of this chapter). For a given scattering parameter, the higher the thermopower is, the lower the carrier concentration is. This picture is nicely illustrated in Fig. V-4 if we take into account the hole concentration data shown previously. Moreover, it is also interesting to appreciate the strong impact of a slight variation in the hole concentration of MS samples in the thermopower as it is illustrated in Fig. V-3b and V-5b. Finally, from partial measurements performed in the parallel direction on reference (x = 0.4) and MS (x = 0.48) samples, we can conclude that the thermopower is little, if not, affected by anisotropy.

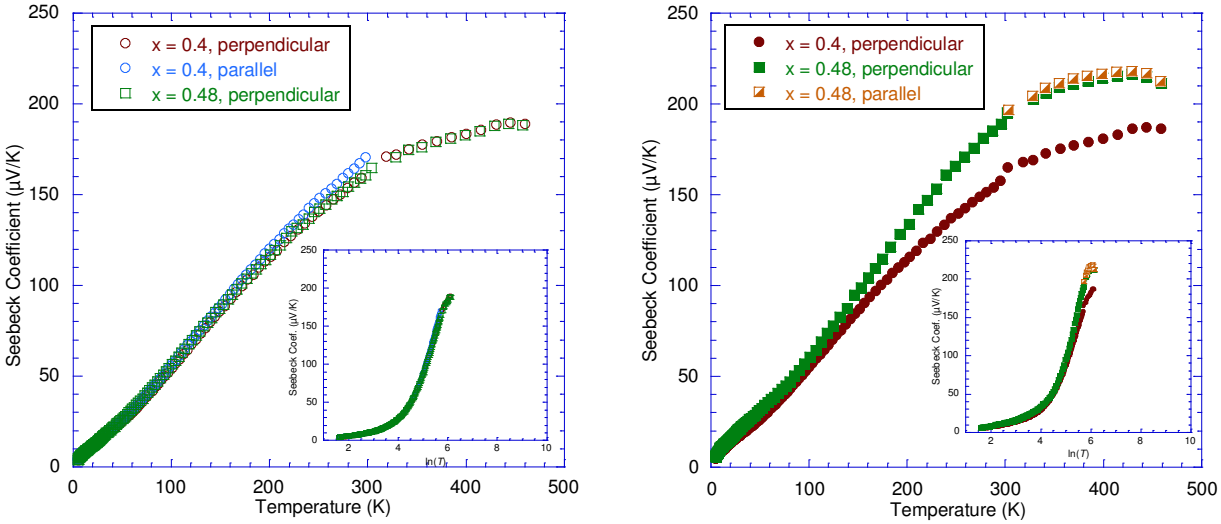

(a) (b)

Figure V-5: Temperature dependence of *S* for (a) reference and (b) MS $Sb_{2-x}Bi_xTe_3$ samples with $x = 0.4$ and 0.48. Partial results obtained along the pressing direction (parallel) are also included. The insets show *S* vs. ln(*T*) showing two trends: 1) a constant slope $\partial S/\partial T$ below 20 K and 2) a constant slope $\partial S/\partial \ln(T)$ ~ 110-140 μV/ln(*K*) from 200 – 300 K.

The temperature dependence of the total thermal conductivity, κ, for the reference and MS samples is depicted in Fig. V-6. $\kappa(T)$ increases with increasing temperature, shows a maximum near 20 K and then decreases smoothly up to 350-400 K depending on the samples to finally increase again. Below 20 K, the thermal conductivity decreases following approximately a *T* law dependence. At room temperature, the thermal conductivity of the sample measured in the perpendicular direction is about 1.2 - 1.6 W/mK. Another clear evidence of the layered structure of the reference sample $x = 0.4$ is provided by a comparison between the thermal conductivity measured in both directions. The anisotropy ratio $\kappa_{perp}/\kappa_{par}$ is around 1.3 at 300 K and is maximum near the peak ($\kappa_{perp}/\kappa_{par}$= 1.5). Hence, the anisotropy ratio is opposite to that of the electrical resistivity, as in single crystals. No evidence of an anisotropy in the MS sample with $x = 0.48$ seems to emerge from these data (Fig. V-6b). This result is consistent with the conclusions drawn from the electrical resistivity data and in agreement with the conclusions of Xie et al. /XIE11/, who reported, for the same composition ($x = 0.48$), an anisotropy of 2-3% with a SPS pressure of 30 MPa.

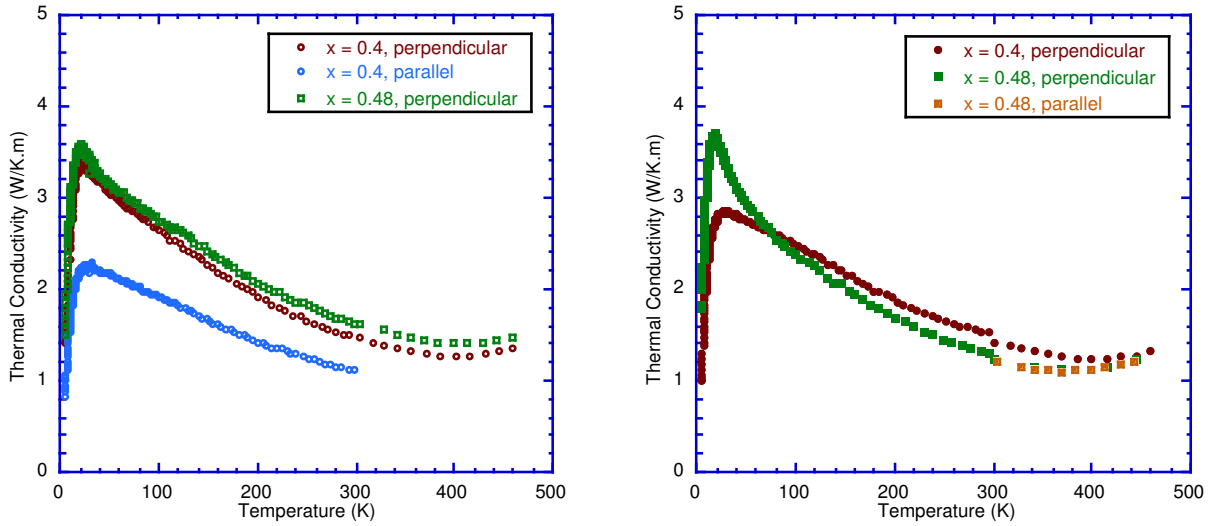

(a) (b)

Figure V-6: Temperature dependence of the total thermal conductivity for (a) reference and (b) MS $Sb_{2-x}Bi_xTe_3$ samples with $x = 0.4$ and 0.48. Partial results for the thermal conductivity along the pressing direction (parallel) are also included.

As discussed in the first chapter, the thermal conductivity is in general the sum of two components:

$$\kappa = \kappa_e + \kappa_L \tag{V-4}$$

where κ_e and κ_L are the electronic and lattice thermal conductivity contributions, respectively. In the extrinsic regime, κ_L is determined using the Wiedemann-Franz law:

$$\kappa_L = LT/\rho \tag{V-5}$$

where L is the Lorenz number and T is the absolute temperature. L depends on the scattering parameters and on the chemical potential as we shall see below. From these results, κ_L appears similar for the two reference samples $x = 0.4$ and 0.48, since the scattering mechanisms and the hole densities are similar. We should invoke a lower lattice thermal conductivity in the sample with a lower Bi content ($x = 0.4$) than in the sample with $x = 0.48$ to be consistent with our experimental values. This remark is in agreement with the observations of Caillat et al. /CAI93/, obtained on single crystals of similar compositions. They related it to the maximum antisite defects (Bi_{Te}) calculated for a composition close to $x = 0.4$ /STA88/.

The total thermal conductivity of the MS samples doesn't show any clear trend compared to the reference sample. To get deeper insights, it is essential to calculate the Lorenz number to

separate the electronic from the lattice contribution. This will be done in section IV.

The enhancement of κ noticed above 350-400 K, depending on the sample, is due to an additional contribution to the thermal conduction attributed to the presence of minority carriers resulting in electron-hole pairs (the so-called bipolar contribution). Actually, in presence of holes and electrons, the electronic thermal conductivity can be expressed as /GOL64/:

$$\kappa_E = \kappa_h + \kappa_{el} + \kappa_{h-el} \qquad \text{(V-6)}$$

where κ_h and κ_{el} are the contributions due to holes and electrons, respectively, and κ_{h-el} is the component due to the electron-hole pairs. We can note that the temperature at which mixed conduction occurs matches well the temperature at which the thermopower starts decreasing.

Based on our previous results, the temperature dependence of the resulting dimensionless figure of merit is plotted for all samples in Fig. V-7. The *ZT*(*T*) curves, with their bell-shape peak near room temperature, are typical of these p-type ternary compounds. For the reference samples, the maximum *ZT* is around 0.9 near *T* = 400 K for the two samples investigated (*x* = 0.4 and 0.48). We also observe that the anisotropy detected in both the electrical and thermal properties cancels out in the temperature range 5 – 300 K for *x* = 0.4. One of the MS sample (*x* = 0.4) shows similar thermoelectric performance to that of the reference while for *x* = 0.48, an improvement is observed with a peak *ZT* of 1.1 at 350 K. This can be attributed to a decrease in the hole

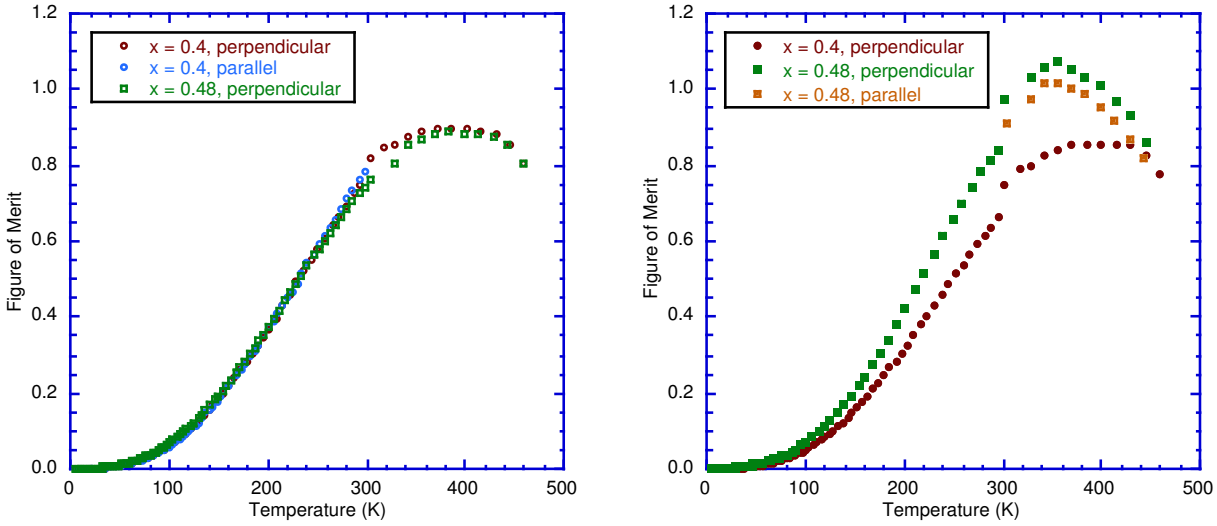

(a) (b)

Figure V-7: Temperature dependence of *ZT* for (a) reference and (b) MS $Sb_{2-x}Bi_xTe_3$ samples with *x* = 0.4 and 0.48. Partial results obtained along the pressing direction (parallel) are also included.

concentration. This last point is essential since it shifts the peak *ZT* to lower temperatures and closer to useful temperatures for our targeted application.

However, even if the thermoelectric performances are higher in one composition, our results contrast with the results of Xie et al. /XIE09a, XIE11/ and Tang et al. /TAN07/, who reported values higher than 1.4 at 300 K. The reasons for such discrepancies are not understood yet. Nevertheless, several studies have recently reported experimental results in this family of materials prepared by the melt spinning method that are in good agreement with our results /BOE08, EBL07a, EBL07b, IVA13/.

I-3) Reproducibility of the processed materials

Since in the past many methods used to prepare the *p*-$Sb_{2-x}Bi_xTe_3$ ternary compounds led to thermoelectric properties that were not reproducible, it was important to determine whether or not the two synthesis routes we proposed are pertinent. In this context, we probed the transport properties of two polycrystalline reference samples (x = 0.48) coming from two different syntheses. Moreover, from one of this ingot, two MS samples were prepared and characterized. The transport and galvanomagnetic data are gathered in Fig. V-8.

These results taken as a whole demonstrate that the techniques used to fabricate our materials shows a good reproducibility. The deviations observed are below few percents in each case. Thus, it makes sense to continue to explore the potential of the melt-spinning approach with the aim to further optimize the thermoelectric properties.

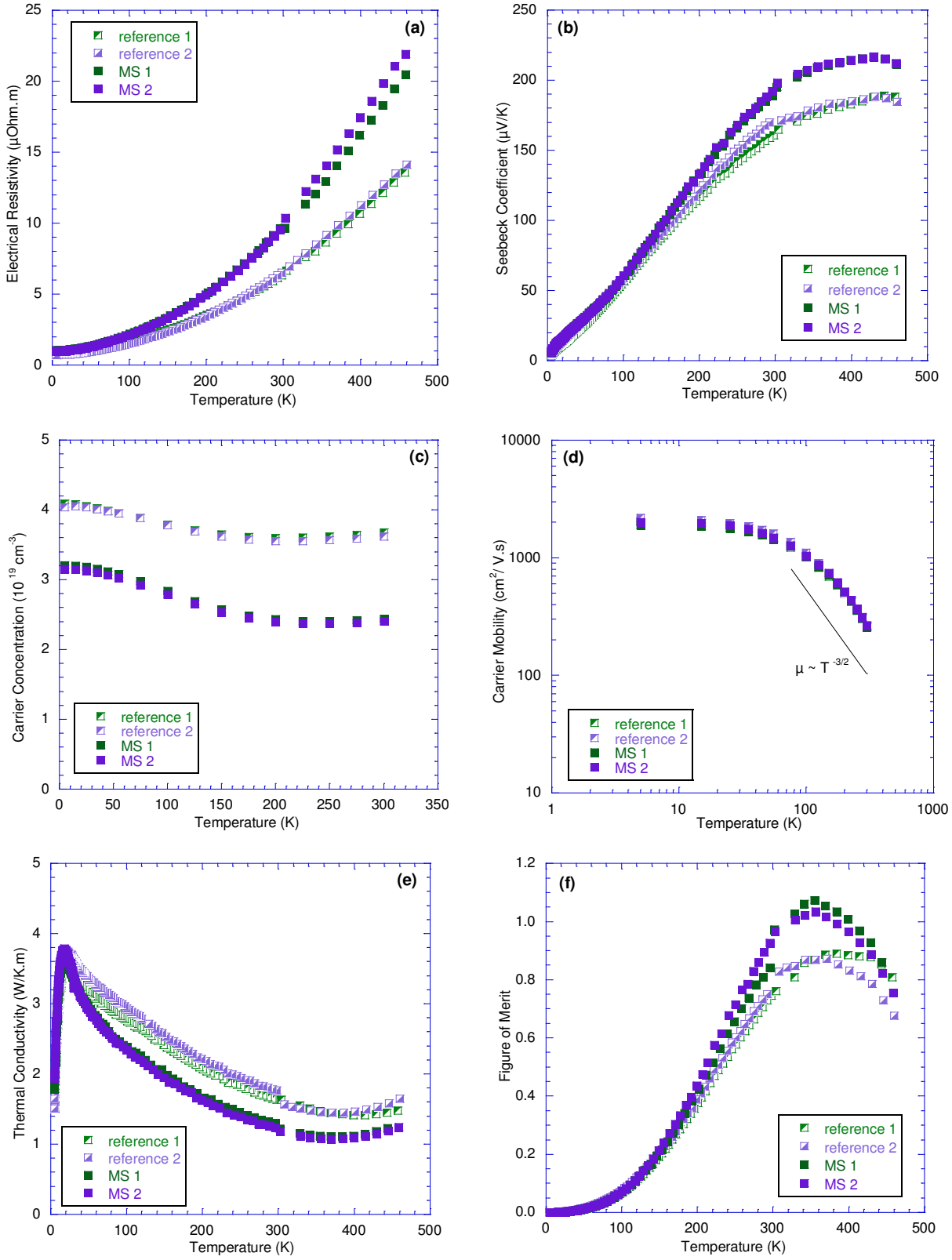

Figure V-8: Temperature dependence of (a) electrical resistivity, (b) thermopower, (c) hole concentration, (d) Hall mobility, (e) total thermal conductivity and (f) *ZT* of two reference and MS $Sb_{1.52}Bi_{0.48}Te_3$ samples. Measurements were performed along the direction perpendicular to the pressing direction.

II) TRANSPORT PROPERTIES OF $Sb_{2-x}Bi_xTe_{3.1}$ SERIES

II-1) Introduction

In the first part, we showed that a combination of melt-spinning and spark plasma sintering leads to enhanced *ZT* values in p-$(Sb_{2-x}Bi_x)Te_3$. The reduction in the total thermal conductivity coupled to a reduction in the hole concentration is believed to be responsible for this increase. Even if *p* can be decreased by increasing the Bi content, adding an excess of Te may have a similar influence. The idea is that less antisite defects could be formed if an excess of Te is added to the initial composition according to the ternary phase diagram. In addition, the excess of Te could compensate a possible evaporation of Te occurring during the melt spinning process, as the ampoule is not sealed (see chapter III). Looking at the phase diagram, if the Te content is outside the domain of homogeneity of the ternary compounds, a ternary solution in equilibrium with Te-rich phase precipitates can be expected. The presence of such precipitates might decrease further the lattice thermal conductivity. According to Abrikosov et al. /ABR77/, the domain of homogeneity of "$Bi_{0.5}Sb_{1.5}Te_3$" is estimated to be $Te_{2.99}$ on the Te-rich side. By choosing $Te_{3.1}$, we should be outside the homogeneity domain.

We propose to explore in this second part the influence of Bi concentration on the transport and galvanomagnetic properties of $(Sb_{2-x}Bi_x)Te_{3.1}$ with x = 0.4; 0.45; 0.48; 0.5 and 0.52. The measurements were performed mainly along the direction perpendicular to the pressing direction between 5 – 460 K on reference and MS samples. In addition, the anisotropy has been probed on some samples (MS with x = 0.4 and 0.5). As in the previous section, we also comment on the reproducibility of our preparation process on these Te-rich ternary compounds with x = 0.4, both on reference and MS samples.

II-2) Thermoelectric and galvanomagnetic properties of $Sb_{2-x}Bi_xTe_{3.1}$

Fig. V-9 shows the temperature dependence of the electrical resistivity ρ for all specimens. In reference samples, $\rho(T)$ follows the same behavior as their counterparts without an excess of Te. With respect to these samples, the excess of Te seems to increase the electrical resistivity. What is more surprising however is the influence of Bi. While increasing the Bi content was expected to result in a smooth increase in ρ, our results do not reveal any clear trend. The ρ values of the MS samples exhibit a significant increase compared to the reference samples

suggesting that the hole concentration is reduced. Another distinct feature concerns the behavior of ρ above 300 K for x = 0.45 and 0.52 where the ρ values tend to saturate indicating the onset of the intrinsic regime.

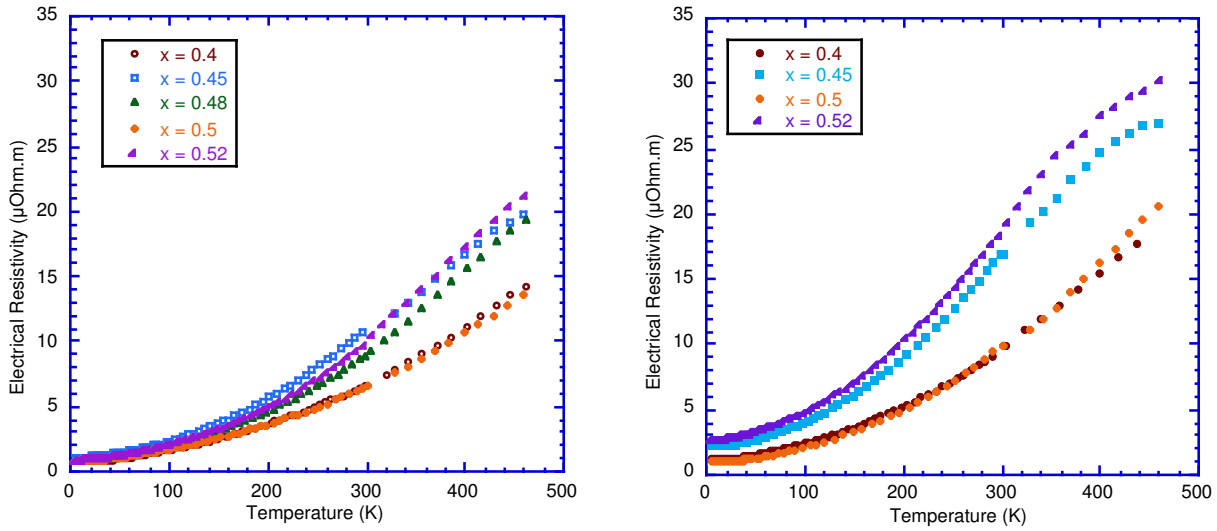

(a) (b)

Figure V-9: Temperature dependence of the electrical resistivity for (a) reference and (b) MS $Sb_{2-x}Bi_xTe_{3.1}$ samples with x = 0.4; 0.45; 0.48; 0.5 and 0.52.

From the positive Hall coefficients, we calculated the hole concentration using the relation (V-1). The data are reported in Fig. V-10. As anticipated, the hole concentration of the reference samples vary erratically with Bi content. At room temperature, p covers the range 2 – 4.2x10^{19} cm^{-3} which is less than in the first series. We can also note that all the MS samples have lower carrier concentrations than their reference counterparts suggesting that the melt-spinning technique generates new defects that provide electrons or reduces (by an as-yet unknown mechanism) the native defects.

The reasons why the hole concentration of the reference samples do not decrease monotonically with increasing the Bi content is not yet fully understood. Yet, because defects might be at the origin of this trend, it is interesting to discuss what might be the consequences of their presence. We have seen in Fig. II-9 that near the melting point, a compound has not a unique carrier concentration but can have a broad range of carrier concentrations due to deviations from stoichiometry (for Sb_2Te_3 the range is in the range 1 - 4 x10^{20} cm^{-3}). Due to this peculiarity, two compounds with close but nonetheless different Bi contents can share common

carrier concentrations. Within this scenario, there is no apparent reason to observe a continuous decrease in the carrier concentration with increasing the Bi content without a strict control of deviations from stoichiometry. In fact, the theories on the defects in the $A_2^{V}B_3^{VI}$ mixed crystals do not take into account the deviations from stoichiometry for one compound /HOR88, NAV96, STA88/.

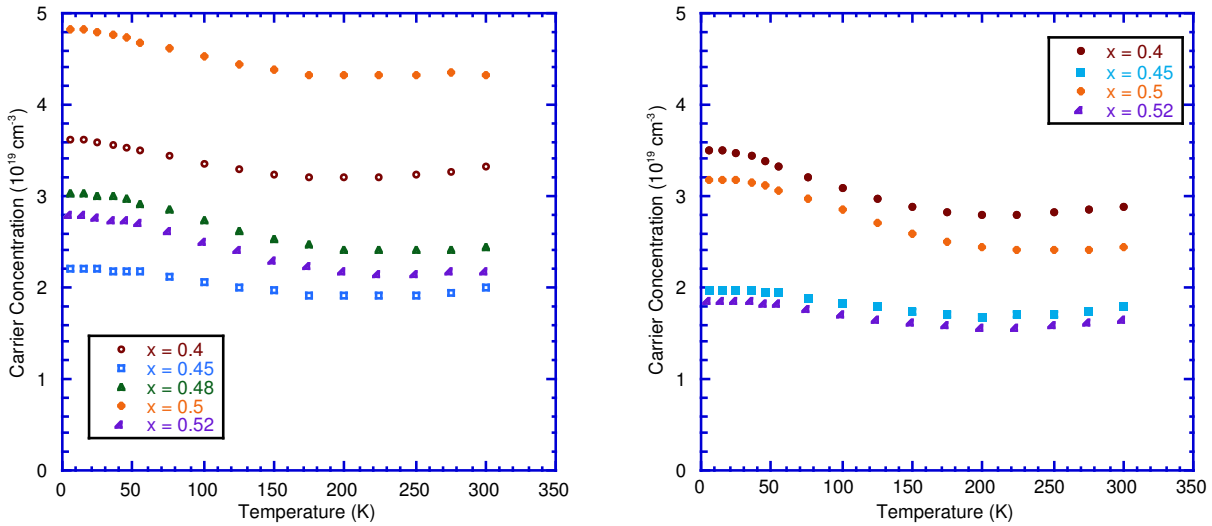

Figure V-10: Temperature dependence of the hole concentration for (a) reference and (b) MS $Sb_{2-x}Bi_xTe_{3.1}$ samples with x = 0.4; 0.45; 0.48; 0.5 and 0.52.

The temperature dependence of the Hall mobility is plotted in Fig. V-11 within the temperature range 5 – 300 K. At low temperatures, the Hall mobility values of these samples containing an excess of Te are always high. The variations with temperature of μ_H follow the same trend indicating that scattering by neutral impurities below 15 K is the dominant mechanism while near 300 K acoustic phonons scattering dominates. Of note, the values of the Hall mobility of the MS samples are slightly lower than those of the reference samples.

The thermopower of the $Sb_{2-x}Bi_xTe_{3.1}$ series is plotted as a function of temperature in Fig. V-12. All the samples show typical trends of degenerate semiconductors and exhibit similar variations as described previously. The values of the carrier concentration faithfully reflect the thermopower data. The influence of the minority carriers is clearly visible on the samples with the lowest carrier concentration.

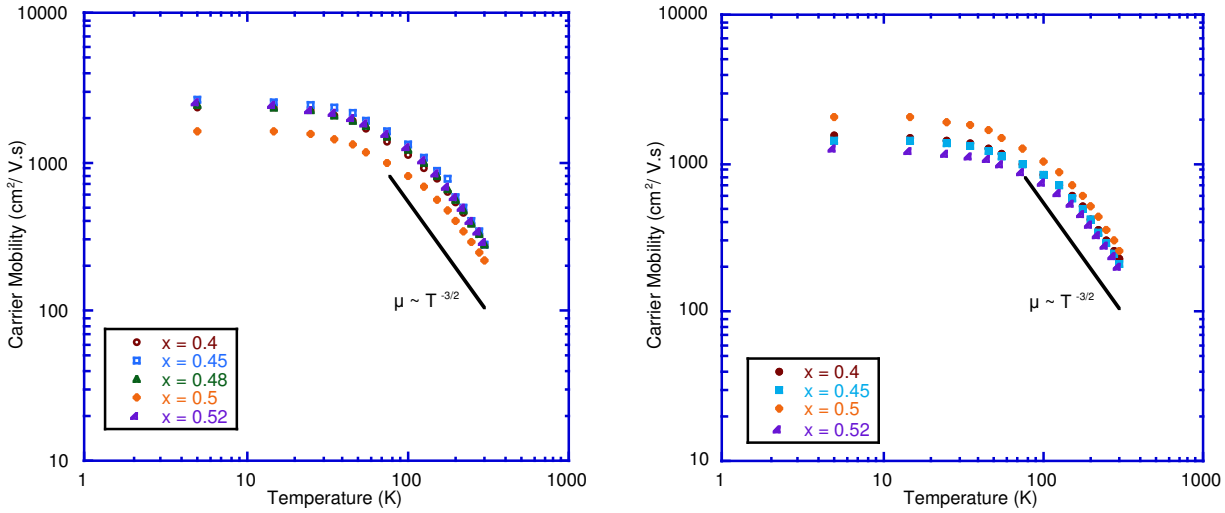

(a) (b)

Figure V-11: Temperature dependence of the Hall mobility for (a) reference and (b) MS $Sb_{2-x}Bi_xTe_{3.1}$ samples with x = 0.4; 0.45; 0.48; 0.5 and 0.52.

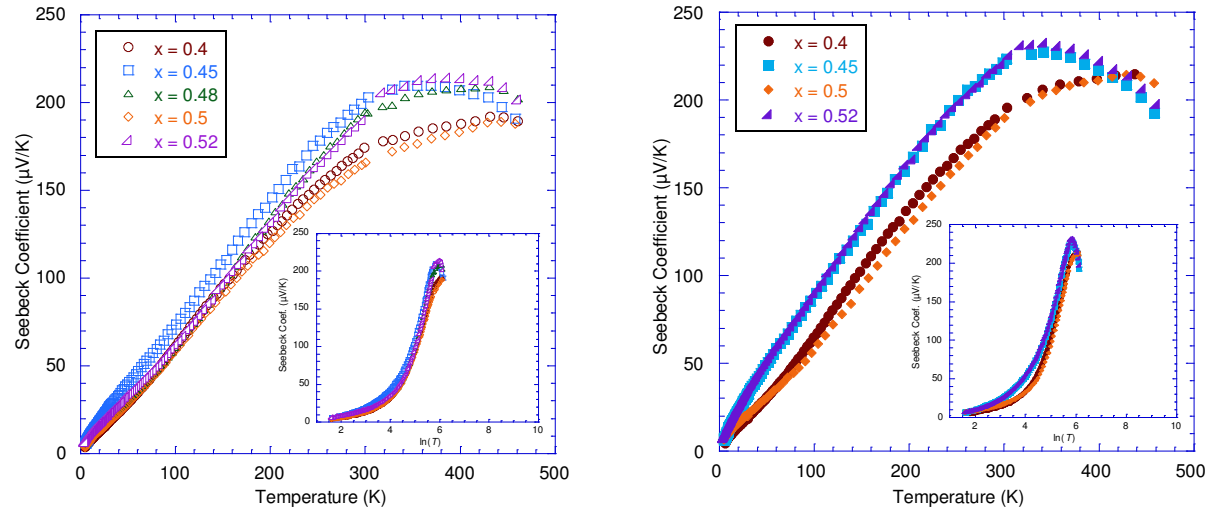

(a) (b)

Figure V-12: Temperature dependence of the thermopower for (a) reference and (b) MS $Sb_{2-x}Bi_xTe_{3.1}$ samples with x = 0.4; 0.45; 0.48; 0.5 and 0.52. The insets show S vs. ln(T) showing two trends: 1) a constant slope $\partial S/\partial T$ below 20 K and 2) a constant slope $\partial S/\partial \ln(T)$ ~ 110-140 μV/ln(K) from 200 – 300 K.

Figure V-13 shows the total thermal conductivity of the reference and MS samples with an excess of Te. As can be observed, there are no new physical phenomena compared to what was already mentioned previously. We confirm that the total thermal conductivity is reduced in the MS samples except for the sample with x = 0.5 at low temperatures. Moreover, the mixed

conduction is all the more pronounced that the carrier concentration is low. To go further, it is necessary to separate the two contributions, electronic and lattice, to the total thermal conductivity. We shall see that the lattice thermal conductivity of the MS samples is reduced.

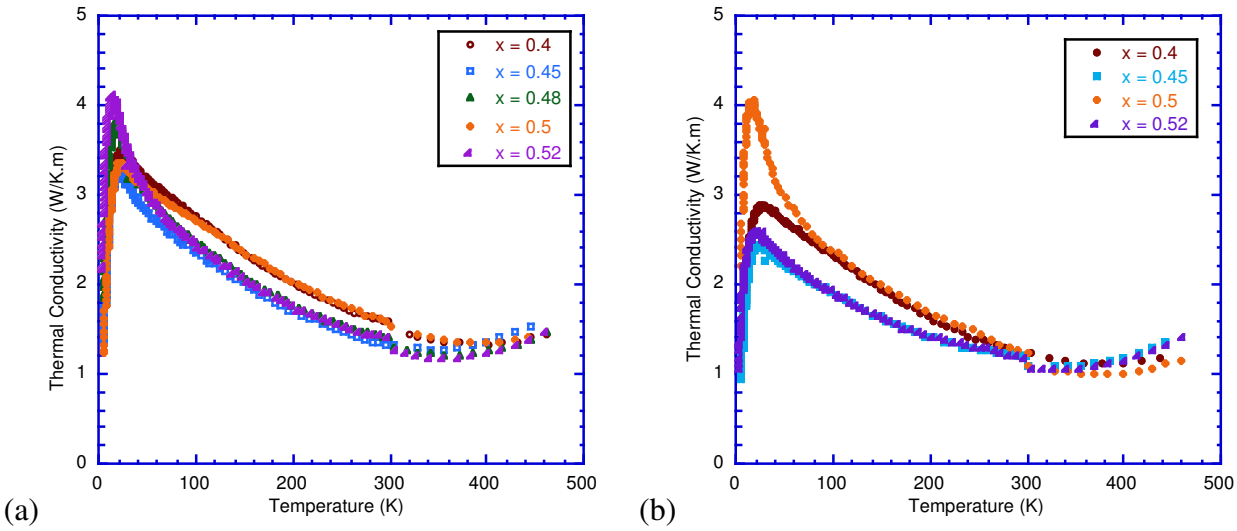

Figure V-13: Temperature dependence of the Hall mobility for (a) reference and (b) MS $Sb_{2-x}Bi_xTe_{3.1}$ samples with x = 0.4; 0.45; 0.48; 0.5 and 0.52.

The temperature dependence of *ZT* is displayed in Figure V-14. An excess of Te seems to be beneficial since the *ZT* values are enhanced by 12% (*ZT* ~1) in the reference sample x = 0.4 and x = 0.48 compared to the previous study. Higher values are obtained in the MS samples with x = 0.4 and x = 0.5 which feature a peak *ZT* of about 1.1 and 1.2 at $T \approx 350$ K. These two samples have an apparent hole concentration of 2.8×10^{19} cm^{-3} and 2.4×10^{19} cm^{-3}, respectively. Lower carrier densities, as in the x = 0.45 and x = 0.52 samples, are *a priori* detrimental to reaching high thermoelectric performance near room temperature.

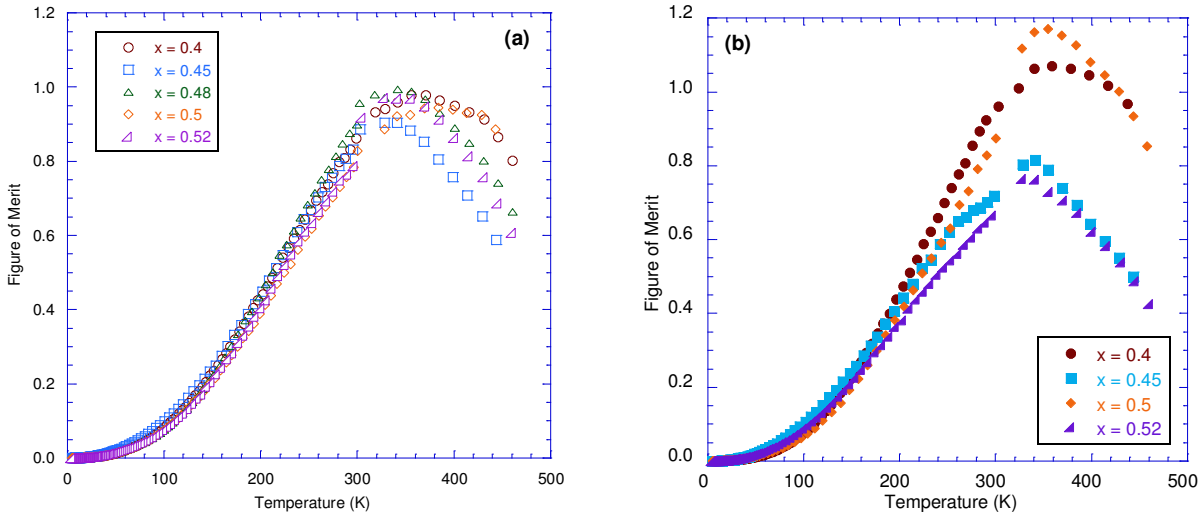

Figure V-14: Temperature dependence of *ZT* for (a) reference and (b) MS $Sb_{2-x}Bi_xTe_{3.1}$ samples with x = 0.4; 0.45; 0.48; 0.5 and 0.52.

II-3) Anisotropy

We have shown in the last section that the anisotropy probed in one MS sample (x = 0.48) was not pronounced. It is interesting to determine whether it is a common feature shared by all MS samples as suggested by some reports /XIE11/ or whether it depends on a complex way on the hole density as observed in single crystals (see chapter II). In this context, this new series of samples containing an excess of Te offers the opportunity to extend our preliminary investigations. Two MS samples (x = 0.4 and x = 0.5) were selected and transport and galvanomagnetic measurements were performed in the two directions, parallel and perpendicular to the pressing direction. The results are displayed in Fig.V-15.

As evidenced by these measurements, the electrical resistivity in both samples is anisotropic. The ρ data in the parallel direction are systematically higher than in the perpendicular direction. The anisotropy ratio, ρ_{par}/ρ_{perp}, lies in the range 1.1-1.2 between 5 and 300 K. There is no apparent deviation between the measurements carried out in the two directions concerning the thermopower suggesting that this coefficient is isotropic. The two Hall coefficients differ only by 5% which is of the same order of magnitude that the measurement uncertainty. For this reason, it is difficult to draw a final conclusion. Nevertheless, we should note that in single crystals, R_{231} always exceeds R_{123} /STO88/.

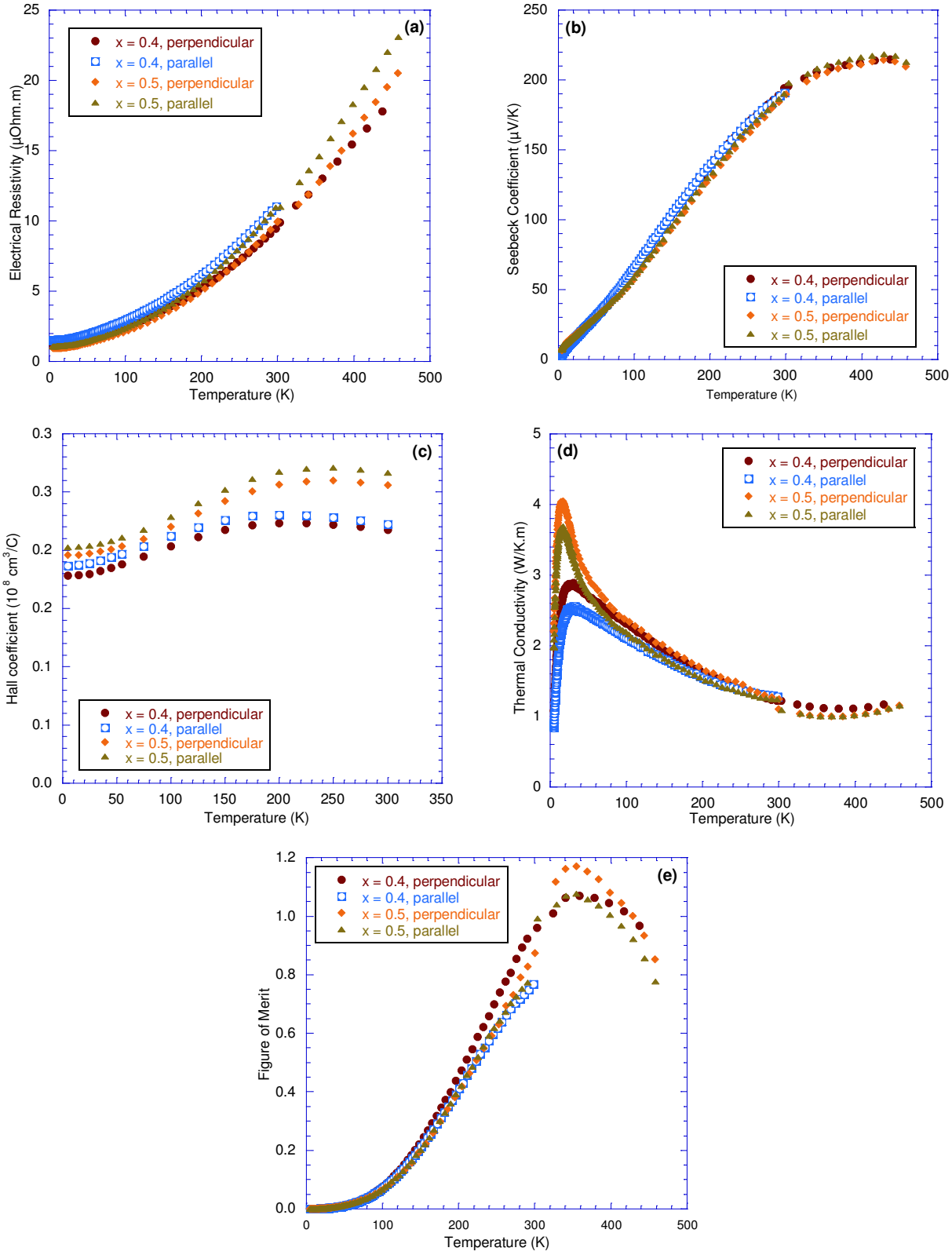

Figure V-15: Temperature dependence of (a) electrical resistivity, (b) thermopower, (c) Hall coefficient, (d) total thermal conductivity and (e) *ZT* of two MS samples: $x = 0.4$ and $x = 0.5$. Measurements were performed along and perpendicular to the pressing direction.

Since $R_{H\text{-}par}$ can be roughly identified to R_{231} and $R_{H\text{-}per}$ to R_{123}, our results suggest a probable (small) anisotropy in the Hall coefficient. If we turn now to the thermal conductivity, we can see that this property is anisotropic below 200 K with, as a rule in these materials, $\kappa_{perp}/\kappa_{par} < 1$. Above 200 K, no strong difference exists between the two directions for both samples. As a consequence of these observations, the dimensionless figure of merit *ZT* is found to be higher in the perpendicular direction above 200 K as illustrated in Fig. V-15e.

II-4) Reproducibility of the processed materials

Similarly to the previous study, we also investigated the reproducibility of our fabrication method in this new series of sample. We measured the transport and galvanomagnetic properties of two polycrystalline reference samples of chemical formula $Sb_{1.6}Bi_{0.4}Te_{3.1}$ coming from two different initial ingots. Moreover, from one of this ingot, two MS samples were prepared and characterized. Electrical, thermal and galvanomagnetic data are presented in Fig. V-16.

Again, the synthesis route we used seems to be reproducible. A very good agreement is observed between the two sets of data for both the reference and the MS samples. The deviation between the measurements never exceeds 5% which is remarkable.

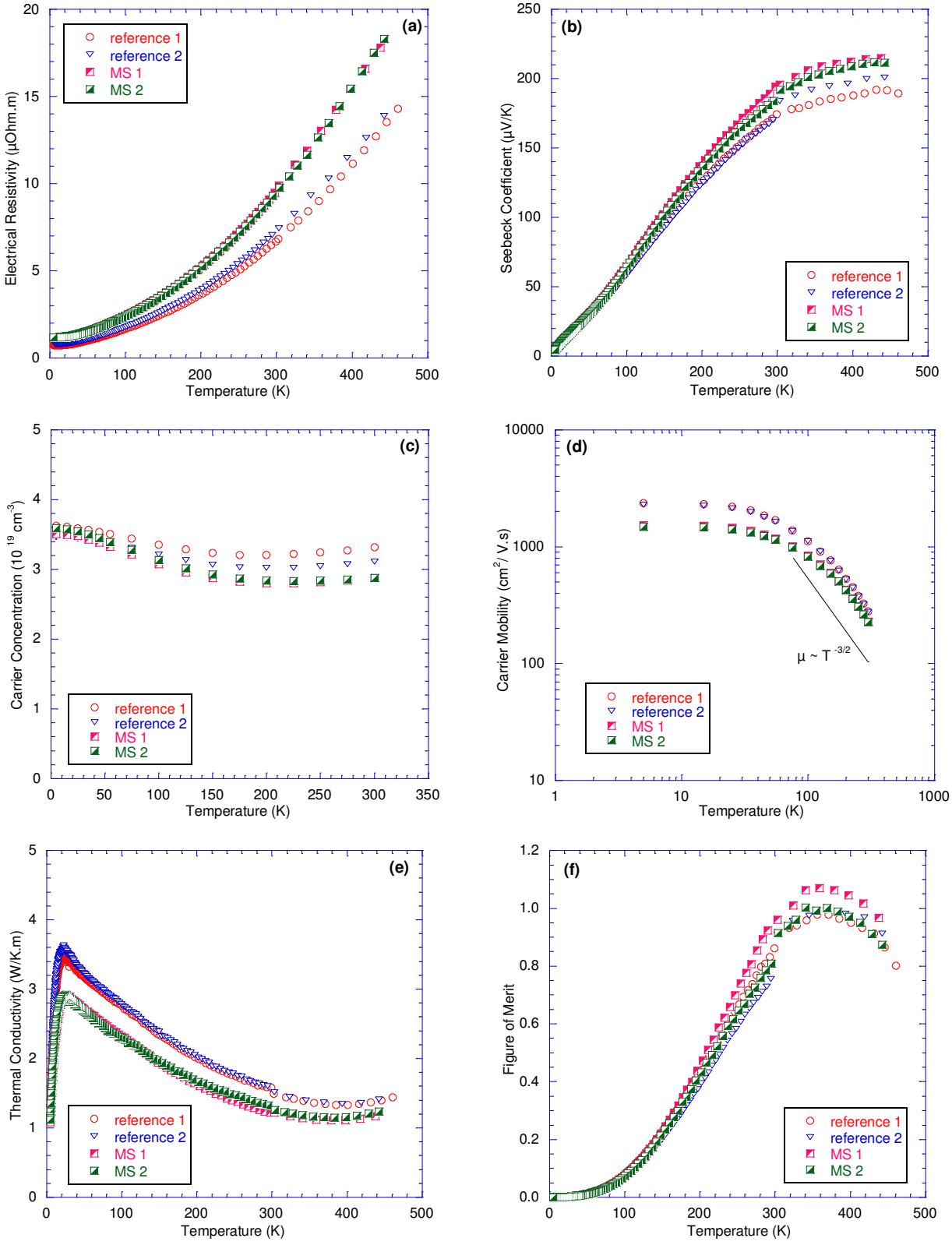

Figure V-16: Temperature dependence of (a) electrical resistivity, (b) thermopower, (c) hole concentration, (d) Hall mobility, (e) total thermal conductivity and (f) *ZT* of two reference and MS $Sb_{1.52}Bi_{0.4}Te_{3.1}$ samples. Measurements were performed along and perpendicular to the pressing direction.

III) INFLUENCE OF SOME PROCESSING PREPARATION ON THE TRANSPORT PROPERTIES OF MS SAMPLES

III-1) Introduction

To complement our investigations, we also tried to investigate the effect of different processing parameters on the thermoelectric properties of our MS samples. Four directions were explored. The first direction concerns the so-called double SPS or Spark Plasma Texturing (SPT). The idea is to deform further a layered material to enhance the anisotropic character of the transport by using a two-step process with SPS. The concept of SPT was proposed first by Kenfaui et al. /KEN12/ in the cobaltite $Ca_3Co_4O_9$ and was then extended to other layered materials including Bi_2Te_3 based compounds /BHA13, LOG14, YAN10b/ with some success in the n-type materials. We applied this technique on the composition $Sb_{1.5}Bi_{0.5}Te_{3.1}$.

The second axis concerns the influence of a post annealing treatment on the thermoelectric properties of the MS samples. Numerous reports /IVA13, KIM13, LEE14, LI08c, ZHA10/ in the literature demonstrated that the temperature and the duration of the annealing step have a strong influence on the electrical and thermal properties of p-$Sb_{2-x}Bi_xTe_3$ polycrystalline samples. The relaxation of defects, interaction of native defects with other defects, grain growth or recombination of Te have been invoked to explain the changes observed. The influence of an annealing process has been investigated on two MS samples: $Sb_{1.52}Bi_{0.48}Te_3$ and $Sb_{1.5}Bi_{0.5}Te_{3.1}$. For the annealing conditions, we selected a temperature of 600 K and a duration of 24 hours according to the work of /IVA13/. Actually, these conditions improved the thermoelectric properties with respect to their polycrystalline materials.

The third direction we explored was related to cold pressing to get more information about the intrinsic electrical and thermal properties of our melt-spun ribbons. Cold-pressed samples studies were focused on $Sb_{1.52}Bi_{0.48}Te_3$ and $Sb_{1.5}Bi_{0.5}Te_{3.1}$.

Finally, we have also devoted our efforts to determine the impact of the initial orientation of the ribbons on the transport properties of MS bulk samples. Instead of grinding the ribbons, we carefully placed them in the graphite die before SPS, one by one and stacked in such a way that their free surface was placed on the top.

It is clear that each previous axis is time-consuming and requires strong efforts to be investigated in detail. Because of the limited time, the reader should consider the next parts, with

short comments, as preliminary results that call for further researches on these materials.

III-2) Double SPS

The electrical, thermal and galvanomagnetic results for the double SPS processed $Sb_{1.5}Bi_{0.5}Te_{3.1}$ sample are presented in Fig. V-17. For comparison purposes, we have also included the results for the corresponding single SPS sample.

It seems from these preliminary results, that the double SPS approach is not a fruitful way of research to pursue because the *ZT* values near 300 K are lower after the second SPS. The reduction in the electrical resistivity, if tentatively attributed to an improved texture, doesn't compensate the increase in the total thermal conductivity. As a result *ZT* is not increased contrarily to what was observed in n-type Bi_2Te_3-Bi_2Se_3 /BHA13, LOG14, YAN10b/, where the improvement was quite spectacular (40-50 % of improvement). A quantitative texture analysis is highly desirable to certify that the reduction in the electrical resistivity is linked to a higher degree of texturation. Actually, we should note that the hole density was not kept constant during the second SPS. The observed increase also contributes to reduce the electrical resistivity. Moreover, as shown recently by /LOG14/ in the parent compounds based on (Bi,Se,Te), a possible reduction in the electrical resistivity due to less grain boundaries perpendicularly to the pressing direction is also possible. The SEM investigations of the double SPS processed sample of p-type did not show the visible improvement in the architecture though (see Fig. III-27).

III-3) Influence of a post-annealing and a cold pressing

The transport properties of the ternary compounds based on Sb_2Te_3-Bi_2Te_3 are known to be extremely sensitive to the preparation methods. As an example, we should just refer to the results obtained on the reference and the MS samples presented before. To illustrate further this aspect, we propose, in this part, to investigate the influence of a post-annealing on the physical properties of two MS samples with and without an excess of Te: $Sb_{1.5}Bi_{0.5}Te_{3.1}$ and $Sb_{1.52}Bi_{0.48}Te_3$. Figures V-18 and V-19 show their different transport properties as a function of temperature. We also include in these graphs the data for cold-pressed ribbons of the same composition.

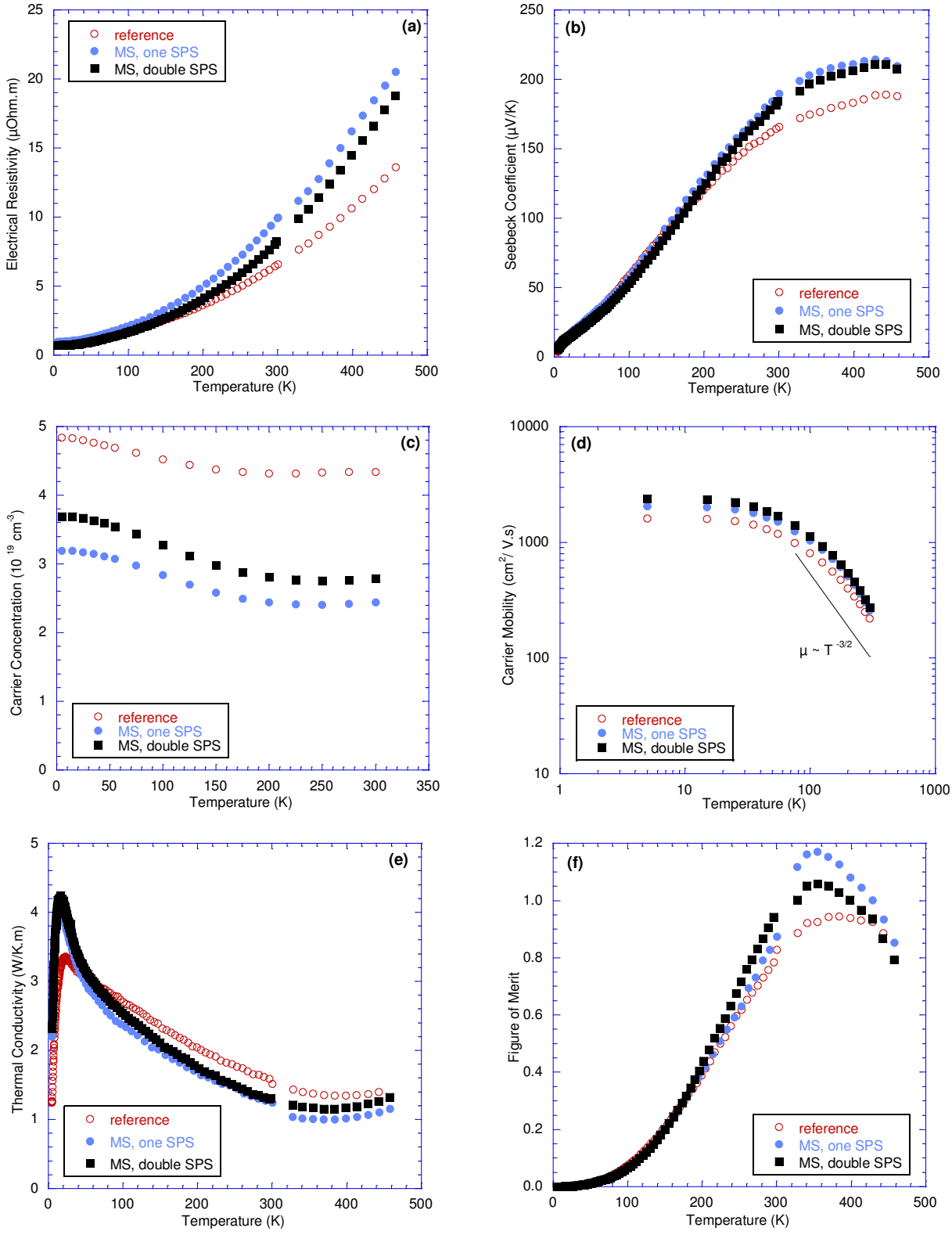

Figure V-17: Temperature dependence of (a) electrical resistivity, (b) thermopower, (c) hole concentration, (d) Hall mobility, (e) total thermal conductivity and (f) *ZT* of reference and MS $Sb_{1.5}Bi_{0.5}Te_{3.1}$ samples pressed one or two times. Measurements were performed along the direction perpendicular to the pressing direction.

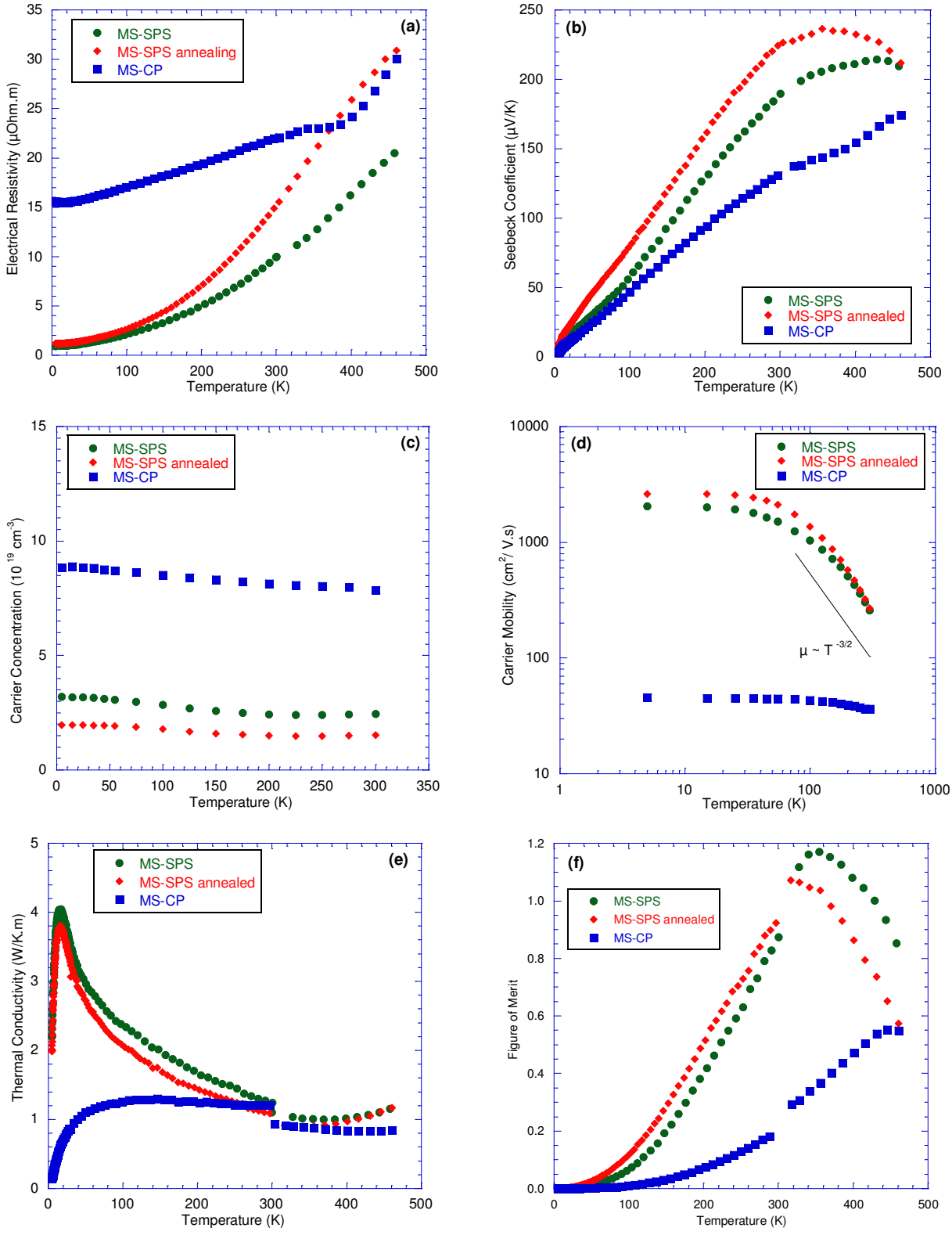

Figure V-18: Temperature dependence of (a) electrical resistivity, (b) thermopower, (c) hole concentration, (d) Hall mobility, (e) total thermal conductivity and (f) *ZT* of MS $Sb_{1.5}Bi_{0.5}Te_{3.1}$ samples annealed or cold pressed. The data for the MS sample is also included. Measurements were performed along the direction perpendicular to the pressing direction.

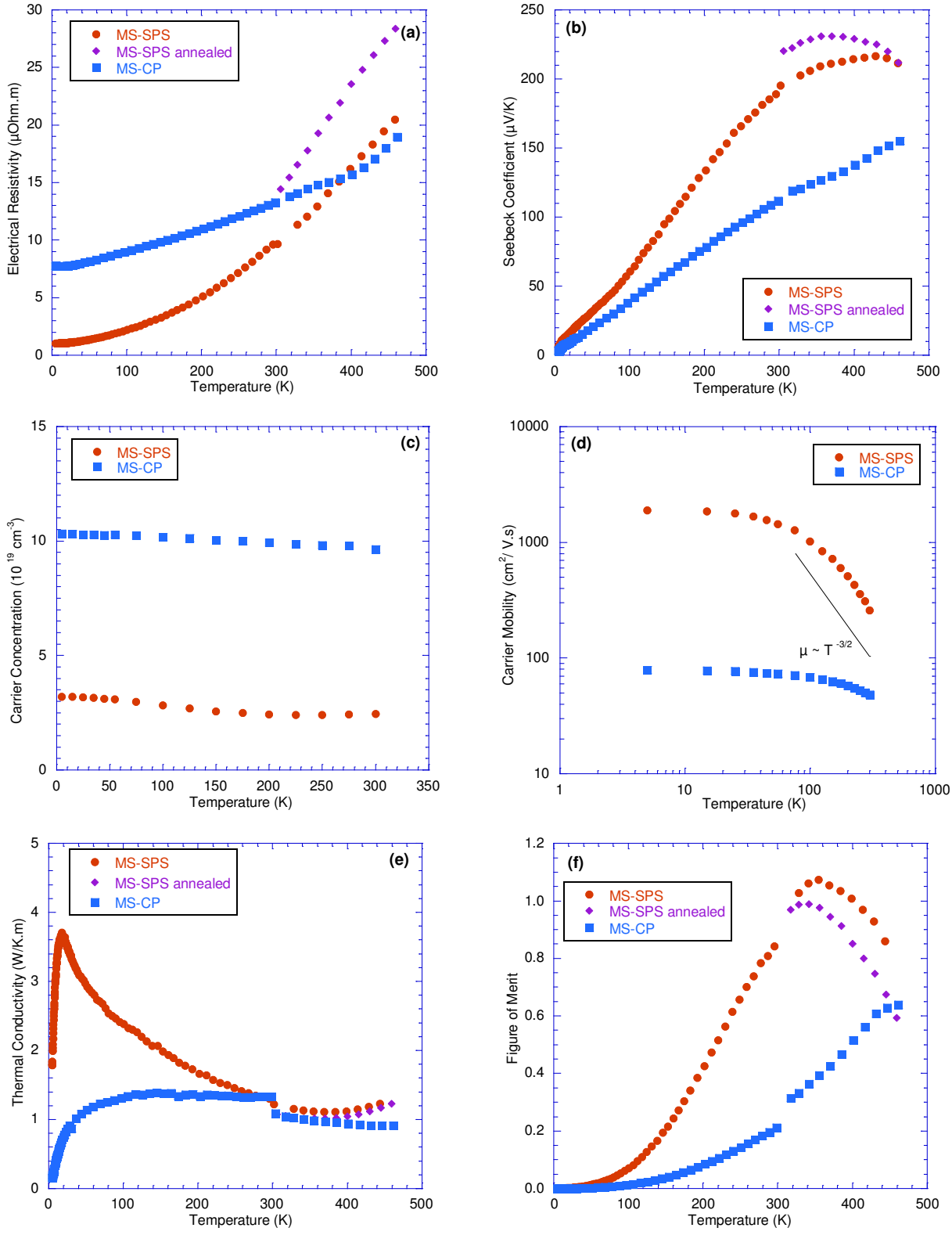

Figure V-19: Temperature dependence of (a) electrical resistivity, (b) thermopower, (c) hole concentration, (d) Hall mobility, (e) total thermal conductivity and (f) *ZT* of MS $Sb_{1.52}Bi_{0.48}Te_3$ samples annealed or cold pressed. The data for the MS sample is also included. Measurements were performed along the direction perpendicular to the pressing direction.

The transport properties of the two cold-pressed samples present drastic differences compared to those of the MS-SPS samples (Fig. V-18 and V-19): a higher electrical resistivity at low temperatures, a higher hole concentration, the absence of a peak in the thermal conductivity, an anomalous temperature dependence of the electrical resistivity and a change in the dominant hole scattering mechanism near 300 K. All these features make these samples unique. However, one key question that remains open is to which extent these properties are intrinsic to the melt-spun ribbons or arise owing to the strong plastic deformation undergone during the uniaxial pressing. It is known that heavy deformations can change drastically the carrier concentration in Bi_2Te_3 /SCH62/. The plastic deformation produces in this material non-basal slips and introduces large concentration of point defects. The predominant electrically active point defects appears to be Te vacancies (V_{Te}) that were found to drive the material from p-type to n-type (we must remember that V_{Te} gives 2 electrons). This scenario should be discarded since our samples have neither an n-type behavior nor a low hole concentration. More relevant are the works performed by /EBL07b/ on melt-spun ribbons of composition ($Sb_{1.6}Bi_{0.4}Te_3$) and with synthesis parameters close to ours. Measurements of the thermopower on isolated ribbons at 300 K lead to a value close to 140 μV/K similar to that of the cold-pressed samples (134 μV/K for $Sb_{1.5}Bi_{0.5}Te_{3.1}$ and 112 μV/K for $Sb_{1.52}Bi_{0.48}Te_3$). This similarity suggests that the measured properties could be intrinsic to the ribbons. To conclude definitively on this point, measurements on isolated ribbons should be performed.

As clearly seen in Fig. V-18, a post annealing treatment modifies the thermoelectric properties of the samples. The main effects are a reduction in the hole density and an increase in the Hall mobility. As a consequence of a lowering of *p*, the *ZT* curve is shifted towards lower temperatures. Thus, this annealing represents another control parameter to tune the hole density. Even if the peak *ZT* is decreased, the average *ZT* on the temperature range of interest for our application is higher at least for $Sb_{1.5}Bi_{0.5}Te_{3.1}$.

In the literature, increased electrical resistivity after annealing was reported for $Sb_{1.5}Bi_{0.5}Te_3$ polycrystals but unfortunately the other transport properties were not measured /MAN02/. The reasons of the hole density decrease during the annealing are not yet fully elucidated. Abrikosov et al. /ABR77/ attributed the change in electrical properties to Te precipitates formed during fast cooling. In such a non-equilibrium process, Te shows retrograde solid solubility and thus precipitates out of the main phase. Further annealing results in an

increase in the solubility of Te which is then incorporated into the solid solution thereby contributing to reduce the deviations from stoichiometry. As a result, the hole density decreases. Since this explanation is plausible, we focused our efforts to examine if Te precipitates or Te-rich phases are present in our ribbons or bulk samples. Although we have found some traces of Te precipitates, we are not fully convinced that they are at the origin of electrical changes. The decrease in the hole concentration could be also caused by grain interfaces trapping the charge carriers at elevated temperatures. Further investigations are required to confirm these hypothesis.

III-4) Alignment of ribbons: influence on the thermoelectric properties

The influence of alignment of ribbons in the graphite die before SPS on the thermal and galvanomagnetic properties of $Sb_{1.5}Bi_{0.5}Te_{3.1}$ sample is presented in Fig. V-20.

It can be seen that the alignment of the ribbons has a (small) positive effect on the thermoelectric performance. The decrease in the total thermal conductivity seems to be more efficient that the increase in the electrical resistivity. At first sight, we could invoke a better texturation in the aligned MS sample than in the grinded MS samples but a quantitative texture analysis is necessary before concluding on this point. We further note that no significant changes in the hole concentration are observed between the two modes of preparation suggesting that the deformation during the grinding step has no impact on the hole density.

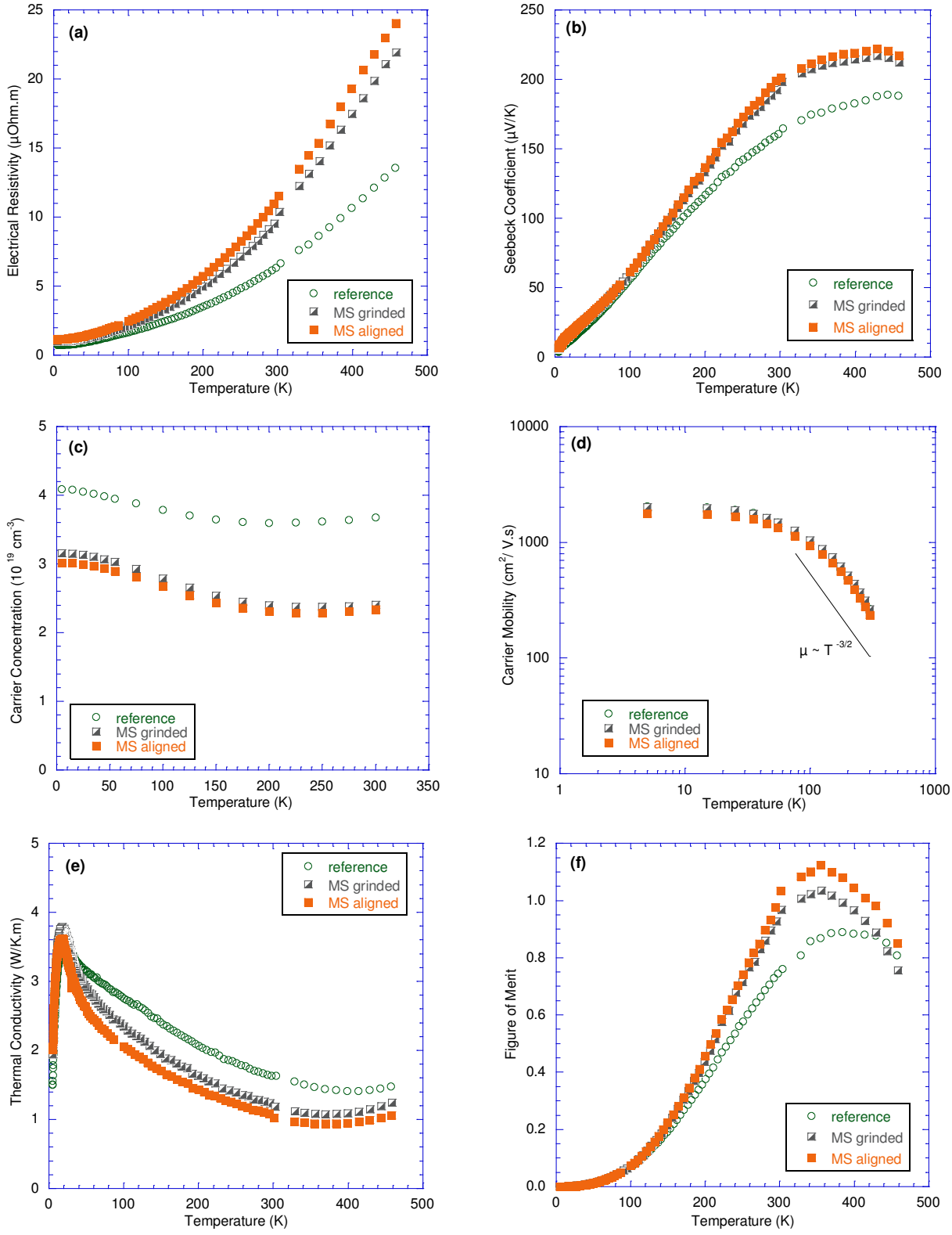

Figure V-20: Temperature dependence of (a) electrical resistivity, (b) thermopower, (c) hole concentration, (d) Hall mobility, (e) total thermal conductivity and (f) *ZT* of MS $Sb_{1.52}Bi_{0.48}Te_3$ samples grinded or aligned. The data for the reference sample is also included for comparison. Measurements were performed along the direction perpendicular to the pressing direction.

IV) INTERPRETATION OF THE $Sb_{2-x}Bi_xTe_3$ MEASUREMENTS

IV-1) Introduction

The semi-classical model based on the transport Boltzmann equation (cf. Annexe 2) is generally used to interpret the electrical transport coefficients (S, ρ, κ_E) of small-band-gap semiconductors. In p-$Sb_{2-x}Bi_xTe_3$ compounds, this approach should also be fruitful but several complications appear. First, the valence band structure is not well known. Two valence bands (upper valence – UVB – and lower valence band – LVB – as discussed in chapter II) play *a priori* a role but their related parameters are not well established yet. Also we speculate that the relative position of the two bands (LVB and UVB) is strongly temperature dependent, as already seen in several other small-band-gap semiconductors /LEN0/, and that the LVB probably shifts towards lower energies with respect to the top of the UVB with increasing temperature. However, these important information are not known to date. Despite these difficulties, we propose to use the semi-classical model within a single-parabolic-valence-band model to interpret further our data. In particular, we will show that this simple approach allows accounting for several common features of our samples such as:

- a constant slope $\partial S/\partial T$ for T < 20 K,

- a constant slope $\partial S/\partial \ln(T)$ of ~ 110-140 µV/ln(K) for 200 K < T < 300 K,

- a close-to-zero slope in electrical resistivity for T < 20 K,

- an electrical resistivity $\rho \propto T^{1.5\pm0.2}$ for 200 K < T < 300 K,

Moreover, this simple model is also useful to estimate the electronic thermal conductivity κ_E. By subtracting this last component to the total thermal conductivity, we have access to the lattice contribution, κ_L, and conclusions about a possible reduction in the lattice thermal conductivity in MS samples can be drawn. Finally, the Debye approximation /CAL59, CAL60/ is implemented to interpret the temperature dependence of κ_L.

IV-2) S and ρ approximation for T < 20 K and for 200 K < T < 300 K

Within a single-parabolic-valence-band model with the relaxation time approximation, the

relaxation time τ can be written as:

$$\tau = aE^{\lambda}(k_BT)^{\beta} \tag{V-7}$$

where a is a constant, E the energy, k_B the Bolztmann constant, T the absolute temperature and λ (the so-called scattering parameter) and β two constants characteristic of the scattering mechanism. For example, for acoustic phonons scattering λ = -1/2, β = -1 while for ionized impurities scattering λ = 1/2, β = 0. The solution of the transport Boltzmann equation gives the following relations for the kinetic coefficients S, ρ, the Lorenz number L and the hole concentration p (see Appendix 2):

$$S = \frac{k_B}{e}\left[\frac{\lambda + \frac{5}{2}F_{\lambda+\frac{3}{2}}(\eta^*)}{\lambda + \frac{3}{2}F_{\lambda+\frac{1}{2}}(\eta^*)} - \eta^*\right] \tag{V-8}$$

$$\rho^{-1} = \sigma = \frac{8\pi a e^2}{3m^*}\left(\frac{2m^*k_BT}{h^2}\right)^{\frac{3}{2}}(k_BT)^{\lambda+\beta}\left(\frac{3}{2}+\lambda\right)F_{\lambda+\frac{1}{2}}(\eta^*) \tag{V-9}$$

$$L = \left(\frac{k_B}{e}\right)^2\left(\frac{\left(\frac{7}{2}+\lambda\right)F_{\lambda+\frac{5}{2}}(\eta^*)}{\left(\frac{3}{2}+\lambda\right)F_{\lambda+\frac{1}{2}}(\eta^*)} - \left(\frac{\left(\frac{5}{2}+\lambda\right)F_{\lambda+\frac{3}{2}}(\eta^*)}{\left(\frac{3}{2}+\lambda\right)F_{\lambda+\frac{1}{2}}(\eta^*)}\right)^2\right) \tag{V-10}$$

$$p = 4\pi\left(\frac{2m^*k_BT}{h^2}\right)^{\frac{3}{2}}F_{\frac{1}{2}}(\eta^*) \tag{V-11}$$

where η^* is the reduced Fermi level, F the Fermi integrals, e the elementary charge, h the Planck constant and m^* the effective mass.

The dependence of S and ρ at low and high temperatures can be evaluated from the properties of the Fermi integrals in both limits.

IV-2-1) Seebeck coefficient *S*

At low temperatures, the degeneracy is high ($\eta^* \gg 1$), and p can be approximated (see Appendix 2) as:

$$p \approx \frac{8}{3}\pi\left(\frac{2m^*k_BT}{h^2}\right)^{\frac{3}{2}}\eta^{*\frac{3}{2}} \quad \text{(V-12)}$$

and S as:

$$S \propto \frac{\left(\lambda+\frac{3}{2}\right)}{\eta^*}, \quad \text{(V-13)}$$

As a result, S can be rewritten as

$$S \propto \left[\left(\lambda+\tfrac{3}{2}\right)m^*p^{-2/3}\right]T \quad \text{(V-14)}$$

Similarly, at high temperatures, if we suppose that the degeneracy is low ($\eta^* \ll -1$), S and p can be approximated to be (see Appendix 2):

$$S \approx \frac{k_B}{e}(\lambda+\frac{5}{2}-\eta^*) \quad \text{(V-15)}$$

$$p \approx 2\left(\frac{2\pi m^*k_BT}{h^2}\right)^{\frac{3}{2}}e^{\eta^*} \quad \text{(V-16)}$$

As a result, S can be rewritten as:

$$S \approx \frac{k_B}{e}\left(\lambda+\frac{5}{2}+\ln\left(\frac{1}{p}\right)+\ln[\frac{2(2\pi k_B)^{\frac{3}{2}}}{h^3}\right)+\frac{3k_B}{2e}[\ln(m^*)+\ln(T)]$$

$$\approx S_0+\frac{3k_B}{2e}[\ln(m^*)+\ln(T)\,] \quad (\eta^* \ll -1), \quad \text{(V-17)}$$

where S_0 is a constant independent of T.

From Equations V-14 and V-17, we see that $S \propto T$ at low temperatures ($\eta^* \gg 1$) and $S \propto \ln(T)$ at high temperatures ($\eta^* \ll -1$). Furthermore, the only variables in S are λ and the carrier concentration p. We notice that higher p values result in a lower slope value in S vs. T in the low temperature limit, but not in the S vs. ln*(T)* slope in the high T limit. We also notice that the slope in S vs. ln*(T)* of our samples for 200 K < T < 300 K is ~ 110-140 μV/K which is close to the predicted value $\frac{3k_B}{2e} = 129$ μV/K according to Eq. (V-17) if we assume that m^* is temperature-independent (remember that p is temperature-independent in our samples between 200 – 300 K).

IV-2-2) Resistivity ρ

At low temperatures ($\eta^* \gg 1$), ρ can be approximated as to be (see Appendix 2):

$$\rho \approx \left(\frac{p}{m^*} \left[\left(\frac{3p}{8\pi} \right)^{2/3} \frac{h^2}{2m^*} \right]^{\lambda} T^{\beta} \right)^{-1} \qquad (\eta^* \gg 1). \qquad \text{(V-18)}$$

Similarly, at high temperatures ($\eta^* \ll -1$), ρ can be written as:

$$\rho \approx \frac{3m^*\sqrt{\pi}}{p\left(\lambda+\frac{3}{2}\right)\Gamma\left(\lambda+\frac{3}{2}\right)} \frac{1}{T^{\lambda+\beta}} \quad (\eta^* \ll -1) \qquad \text{(V-19)}$$

From Equations V-18 and V-19, we see that $\rho \propto T^{-\beta}$ at low temperatures ($\eta^* \gg 1$) and $\rho \propto T^{-\lambda-\beta}$ at high temperatures ($\eta^* \ll -1$). The only variables in ρ are λ, β and the carrier concentration p. We also notice that a higher p results in a lower ρ value as expected. This relationship can be readily verified using any of the ρ figures in Chapter V.

One can satisfactory use Equations V-18 and V-19 to shed light on the dominant scattering mechanism in the low-temperature and high-temperature limits, respectively. At low temperatures, we have seen that both the carrier concentration and ρ are relatively constant for T < 15 K. Thus, the low-temperature dominant scattering mechanism should have a β value of zero. Assuming that m^* is not T-dependent in this temperature range, the only possible scattering mechanisms for our samples are (a) ionized impurities scattering and (b) neutral impurity scattering. On the other hand, in the high temperature range, all samples have a functional form of ρ that is proportional to ~ $T^{3/2}$. As a result, we conclude that the dominant scattering mechanism for our samples in this temperature range is acoustic phonon scattering if the nondegenerate approximation is valid.

IV-3) Lattice thermal conductivity of $Sb_{2-x}Bi_xTe_3$ polycrystals

It is well know that in $Sb_{2-x}Bi_xTe_3$ single crystals, the lattice and electronic components of the thermal conductivity are usually comparable at 300 K making their separation a complex task /GOL64/ The challenge is even more difficult in our polycrystals due to the total thermal

conductivity found to be extremely small at low temperatures (the peak is around 3-4 W/mK). We speculate that the electronic part, κ_E should contribute even at low temperatures due to the low electrical resistivity values. It is thus fundamental to calculate the temperature dependence of the Lorenz number as accurately as possible. Another difficulty comes from the fact that L depends strongly on the scattering parameter λ (see Equation V-10) that varies with temperature. Very often, these constraints are not taken into account in the literature and the Lorenz number is taken arbitrarily either to the value of the degenerate case (L = 2.44 x10^{-8} V^2/K^2) /GOL64/ or close to L = 2.0 x10^{-8} V^2/K^2. This is obviously not satisfactory and a more careful treatment should be done.

Considering our results, we supposed that accoustic phonons scattering is the dominant scattering mechanism between 300 – 50 K while ionized impurities dominate below 50 K. Since impurity scattering will be of increasing importance as temperature decreases and that the degeneracy of the samples increases with decreasing temperature, we expect that L should tend to the elastic limit, i.e. L = 2.44 x10^{-8} V^2/K^2. Using the scattering parameter λ, we can calculate both the density of state effective mass m^* and the reduced Fermi level η^* by combining the thermopower and hole density data following Equations (V-17 for S) and (V-19 for p). For each temperature, the set of (λ, m^*, η^*) were then used to calculate the Lorenz number L from Eq. V-10. Tables V-1 and V-2 give the Lorenz number and the density of state effective mass for the references and MS $Sb_{2-x}Bi_xTe_3$ and $Sb_{2-x}Bi_xTe_{3.1}$ samples at 300 K.

x	m^*/m_0	L (x10^{-8} $V^2.K^{-2}$)
0.4 ref	1.1	1.69
0.48 ref	1.1	1.69
0.4 MS	1.2	1.71
0.48 MS	1.1	1.63

Table V-1: Reduced density of state effective mass m^*/m_0 (m_0: free electron mass) and Lorenz number L calculated at 300 K for reference and MS $Sb_{2-x}Bi_xTe_3$ samples.

We can note that m^* doesn't show strong varitions between the different compositions and that the obtained values are consistent with values obtained in single crystals using similar

models /CAI92b/. Figures V-21 gives the temperature dependence of L as a function of temperature for the reference sample $Sb_{1.6}Bi_{0.4}Te_3$ as an example. We note that L varies drastically between 5 and 300 K. At 300 K, L is close to $1.7x10^{-8}$ V^2/K^2 and then increases with decreasing temperature towards the elastic limit.

x	m^*/m_0	L ($x10^{-8}$ $V^2.K^{-2}$)
0.4 ref	1.1	1.67
0.45 ref	1.0	1.62
0.48 ref	1.1	1.63
0.50 ref	1.2	1.68
0.52 ref	0.95	1.64
0.4 MS	1.2	1.63
0.45 MS	1.1	1.58
0.50 MS	1.0	1.64
0.52 MS	1.0	1.59

Table V-2: Reduced density of state effective mass m^*/m_0 (m_0: free electron mass) and Lorenz number L calculated at 300 K for reference and MS $Sb_{2-x}Bi_xTe_{3.1}$ samples.

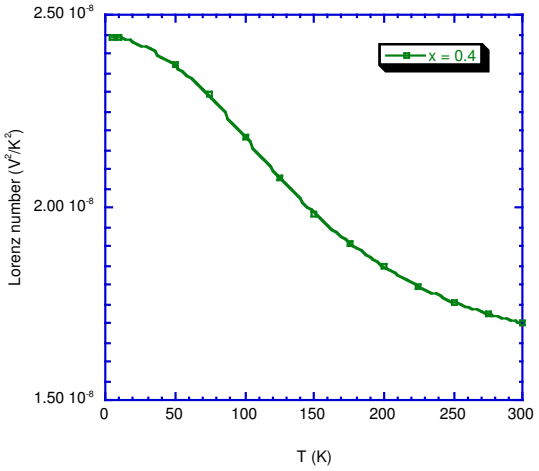

Figure V-21: Temperature dependence of the Lorenz number L for the reference $Sb_{1.6}Bi_{0.4}Te_3$ sample.

From *L(T),* we calculated the electronic contribution, κ_E, and subtracted this contribution to the total thermal conductivity, κ, to assess the lattice thermal conductivity, κ_L. Figure V-22 shows that, for the reference $Sb_{1.6}Bi_{0.4}Te_3$ samples, the contribution of κ_E to the total thermal conductivity is about 50% at 300 K, 46 % at 100 K and always amounts to 17% near the peak (20 K). The same conclusions can be drawn for the other compositions.

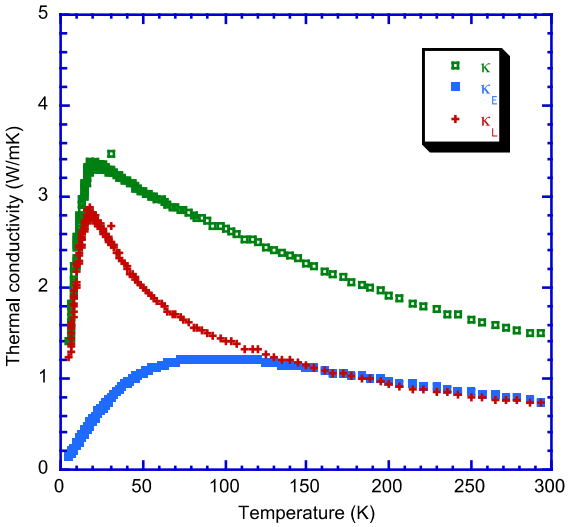

Figure V-22: Temperature dependence of κ, κ_E and κ_L for reference $Sb_{1.6}Bi_{0.4}Te_3$ samples. Note that the contribution of κ_E near the peak is not negligible.

The knowledge of the lattice thermal conductivity allows us to appreciate whether the melt-spinning technique is an effective route to further decreasing κ_L as claimed by Xie et al. /XIE09a, XIE09b, XIE11/ and Fan et al. /FAN10/. Surprisingly, as evidenced in Figures V-23, this strategy doesn't seem to have any noticeable influence near 300 K on both series of samples investigated. The situation is even more complicated at low temperatures where in some cases the MS samples present reduced lattice thermal conductivity and in other cases the opposite situation is observed. This unexpected behavior, difficult to explain, suggests that the microstructures of reference and MS samples are not so different and that only the changes in the electrical properties are responsible for these differences. We also believe that erroneous conclusions can be drawn depending on how the electronic lattice contribution is derived.

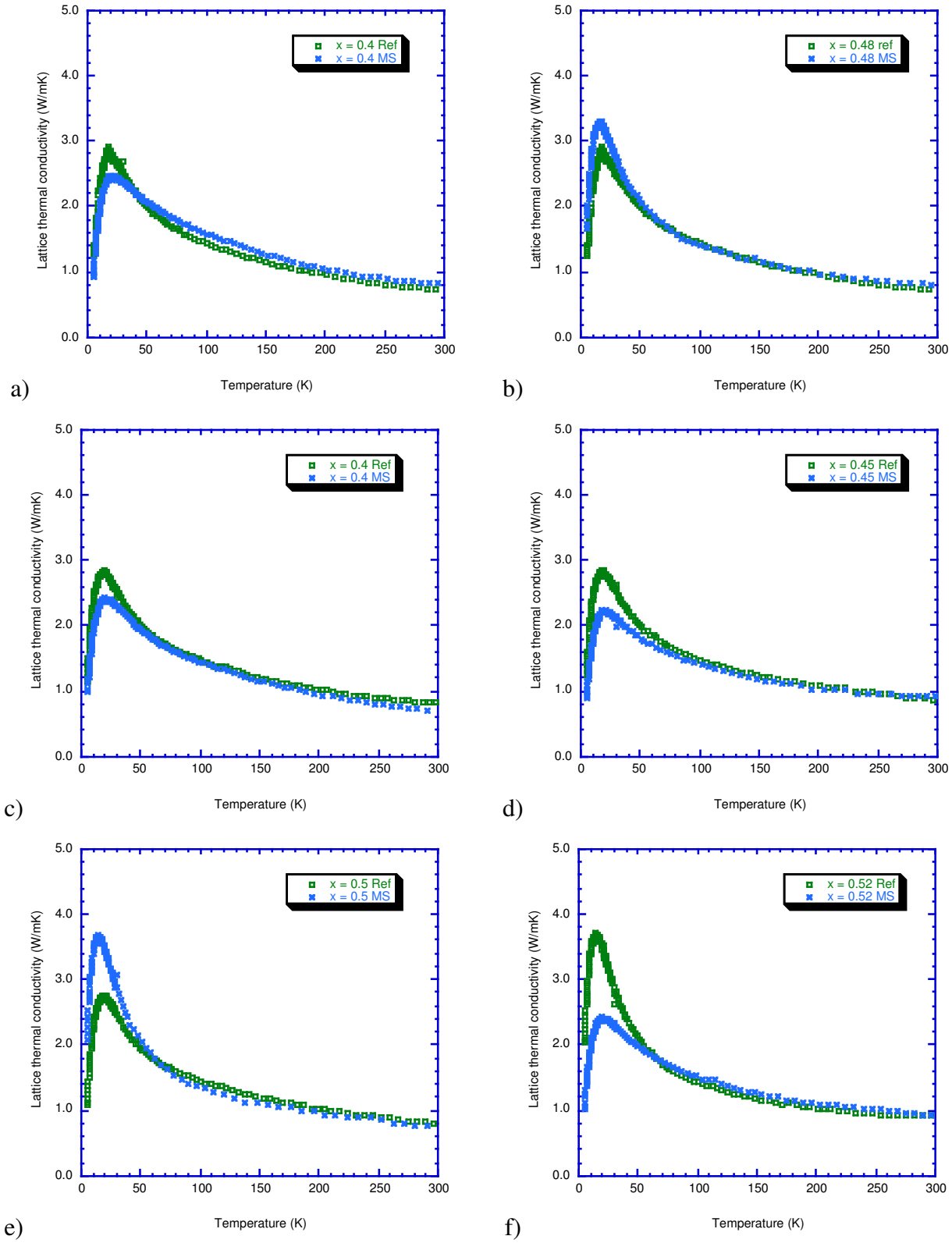

Figure V-23: Temperature dependence of the lattice thermal conductivity perpendicular to the pressing direction for (a) $Sb_{1.6}Bi_{0.4}Te_3$, (b) $Sb_{1.52}Bi_{0.48}Te_3$, (c) $Sb_{1.6}Bi_{0.4}Te_{3.1}$, (d) $Sb_{1.55}Bi_{0.45}Te_{3.1}$ (e) $Sb_{1.5}Bi_{0.5}Te_{3.1}$ and (f) $Sb_{1.48}Bi_{0.52}Te_{3.1}$.

To gain further insights on the temperature dependence of the lattice thermal conductivity, we used the Debye-Callaway model /CAL59, CAL60/ and performed theoretical fits of κ_L for all samples using the following expression:

$$\kappa_L(T) = \frac{k_B}{2\pi^2 v}\left(\frac{k_B T}{\hbar}\right)^3 \int_0^{\theta_D/T} \frac{x^4 e^x}{\tau^{-1}\left(e^x - 1\right)^2} dx \qquad \text{(V-20)}$$

where $x=\hbar\omega/k_B T$ is a dimensionless parameter, is the phonon frequency, k_B is the Boltzmann constant, $\hbar$ is the reduced Planck constant, $_D$ is the Debye temperature, v is the average velocity of sound and τ is the phonon scattering relaxation time.

Equation (V-20) has been fitted to the experimental results considering four phonon scattering mechanisms:

$$\tau^{-1} = \frac{V}{M} + A\omega^4 + B\omega^2 T e^{-\theta_D/3T} + C\omega T^3 \qquad \text{(V-21)}$$

where the coefficients *M*, *A*, *B* and *C* are adjustable parameters.

The first term in Eq. (V-21) takes into account the grain-boundary scattering (with *M* representing the mean grain size). The second term represents point-defect scattering (Rayleigh-type scattering). The third term concerns phonon-phonon Umklapp processes. This term was used to successfully describe covalent semiconductors /GLA64, SLA64/. Finally, the last term describes the normal scattering.

Taking the Debye temperature $_D$ = 160 K /GUL59/ and the velocity of sound v = 2900 m/s /DYC02/, the adjustable parameters have been determined for each value of x and are listed in Table V-3. In figure V-24 and V-25 are compared the experimental results to the fits. It can be seen that this model depicts quite well the lattice thermal conductivity in the range of temperature investigated.

The grain size *M*, determined from the best fits to the data, is on the order of the micron scale. These values are in fair agreement with the observations made on our samples from back-scattering electron images.

Composition (x, z)	*M (μm)*	*A (10^{-43} s^3)*	*B (10^{-18} $s\ K^{-1}$)*	*C*
Ref (0.4, 3)	8.7	253	16.8	0.1222
Ref (0.48, 3)	14.7	238	10.6	0.131
MS (0.4, 3)	6.3	230	9.5	0.2156
MS (0.48, 3)	19.1	270	18.6	0.0886
Ref (0.4, 3.1)	10.1	259	14.6	0.131
Ref (0.45, 3.1)	11.5	263	13.4	0.1329
Ref (0.5, 3.1)	9.3	254	14.6	0.1405
Ref (0.52, 3.1)	36	313	18.3	0.0579
MS (0.4, 3.1)	6.6	260	12.4	0.1819
MS (0.45, 3.1)	6.7	285	8.3	0.215
MS (0.5, 3.1)	30	277	22.2	0.0655
MS (0.52, 3.1)	8.9	290	7.4	0.1806

Table V-3: Lattice thermal conductivity fitting parameters for $Sb_{2-x}Bi_xTe_z$ samples, defined by Eq. V-20 and V-21..

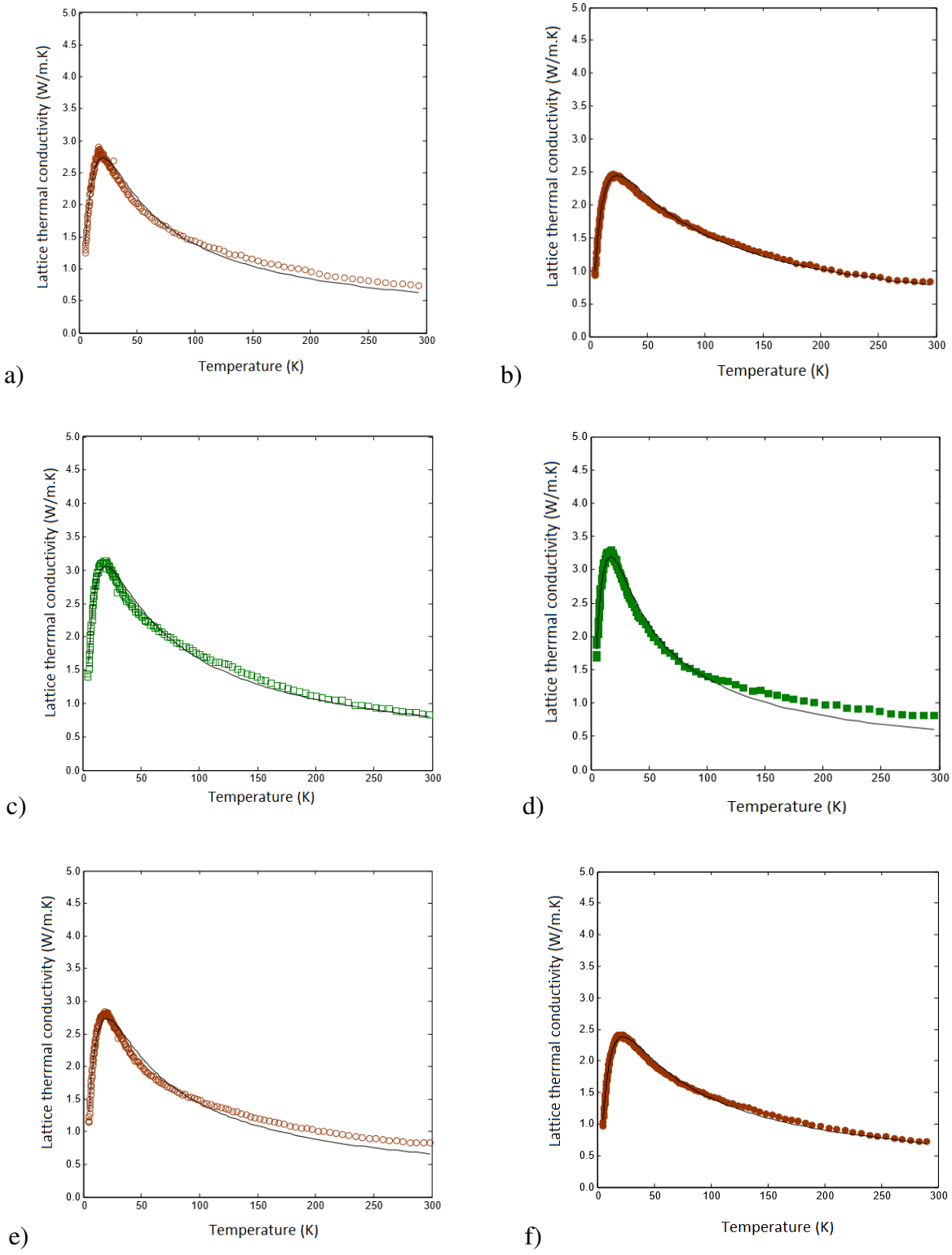

Figure V-24: The lattice thermal conductivity, κ_L, perpendicular to the pressing direction for (a) reference $Sb_{1.6}Bi_{0.4}Te_3$, (b) MS $Sb_{1.6}Bi_{0.4}Te_3$, (c) reference $Sb_{1.52}Bi_{0.48}Te_3$, (d) melt-spun $Sb_{1.52}Bi_{0.48}Te_3$, (e) reference $Sb_{1.6}Bi_{0.4}Te_{3.1}$ and (f) MS $Sb_{1.6}Bi_{0.4}Te_{3.1}$ with the continuous line indicating the numerical fitting result of the Debye-Callaway model.

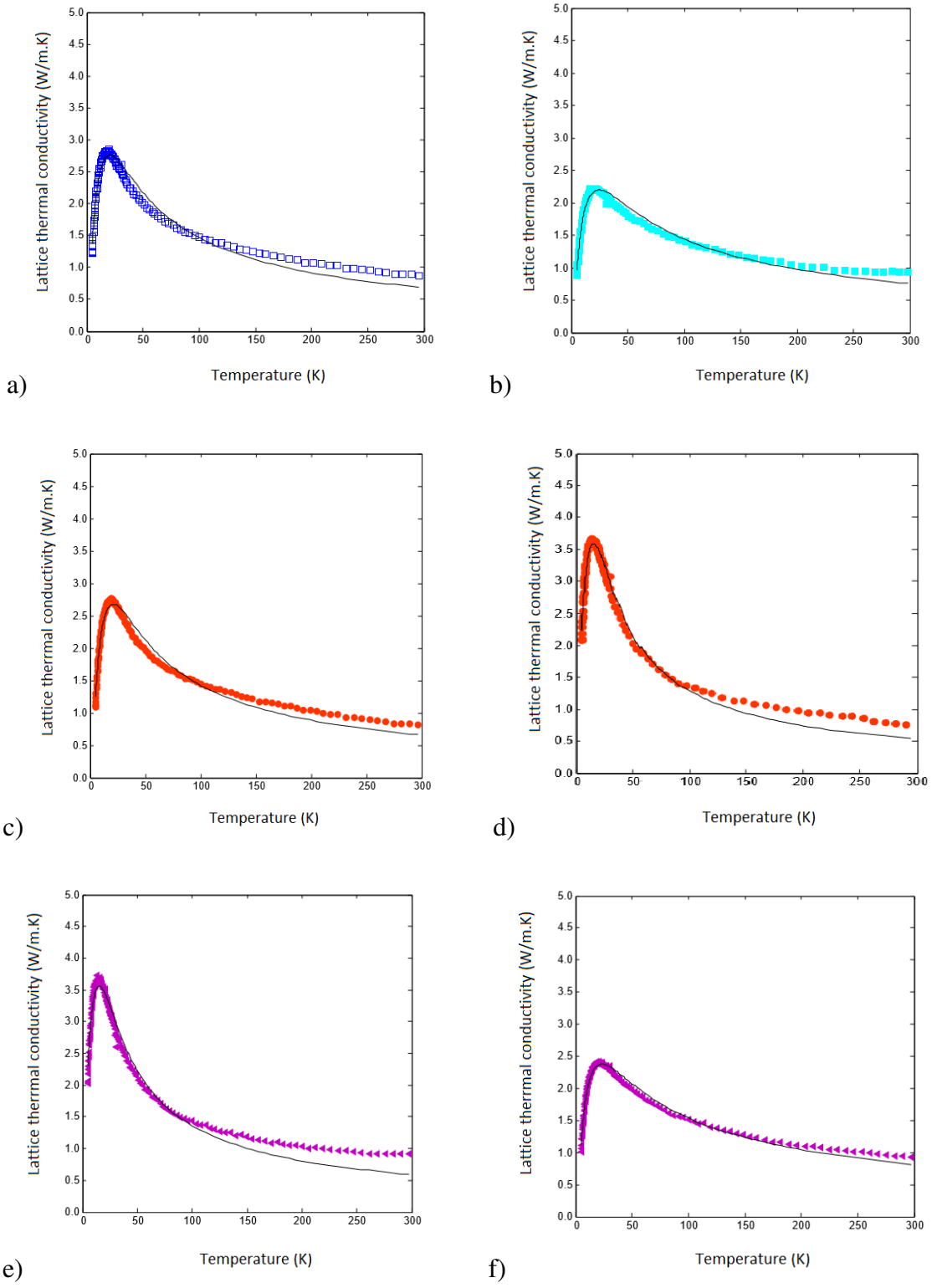

Figure V-25: The lattice thermal conductivity, κ_L, perpendicular to the pressing direction for (a) reference $Sb_{1.55}Bi_{0.45}Te_{3.1}$, (b) MS $Sb_{1.55}Bi_{0.45}Te_{3.1,}$ (c) reference $Sb_{1.5}Bi_{0.5}Te_{3.1,}$ (d) melt-spun $Sb_{1.5}Bi_{0.5}Te_{3.1,}$ (e) reference $Sb_{1.48}Bi_{0.52}Te_{3.1}$ and (f) MS $Sb_{1.48}Bi_{0.52}Te_{3.1}$ with the continuous line indicating the numerical fitting result of the Debye-Callaway model.

V) TRANSPORT PROPERTIES OF $(Sb_{1.52}Bi_{0.48})_{1-y}Sn_yTe_{3+z}$

V-1) Introduction

The previous paragraphs evidenced that the melt spinning approach combined with the SPS densification contribute to a reduction in the total thermal conductivity. However, tuning the electical properties was found to be a much more challenging task due to difficulties in controlling the concentration of intrinsic defects that govern the electronic transport properties. As already discussed, the strong p-type character of the Sb_2Te_3 rich $Sb_{2-x}Bi_xTe_3$ solid solutions is linked to electrically active defects. The most probable antisite defects are Sb_{Te} or Bi_{Te} (Sb or Bi atoms are located on Te sites). The formation of these defects is influenced by bond polarity /HOR86/. Low bond polarity favors the formation of antisite defects since their formation energy is low. A weak difference in electronegativity between atoms decreases the bond polarity and increases the antisite defects. The Pauling's electronegativity (P_E) values of Bi (P_E = 2.02), Sb (P_E = 2.05) and Te (P_E = 2.10), show that a small electronegativity difference between Bi/Sb and Te, minimizes the energy formation of antisite defects in these solid solutions. Substituting Bi for Sb changes the hole carrier concentration as seen previously but the control of the hole concentration is not as straightforward as it was discussed. Suppressing the antisite defects by extrinsic doping could be a good alternative allowing for a better control of the carrier concentration. Several dopants such as In (P_E = 1.78) or Ga (P_E = 1.81) /LOS93, NAV91/ were shown effectively suppressing the antisite defect formation by increasing the bond polarity and thus, the migration energy of Bi/Sb to Te sites. Within this scenario, while In and Ga belong to group III and are believed to populate preferentially the Bi sites, they act as donors and not as acceptors as one might naively expect. Another interesting dopant is Sn (P_E = 1.96). Santhanam et al. /SAN11/ investigated the effect of Sn in p-type $Sb_{1.5}Bi_{0.5}Te_3$ solid solutions prepared by ball milling and densified by hot pressing. Three samples with 1, 2 and 3 at.% Sn were synthesized and studied. The transport properties results showed that the electrical resistivity increases for 1 and 2 at.% Sn while at the highest doping level (3 at. %), the electrical resistivity is lower than that of the reference undoped sample. This favorable effect combined with a reduced lattice thermal conductivity due to additional phonon scattering mechanisms leads to an increase in *ZT*. The amphoteric character of Sn reported by Santhanam et al. /SAN11/ seems however to not have been reported in single crystals /KUL12/.

Another specific feature of Sn was underlined by Jaworski et al./JAW09/. These authors showed that Sn in p-type Bi_2Te_3 single crystals behaves like a resonant impurity thereby enhancing the thermopower due to resonant scattering. The concept of an impurity-induced resonant state also known as a "virtual bound state", was first introduced by Friedel /FRI56/ as a bound state with a positive energy with respect to the band edge, i.e. with the same energy as an extended state. If this state can resonate with a component of that extended states, it builds up two extended states of slightly different energies; these in turn have the same energies as the extended states with whom they will resonate, and so on, until an excess density of states arises over a narrow energy range in the band of the host materials. This distortion of the density of states can be exploited advantageously if the chemical potential can be shifted to lie in the close proximity of this excess density. Indeed, since the thermopower, as a first approximation, is sensitive to the slope of the density of states near the Fermi level, the presence of the distortion will boost the thermopower. It is important to note that this mechanism does not involve any scattering, it is in essence temperature independent, except for the temperature dependence of the band structure itself /JOV08/. Thus, this mechanism is suitable for enhancing the *ZT* in practically all thermoelectric materials below, near or above room temperature. The most spectacular results obtained over the last years using this mechanism was observed in Tl doped p-type PbTe where the *ZT* values was double leading to *ZT* = 1.5 at 800 K /HER08/.

Considering all these statements, substituting Sn for Sb (or Bi) seems to be a worthwhile way of research to pursue. The substitution of Sn for Sb (or Bi) should modify the hole carrier concentration by changing the polarity of the chemical bonds and may also potentially act as resonant impurity to boost the thermopower.

The next paragraphs report and discuss the thermoelectric and galvanomagnetic results obtained in two series of Sn-doped polycrystalline samples in the temperature range 5 – 450 K. The first series is based on $(Sb_{1.52}Bi_{0.48})_{1-y}Sn_yTe_3$ with $y = 0$; 0.15 ; 0.05 ; 0.006 while the second series consists in $(Sb_{1.52}Bi_{0.48})_{1-y}Sn_yTe_{3.1}$ with $y = 0$; 0.006 ; 0.003 ; 0.001. For practically each of these compositions, two samples have been prepared: one by the conventional synthesis route (see chapter III) and the second by a prior melt-spinning step. The transport and galvanomagnetic properties of both reference and melt-spun (MS) samples were measured in the direction perpendicular to the pressing direction, since the peak *ZT* is obtained in this direction. In the first

series of samples, the nominal Sn concentration was selected to fit the same range as Santhanam et al. /SAN11/ in order to examine whether the amphoteric character of Sn manifests itself also in our samples. The second series of samples with lower Sn concentration and an excess of Te allows extending the carrier concentration obtained in the first series and to discuss the presence of an impurity band in $(Sb_{1.52}Bi_{0.48})_{1-y}Sn_yTe_3$.

V-2) Thermoelectric and galvanomagnetic properties of $(Sb_{1.52}Bi_{0.48})_{1-y}Sn_yTe_3$

The temperature dependence of the electrical resistivity for polycristalline samples $(Sb_{1.52}Bi_{0.48})_{1-y}Sn_yTe_3$ is shown in figure V-26 for y = 0, 0.006, 0.03 and 0.15. The electrical resistivity increases with increasing temperature regardless of the compositions and the synthesis route employed. The addition of Sn has a strong impact on the electrical resistivity. Above 200 K, the Sn-doped samples have lower electrical resistivities than the undoped samples while at lower temperatures (T < 200 K), the opposite situation is observed. Moreover, the deviation from the undoped compounds is all the more prounouced than the Sn concentration is high. At 460 K, the electrical resistivity is around 16 μΩ.m for the reference sample while it drops to 5.5 μΩ.m for the heaviest doping level (y = 0.15). From these simple observations, it seems that the materials become more and more degenerate (the metallic character is more pronounced) for T > 200 K. Yet, another mechanism must be at play below 200 K to explain the behavior of the electrical resistivity in the full temperature range.

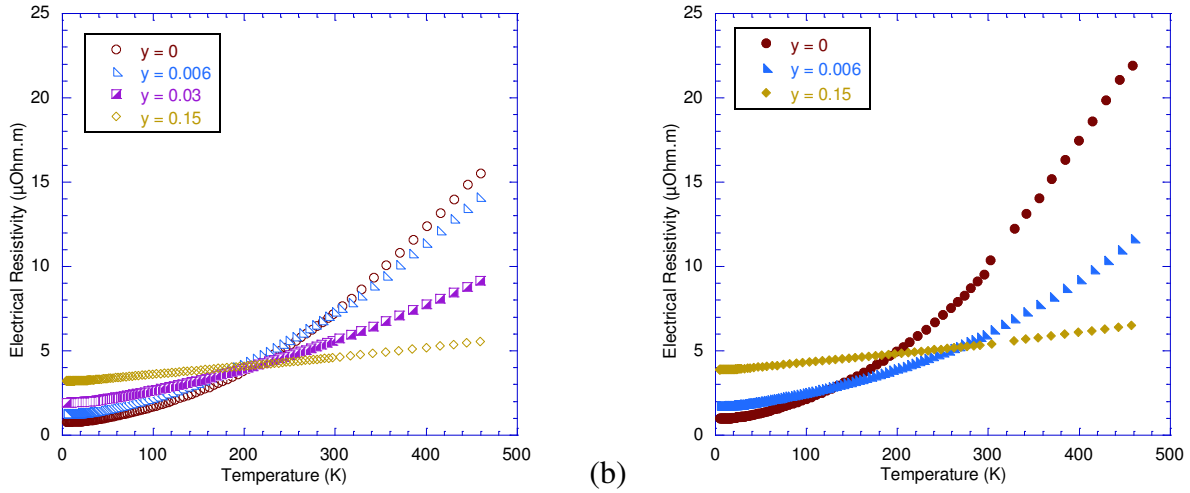

Figure V-26: Temperature dependence of the electrical resistivity a) for reference samples and b) for MS samples.

The influence of Sn on the melt-spun samples is similar to the reference samples. The general trend (increase in the electrical resistivity as noted in the first section of this chapter) is quite well satisfied except for the sample with y = 0.006.

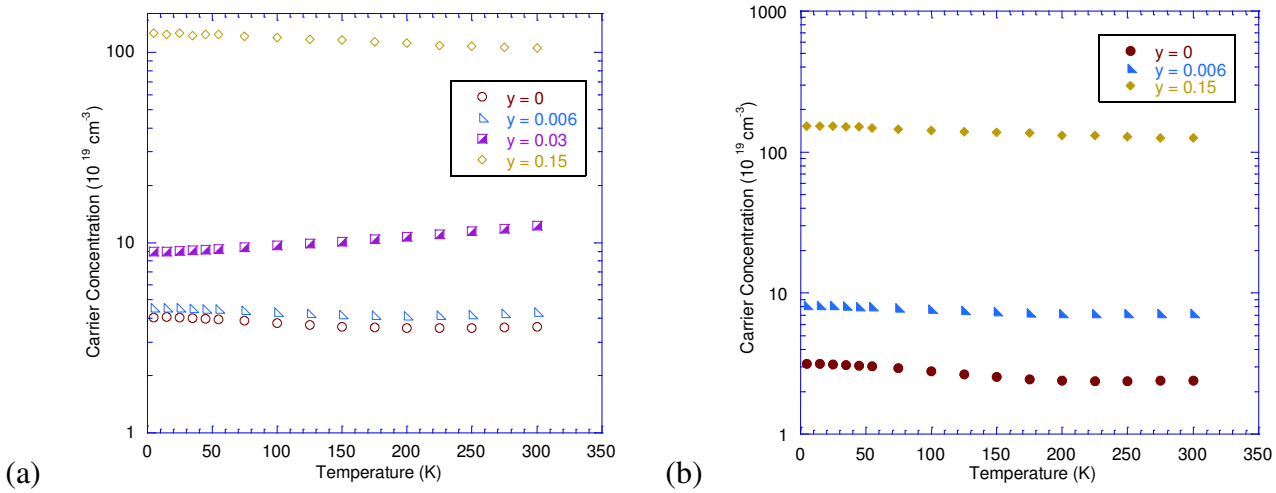

Figure V-27: Temperature dependence of the Hall carrier concentration a) for reference samples and b) for MS samples.

All the previous remarks suggest that the carrier concentration and the carrier mobility are affected by the presence of Sn and by the melt-spinning process. As seen in Fig. V-27 where the variation of the hole concentration p is plotted as a function of temperature (deduced from the measurement of the Hall coefficient, R_H, and assuming the same hypothesis as before: $p = 1/eR_H$), the substitution of Sn for Sb/Bi has a strong impact on p which remains the majority carriers for all y values. The fact that the introduction of Sn increases the hole density suggests that Sn behaves like an acceptor in the whole concentration range investigated. Noteworthy, our results differ from those of Santhanam et al. /SAN11/, but are in good agreement with the work of Kulbachinskii et al. /KUL12/ performed on single crystals. This discrepancy illustrates again the strong influence of the fabrication process on the intrinsic defects that govern all the electronic properties. It is interesting to note that for $y = 0.15$, the hole concentration for the reference and the MS samples is higher by more than one order of magnitude compared to the samples without Sn, while the electrical resistivity only shows a threefold decrease at 300 K. This observation suggests that the carrier mobility is strongly affected when samples are doped by Sn. Figure V-28 supports clearly this expectation since a dramatic decrease in the Hall carrier mobility is evidenced. At low temperatures, it amounts to almost two orders of magnitude and, at 300 K, one

order of magnitude. Moreover, while the mobility is still temperature independent at low temperatures (suggesting that scattering by ionized impurities is always the dominant scattering mechanism if we assume that holes are degenerate), the $T^{-3/2}$ dependence observed for $x = 0$ evolves into a T^0 dependence for $x = 0.15$. This means that an additional scattering channel opens when Sn is introduced. We speculate that scattering by ionized impurities is the most probable mechanism. This mechanism, which has a typical $T^{3/2}$ dependence in the case of classical statistic or T^0 in the degenerate case could be responsible for the change observed in our experimental data. In the light of these results, the increase in the electrical resistivity with the Sn content observed for $T < 200$ K is attributed to the stronger decrease in the mobility with respect to the increase in the carrier density. For $T > 200$ K, the opposite situation is observed thereby explaining the behavior of the electrical resistivity when y increases.

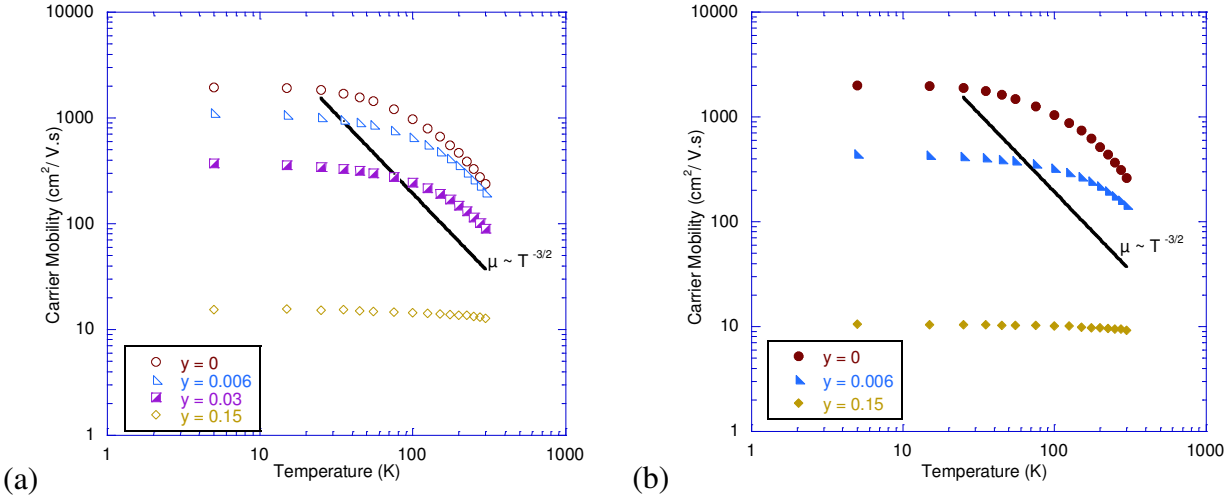

Figure V-28: Temperature dependence of the Hall mobility a) for reference samples and b) for MS samples.

We turn to the temperature dependence of the thermopower now shown in Figure V-29. All samples have positive thermopower indicating hole transport, which is consistent with positive Hall coefficients found in these samples. Sn has also a strong effect on the thermopower. The room temperature thermopower decreases drastically with the addition of Sn to a value of approximately 25 μV/K for $x = 0.15$ for both the reference and the MS samples. Thus, upon increasing the Sn content, the system becomes more degenerate in good agreement with the Hall measurements. This situation corresponds to a shift of the Fermi level inside the valence bands as

y increases. Hence, if the density of extrinsic carriers in the Sn-doped samples increases, the presence of thermal excitation across the band gap becomes less evident on *S* versus *T* curves. This fact is well observed on our *S* data above room temperature for the heaviest Sn content (*y* = 0.15).

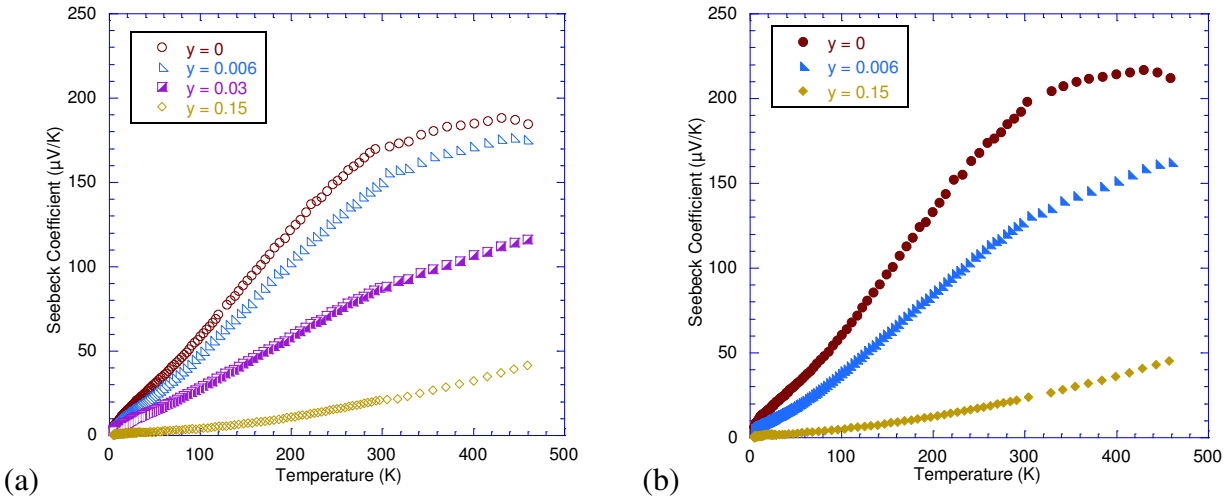

Figure V-29: Temperature dependence of the thermopower a) for reference samples and b) for MS samples.

The temperature dependence of the total thermal conductivity, κ, of the $(Sb_{1.52}Bi_{0.48})_{1-y}Sn_yTe_3$ series is displayed in Figure V-30. For $T < 300$ K, $\kappa(T)$ increases as the temperature decreases and develops a well-defined peak near 20 K for $y = 0$; 0.006 and 0.03. Below this peak, κ decreases quite linearly with *T*. A similar behavior is observed for the heaviest Sn doping for $T < 25$ K. Above 25 K, the thermal conductivity increases slightly and tends to saturate above room temperature. We can note that as Sn is incorporated into the structure, κ is diminished below 150 K with the largest reduction occuring near the dielectric maximum. As shown by the electrical resistivity that increases with *y* below 150 K, the lowering of κ is mainly due to a decrease in the lattice thermal conductivity, in good agreement with previous reports /KUL12, SAN11/. At room temperature, the values range from 1.7 to 2.4 W/mK on going from *y* = 0 to *y* = 0.15 for the reference samples. Above room temperature, as the influence of the minority carrier decreases as the Sn content increases, the increase in the thermal conductivity originates from the ambipolar contribution that diminishes and is no longer observed for *y* = 0.03 and *y* = 0.15. The MS samples show quite similar trends. However, the values at low

temperatures are lower suggesting again that the melt-spinning approach contributes to decrease the lattice thermal conductivity.

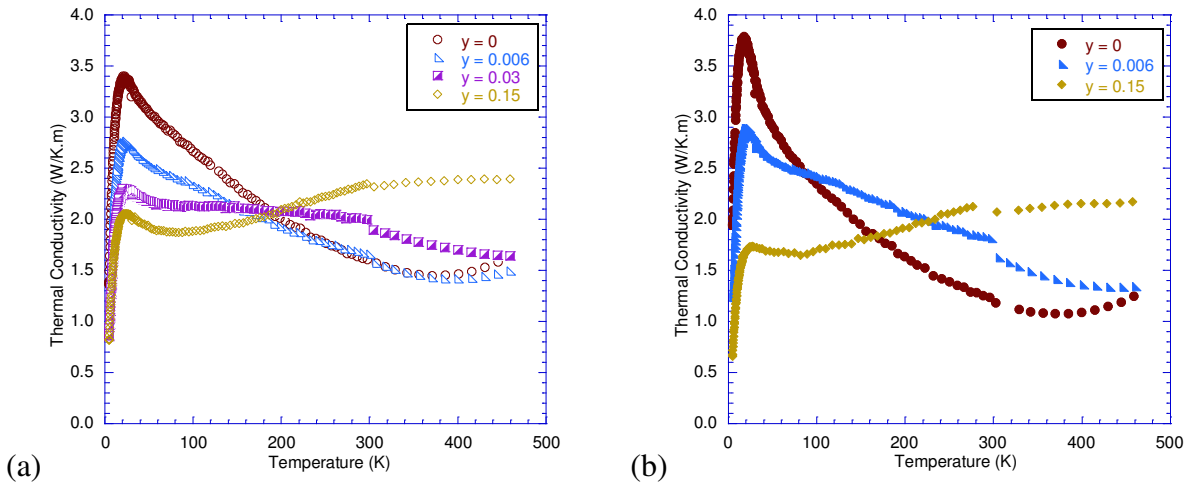

Figure V-30: Temperature dependence of the thermal conductivity a) for reference samples and b) MS samples.

To gain further insight into the influence of Sn on the reduction of the lattice thermal conductivity, we tried to estimate the electronic contribution, κ_E, for T < 300 K. The exact calculation of this contribution is again complicated but we propose to follow the same approach as before (see §IV-3 in this chapter) to calculate the Lorentz number L. We assume that for y = 0.006, the same scattering mechanisms apply as for y = 0. For the highly doped sample, y = 0.15, we considered that the material is fully degenerate in the whole temperature range so that a constant value L = 2.44 x10^{-8} V^2/K^2 was used. For y = 0.03, the situation is more complicated because the scattering parameter, λ, is not well defined near room temperature. Nevertheless, an estimation of λ at 300 K was made possible from the temperature dependence of the Hall mobility, $\mu_H \sim T^n$, as suggested by /LUK12/ .These authors identified as a first approximation the exponent n to the scattering parameter λ. Following this procedure, we find that at room temperature, L = 2x10^{-8} V^2/K^2 and at 100 K, L = 2.35x10^{-8} V^2/K^2. Since impurity scattering will become more and more important as the temperature decreases and that the degeneracy of this sample will also increase, we speculate that L should tend to the elastic limit, i.e. L = 2.44 x10^{-8} V^2/K^2. Using this approach, we derived the temperature dependence of the lattice thermal conductivity for all samples. The results, presented in Fig. V-31, clearly evidence that the lattice thermal conductivity in $Sb_{2-x}Bi_xTe_3$ reference or MS samples is further decreased by increasing the Sn concentration.

Due to a lack of time, the Debye-Callaway model has not been implemented in this part, but we strongly believe that useful information could be extracted from this model. For example, the influence of the Sn content is believed to increase the point defect scattering. Such influence should manifest itself by a strong increase in the coefficient *A* in Eq. V-21.

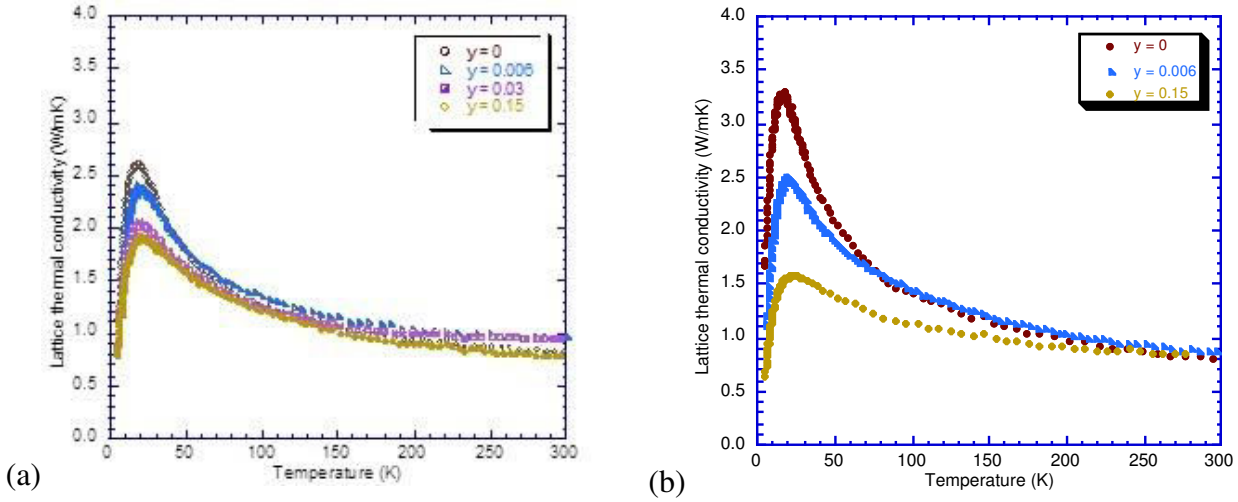

Figure V-31: Temperature dependence of the lattice thermal conductivity a) for reference samples and b) MS samples. By increasing the Sn content, the lattice thermal conductivity is further degraded.

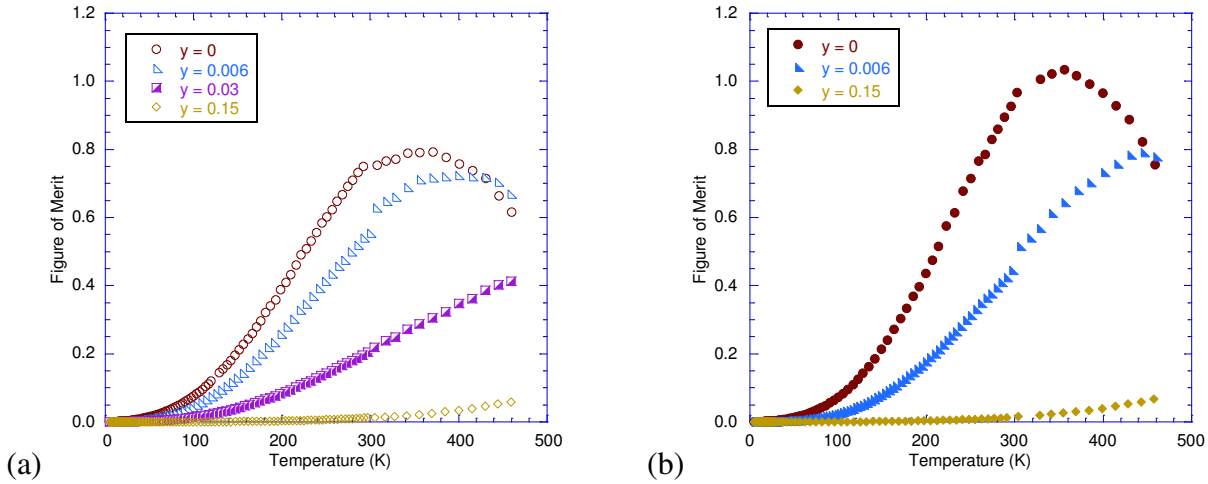

Figure V-32: Temperature dependence of the dimensionless figure of merit ZT a) for reference samples and b) MS samples.

The resulting dimensionless figure of merit *ZT* versus temperature is plotted in Figure V-32. It is clearly seen that the Sn range investigated does not help to improve the thermoelectric performance since the maximum value of *ZT* is obtained in the undoped reference or MS sample. High concentration of Sn is clearly detrimental to optimizing the thermoelectric performances

due to an excess of holes that makes the material too metallic. As a result, the peak *ZT* is shifted towards higher temperatures and its value tends to zero.

V-3) Thermoelectric and galvanomagnetic properties of $(Sb_{1.52}Bi_{0.48})_{1-y}Sn_yTe_{3.1}$

The conclusions of the last paragraph suggest that a minute amount of Sn should be more beneficial in order to not disturb too much the hole concentration. Moreover, we have seen that an excess of Te allows reducing the hole concentration and pushing the chemical potential towards the top of the valence band. The combination of this two effects could provide a more effective way of tuning the hole density. The next parts describe the transport and galvanomagnetic properties of reference and MS samples over the temperature range 5 – 500 K. Most of the comments described before are also applicable for these samples. For this reason, only short comments will be made.

As shown in Figure V-33, adding a minute amount of Sn, *y*, from $y = 0.001$ to $y = 0.006$ increases sligthly and monotonically the Hall carrier concentration, *p,* of $(Sb_{1.52}Bi_{0.48})_{1-y}Sn_yTe_{3.1}$ samples in the whole temperature range. In the reference materials, this corresponds to a value increasing from $p \sim 2.5 \times 10^{19}$ cm^{-3} for $y = 0$ to $p \sim 4 \times 10^{19}$ cm^{-3} for $y = 0.006$ at 300 K. In the MS samples, the previous remarks still hold near 300 K but as the temperature decreases, *p* tends to a similar value.

A reduction in the Hall mobility is always observed upon adding small amounts of Sn as shown in Figure V-34. The degradation increases with increasing the Sn content. At low temperatures, the mobility values remain robust (above 1000 cm^2/Vs) and the temperature dependence is always constant. Near 300 K, the variations in temperature of the Hall mobility is dominated by acoustic phonons (variation close to a $T^{-3/2}$ law) for the reference and MS samples with $y = 0.001$ and 0.003. For $y = 0.006$, the influence of ionized impurities on the hole transport starts to play a role.

As a consequence of these observations, the electrical resistivity is not too much disturbed below 200 K as illustrated in Figure V-35. At higher temperatures, the electrical resistivity decreases with increasing the Sn content for all prepared samples.

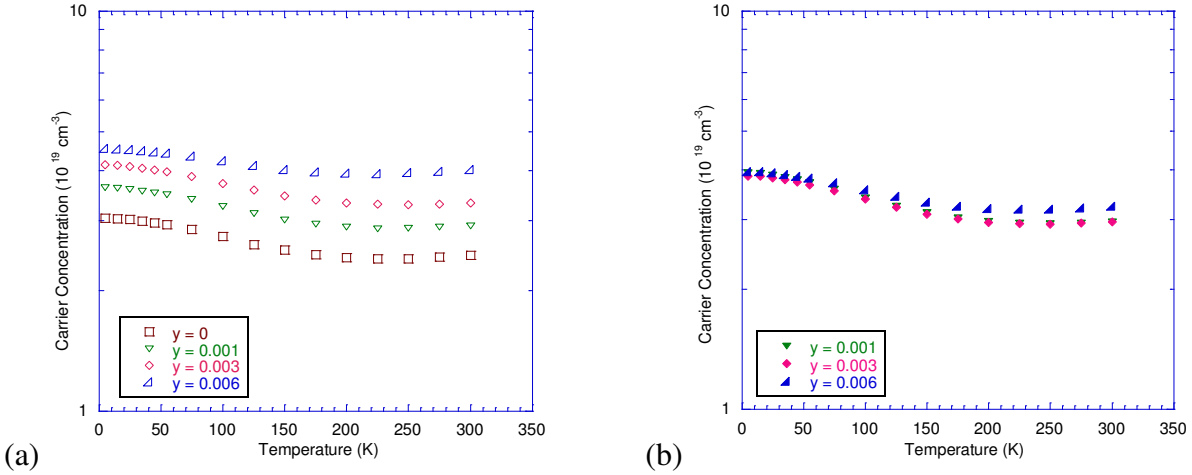

Figure V-33: Temperature dependence of the Hall carrier concentration a) for reference samples and b) for MS samples.

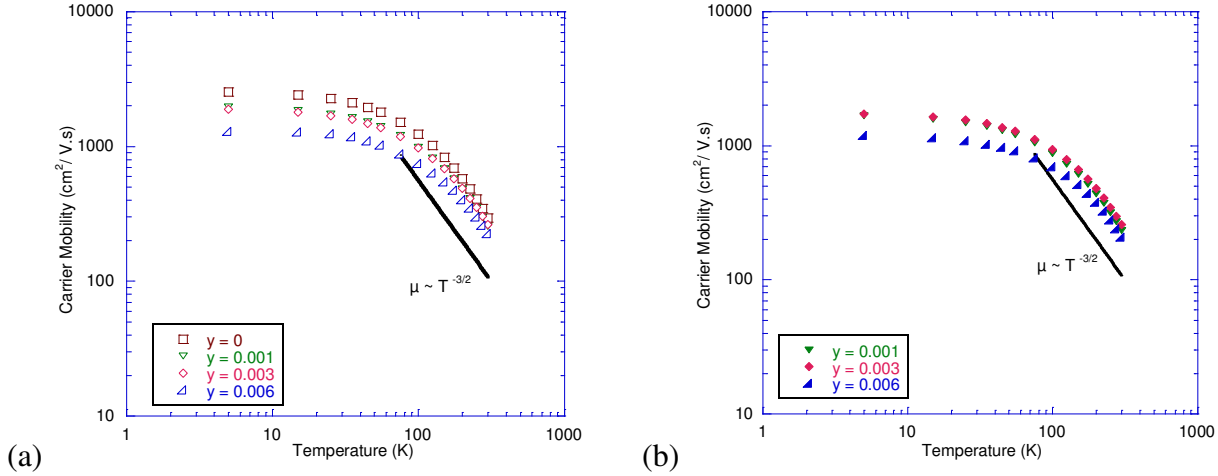

Figure V-34: Temperature dependence of the Hall mobility a) for reference and b) for MS samples.

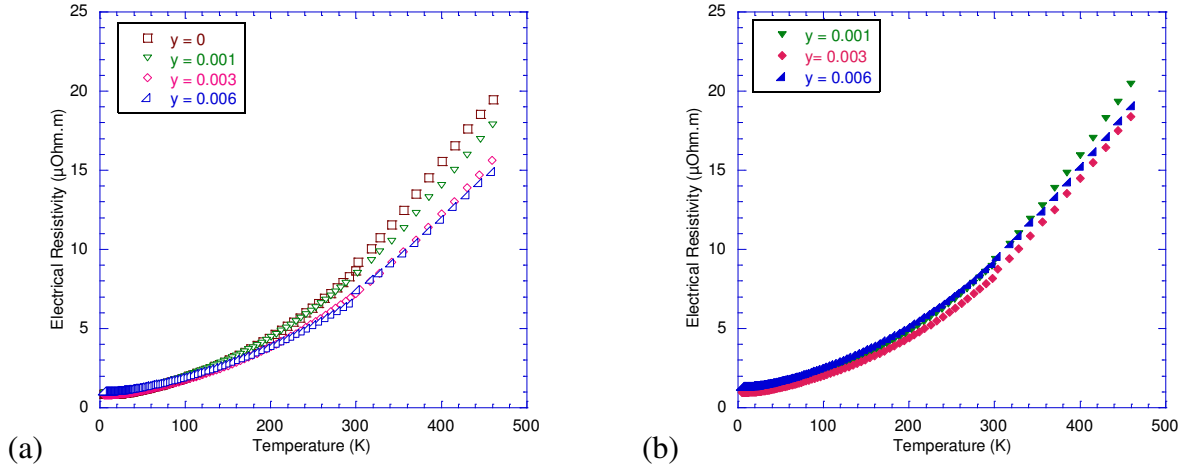

Figure V-35: Temperature dependence of the electrical resistivity a) for reference and b) for MS samples.

The variations in the thermopower with temperature of the samples are shown in Figure V-36. Upon increasing the Sn content up to y = 0.006, the system maintains a behavior typical to that of a degenerate semiconductor. However, the gradual increase in the hole density leads to a decrease in the thermopower. This corresponds again to a shift of the Fermi level from a position close to the top of the valence bands to a location deeper inside the valence bands. We note that the influence of the minority carrier is still observed above 400 K in these lightly Sn doped samples. The intrinsic regime seems to start at the highest temperature probed (470 K) for the reference samples with y = 0, 0.001 and 0.003.

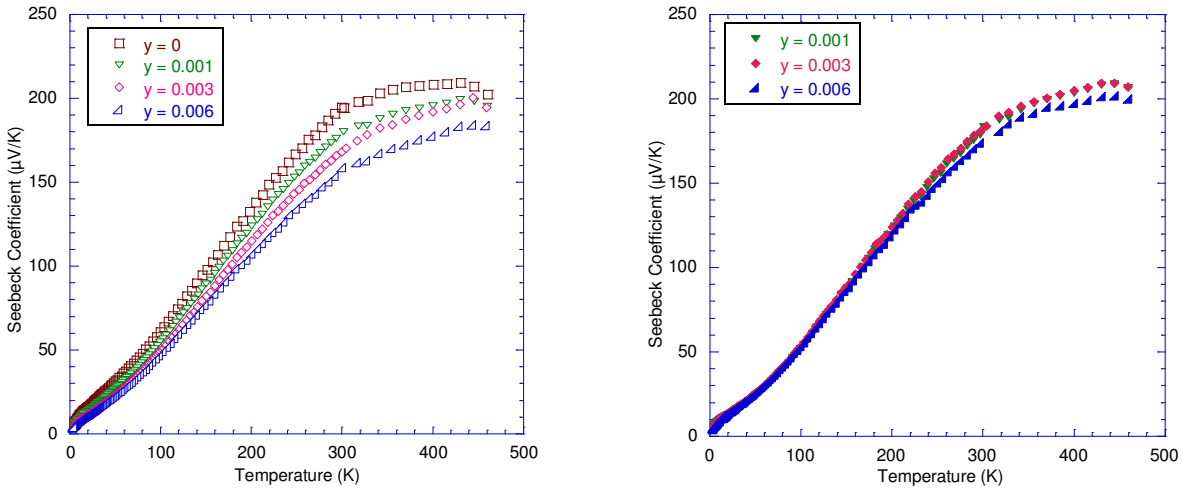

Figure V-36: Temperature dependence of the thermopower a) for reference samples and b) for MS samples.

The total thermal conductivity is plotted in Figure V-37 versus temperature. The influence of Sn on the phononic part can be easily appreciated at low temperatures (below 100 K) even for the samples containing small amounts of Sn. Above 100 K, the electronic contribution, which increases with the Sn level, is responsible for the inversion of the trend noted at low temperatures. Above 380 K, the thermal excitations across the band gap manifest themselves and result in an increase in the total thermal conductivity.

From the previous electrical and thermal results, an estimation of the dimensionless figure of merit *ZT* is provided in Figure V-38 for the series $(Sb_{1.52}Bi_{0.48})_{1-y}Sn_yTe_{3.1}$. One can see that the combination of a small amount of Sn with an excess of Te doesn't help to boost the *ZT* values. A degradation is systematically observed in the whole temperature range and the method used to prepare the sample.

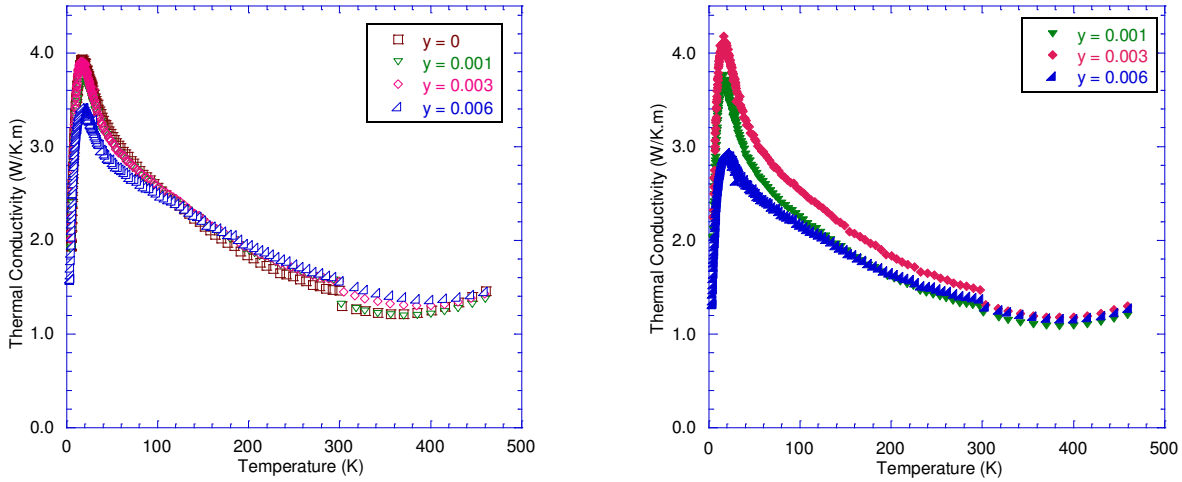

Figure V-37: Temperature dependence of the thermal conductivity a) for reference samples and b) MS samples.

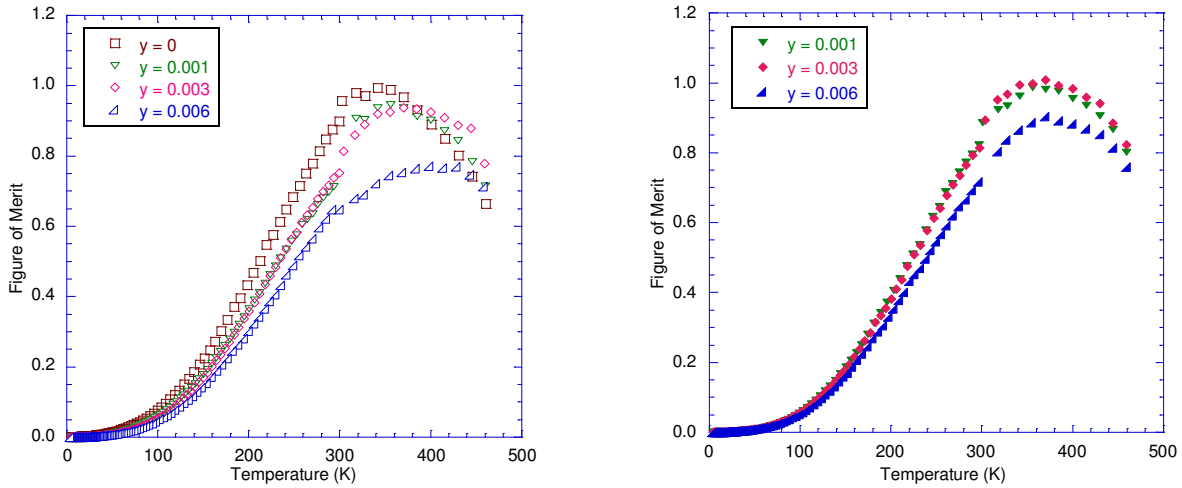

Figure V-38: Temperature dependence of the dimensionless figure of merit ZT a) for reference samples and b) MS samples.

V-4) Is Sn a resonant impurity in $(Sb_{1.52}Bi_{0.48})_{1-y}Sn_yTe_3$?

By changing the Sn and the Te contents, we were able to tune the hole density in a broad range (more than two orders of magnitude) in *p*-$Sb_{1.52}Bi_{0.48}Te_3$. This offers us the opportunity to probe whether Sn plays the role of a resonant impurity in this composition as in Bi_2Te_3 /JAW09/. A simple way to probe such phenomena, is through the dependence of the thermopower versus the hole density, called the Pisarenko plot introduced by Ioffe /IOF60/. Indeed, the Pisarenko plot

enables determining whether one has successfully increased the thermopower for a given carrier concentration and scattering mechanism. We calculated the hole dependence of the thermopower coefficient $S(p)$, using Equations V-14 and V-17, for p-$Sb_{1.52}Bi_{0.48}Te_3$, taking into account, as a rough approximation, that the structure of the valence bands can be assimilated to a single parabolic band characterized by a density of states effective mass of 1.1 m_0 (as determined previously for p-$Sb_{1.52}Bi_{0.48}Te_3$). This calculation was performed for two different scattering parameters, λ, evidenced in the previous paragraphs: acoustic phonon scattering (λ = -1/2) and ionized impurity scattering (λ = 3/2). The calculations have been performed at 300 K. From Fig. V-39, we see that in our samples, the filling of the valence band upon Sn doping plays an important role in changing the thermopower. Moreover, our results match nicely to the calculated Pisarenko relation for acoustic phonon scattering (λ = -1/2), showing no change in the dominant scattering mechanism with Sn doping. This conclusion suggests that the evolution of the temperature dependence of the hole mobility above 200 K is a consequence of an increase of the degeneracy of the hole gas when the Sn content increases.

Since no departure from the $S(p)$ dependence is evidenced in Fig. V_39 indicative of the presence of a resonant level in $Bi_{2-x}Sn_xTe_3$, as it was the case for $Bi_{2-x}Sn_XTe_3$ /JAW09/, we should conclude that Sn is not a resonant impurity in $(Sb_{1.52}Bi_{0.48})_{1-y}Sn_yTe_3$.

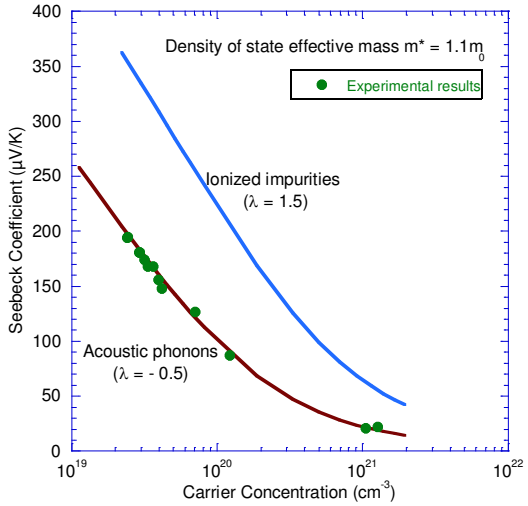

Figure V-39: Pissarenko relation (red and blue line) for p-type $Sb_{2-x}Bi_xTe_3$ as calculated at 300 K. The symbols are for our data.

CONCLUSION

In this chapter, the transport and galvanomagnetic results of the reference and MS samples of general formula *p*-$(Sb_{1-x}Bi_x)_2Te_{3+z}$ have been discussed in details and interpreted, when possible, using semi-classical electron and phonon models. We have shown that our polycrystalline samples densified by SPS are more or less anisotropic and for this reason, it was essential to probe, in the same direction, all the transport properties in order to evaluate correctly the dimensionless thermoelectric figure of merit, *ZT*. The carrier concentration was found to be very sensitive to the Bi content, *x*, the Te content, *z*, the preparation procedure (influence of the synthesis route, of the pressing (cold or hot) and of the annealing step) as a result of changes in the concentration of intrinsic native charged defects that are responsible for deviations from stoichiometry. Our results unambiguously show that little changes in the hole concentration can have dramatic effects on *ZT*. A precise control of the hole density in these ternary systems, either in single or polycrystalline form, is really a challenging task. While we obtained *ZT* values that exceed those of single crystals or polycrystalline materials used in commercial modules using the melt spinning method, our data remain well below those claimed by two other groups (*ZT* ~ 1.6 – 1.8 at 300 K !!!). The huge discrepancy between these results raises concerns about their credibility since similar composition and experimental parameters were used in this study and that recent experimental results led to values in good agreement with our observations /BOE08, EBL07a, EBL07b, IVA13/. Important is also the fact that no clear evidence was found concerning the reduction in the lattice thermal conductivity in MS samples.

Finally, an attempt to boost the *ZT* through Sn doping has also been carried out. However, in contrast to the results obtained in the binary compound Bi_2Te_3, Sn was not found to act as a resonant impurity in the ternary derivatives.

CONCLUSIONS AND FUTURE DIRECTIONS

This thesis concludes with a brief summary of objectives and findings and some thoughts for future research studies. They are summarized in the following sections.

The aim of this thesis work was to fabricate high efficient *p*-type thermoelectric materials for applications in heat pumps near 300 K. The best materials targeting this temperature are the solid solutions formed from the two binary compounds Sb_2Te_3 and Bi_2Te_3. Commercial modules using these alloys have *ZT* (dimensionless figure of merit) around 0.9 – 1.0. The recent advances in the nanostructuration of bulk materials suggested that *ZT* could be significantly increased in (Bi,Sb,Te) solid solutions by creating nano-sized features. Among the methods used to fabricate bulk nanomaterials, the melt-spinning (MS) technique proved to be particularly spectacular since *ZT* values around 1.5 – 1.8 at 300 K were claimed by two independent groups /FAN10, XIE09/. Such level of performance is really exciting because it corresponds to what is needed to consider thermoelectric heat pumps as potentially interesting from the viewpoint of its coefficient of performance. For this reason, we decided to explore the electrical and thermal properties of *p*-$Sb_{2-x}Bi_xTe_{3+z}$ samples fabricated by the MS method. Influence of Sn on the thermoelectric properties of this family of compounds has also been considered.

Considerable efforts were devoted to acquire knowledge on the MS technique as this method had never been implemented in the team. A careful optimization of the parameters that governs the MS method leads to the production of ribbons with good crystallinity. Detailed analyses of the nano-microstructure and chemical homogeneity of these ribbons were performed using advanced tools (TEM, SEM, XRD). It was found that the surface in contact with the wheel presents marked differences with the free surface. The presence of nanograins and amorphous zones were identified near the contact surface where the cooling rate can be as large as 10^4 K/s. To keep as much as possible the nano-sized features, we densified the ribbons using the Spark Plasma Sintering (SPS) technique, which is known to be a rapid sintering process. Samples with a density higher than 95 % were produced by SPS allowing for further physical characterizations. In order to investigate how the MS technique and resulting microstructure affects the thermoelectric properties, we also fabricated bulk samples (called reference samples) with the same composition via a normal process.

The physical characterizations were based on electrical, thermal, galvanomagnetic and thermodynamic measurements. In order to have a deeper insight about the basic mechanisms that are responsible for the macroscopic behavior of the samples, the measurements were performed between 5 and 500 K. Low- (5-300 K) and high-temperature (300-460 K) facilities were used to probe this wide temperature range.

Among the numerous results obtained on reference or melt-spun $(Sb_{2-x}Bi_x)_{1-y}Sn_yTe_{3+z}$ samples, the more salient are summarized below:

- The presence of an anisotropic behavior in the electrical, thermal and galvanomagntic properties of both the reference and MS samples has been evidenced. This is due to a preferred orientation of grains during the SPS resulting from the lamellar character of the crystalline structure. As a consequence, due care had to be taken to measure in the same direction both electrical and thermal properties to correctly evaluate the *ZT*. The anisotropy depends on the carrier density (hole here), a behavior reminiscent to that observed in single crystals. The best direction for *ZT* is the direction perpendicular to the pressing direction.

- The native charged defects in $Sb_{2-x}Bi_xTe_{3+z}$ compounds responsible for deviations from stoichiometry play a major role in the optimization of the electrical properties. The number of such defects, and as a consequence the number of charge carriers, was found to be extremely dependent on the Bi and Te contents and the fabrication process including the densification and the post-annealing steps. The sensitivity of the carrier concentration to all these parameters makes a precise control of the electrical properties (and thus of *ZT*) very challenging. In particular, it was found that the MS method associated to SPS, while being effective in preparing high-performance $Sb_{2-x}Bi_xTe_{3+z}$ compounds, does not provide a full control on the intrinsic defects.

- Numerous similarities were found in the transport properties of $Sb_{2-x}Bi_xTe_{3+z}$ compounds suggesting that these samples follow the same physic. Based on Boltzmann transport equations, we were able to explain the observed similarities.

- The melt-spinning method was found to be able to further reduce the total thermal conductivity of the samples, but no clear evidence of a decrease in the lattice thermal conductivity was found. We proposed to interpret this latter using the semi-classical Debye transport model with four scattering mechanisms: point defects, grain boundaries, Umklapp and normal processes.

- The influence of Sn on the transport properties of $Sb_{2-x}Bi_xTe_{3+z}$ compounds revealed that Sn acts as an acceptor. Besides changing the hole density, Sn atoms also act as scattering centers influencing both the electrical and thermal properties. By changing the Sn and Te contents, we were able to vary the hole density over two orders of magnitude in $(Sb_{2-x}Bi_x)_{1-y}Sn_yTe_{3+z}$ compounds. We found that the presence of Sn degrades systematically the *ZT* values with respect to the undoped samples. Moreover, no evidence of clear effect of Sn on the thermopower was found based on the Pisarenko plot suggesting that Sn does not behave as a resonant impurity in $Sb_{2-x}Bi_xTe_3$ compounds.

Future directions

In this work, many interesting results were shown and discussed. The MS approach combined with the SPS proved to be a powerful method to produce *p*-$Sb_{2-x}Bi_xTe_3$ samples with *ZT* values higher than the state-of-the-art results. However, as already discussed, our values remain much lower than those of Xie et al. /XIE09/and Fan et al. /FAN10/. It is thus natural to ask whether further improvements of the thermoelectric performance of these materials may be achieved. We believe that the results of Xie et al. and Fan et al. were overestimated. Indeed, if they were true and reproducible, industry based on Peltier modules would have benefited from this breakthrough to expand their markets. However, unfortunately, nothing happened five years later after the publication of these unprecedented results.

It is certainly possible to further slightly increase the *ZT* values by 10 % by tuning the electrical properties. Exploring new dopants such as In could be a possibility. As In is supposed to act as a donor, it could help to reduce the hole density below the limit of $2x10^{19}$ cm^{-3} reached in this work. Following the same idea, adding Se could be also an interesting path as Se plays also the role of a donor. Exploring lower carrier densities could lead to an increase in the power factor. Another alternative could be the control of the hole density with careful post-annealing treatments. We have seen that the effect of annealing is to reduce the carrier concentration. Optimizing the annealing temperature and the duration could then increase the power factor too.

CONCLUSIONS ET PERSPECTIVES

Les principales conclusions de ce travail de thèse sont résumées dans les paragraphes qui suivent. Quelques idées pour des travaux de recherche futurs sont également mentionnées.

L'un des objectifs principal de cette étude était de fabriquer des matériaux thermoélectriques de type *p* performants pour des applications dans des pompes à chaleur fonctionnant au voisinage de la température ambiante. Les meilleurs matériaux à 300 K sont les solutions solides à base des composés binaires Sb_2Te_3 et Bi_2Te_3. Des modules commerciaux utilisant ces alliages ont des facteurs de mérite adimensionnels *ZT* se situant entre 0,9 – 1,0. Suite aux avancées récentes obtenues dans des matériaux massifs nanostructurés, il est suggéré que des *ZT* améliorés et ce, de manière significative, sont possibles dans les composés (Bi, Sb, Te) contenant des motifs de taille nanométrique. Parmi les méthodes utilisées pour fabriquer des matériaux massifs nanostructurés, la technique de trempe sur roue (ou melt-spining - MS - en anglais) s'est avérée être une méthode efficace puisque des valeurs de *ZT* comprises entre 1,5 et 1,8 ont été clamées par deux groupes de recherche indépendants /FAN10, XIE09/. Un tel niveau de performance est tout à fait excitant car il correspond à ce qui est nécessaire pour considérer les pompes à chaleur thermoélectriques comme potentiellement viables en terme de coefficient de performance (C.O.P.). Pour cette raison, nous avons décidé d'explorer les propriétés électriques et thermiques d'échantillons $Sb_{2-x}Bi_xTe_{3+z}$ fabriqués par la méthode MS. L'influence de l'étain sur ces compositions a également été considérée au cours de ce travail de thèse.

Des efforts importants ont été mis en œuvre pour maitriser la technique MS car l'équipe ne possédait aucune expérience sur ce procédé d'élaboration. Une optimisation soignée des paramètres d'élaboration qui gouvernent la méthode MS a permis d'obtenir des rubans avec une bonne cristallinité et une bonne stoechiométrie. Des analyses pointues de la nano/micro-structure ainsi que de l'homogénéité chimique des rubans ont été réalisées en utilisant des outils performants (DRX, MEB, MET). Il a été montré que la surface des rubans en contact avec la roue présente des différences marquées par rapport à la surface libre. La présence de grains de taille nanométrique et de zones amorphes a été identifiée au voisinage de la surface en contact avec la roue où la vitesse de refroidissement peut être très élevée (de l'ordre de 10^6 K/s). Pour garder cette microstructure unique, nous avons densifié les rubans à l'aide d'un frittage rapide (ou Spark Plasma Sintering – SPS – en anglais), qui limite la croissance des grains. Des échantillons ayant

une densité relative de plus de 95% ont été produits par SPS en vue de caractérisations électriques et thermiques ultérieures. De manière à apprécier l'impact de la méthode MS sur les propriétés thermoélectriques, nous avons aussi fabriqués des échantillons massifs de référence de même composition à partir de méthodes traditionnelles.

Des caractérisations électriques, thermiques et thermodynamiques ont été menées. De manière à avoir une connaissance approfondie des mécanismes de base qui sont responsables du comportement macroscopique de nos échantillons, les mesures ont été réalisées entre 5 et 500 K. Des équipements basse température (5-300 K) et haute température (300-500 K) ont été utilisés pour sonder cette large gamme de température.

Parmi les très nombreux résultats obtenus sur les échantillons de référence ou sur les échantillons préparés par MS, les plus marquants sont rappelés dans les paragraphes suivants :

- Une anisotropie des propriétés électriques, galvanomagnétiques et thermiques a été mise en évidence dans les échantillons de référence et MS. Cette anisotropie est intimement liée à une texturation des échantillons durant le procédés de frittage par SPS faisant suite au caractère lamellaire de la structure cristalline. Par voie de conséquence, nous avons veillé à mesurer dans la même direction les propriétés électriques et thermiques pour évaluer correctement le facteur *ZT*. L'anisotropie dépend de la concentration de porteurs (ici les trous), caractéristique rémanente à celle notée dans des monocristaux. La direction préférentielle, en terme de performance pour le facteur *ZT*, est suivant la direction perpendiculaire à la direction de pressage par SPS.

- Les défauts natifs chargés électriquement dans les composés $Sb_{2-x}Bi_xTe_{3+z}$ responsables des écarts à la stoechiométrie joue un rôle important dans l'optimisation des propriétés électriques. Nous avons démontré que la concentration de tels défauts, et donc de la concentration des porteurs de charge, dépend de manière drastique de la teneur en bismuth et d'un excès de tellure mais aussi des procédés de fabrication incluant la méthode de compaction (à chaud ou à froid) et d'un recuit ultérieur. La sensibilité de la concentration de porteurs à l'ensemble de ces paramètres rend le contrôle précis des propriétés électriques (et donc du facteur *ZT*) extrêmement compliqué. En particulier, nous avons mis en évidence que la technique MS combinée au SPS, bien qu'effective pour préparer des composés $Sb_{2-x}Bi_xTe_{3+z}$ performants d'un point de vue thermoélectrique, ne permet pas un contrôle rigoureux des défauts intrinsèques.

- De nombreuses similarités concernant les propriétés de transport des composés $Sb_{2-x}Bi_xTe_{3+z}$ ont été montrées suggérant que ces échantillons suivent la même physique. A partir d'un modèle semi-classique basé sur l'équation de transport de Boltzmann, nous avons été capable d'expliquer les similarités rencontrées.

- La technique de trempe sur roue s'est avérée être une technique efficace pour réduire la conductivité thermique totale des échantillons mais aucune évidence claire d'une diminution de la composante de réseau n'a pu être établie. Nous avons interprété cette dernière à partir du modèle semi-classique de Debye et en introduisant quatre mécanismes de diffusion des phonons : diffusion par les joints de grains, diffusion par les défauts ponctuels et diffusion par les phonons (processus normaux et Umklapp).

- L'influence de l'étain sur les propriétés thermoélectriques des composés $Sb_{2-x}Bi_xTe_{3+z}$ a révélé que Sn se comporte comme un accepteur. En plus de modifier la densité de trous, les atomes de Sn agissent aussi comme des centres diffuseurs, influant les propriétés électriques et thermiques. En modifiant les teneurs en Sn et Te, nous avons été capables de modifier la concentration de porteurs sur deux ordres de grandeur dans la famille $(Sb_{1.52}Bi_{0.48})_{1-y}Sn_yTe_{3+z}$. Nous avons trouvé que la présence de Sn dégrade systématiquement le facteur *ZT* par rapport aux composés non alliés. De plus, la dépendance du pouvoir thermoélectrique en fonction de la concentration de porteurs (courbe de Pissarenko) exclut tout effet de résonnance de Sn dans $Sb_{2-x}Bi_xTe_{3+z}$.

Perspectives

Dans ce travail, de nombreux résultats scientifiques ont été montrés et discutés. Nous avons prouvé que la technique MS combinée au SPS est une méthode puissance pour produire des échantillons de type *p* $Sb_{2-x}Bi_xTe_{3+z}$ denses avec des facteurs *ZT* (1,2 à 300 K) supérieurs à ceux de l'état de l'art. Cependant, et comme nous l'avons déjà souligné, nos valeurs restent encore inférieures à celles clamées par Xie et al. /XIE09/et Fan et al. /FAN10/. Il est donc naturel de se demander si le facteur *ZT* peut être encore davantage amélioré. Nous pensons que les résultats de Xie et al. /XIE09/et Fan et al. /FAN10/ ont été surestimés. En effet, s'ils étaient réels et reproductibles, l'industrie basée sur les modules Peltier aurait bénéficiée de cette percée pour

étendre leur marché. Malheureusement, aucun signe n'a été noté cinq ans après la publication de ces résultats sans précédent.

Il est certainement possible d'augmenter les valeurs de *ZT* de ces matériaux de l'ordre de 10% en contrôlant davantage les propriétés électriques. L'exploration de nouveaux dopants comme l'indium pourrait être une possibilité. En effet, In, qui est supposé se comporter comme un donneur, pourrait aider à réduire la concentration de porteurs en dessous de la limite atteinte dans cette thèse ($2x10^{19}$ cm^{-3}). Suivant le même ordre d'idée, ajouter du sélénium pourrait aussi s'avérer être une voie de recherche intéressante puisque Se joue aussi le rôle de donneurs. L'exploration de matériaux avec des faibles concentrations de porteurs pourrait donner lieu à des facteurs de puissance plus élevés que ceux montrés dans ces travaux. Une autre alternative pourrait être le contrôle de la concentration de trous à partir de recuits. Nous avons en effet montré que le recuit a pour effet de réduire la concentration de trous. Optimiser le recuit (en terme de température et durée) pourrait donc aussi augmenter le facteur de puissance.

APPENDIX 1

Influence of some melt-spinning process parameters on the transport properties of MS samples

The melt-spinning is a quite complicated process with a variety of parameters that can be tuned for each new composition and according to the desired results. Adjusting the speed of the wheel, the heating temperature, the nozzle's diameter, the distance between the tube and the wheel's surface, the pressure in the chamber and the overpressure rate are a set of parameters available for the operator. Some of these parameters are defined empirically and should be fixed in a quite narrow range to have successful melt-spinning processes. Variation of others does not have strong impact on the resulting properties while some can have quite strong influence at least in our case. Talking about the heating temperature, we should mention that this parameter varied slightly in each run but was attempted to be fixed in the range of 630-700°C depending on the heating effectiveness: if the temperature was too low, the melt could not be ejected from the tube due to the high viscosity, even if overpressure was applied; if the temperature was too high, melt was ejected spontaneously even without application of overpressure. Here we present our study on the influence of three parameters on the thermoelectric properties of the MS-SPS samples: the nozzle's diameter, the distance to the wheel surface and the speed of the wheel.

The electrical, thermal and galvanomagnetic results for the set of MS samples of $Sb_{1.6}Bi_{0.4}Te_{3.1}$ prepared in tubes with nozzle diameters of 0.5, 0.7 and 1 mm are presented in Fig. A1-1. The results of the reference sample are also included for comparison. It can be noticed that all the MS samples demonstrate minor differences in their transport properties, with no logical evolution of the properties with the nozzle diameter. Compared to the reference material, the general dependences observed in the previous studies and described in Chapter V, like decrease of thermal conductivity, in parallel with increase of electrical resistivity, were found here as well. The leading results of the thermoelectric figure of merit (ZT ~ 1.1 at 360 K) for the sample prepared using a tube with a nozzle diameter of 1 mm was achieved through a combination of minor beneficial effects of the electrical resistivity, thermal conductivity and thermopower, gaining about additional 10% performance with regard to the reference material. This effect could be explained by the variation of the ejection speed of the melt through the nozzle. In other

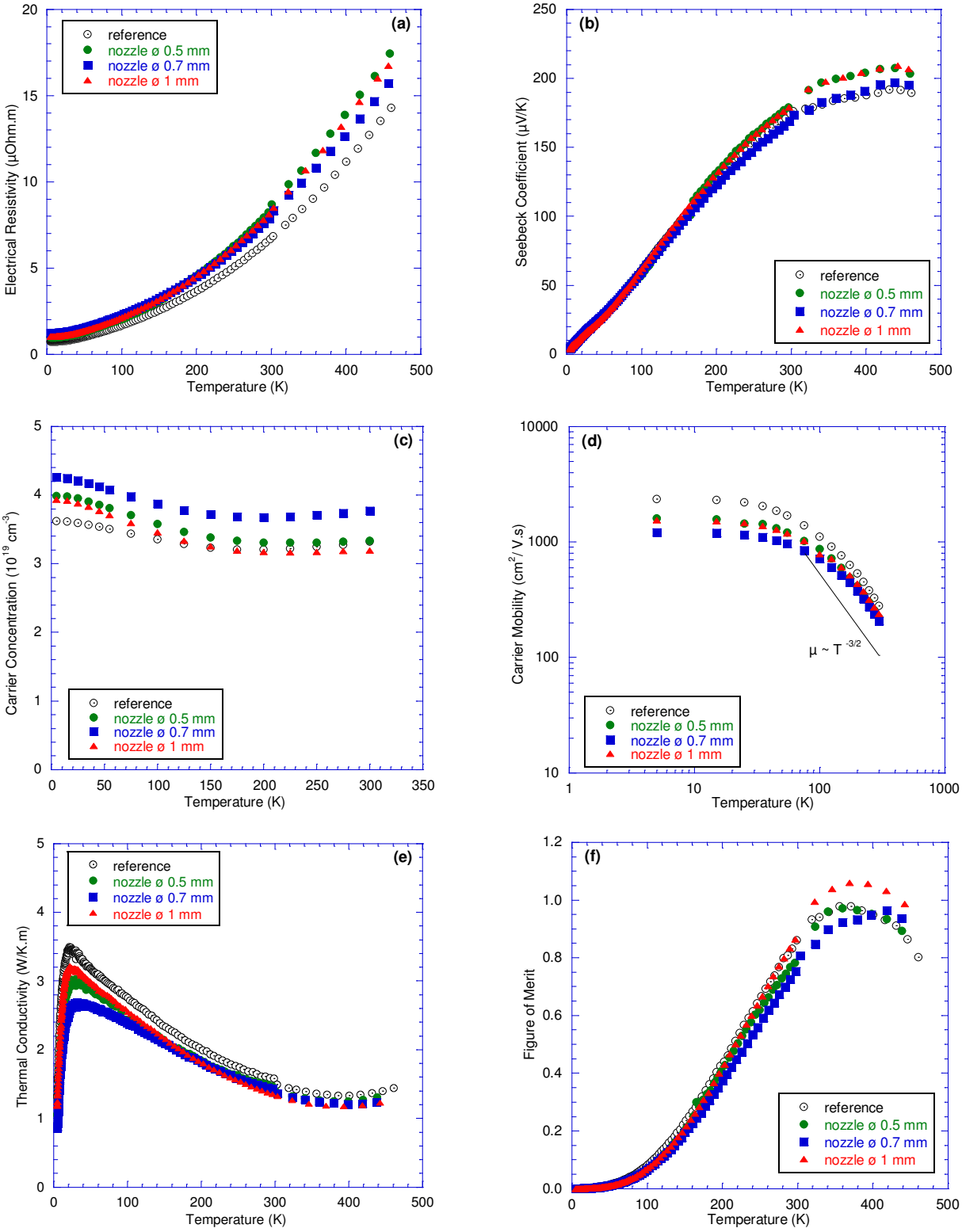

Figure A1-1: Temperature dependence of (a) electrical resistivity, (b) thermopower, (c) hole concentration, (d) Hall mobility, (e) total thermal conductivity and (f) *ZT* of reference and MS $Sb_{1.6}Bi_{0.4}Te_{3.1}$ samples prepared via melt-spinning with variation of nozzle's diameter in the tubes. Measurements were performed along the direction perpendicular to the pressing direction.

words, the smaller the diameter of the nozzle was, the longer the time it took to go out from the tube was. Thus a stronger deviation from the heating temperature could be obtained. Finally, the influence of the nozzle diameter can possibly be neglected if the variation of heating temperature is small, and thus the variation in viscosity. Minor changes can also be expected when decreasing the quantity of the material loaded in the tube.

Much stronger impact was found out during the study of the change of the distance *d* from the tube bottom to the surface of the wheel and the linear wheel speed *v*, the nozzle diameter being set to 1 mm, for which the best results were previously obtained. The results of the transport properties and galvanomagnetic measurements of MS samples can be seen in Fig. A1-2 alongside with the data for the reference sample of $Sb_{1.6}Bi_{0.4}Te_{3.1}$ composition.

First of all let's see the impact of the distance *d*, which was set as 0.7 and 1 mm, for the tube's nozzle diameter 1 mm. An unexpected strong degradation of the thermoelectric performance was found for the sample prepared with the shortest distance. The data resemble to some extent to those obtained for the cold-pressed samples (see Chapter V, section III-3): low thermopower values in the whole range of temperature, a higher hole concentration, absence of a maximum peak in the thermal conductivity and change in the scattering mechanisms near 300 K. The electrical resistivity behavior, contrarily to the cold-pressed samples, was not anomalous though the rise of values with the increase of temperature was much slower than for the other samples. A value of 8 µOhm.m was obtained at 460 K while it reached 18 µOhm.m for the MS sample prepared using *d* of 1 mm. Similar results were obtained in few other experiments for which a too strong overheating was observed, reaching over 700°C instantaneously. Logically, when the distance is larger, the melt jet will travel a longer way in the atmosphere. This may decrease the average cooling rate, and the influence of the gravitation force is probably not negligible. However, for the moment, we can just speculate on the viscosity problems, where the shorter distance between the wheel and bottom of the tube may somehow slow down the ejection process and thus extend the heating of material. For a more well-founded explanation further studies should be performed. In all following experiments, the rule "distance = diameter of the nozzle" was maintained to prevent such influence.

Looking now to the influence of the linear speed of the wheel, we used the maximum speed available for our system, i.e. about 42 m/s, and decreased it down to 36 m/s for comparison (see

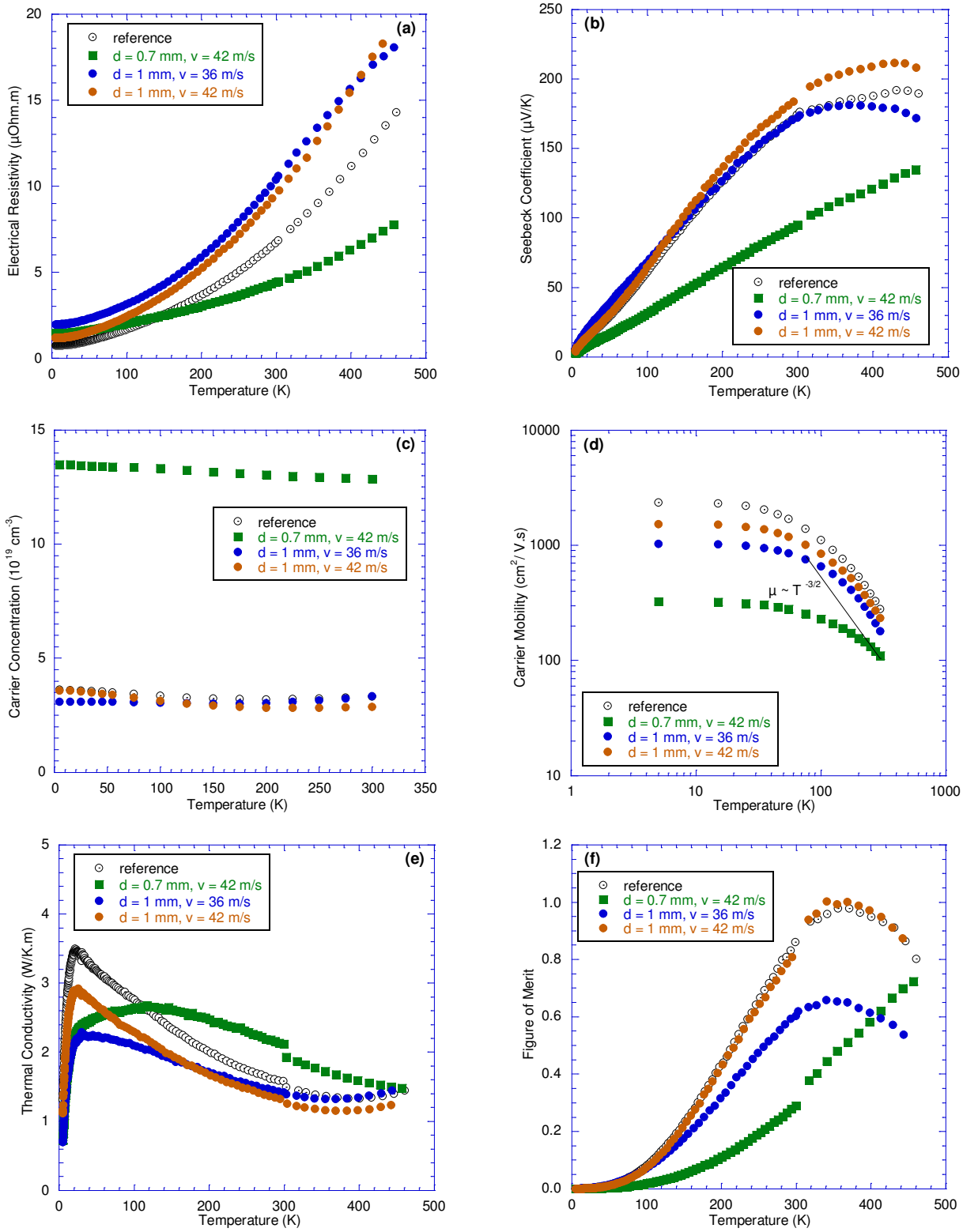

Figure A1-2: Temperature dependence of (a) electrical resistivity, (b) thermopower, (c) hole concentration, (d) Hall mobility, (e) total thermal conductivity and (f) *ZT* of reference and MS $Sb_{1.6}Bi_{0.4}Te_{3.1}$ samples prepared via melt-spinning with variation of distance from the nozzle to the surface of wheel and linear speed of the wheel.

Fig.A1-2). Both samples possess rather classical behavior peculiar to other MS samples. The main difference can be noticed in the thermal conductivity of the sample prepared at the slower speed. Despite decreased thermal conductivity values compared to the reference sample can be observed at temperatures below ambient, no effect can be seen at higher temperatures. Possessing in the same time higher electrical resistivity, we suppose that the lower speed prepared sample was influenced by a less efficient cooling rate alongside with the introduction of some additional scattering mechanisms, which is proved by the results of Hall mobility. The combination of these peculiar features caused the value of the thermoelectric figure of merit to be decreased down to 50% compared either to the reference sample or to the sample prepared at higher speed. Unfortunately, we could not study the influence of speed higher than 42 m/s due the limitations of our system.

As a conclusion, we can say first of all that specific attention should be paid to the maintaining of the temperature of the melt below 700°C to avoid strong overheating that seems to have an impressive unfavorable impact on the transport properties. If following this advice, the nozzle diameter seems not to be a dominant parameter and has no strong influence on the thermoelectric properties of the melt-spun samples. The distance from the bottom of the tube to the wheel surface was found to be a parameter that can change drastically the nature of all the properties but a deeper study should be carried out to explain this result. At the moment, we can just suggest to follow the rule that distance between the wheel and the tube should be at least equal to the nozzle diameter. Finally, the decrease of the wheel speed, as could be expected, causes the decrease of the thermoelectric figure of merit due to the diminution of the cooling rate.

Appendix 2

Semi-classical Transport Model

We recall from Chapter I that the thermoelectric performance of a materials system depends on its dimensionless thermoelectric figure of merit (ZT):

$$ZT = S^2T/\rho(\kappa_e + \kappa_L) \tag{A2-1}$$

According to equation A2-1, *ZT* depends on the electrical resistivity (ρ), the Seebeck coefficient or thermopower (*S*), the electrical thermal conductivity (κ_e), the lattice thermal conductivity (κ_L) and the temperature (*T*).

We used the semi-classical model to interpret the various transport coefficients (*S*, ρ, κ_e) of our samples. This model is based on the Boltzmann Transport Equation (BTE). The generalized BTE under the relaxation time approximation (RTA) was defined as following /ASH76a/:

$$\frac{\partial f}{\partial t} + \mathbf{v} \cdot \frac{\partial}{\partial \mathbf{r}} f + \boldsymbol{F} \cdot \frac{1}{\hbar} \frac{\partial}{\partial \mathbf{k}} f = -\frac{f(\mathbf{k}) - f_e(\mathbf{k})}{\tau_e(\mathbf{k})} \tag{A2-2}$$

with a distribution function solution:

$$f(t) = f_e(t) - \int_{-\infty}^{t} dt' P(t,t') \frac{d}{dt'} f^0(t') \tag{A2-3}$$

where **r** is the real space coordinates, ***F*** is an external force, **k** is the reciprocal space coordinates, and τ_e is the electron relaxation time. Equation A2-3 expresses the distribution function as the local equilibrium distribution $f_e(t)$ plus a correction term, in which $P(t,t')$ denotes the fraction of electrons that actually survive from time *t'* to time *t* without suffering any further collisions. The local equilibrium distribution $f_e(t)$ is the Fermi-Dirac distribution function which will be defined in the next paragraphs.

The BTE under the RTA and in the stationary state has been studied for 1D, 2D, and 3D systems previously /ASH76b, HIC93a, HIC93b, SUN99/. For a simple one-band model in ζ dimensions, the carrier density (*p*), the electrical conductivity ($\sigma = 1/\rho$), the thermopower (*S*) and the electrical thermal conductivity (κ_e) are derived as /ASH76b, HIC93a, HIC93b/:

$$p = \int 2\frac{d\boldsymbol{k}}{(2\pi)^{\zeta}} f_e(E), \tag{A2-4}$$

$$\sigma = \mathcal{L}_{\zeta}^{(0)}, \tag{A2-5}$$

$$S = -\frac{1}{eT}\frac{\mathcal{L}_{\zeta}^{(1)}}{\mathcal{L}_{\zeta}^{(0)}}, \tag{A2-6}$$

$$\kappa_e = \frac{1}{e^2 T}\left(\mathcal{L}_{\zeta}^{(2)} - \frac{\left(\mathcal{L}_{\zeta}^{(1)}\right)^2}{\mathcal{L}_{\zeta}^{(0)}}\right), \tag{A2-7}$$

where T is the temperature in degrees Kelvin, and the integral function $\mathcal{L}_{\zeta}^{(\alpha\prime)}$ is given by

$$\mathcal{L}_{\zeta}^{(\alpha\prime)} = 2e^2 \int \frac{d\mathbf{k}}{(2\pi)^{\zeta}}\left(-\frac{\partial f_e}{\partial E}\right)\tau_e\, \mathbf{v}(\mathbf{k})\mathbf{v}(\mathbf{k})(E(\mathbf{k}) - E_f)^{\alpha\prime}, \tag{A2-8}$$

where the factor of 2 accounts for the two electron spin states, ζ is the dimension of the system under consideration, $\alpha' = 0, 1, 2$, while $d\boldsymbol{k}$ is the differential element in ζ dimensional $\boldsymbol{k}$ space, E(**k**) denotes the carrier dispersion relation, τ_e is the electron relaxation time which in general depends on $E(\boldsymbol{k})$ and the absolute temperature T, E_f is the Fermi energy, e the elementary charge, **v** the velocity and $f_e(E)$ is the Fermi-Dirac distribution function defined by:

$$f_e(E) = \frac{1}{1 + exp^{(E-E_f)/(k_B T)}} \tag{A2-9 }$$

The calculation of the Equation (A2-8) requires knowledge of the charge carrier relaxation time τ_e for the entire electron distribution. In general, different scattering mechanisms have different τ_e terms. To consider the collective contribution of different scattering mechanisms for practical situations, Matthiessen's rule /ASH76a/ is used:

$$\frac{1}{\tau_e} = \sum_i \frac{1}{\tau_{e,i}} \tag{A2-10}$$

In any actual materials system, there are many energy bands that need to be taken into consideration due to the near degeneracy of the multiple carrier pockets at the conduction band

and valence band extrema. For a multi-band system, the p and $\mathcal{L}_{\zeta}^{(\alpha\prime)}$ in Equations A2-4 to A2-7 need to be replaced by the sum $p_{total} = \sum_b p_b$ and $\mathcal{L}_{\zeta,total}^{(\alpha\prime)} = \sum_b \mathcal{L}_{\zeta,b}^{(\alpha\prime)}$ for contributions from each subband b. The quantities p, σ, S, κ_e and Lorenz number L then become:

$$p_{total} = \sum\nolimits_b p_b\,, \tag{A2-11}$$

$$\sigma_{total} = \sum\nolimits_b \mathcal{L}_{\zeta,b}^{(0)}\,, \tag{A2-12}$$

$$S_{total} = -\frac{1}{eT}\frac{\sum_b \mathcal{L}_{\zeta,b}^{(1)}}{\sum_b \mathcal{L}_{\zeta,b}^{(0)}}, \tag{A2-13}$$

$$\kappa_{e,total} = \frac{1}{e^2T}\left(\sum\nolimits_b \mathcal{L}_{\zeta,b}^{(2)} - \frac{\left(\sum_b \mathcal{L}_{\zeta,b}^{(1)}\right)^2}{\sum_b \mathcal{L}_{\zeta,b}^{(0)}}\right). \tag{A2-14}$$

$$L = \frac{\kappa_e}{\sigma T} = \frac{1}{e^2T^2}\left(\frac{\sum_b \mathcal{L}_{\zeta,b}^{(2)}}{\sum_b \mathcal{L}_{\zeta,b}^{(0)}} - \left(\frac{\sum_b \mathcal{L}_{\zeta,b}^{(1)}}{\sum_b \mathcal{L}_{\zeta,b}^{(0)}}\right)^2\right)$$

Instead of going directly into solving the BTE under RTA with all the complicated relaxation times, let us make a few approximations to get a better sense of the transport coefficients. Assuming the materials system of interest has: 1) only one ellipsoidal carrier pocket and 2) one dominant scattering mechanism; Equation A2-8 in 3D becomes:

$$\mathcal{L}^{(0)} = \frac{8\pi r^2}{3m_{cond}^* h^3}(2m^* k_B T)^{3/2}\int_{E_0/(k_BT)}^{\infty} \frac{\tau_e\left(r - \frac{E_0}{k_BT}\right)^{3/2}\exp^{r-\eta^*}}{(\exp^{r-\eta^*}+1)^2}\,dr\,, \tag{A2-15}$$

$$\mathcal{L}^{(1)} = \frac{8\pi r^2 k_B T}{3m_{cond}^* h^3}(2m^* k_B T)^{3/2}\int_{E_0/(k_BT)}^{\infty} \frac{\tau_e\left(r - \frac{E_0}{k_BT}\right)^{3/2}\exp^{r-\eta^*}}{(\exp^{r-\eta^*}+1)^2}(e-\eta^*)dr\,, \tag{A2-16}$$

$$\mathcal{L}^{(2)} = \frac{8\pi r^2 (k_B T)^2}{3m_{cond}^* h^3}(2m^* k_B T)^{3/2}\int_{E_0/(k_BT)}^{\infty} \frac{\tau_e\left(r - \frac{E_0}{k_BT}\right)^{3/2}\exp^{r-\eta^*}}{(\exp^{r-\eta^*}+1)^2}(r-\eta^*)^2 dr\,, \tag{A2-17}$$

where:

$$r = E/(k_B T), \tag{A2-18}$$

$$\eta^* = E_f/(k_B T), \tag{A2-19}$$

and E_0 is the band edge energy, E the energy, k_B the Boltzmann constant, h the Planck constant, m^* the effective mass and m^*_{cond} the conductivity effective mass.

The dependence of the electron relaxation time τ_e versus E and T can be expressed as:

$$\tau_e = aE^{\lambda}(k_B T)^{\beta} \tag{A2-20}$$

where a is a constant and λ and β, two parameters characteristic of the scattering mechanism.

Combining Equations A2-15-A2-17 with A2-20 and applying the uv-substitution formula to the integrals with an energy reference on E_0 gives:

$$\mathcal{L}^{(0)} \propto (k_B T)^{\frac{3}{2}+\lambda}\left(\frac{3}{2}+\lambda\right)\int_0^{\infty}\frac{r^{\frac{1}{2}+\lambda}}{\exp^{r-\eta^*}+1}dr\,, \tag{A2-21}$$

$$\mathcal{L}^{(1)} \propto \left[\left((k_B T)^{\frac{5}{2}+\lambda}\left(\frac{5}{2}+\lambda\right)\int_0^{\infty}\frac{r^{\frac{3}{2}+\lambda}}{\exp^{r-\eta^*}+1}dr\right) - \left(k_B T\eta^*\mathcal{L}^{(0)}\right)\right]. \tag{A2-22}$$

$$\mathcal{L}^{(2)} \propto \left[\left((k_B T)^{\frac{7}{2}+\lambda}\left(\frac{7}{2}+\lambda\right)\int_0^{\infty}\frac{r^{\frac{5}{2}+\lambda}}{\exp^{r-\eta^*}+1}dr\right) - 2k_B T\eta^*\mathcal{L}^{(1)}\right]. \tag{A2-23}$$

We quickly see that the transport coefficient calculation now boils down to simply the computation of the integrals in Equations A2-21, A2-22 and A2-23. Remember that the only assumptions made so far are: (a) there is only one ellipsoidal carrier pocket for the materials system of interest and (b) there is only one dominant electron scattering mechanism.

Using Sommerfeld's definition for the Fermi-Dirac integral of order j /BLA82/:

$$F_j(\eta^*) = \int_0^{\infty}\frac{r^j}{\exp^{r-\eta^*}+1}dr \quad (j > -1) \tag{A2-24}$$

and combining Equations A2-21, A2-22 and A2-23, the kinetic transport coefficients, the Lorenz number and the carrier concentration can be reformulated. In the case of a parabolic band (m^* = m^*_{cond}), it leads to:

$$S = \frac{k_B}{r}\left[\frac{\lambda + \frac{5}{2}F_{\lambda+\frac{3}{2}}(\eta^*)}{\lambda + \frac{3}{2}F_{\lambda+\frac{1}{2}}(\eta^*)} - \eta^*\right] \quad \text{(A2-25)}$$

$$\sigma = \frac{8\pi a r^2}{3m^*}\left(\frac{2m^* k_B T}{h^2}\right)^{\frac{3}{2}}(k_B T)^{\lambda+\beta}\left(\frac{3}{2}+\lambda\right)F_{\lambda+\frac{1}{2}}(\eta^*) \quad \text{(A2-26)}$$

$$\kappa_e = L\sigma T \quad \text{(A2-27)}$$

$$L = \left(\frac{k_B}{r}\right)^2\left(\frac{\left(\frac{7}{2}+\lambda\right)F_{\lambda+\frac{5}{2}}(\eta^*)}{\left(\frac{3}{2}+\lambda\right)F_{\lambda+\frac{1}{2}}(\eta^*)} - \left(\frac{\left(\frac{5}{2}+\lambda\right)F_{\lambda+\frac{3}{2}}(\eta^*)}{\left(\frac{3}{2}+\lambda\right)F_{\lambda+\frac{1}{2}}(\eta^*)}\right)^2\right) \quad \text{(A2-28)}$$

$$p = 4\pi\left(\frac{2m^* k_B T}{h^2}\right)^{\frac{3}{2}}F_{\frac{1}{2}}(\eta^*) \quad \text{(A2-29)}$$

In general, Fermi-Dirac integrals can be calculated numerically, but there are two limit cases in which the integrals are simplified. The first case, also called the nondegenerate approximation, is when the Fermi level is negative and remote from the band edge for a few $k_B T$ (at least $2k_B T$). In this approximation, we can neglect 1 in the denominator of Equation A2-24 :

$$F_j(\eta^*) \approx \Gamma(j+1)\exp^{\eta^*} \quad (\eta^* \ll -1), \quad \text{(A2-29)}$$

where Γ is the Gamma function with $\Gamma(1/2) = \sqrt{\pi}$, $\Gamma(3/2) = \sqrt{\pi}/2$ and $\Gamma(p+1) = p\Gamma(p)$ where p is an integer.

In the second limit case (called degenerate approximation) the Fermi level is positive and remote from the band edge for a few $k_B T$ (at least $2k_B T$). Then we have:

$$F_j(\eta^*) \approx \frac{\eta^{*j+1}}{j+1}\left(1 + \frac{\pi^2 j(j+1)}{6\eta^{*2}}\right) \quad (\eta^* \gg 1), \tag{A2-30}$$

These two approximations are used in chapter V to derive the thermopower and the electrical resistivity at low (degenerate approximation) and high (non degenerate approximation) temperature.

APPENDIX 3

Finite Element COMSOL Modeling

The modeling of the thermoelectric performance of any module working either in refrigeration or power generation mode is not straightforward due to the complexity of the coupled differential equations that should be solved. Despite simple analytical solutions, often based on crude assumptions, can provide a first rough estimation, numerical techniques are highly desirable to take into account all the physical phenomena. Among all the available numerical programs, the COMSOL software package provides a lot of flexibility both in the manipulation of the governing equations and the selection of appropriate solvers. Whereas competitors have constrained equations governing thermoelectric effects, COMSOL permits the user to select which terms to incorporate, such as the Thomson heat, to determine the overall impact on the module performance. This ability to alter the governing equations is critical to determining which models are appropriate under specific conditions and thus COMSOL proves to be an ideal tool for this study. COMSOL is based on the finite elements or volume analysis.

Generally, the steps for finite elements or volume analysis are:

1. Selection of the general governing physics (viz. heat transfer),
2. Creation of appropriate subdomains (geometries),
3. Application of appropriate boundary and subdomain conditions (viz. temperatures, insulation, grounding, internal heating, etc.),
4. Meshing of the subdomains into an appropriate number of elements,
5. Selecting and utilizing a solver algorithm,
6. Postprocessing to acquire pertinent information.

The general form of the first steady-state coupled governing equations that dictate the thermoelectric behavior within and on a subdomain is the following:

$$\mathbf{q} = T \cdot S \cdot \mathbf{J} - \kappa \cdot \nabla T, \tag{A3-1}$$

where $\mathbf{q}$ is the vector form of the heat flux on a boundary of a thermoelectric subdomain (volume), S, the Seebeck coefficient, $\mathbf{J}$ the vector describing the current flux on a boundary, κ the thermal conductivity and T the absolute temperature. Equation (A3-1) demonstrates the combination of the Peltier effect and the Fourier law. The second important equation defines $\mathbf{J}$

and has the following form:

$$\mathbf{J} = \sigma(\mathbf{E} - S \cdot \nabla T), \tag{A3-2}$$

where σ is the electrical conductivity and $\mathbf{E}$ is the electric field vector. In other words, it is a combination of the Ohm's law and the Seebeck effect.

The thermoelectric legs also are governed by the following equations:

$$\nabla \cdot \mathbf{q} = Q_{Joule}\,, \tag{A3-3}$$

$$\nabla \cdot \mathbf{J} = 0\,, \tag{A3-4}$$

which conclude that the internal "Joule" heating is present within the thermoelectric legs and that the current is conserved. Q_{Joule} appearing in (A3-3) represents the heat dissipated per unit time and volume. Several forms of internal heating are present and are given by:

$$Q_{Joule} = \mathbf{J}^2/\sigma = \mathbf{E}\cdot\mathbf{J} - S\nabla T \cdot \mathbf{J} \tag{A3-5}$$

Combining Eq. A3-1 – A3-5, we can derive the general heat equation:

$$T\mathbf{J} \cdot \nabla S + \frac{dS}{dT} T\nabla T \cdot \mathbf{J} - \nabla(\kappa \nabla T) = \mathbf{J}^2/\sigma, \tag{A3-6}$$

The first term of Eq. (A3-6), which can be considered as a bulk Peltier effect, is usually nil since the gradient of the Seebeck coefficient is zero unless the leg has functionally graded doping. The second term describes the Thomson heat, which accounts for the electric potential change due to the temperature dependence of the Seebeck coefficient. The last term is the heat dissipated due to the Fourier law. Any metal or ceramic is assumed to have S = 0 and any ceramic is assumed to have σ = 0. These assumptions permit the use of all above governing equations in any material subdomain (see Fig. A3-1 for our case).

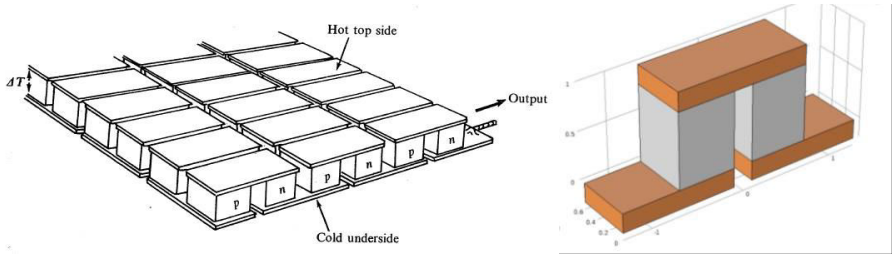

Figure A3-1: a) Schematic multicouple arrangement and b) Finite elements analysis model of a pair of *n*- and *p*-legs also called thermocouple using COMSOL, where the gray color corresponds to the thermoelectric *n*- and *p*-materials, and the brown color to the metallic electrodes.

One of the main motivation of using COMSOL was to get a simple access to the performance of a thermocouple and verify if the combination of the materials prepared in the behalf of this project (*p*-type of IJL and *n*-type of CRISMAT) can compete with commercial modules. One way to probe the thermoelectric figure of merit of a thermocouple, Z_{np}, is to calculate the maximum temperature difference ΔT_{max} at the ends of the thermocouple (this case corresponds to the situation where the boundary condition for heat at the cold side is zero). Actually, it can be shown that $\Delta T_{max}$is directly related Z_{np} through the following relation:

$$\Delta T_{max} \sim \frac{1}{2} Z_{np} {T_c}^2, \tag{A3-7}$$

where T_c is the temperature at the the cold side.

As a reference for our modeling, we used the Melcor (one of the most important commercial producer of thermoelectric modules) material property data for both *p*-type and *n*-type Bi_2Te_3 based compounds. The geometrical dimensions of the two legs were the same (1.3 mm x 1 mm x 1 mm).

The results deduced from COMSOL can be seen in Fig. A3-2. The maximum temperature drop was found to be 63.1°C when applying 3.7 A of current if the hot side temperature is fixed to room temperature (25°C).

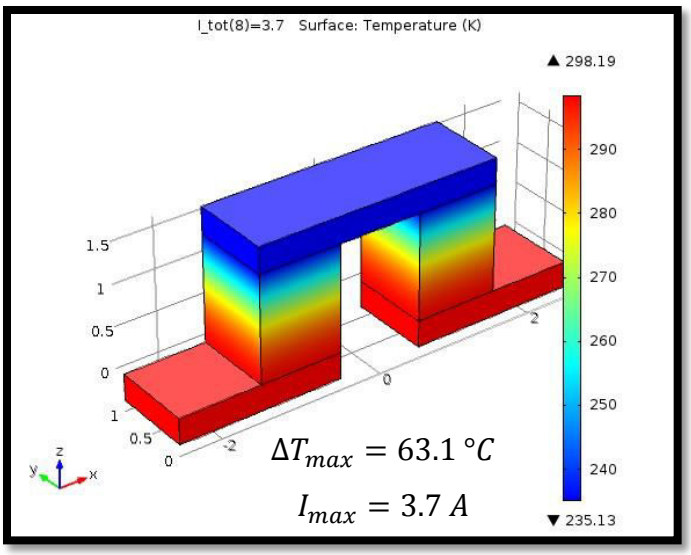

Figure A3-2: Temperature profil of a thermocouple based on Melcor commercial materials. The dimensions, effective ΔT_{max} and I_{max} are mentioned.

Then, the modeling of the thermocouple (assuming the same geometry) but using the thermoelectric properties obtained in the frame of this project was performed. The *p*-type transport properties were chosen from samples prepared during this thesis while the properties of the material for the *n*-type leg was provided by Dr Quentin Lognone as a result of his PhD work performed in the laboratory of CRISMAT (Caen, France). The results can be seen in Fig. A3-3. The maximum temperature drop was 65.2°C for a current of 3.3 A. This corresponds to an improvement of 3%. Higher improvement could be reached if the *n*-type leg had better thermoelectric properties.

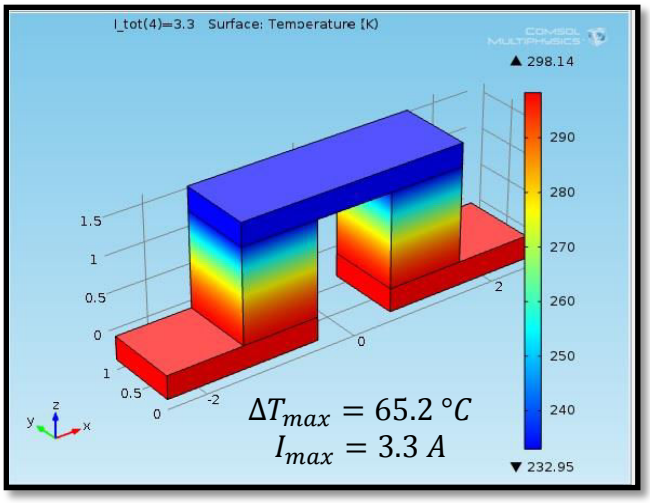

Figure A3-3: Temperature profile of a thermocouple based on materials developed in this project. The dimensions, effective ΔT_{max} and I_{max} are mentioned.

COMSOL Multiphysics proved to be a powerful tool to get an idea about the performance of the thermocouple without creating a physical prototype, saving time, forces and materials. We showed that the thermoelectric figure of merit of the thermocouple from the materials obtained in this project demonstrates advanced performance compared to the commercial one. Further improvements can be achieved if the geometry of the module is revised (to see depending on the paragraph).

BIBLIOGRAPHY:

/ABR77/ Abrikosov N.Kh., Bankina V.F., Kolomoets L.A., Dzhaliashvili N.V. (1977) Izv. Akad. Nauk. SSSR, Neorg. Mater., 13, 827.

/ABR78/ Abrikosov N.Kh., Svechnikov, T.E., Chijevskaya, S.N. (1978) Izv. Akad. Nauk. SSSR, Neorg. Mater., 14, 43.

/ABR79a/ Abrikosov, N.Kh., Ivanova, L.D., Aladashvili, M.S. (1979) Izv. A.N. SSSR, Neorg. Mat., 15, 1766.

/ABR79b/ Abrikosov, N.Kh., Ivanova, L.D. (1982) Izv. A.N. SSSR, Neorg. Mat., 15, 1181.

/ABR80/ Abrikosov N.Kh., Porestskaya, L.V., Basheleishvili, Z.V. (1980) Izv. Akad. Nauk. SSSR, Neorg. Mater., 16, 1390.

/ABR81/ Abrikosov N.Kh., Danilova – Dobryakova, G.T. (1981) Izv. Akad. Nauk. SSSR, Neorg. Mater., 17, 606.

/ABR82a/ Abrikosov, N.Kh., Ivanova, L.D. (1982) Izv. A.N. SSSR, Neorg. Mat., 18, 560.

/ABR82b/ Abrikosov N.Kh., Danilova – Dobryakova, G.T. (1982) Izv. Akad. Nauk. SSSR, Neorg. Mater., 18, 565.

/ABR83/ Abrikosov N.Kh., Porestskaya, L.V. (1983) Izv. Akad. Nauk. SSSR, Neorg. Mater., 19, 388.

/ALT09/ Altenkirch, E. (1909) Phys. Zeits., 10, 560.

/ALT11/ Altenkirch, E. (1911) Phys. Zeits., 12, 920.

/AND06/ Androulakis, J., Hsu, K.F., Pcionek, R., Kong, H., Uher, C., D'Angelo, J.J., Downey, A., Hogan, T., Kanatzidis, M.G. (2006). Adv. Mater., 18, 1170.

/AND07/ Androulakis, J., Lin, C.H., Kong, H.J., Uher, C., Wu, C.I., Hogan, T., Cook, B.A., Caillat, T., Paraskevopoulos, K.M., Kanatzidis, M.G. (2007) J. Am. Chem. Soc., 129, 9780.

/AND11/ Androulakis, J., Todorov, I., He, J., Chung, D.Y., Dravid, V., Kanatzidis, M. (2011) J. Am. Chem. Soc., 133, 10920.

/ASH76/ Ashcroft, N.E., Mermin, N.D. (1976) Solid state phisics, Saunders College Publishing, New York.

/BAL82/ Balageas, D. L. (1982) Rev. Phys. Appl., 17, 227.

/BAN95/ Bandhari, C.M. (1995) in CRC Handbook of Thermoelectrics, M. Rowe (Ed.), CRC Press, Boca Raton, F.L., 55.

/BAR76/ Barash, A.S., Zhukova, T.B., Parparov, E.Z. (1976) Izv. A.N. SSSR, Neorg. Mat., 12, 1552.

/BAS80/ Bass, J.C., Elsner, N.B. (1980) Proc. III Inter. Conf. on Thermoelectric Energy Conversion, Arlington, U.S.A., 8.

/BER10/ Berardan, D., Byl, C., Dragoe, N. (2010) J. Am. Chem. Soc., 93, 2352.

/BHA13/ Bhame, S.D., Pravarthana, D., Prellier, W., Noudem, J.G. (2013) Appl. Phys. Lett., 102, 211901.

/BIR06/ Birkholz, M. (2006) Thin Film Analysis by X-ray Scattering. John Wiley & Sons.

/BIR58/ Birkholz, Z. (1958) Naturforsch A, 13, 780.

/BIR89/ Birkholz, U. (1989) Proc. 8th Inter. Conf. Thermoelectric Energy Conversion, Nancy, France, 98.

/BIR95/ Birkholz, U., Gross, E., Stöhrer, U. (1995) in CRC Handbook of Thermoelectrics, M. Rowe (Ed.), CRC Press, Boca Raton, F.L., 287.

/BIS11/ Biswas, K., He, J., Zhang, Q., Wang, G., Uher, C., Dravid, V.P., Kanatzidis, M.G. (2011) Nature Chem., 3, 160.

/BIS12/ Biswas, K., He, J., Blum, I.D., Wu, C.I., Hogan, T.P., Seidman, D.N., Dravid, V.P., Kanatzidis, M.G. (2012) Nature, 489, 414.

/BLA57/ Black, J., Conwell, E.M., Seigle, L., Spencer, C.W. (1957) J. Phys. Chem. Solids, 2, 240.

/BLA82/ Blakemore, J.S. (1982) Solid-State Electronics, 25, 1067.

/BLU02/ Blumm, J., Opfermann, J. (2002) High Temp. - High Press. 34, 515.

/BOE08/ Boettner, H., Ebling, D., Jacquot, A., Kühn, U., Schmidt, J. (2008) Mater. Res. Soc. Symp. Proc., Vol. 1044, U04-01.

/BOE93/ Boettinger, W.J, Perepezko, J.H. (1993) in Rapidly Solidified Alloys: Processes, Structures, Properties, Applications. Liebermann HH. (Ed.) New York: Marcel Dekker Inc.

/BOU08/ Boukai, A.I., Bunimovich, Y., Tahir-Kheli, J., Yu, J.K., Goddard, W.A., Heath J. R. (2008) Nature, 451, 168.

/BRE69/ Brebrick, R.F. (1969) J. Phys. Chem. Solids, 30, 719.

/BRO06/ Brown, S.R., Kauzlarich, S.M., Gascoin, F., Snyder, G. (2006) J. Chem. Mater., 18, 1873.

/BUB11/ Bubnova, O., Khan, Z.U., Malti, A., Braun, S., Fahlman, M., Berggren, M., Crispin, X. (2011) Nature Mater.10, 429.

/BUX09/ Bux, S.K., Blair, R.G., Gogna, P.K., Lee, H., Chen, G., Dresselhaus, M.S., Kaner, R. B., Fleurial, J.-P. (2009) Adv. Funct. Mater., 19, 2445.

/BUX10/ Bux, S.K., Fleurial, J.-P., Kaner, R.B. (2010) Chem. Com., 46, 8311.

/BUX11/ Bux, S.K., Yeong, M.T., Toberer, E.S., Snyder, G.J., Kaner, R.B., Fleurial, J.-P. (2011) J. Mater. Chem., 21, 12259.

/BYR06/ Byrne, C.J., Theisen, E.A., Reed, B.L., Steen, P.H. (2006) Metall. Mater. Transact., 37B, 445.

/CAH03/ Cahill, D.G., Ford, W.K., Goodson, K.E., Mahan, G.D., Majumdar, A., Maris, H.J., Merlin, R., Phillpot, S.R. (2003) J. Appl. Phys., 93, 793.

/CAI91/ Caillat T. (1991) Doctoral Thesis, INPL, France.

/CAI92a/ Caillat, T., Carle, M., Perrin, D., Scherrer, H., Scherrer, S. (1992) J. Phys. Chem. Solids, 53, 227.

/CAI92b/ Caillat, T., Carle, M., Pierrat, P., Scherrer, H., Scherrer, S. (1992) J. Phys. Chem. Solids, 53, 1121.

/CAI93/ Caillat, T., Gailliard, L., Scherrer, H., & Scherrer, S. (1993). J. Phys. Chem. Solids, 54, 575.

/CAI97a/ Caillat, T., Fleurial, J.-P., Borshchevsky, A. (1997) J. Phys. Chem. Solids, 58, 1119.

/CAI97b/ Caillat, T., Fleurial, J.-P., Borshchevsky, A. (1997) Mat. Res. Soc. Symp. Proc., 478, 103.

/CAI99/ Caillat, T., Fleurial, J-P., Snyder, G.J., Zoltan, A., Zoltan, D., Borshchevsky, A. (1999) Proc. XVII Inter. Conf. on Thermoelectrics, Baltimore, USA, 473.

/CAL59/ Callaway, J. (1959) Phys. Rev., 113, 1046.

/CAL60/ Callaway, J., von Baeyer, H. C. (1960). Phys. Rev., 120, 1149.

/CAN78/ Cantor, B. (Ed.) (1978) Rapidly Quenched Metals III, Metals Society, London.

/CAO08/ Cao, Y.Q., Zhao, X.B., Zhu, T.J., Zhang, X.B., Tu, J.P. (2008) Appl. Phys. Lett., 92, 143106.

/CAP63/ Cape, J. A., Lehman, G. W. (1963) J. Appl. Phys. 34, 1909.

/CAR14/ Carrete, J., Mingo, N., Curtarolo, S. (2014) Appl. Phys. Lett., 105, 101907.

/CAR97/ Carpenter, J. K., Steen, P. H. (1997) Intl. J. Heat Mass Transfer, 40, 1993.

/CAS79/ Castanet, R., Bergman, C., Mathieu, J. C. (1979) CALPHAD, 3, 205.

/CHA65/ Champness, C. H., Chiang, P. T., Parekh, P. (1965). Can. J. Phys., 43, 653.

/CHE01a/ Chen, G. (2001) Semiconductors and Semimetals, T. Tritt (Ed.), Academic Press, 71, 203.

/CHE01b/ Chen, L.D., Kawahara, T., Tang, X.F., Goto, T., Hirai, T., Dyck, J.S., Chen, W., Uher, C. (2001) J. Appl. Phys., 90, 1864.

/CHE05/ Chen, W., Anselmi-Tamburini, U., Garay, J.E., Groza, J.R., Munir, Z.A. (2005) Mater. Sci. Engin. A, 394, 132.

/CHE14/ Chen, Ch.-L., Wang, H., Chen, Y.-Y., Day, T., Snyder, G.J. (2014) J. Mater. Chem. A, 2, 11171.

/CHE80/ Chen, H., Leamy, H., Miller, C. (1980) Ann. Rev. Mater. Sci., 10, 363.

/CHI95/ Chizevskaya S.N., Shelimova, L.E. (1995) Int. J. Inorg. Mater., 31, 1083

/CHR10/ Christensen, M., Johnsen, S., Iversen, B.B. (2010) Dalton Trans., 39, 978.

/CHU11/ Chubilleau, C., Lenoir, B., Migot, S., Dauscher, A. (2011) J. Coll. Interf. Science, 357, 13.

/CLA75/ Clark III, L. M., Taylor, R. E. (1975) J. Appl. Phys., 46, 714.

/COC88/ Cochrane, R.W., Strom-Olsen, J.O. (1988) Eds, Rapidly Quenched Metals VI, Elsevier, London.

/COO96/ Cook, B.A., Harringa, J.L., Tan, Z.S., Jesser, W.A. (1996) Proc. XV Inter. Conf. on Thermoelectrics, Pasadena, USA, 122.

/COW61/ Cowan, R. D. (1961) J. Appl. Phys., 32, 1363.

/COW63/ Cowan, R. D. (1963) J. Appl. Phys., 34, 926.

/CRE99/ Creagh, D.C., Hubbel, J.H. (1999) International Tables for Crystallography C, (Eds.) Wilson, A. J. C., Prince, E., Kluwer, Dordrecht, 220.

/CUF63/ Cuff, K.F., Horst, R.B., Weaver, J.L., Hawkins, S.R., Kooi, C.F., Enslow, G.M. (1963) Appl. Phys. Lett., 2, 145.

/CUL06/ Culp, S.R., Poon, S.J., Hickman, N., Tritt, T.M., Blumm, J. (2006) Appl. Phys. Let., 88, 042106.

/CUL08/ Culp, S.R., Simonson, J.W., Poon, S.J., Ponnambalam, V., Edwards, J., Tritt, T.M. (2008) Appl. Phys. Let., 93, 022105.

/DAS11/ Dasgupta, T., Stiewe, C., Hassdorf, R., Zhou, A.J., Boettcher, L., Mueller, E. (2011) Phys. Rev. B, 83, 235207.

/DEG85/ Degiovanni, A. (1985) High Temp., High Press., 17, 683.

/DEG86/ Degiovanni, A., Laurent, M. (1986) Rev. Phys. Appl., 21, 229.

/DEN08/ Deng, S., Tang, X., Li, P., Zhang, Q. (2008) J. Appl. Phys., 103, 073503.

/DIE10/ Diez, J.C., Rasekh, S., Madre, M.A., Guilmeau, E., Marinel, S., Sotelo, A. (2010) J. Electr. Mat., 39, 1601.

/DIS64/ Dismukes, J.P., Ekstrom, L., Steigmeier, E.F., Beers, D.S. (1964) J. Appl. Phys., 35, 2899.

/DRE07/ Dresselhaus, M.S., Chen, G., Tang, M.Y., Yang, R.G., Lee, H., Wang, D.Z., Ren,

Z.F., Fleurial, J.P., Gogna, P. (2007) Adv. Mater., 19, 1043.

/DYC02/ Dyck, J.S., Chen, W., Uher, C., Drašar, Č., Lošťák, P. (2002) Phys. Rev. B, 66, 125206.

/EBL07a/ Ebling, D. G., Jacquot, A., Bottner, H., Schmidt, J., Spies, P. (2007) Proceedings Seventh International Workshop on Micro and Nanotechnology for Power Generation and Energy Conversion Applications (pp. 305-310).

/EBL07b/ Ebling, D.G., Jacqout, A., Jägle, M., Böttner, H., Kühn, U., Kirste, L. (2007) Phys. Stat. Sol. (RRL), 1, 238.

/EBL09/ Ebling, D.G., Jacquot, A., Bottner, H., Kirste, L., Schmidt, J., Aguirre, M. (2009) J. Electr. Mater., 38, 7.

/FAN06/ Fan, X.A., Yang, J.Y., Chen, R.G., Yun, H.S., Zhu,W., Bao, S. Q., Duan, X.K. (2006). J. Phys. D: Appl. Phys., 39, 740.

/FAN10/ Fan, S., Zhao, J., Guo, J., Yan, Q., Ma, J., Hng, H.H. (2010) Appl. Phys. Lett., 96, 182104.

/FAN14/ Fang, H., Luo, Zh., Yang, H., Wu, Y. (2014) Nano Lett., 14, 1153.

/FAU64/ Faure, J. (1964) "Détermination de la diffusivité thermique des isolants par la méthode du signal très bref", Rapport Ispra EUR - 1822-FR.

/FED14/ Fedotov, A.S., Svito, I.A., Gusakova, S.V., Shepelevich, V.G., Saad, A., Mazanik, A.V., Fedotov, A.K. (2014) Proceed. 12th European Conference on Thermoelectrics.

/FIS00/ Fisher, I.R., Bud'ko, S.L., Song, C., Canfield, P.C., Ozawa, T.C., Kauzlarich, S.M. (2000) Phys. Rev. Lett., 85, 1120.

/FLE88/ Fleurial J.P. (1988) Doctoral Thesis, INPL, France.

/FRI56/ Friedel, J. (1956) Canad. J. Phys., 34, 1190.

/FUKU10/ Fukuoka, H., Yamanaka, S., (2010) Chem. Mater., 22, 47.

/GAI89/ Gailliard L. (1989) Doctoral Thesis, INPL, France.

/GAO11/ Gao, H.L., Zhu, T., Liu, X., Chen, L., Zhao, X.B. (2011) J. Mater. Chem., 21, 5933.

/GAR99/ Garreau, S., Louam, G., Lefrant, S., Buisson, J.-P., Froyer, G. (1999) Synthetic Metals, 101, 312.

/GEL10/ Gelbstein, Y., Dado, B., Ben-Yehuda, O., Sadia, Y., Dashevsky, Z., Dariel, M.P. (2010) Chem. Mater., 22, 1054.

/GER02/ Gerovac, N., Snyder, G. J., Caillat, T. (2002) Proc. XXI Intern. Conf. Thermoelectrics, ICT'02, p.31.

/GIR10/ Girard, S.N., He, J., Li, C., Moses, S., Wang, G., Uher, C., Dravid, V.P., Kanatzidis, M.G. (2010) Nano Lett., 10, 2825.

/GLA64/ Glassbrenner, C. J., Slack, G. A. (1964) Physical Review, 34, A1058.

/GLA65/ Glatz, A.C. (1965) J. Electrochem. Soc., 112, 1204.

/GLA86/ Glazov, V.M.,Yatmanov, Yu.V. (1986) lzv. Akad. Nauk SSSR, Neorg. Mater., 22, 1, 36.

/GLA95/ Glazov, V.M., Potemkin, A.Ya., Akopyan, R.A. (1996) lzv. Akad. Nauk SSSR, Neorg. Mater, 32, 1277.

/GOG88/ Gogishvili, O.S., Lalikin, S.P., Krivoruchko, S.P., Pyrychidi, K.I., Zanava, E.S. (1988) VII "Chemistry, physics and technical application of chalcogenides" conference theses, Uzhhorod, 368.

/GOG91/ Gogishvili, O.S., Kononov, G.G., Krivoruchko, S.P., Lavrinenko, I.P., Ovsyanko, I.I. (1991) lzv. Akad. Nauk SSSR, Neorg. Mater., 27, 923.

/GOL09/ Goldsmid H. J. (2009) Introduction to Thermoelectricity, Springer Series in Materials Science, V. 121.

/GOL54/ Goldsmid H.J., Douglas R.W. (1954) Brit. J. Appl. Phys., 5, 386.

/GOL55/ Goldsmid, H J. (1955) Int. J. Electr., 1, 218.

/GOL58/ Goldsmid H.J., Sheard A.R., Wright D.A.(1958) Brit. J. Appl. Phys., 9, 365.

/GOL64/ Goldsmid, H. J. (1964). Thermoelectric Refrigeration, Plenum Press, New York.

/GOL68/ Goldsmid, H J., Underwood, F.A. (1968) Adv. Energy Conv., 7, 297.

/GOL73/ Goltsman B.M., Kudinov B.A., Smirnov I.A. (1973) Thermoelectric Semiconductor Materials Based on Bi_2Te_3 – Army Foreign Science and Technology Center.

/GOL86/ Goldsmid, H.J. (1986) Electronic Refrigeration, Pion Limited Publishing, London.

/GOL88/ Goldsmith, H.J., Gopinathan, K.K., Matthews, D.N., Taylor, K.N.R., Baird, C.A. (1988) J. Phys. D, 21, 344.

/GOL99/ Goldsmid, H. J., Sharp, J. W. (1999) J. Electr. Mater., 28, 869.

/GOO58/ Goodman, C.H.L. (1958) J. Phys. Chem. Solids, 6, 305.

/GRO03/ Groza, J.R., Zavaliangos, A. (2003) Rev. Adv. Mater. Sci., 5, 24.

/GUL59/ Gultyaev, P.V., Petrov, A.V. (1959) Sov. Phys., 1, 330.

/HAK10/ Haken, W. (1910) Ann. Phys., 32, 291.

/HAM10/ Harnwunggmoung, A., Kurosaki, K., Muta, H., Yamanaka, S. (2010) Appl. Phys. Lett., 96, 202107

/HAN58/ Hansen, M. (1958) Constitution of Binary Alloys, Mc Graw Hill, N.Y.

/HAR00/ Harman, T.C., Taylor, P.J., Spears, D.L., Walsh, M.P. (2000) J. Electron. Mater., 29, L1.

/HAR02/ Harman, T.C., Taylor, P.J., Walsh, M.P., LaForge, B.E. (2002) Science, 297, 2229.

/HAR55/ Harman, T.C., Miller, S.E., Goering, H.L. (1955) Phys. Rev., 100, 1262.

/HAR59/ Harman, T.C., Cahn, Logan, M.J. (1959) J. Appl. Phys. 30, 1351;

/HAR95/ Harringa, J., Cook, B., Han, S. (1995) CRC Handbook of Thermoelectrics, M. Rowe (Ed.), CRC Press, Boca Raton, F.L., 12-1.

/HAR96/ Harman, T.C., Spears, D.L., Manfra, M.J. (1996) J. Electron. Mater., 25, 1121.

/HAR99/ Harman, T.C., Spears, D.L., Walsh, M.P. (1999) J. Electron. Mater., 28, L1.

/HAS11/ Hashibon, A., Elsässer, C. (2011) Phys. Rev. B, 84, 144117.

/HE10/ He, J.Q., Sootsman, J.R., Girard, S.N., Zheng, J.C., Wen, J., Zhu, Y., Kanatzidis, M.G., Dravid, V.P. (2010) J. Am. Chem. Soc., 132, 8669.

/HE11/ He, J.Q., Sootsman, J.R., Xu, L. Q., Girard, S.N., Zheng, J.C., Kanatzidis, M.G., Dravid, V.P. (2011) J. Am. Chem. Soc., 133, 8786.

/HER03/ Hermann, R.P., Jin, R.J., Schweika, W., Grandjean, F., Mandrus, D., Sales, B.C., Long, G. (2003) Phys. Rev. Lett., 90, 135505.

/HER08/ Heremans, J.P., Jovovic, V., Toberer, E.S., Saramat, A., Kurosaki, K., Charoenphakdee, A., Yamanaka, Sh., Snyder, G.J. (2008) Science, 321, 554.

/HER12/ Heremans, J.P., Wiendlocha, B., Chamoire, A.M. (2012) Energy Environ. Sci., 5, 5510.

/HIC93a/ Hicks, L.D., Dresselhaus, M.S. (1993) Phys. Rev. B, 47, 12727.

/HIC93b/ Hicks, L.D., Harman, T.C., Dresselhaus, M.S. (1993) Appl. Phys. Lett., 63, 3230.

/HIC93c/ Hicks, L.D., Dresselhaus, M.S. (1993) Phys. Rev. B, 47, 16631.

/HIC96/ Hicks, L.D., Harman, T.C., Sun, X., Dresselhaus, M.S. (1996) Phys. Rev. B, 53, R10493.

/HOC08/ Hochbaum, A. I., Chen, R., Delgado, R. D., Liang, W., Garnett, E. C., Najarian, M., Majumdar, A., Yang, P. (2008) Nature 451, 163.

/HOM12/ Homer M.D., Medlin L. (2012) Microsc. Microanal., 18 (Suppl 2) 1482.

/HON64/ Honda, H., Sanada, Y., Inoue, K. (1964) Carbon 1, 127.

/HOR76/ Horak, J., Tichy, L., Lostak, P.,Vasko, A. (1976) Cryst. Lattice Defects, 6, 223.

/HOR80/ Horst, R.B., Williams, L.R. (1980) Proc. III Inter. Conf. on Thermoelectic Conversion, Arlington, USA, 183.

/HOR86/ Horak, J., Cermak, K., Koudelka, L. (1986) J. Phys. Chem. Solids, 47, 805.

/HOR88/ Horak, J., Stary, Z., Klikorka, J. (1988) Phys. Status Solidi, 147, 501.

/HOR90/ Horak, J., Stary, Z., Lostak, P., Pancir, J. (1990) J. Phys. Chem. Solids, 51, 1353.

/PEC94/ Pecheur, P., Toussaint, G. (1994) J. Phys. Chem. Solids, 55, 327

/HOR95/ Horak, J., Drasar, C., Novotny, R., Karamazov, S., Lostak, S. (1995) Phys. Status Solidi, 149, 549.

/HSU04/ Hsu, K.F., Loo, S., Guo, F., Chen, W., Dyck, J.S., Uher, C., Hogan, T., Polychroniadis, E.K., Kanatzidis, M.G. (2004) Science, 303, 818.

/HUA85/ Huang, S.C., Laforce, R., Ritter, A., Goehner, R. (1985) Met. Trans. A, 16, 1773.

/HYU01/ Hyun, D.B., Hwang, J.S., Shim, J.D., Oh, T.S. (2001) J. Mat. Sci., 36, 1285.

/IKE07/ Ikeda, T., Collins, L.A., Ravi, V.A., Gascoin, F.S., Haile, S.M., Snyder, G.J. (2007) Chem. Mater., 19, 763.

/IOF56/ Ioffe, A.F. (1956) Dokl. Akad. Nauk SSSR, 106, 981.

/IOF57a/ Ioffe, A.F. (1957) Semiconductor Thermoelements and Thermoelectric Cooling, Infosearch, London.

/IOF57b/ Ioffe, A.F., Airapetyants, S.V., Efimova, B.A., Stavitskaya, T.S., Stil'bans, L.S., Sysoeva, L.M., (1957) SSSR, Zh. Tekh. Fiz., 27, 2167.

/IOF60/ Ioffe, A. F. (1960) Physics of semiconductors. Infosearch, London.

/IVA13/ Ivanova, L.D., Petrova, L.I., Granatkina, Yu.V., Leontyev, V.G., Ivanov, A.S., Varlamov, S.A., Prilepo, Yu.P., Sychev, A.M., Chuik, A.G., Bashkov, I.V. (2013) Inorg. Mater., 49, 120.

/JAM74/ Jamet, J., Jalin, R., Letourneur, C. (1974) Recherche aérospatiale 4, 233.

/JAN94/ Jandl, P., Birkholz, U. (1994) J. Appl. Phys., 76, 7351.

/JAW09/ Jaworski, C.M., Kulbachinskii, V., Heremans, J.P. (2009) Phys. Rev. B, 80, 233201.

/JEN08/ Jeng, M.-S., Yang, R., Song D., Chen, G. (2008) J. Heat Transfer, 130, 042410.

/JIE13/ Jie, Q., Wang, H., Liu, W., Wang, H., Chen, G., Ren, Z. (2013) Phys. Chem. Chem. Phys., 15, 6809.

/JOH11/ Johnsen, S., He, J., Androulakis, J., Dravid, V.P., Todorov, I., Chung, D. Y., Kanatzidis, M. G. (2011) J. Am. Chem. Soc., 133, 3460.

/JOS08/ Joshi, G., Lee, H., Lan, Y., Wang, X., Zhu, G., Wang, D., Gould, R.W., Cuff, D.C., Tang, M.Y., Dresselhaus, M.S., Chen, G., Ren, Z. (2008) Nano Letters, 8, 4670.

/JOS11/ Joshi, G., Yan, X., Wang, H., Liu, W., Chen, G., Ren, Z. (2011) Adv. Ener. Mat., 1, 643.

/JOS95/ Josell, D., Warren, J., Cezairliyan, A. (1995) J. Appl. Phys., 78, 6867.

/JOV08/ Jovovic, V., Thiagarajan, S. J., Heremans, J. P., Komissarova, T., Khokhlov, D., Nicorici, A. (2008) J. Appl. Phys., 103, 053710.

/KAM12/ Kamal, M., Mohammad, U. (2012), A Review: Chill-Block Melt Spin Technique, Theories & Applications, Bentham e-Books.

/KAN01/ Kanatzidis, M.G. (2001) Semiconductors and Semimetals, T.M. Tritt, (Ed.), Academic Press, 69, 51.

/KAN09/ Kanatzidis, M. G. (2009) Chem. Mater., 22, 648 and references therein.

/KAT07/ Katsuyama, S., Okada, H. (2007) J. Jpn Soc. Powder & Powder Metal., 54, 375.

/KAU07/ Kauzlarich, S.M., Brown, S.R., Snyder, G. J. (2007) Dalton Trans., 2099.

/KEN12/ Kenfaui, D., Lenoir, B., Chateigner, D., Ouladdiaf, B., Gomina, M., Noudem, J.G. (2012) J. Eur. Cer. Soc., 32, 2405.

/KEP98/ Keppens, V., Mandrus, D., Sales, B.C., Chakoumakos, B.C., Dai, P., Coldea, R., Maple, M.B., Gajewski, D.A., Freeman, E.J., Bennington, S. (1998) Nature, 395, 876.

/KIM04/ Kim, S. S., Yamamoto, S., Aizawa, T. (2004). J. All. Comp., 375, 107.

/KIM06/ Kim, W., Zide, J., Gossard, A., Klenov, D., Stemmer, S., Shakouri A., Majumdar, A. (2006) Phys. Rev. Lett., 96, 045901.

/KIM13/ Kim, D.H., Kwon, I.H., Kim, C., Han, B., Im, H.-J., Kim, H. (2013) J. All. Comp., 548, 126.

/KIM98/ Kim, S.-G., Mazin, I.I., Singh, D.J. (1998) Phys. Rev. B, 57, 6199.

/KOG99/ Koga, T., Harman, T.C., Cronin S.B., Dresselhaus, M.S. (1999) Phys. Rev. B, 60, 14286.

/KOH76/ Kohler, H. (1976) Phys. Status Solidi B, 74, 591.

/KOH77/ Köhler, H., Freudenberger, A. (1977) Phys. Status Solidi B, 84, 195.

/KOU13/ Koumoto, K., Mori, T. (2013) Thermoelectric Nanomaterials, Springer Series, 193.

/KOV04/ Kovnir, K.A., Shevelkov, A.V. (2004) Russ. Chem. Rev., 73, 923-938.

/KUL00/ Kulbachinskii, V.A., Kaminskii, A.Yu., Kytin, V.G., Lost'ak, P., Drasar, C., de Visser, A. (2000) JETP, 90, 1081.

/KUL12/ Kulbachinskii, V.A., Kytin, V.G., Kudryashov, A.A., Lunin, R.A. (2012) J. Solid State Chem., 193, 83.

/KUO09/ Kuo, C.H., Jeng, M.S., Ku, J.R., Wu, S.K., Chou, Y.W., Hwang, C.S. (2009) J. Elec. Mater., 38, 1956.

/KUZ03/ Kuznetsov, V.L., Kuznetsova, L.A., Rowe, D.M. (2003) J. Phys. Condens. Matter, 15, 5035.

/LAL11/ LaLonde A.D., Pei Y., Snyder G.J. (2011) Energy Environ. Sci., 4, 2090.

/LAN09/ Lan, Y., Poudel, B., Ma, Y., Wang, D., Dresselhaus, M. S., Chen, G., Ren, Z. (2009) Nano Letters, 9, 1419.

/LAN10/ Lan, Y., Minnich, A.J., Chen, G., Ren, Z. (2010) Adv. Funct. Mat., 20, 357.

/LAN39/ Lange P. W. (1939) Naturwissenschaften, 27(8), 133.

/LAR00/ Larson, P., Mahanti, S.D., Kanatzidis, M.G. (2000) Phys. Rev. B, 61, 8162.

/LAT09/ Latessa, G., Brunetti, F., Reale, A., Saggio, G., Di Carlo, A. (2009) Sensors and Actuators B: Chemical, 139, 304.

/LEE14/ Lee, D.H., Lee, J.U., Jung, S.J., Baek, S.H., Kim, J.H., Kim, D.I., Hyun, D.B., Kim, J.S. (2014) J. Electr. Mater., 43, 2255.

/LEN01/ Lenoir, B., Scherrer, H., Caillat, T. (2001) Semiconductors and Semimetals, 69, 101.

/LEN96/ Lenoir, B., Cassart, M., Michenaud, J.-P., Scherrer, H., Scherrer, S. (1996) J. Phys. Chem. Solids, 57, 89.

/LEN98/ Lenoir, B., Dauscher, A., Cassart, M., Ravich, Yu. I., Scherrer H. (1998) J. Phys. Chem. Solids, 59, 129.

/LI06/ Li, J. F., Liu, J. (2006) Phys. Stat. Sol. (A) Appl. Mater., 203, 3768.

/LI08a/ Li, H., Tang, X., Su, X., Zhang, Q. (2008) Appl. Phys. Lett., 92, 202114.

/LI08b/ Li, J.Q., Feng, X.W., Sun, W.A., Ao, W.Q., Liu, F.S., Du, Y. (2008) Mater. Chem. Phys., 112, 57.

/LI08c/ Li, S., Soliman, H., Zhou, J., Toprak, M., Muhammed, M., Platzek, D., Ziolkowski, P., Müller, E. (2008) Chem. Mater., 20, 4403.

/LI09/ Li, H., Tang, X., Zhang, Q. (2009) J. Elec. Mat., 38, 1224.

/LI09/ Li, H., Tang, X., Zhang, Q., Uher, C. (2009) Appl. Phys. Lett., 94, 102114.

/LI09a/ Li, H., Tang, X., Su, X., Zhang, Q., Uher, C. (2009) J. Phys.D : Appl. Phys., 42, 145409.

/LI12/ Li, J., Sui, J., Pei, Y., Barreteau, C., Berardan, D., Dragoe, N., Cai, W., He, J., Zhao, L. D. (2012) Energy Envir. Science, 5, 8543.

/LI12a/ Li, G., Gadelrab, K.R., Souier, T., Potapov, P.L., Chen, G., Chiesa, M. (2012) Nanotechnol., 23, 065703.

/LIT98/ Littleton, R.T., Tritt, T.M., Feger, C.R., Kolis, J., Wilson, M.L., Marone, M. (1998) Appl. Phys. Lett. 72, 2056.

/LIU07/ Liu, W.-S., Zhang, B.-P., Li, J.-F., Zhao, L.-D. (2007) J. Phys. D: Appl. Phys. 40, 566.

/LIU10/ Liu, W., Tang, X.F., Sharp, J. (2010) J. Phys. D, 43, 085406

/LIU12a/ Liu, W., Tan, X., Yin, K., Liu, H., Tang, X., Shi, J., Zhang, Q., Uher, C. (2012) Phys. Rev. Lett. 108, 166601.

/LIU12b/ Liu, W., Yan, X., Chen, G., Ren, Zh. (2012) Nano Energy 1, 42.

/LOG14/ Lognoné, Q., Gascoin, F., Lebedev, O.I., Lutterotti, L., Gascoin, S., Chateigner, D. (2014) J. Amer. Ceram. Soc., 1.

/LOS93/ Lošťák, P., Navratil, J., Šrámkova, J., Horak, J. (1993) Phys. Stat. Sol. A, 135, 519.

/LUK12/ Lukas, K.C., Liu, W.S., Joshi, G., Zebarjadi, M., Dresselhaus, M.S., Ren, Z.F., Chen, G., Opeil, C.P. (2012) Phy. Rev. B, 85, 205410.

/MA08/ Ma, Y., Hao, Q., Poudel, B., Lan, Y., Yu, B., Wang, D., Chen, G., Ren, Zh. (2008) Nano Lett., 8, 2580.

/MAH98/ Mahan, G.D. (1998) In Solid State Physics, Ehrenreich, H., Spaefen, F. (Ed.), Academic Press, 51, 81.

/MAI02/ Maier, D. (2002) Solid State Comm. 122, 565.

/MAI93/ Maillet, D., André, S., Degiovanni, A. (1993) J. Phys. III, 883.

/MAL68/ Mallinson, R.B., Rayne, J.A., Ure, R.W. (1968) Phys. Rev., 175, 1049.

/MAL92/ Maldonado, O. (1992) Cryogenics 32, 908.

/MAN02/ Manyakin, S.M., Volkov, M.P. Proc.V.21" Int. Conf. Thermoelectrics, USA (2002), p.21.

/MAR09/ Mars, K., Ihou-Mouko, H., Pont, G., Tobola, J., Scherrer, H. (2009). J. Electr. Mat., 38, 1360.

/MAR13/ Martín-González, M., Caballero-Calero, O., Díaz-Chao, P. (2013) Ren. Sustain. Ener. Rev., 24, 288.

/MAR98/ Martin-Lopez, R., Zayakin, Z., Lenoir, B., Brochin, F., Dauscher A., Scherrer, H. (1998) Philos. Mag. Lett., 78, 283.

/MAS82/ Masumoto, T., Suzuki, K. (1982) Eds, Rapidly Quenched Metals IV, Japan Institute of Metals, Sendai.

/MED09/ Medlin, D.L., Snyder, G.J. (2009) Curr. Opin. Coll. Interf. Sci.,14, 226.

/MIL65/ Miller, G.R., Li, C. (1965) J. Phys. Chem. Solids, 26, 173.

/MIN09/ Minnich, A.J., Dresselhaus, M.S., Ren, Z.F., Chen, G. (2009) Energy Environ. Sci. 2, 466.

/MOR97/ Morelli, D.T., Meisner, G.P., Chen, B.X., Hu, S.Q., Uher, C. (1997) Phys. Rev. B, 56, 7376.

/NAV91/ Navratil, J., Lošťák, P., Horák, J. (1991) Cryst. Res. Techn., 26, 675.

/NAV96/ Navratil, J., Starý, Z., Plechacek, T. (1996) Mater. Res. Bull., 31, 1559.

/NGU12/ Nguyen, P.K., Lee' K.H., Moon, J., Kim, S.I., Ahn, K.A., Chen, L.H., Lee, S.M., Chen, R.K., Jin, S., Berkowitz, A.E. (2012) Nanotechnol., 23, 415604.

/NIK61/ Nikitin, E.N., Bazanov, V.G., Tarasov, V.I. (1961) Sov. Phys. Solid State, 3, 2648.

/NOL00a/ Nolas, G.S., Kaeser, M., Littleton, R.T., Tritt, T.M. (2000) Appl. Phys. Lett., 77, 1855.

/NOL00b/ Nolas, G.S., Takizawa, H., Endo, T., Sellinschegg, H., Johnson, D.C. (2000) Appl. Phys. Lett., 77, 52.

/NOL01/ Nolas, G.S., Slack, G.A., Schujman, S.B. (2001) Semiconductors and Semimetals, T.M. Tritt (Ed.), Academic Press, 69, 255.

/NOL04/ Nolas, G.S., Yang, J., Takizawa, H. (2004) Appl. Phys. Lett., 84, 5210.

/NOL98a/ Nolas, G.S., Cohn, J.L., Slack, G.A., Schujman, S.B. (1998) Appl. Phys. Lett., 73, 178.

/NOL98b/ Nolas, G.S., Cohn, J.L., Slack, G.A. (1998) Phys. Rev. B, 58, 164.

/OHT08/ Ohta, H., Mune, Y., Koumoto, K., Mizoguchi, T., Ikuhara, Y. (2008) Thin Sol. Films, 516, 5916.

/OHT96/ Ohtaki M, Tsubota T, Eguchi K, Arai H. (1996) J. Appl. Phys., 79, 1816.

/OLE85/ Oleshko, E.V., Korolyshin, V.N. (1985) Soviet Phys., Solid State, 27, 1723.

/OMO00/ Omori, M. (2000) Mat. Sci. Eng. A, 287, 183.

/PAR61/ Parker, W. J., Jenkins, R. J., Butler, C. P., Abbott, G. L. (1961) J. Appl. Phys., 32, 1679.

/PEC94/ Pecheur, P., Toussaint, G. (1994) J. Phys. Chem. Solids, 55, 327.

/PEI06/ Pei, Y.Z., Chen, L.D., Zhang, W., Shi, X., Bai, S.Q., Zhao, X.Y., Mei, Z.G., Li, X.Y. (2006) Appl. Phys. Lett. 89, 221107.

/PEI08/ Pei, Y.Z., Bai, S.Q., Zhao, X.Y., Zhang, W., Chen, L.D. (2008) Solid State Sci., 10, 1422.

/PEI09/ Pei, Y.Z., Yang, J., Chen, L.D., Zhang, W., Salvador, J.R., Yang, J.H. (2009) Appl. Phys. Lett., 95, 042101.

/PEI11/ Pei, Y., LaLonde, A.D., Iwanaga, S., Snyder, G.J. (2011) Energy Environ. Sci., 4, 2085.

/PEL34/ Peltier, J.C. (1834) Ann. Chim., LVl 371.

/PER07/ Peranio N., Eibl O. (2007) Phys. Stat. Sol. (a), 204, 3243.

/PER08/ Peranio N., Eibl O. (2008) J. Appl. Phys., 103, 024314.

/POU06/ Poudeu, P.F.P, D'Angelo, J., Downey, A.D., Short, J.L., Hogan, T.P., Kanatzidis, M.G. (2006) Ang. Chem. - International Edition, 45, 3835.

/POU08/ Poudel, B., Hao, Q., Ma, Y., Lan, Y., Minnich, A., Yu, B., Yan, X., Wang, D., Muto, A., Vashaee, D., Chen, X., Liu, J., Dresselhaus, M.S., Chen, G., Ren, Z. (2008) Science, 320, 634.

/POU09/ Poudeu, P.F.P., Guéguen, A., Wu, C.-I., Hogan, T., Kanatzidis, M.G. (2009) Chem. Mat., 21, 1683.

/PUY04/ Puyet, M., Lenoir, B., Dauscher, A., Dehmas, M., Stiewe, C., Muller, E. (2004) J. Appl. Phys., 95, 4852.

/RAV70/ Ravich, Y.I., Efimova, B.A., Smirnov, I.A. (1970) Semiconducting Lead Chalcogenides, L.S. Stilbans (Ed.), Plenum Press, New York.

/REC07/ Recknagel, C., Reinfried, N., P, H., Schnelle, W., Rosner, H., Yu, G., Leithe-Jasper, A. (2007) Sci. Technol. Adv. Mater., 8, 357.

/ROS59/ Rosi, F.D., Abeles, B., Jensen, R.V. (1959) J. Phys. Chem. Solids, 10, 191.

/ROS61/ Rosi, F.D., Hocking, E.F., Lindenblad, N.E. (1961) RCA Rev., 22, 82.

/ROS68/ Rosi, F.D. (1968) Solid-State Electronics, 11, 833.

/ROW12a/ Rowe, D.M (Ed). (2012) Thermoelectrics and Its Energy Harvesting – Materials, Preparation and Characterization in Thermoelectrics, CRC Press, V1.

/ROW12b/ Rowe, D.M (Ed). (2012) Thermoelectrics and Its Energy Harvesting – Modules, Systems and Applications in Thermoelectrics, CRC Press, V2.

/ROW74/ Rowe, D.M. (1974) J. Phys. D, 7, 1843.

/ROW81/ Rowe, D.M., Shukla, V., Savvides, N. (1981) Nature, 290, 765.

/ROW83/ Rowe, D.M., Bhandari, C.M. (1983) Modern Thermoelectrics, Reston Publishing Co., Reston, VA.

/ROW95/ Rowe, D.M. (1995) CRC Handbook of Thermoelectrics, CRC Press, Boca Raton, FL.

/SAL00/ Sales, B.C., Chakoumakos, B.C., Mandrus, D. (2000) Phys. Rev. B, 61, 2475.

/SAL13/ Salvador J.R., Waldo, R.A., Wong, C.A., Tessema, M., Brown, D.N., Miller, D.J., Wang, H., Wereszczak, A.A., Cai, W. (2013) Mater. Sci. Eng. B, 178, 1087.

/SAL60/ Salli, I.V., Miroshnichenko, I.S. (1960) Dok. Akad. Nauk SSSR, 132, 557.

/SAN11/ Santhanam, S., Takas, N. J., Nolting, W. M., Poudeu, P. F., Stokes, K. L. (2011) In MRS Proceedings, V. 1329.

/SAS14/ Sassi, S., Candolfi, C., Vaney, J.B., Ohorodniichuk, V., Masschelein, P., Dauscher, A., Lenoir, B. (2014) Appl. Phys. Lett., 104, 212105.

/SAT57/ Satterwaite, C.B., Ure, R.W. (1957) J. Phys. Rev., 108, 1164.

/SCH62/ Schultz, J.M., McHugh, J.P., Tiller, W.A. (1962) J. Appl. Phys., 33, 2443.

/SEE23/ Seebeck, T.J. (1823) Abh. Akad. Wiss. Berlin, 265.

/SEH62/ Sehr, R., Testardi, L.R. (1962) J. Phys. Chem. Solids, 23, 1219.

/SHI08/ Shi, X., Kong, H., Li, C.P., Uher, C., Yang, J., Salvador, J.R., Wang, H., Chen, L., Zhang, W. (2008) Appl. Phys. Lett., 92, 182101.

/SHI10/ Shi, X., Yang, J., Bai, S., Yang, J., Wang, H., Chi, M., Salvador, J.R., Zhang, W., Chen, L., Wong, W. (2010) Adv. Func. Mater., 20, 755.

/SKR95/ Skrabek, E., Trimmer, D.S. (1995) In CRC Handbook of Thermoelectrics, M. Rowe (Ed.), CRC Press, Boca Raton, F.L., 267.

/SLA64/ Slack, G.A., Galginaitis, S. (1964) Phys. Rev., 133, A253.

/SLA74/ Slack, G.A. (1974) Solid State Phys., 34, 1.

/SLA95/ Slack, G.A. (1995) In CRC Handbook of Thermoelectrics, D.M. Rowe (Ed.), CRC Press, Boca Raton, FL, 407.

/SMI62a/ Smith, G.E., Wolfe, R (1962) J. Appl. Phys., 33, 841.

/SMI62b/ Smith, M.J., Knight, R.J., Spencer, C.W. (1962) J. Appl. Phys., 33, 2186.

/SON09/ Soni, A., Yanyuan, Z., Ligen, Y., Aik, M.K.K., Dresselhaus, M.S., Xiong, Q. (2012) Nano Lett., 12, 1203.

/SOO06/ Sootsman, J.R., Pcionek, R.J., Kong, H., Uher, C., Kanatzidis, M.G. (2006) Chem. Mater., 18, 4993.

/SOO08/ Sootsman, J.R., Kong, H., Uher, C., D'Angelo, J.J., Wu, C.I., Hogan, T.P., Caillat, T., Kanatzidis, M.G. (2008) Ang. Chem. – Intern. Ed., 47, 8618.

/SOO09/ Sootsman, J. R., Chung, D. Y., Kanatzidis, M. G. (2009) Ang. Chem. – Intern. Ed., 48, 8616 and references therein.

/STA88/ Stary Z., Horak J., Stordeur M., Stolzer M. (1988) J. Phys. Chem. Solids, 49, 29.

/STE85/ Steeb, S., Warlimont, H. (1985) Eds, Rapidly Quenched Metals V, North-Holland, Amsterdam.

/STE97/ Steen, P. H., Karcher, C. (1997) Ann. Rev. Fluid Mechanics, 29, 373.

/STO81/ Stordeur, M., Langhammer, H. T., Sobotta, H., Riede, V. (1981) Phys. Stat. Sol. B, 104, 513.

/STO86/ Stordeur M. (1986) Doctoral Thesis, Universität Halle-Wittenberg.

/STO88/ Stordeur, M., Stölzer, M., Sobotta, H., Riede, V. (1988) Phys. Stat. Sol. B, 150, 165.

/STR08/ Strange, E.H., Pim, C. A. (1908) U.S.Patent No.905758.

/SUI13/ Sui, J., Li, J., He, J., Pei, Y. L., Berardan, D., Wu, H., Dragoe, N., Cai, W., Zhao, L. D. (2013) Energy Environ. Sci., 6, 2916.

/SUN99/ Sun, X., Zhang, Z., Dresselhaus, M.S. (1999) Appl. Phys. Lett., 74, 4005.

/SUR01/ Suryanarayana, C. (2001) Prog. Mater. Sci., 46, 1.

/SUS76/ Susmann, H., Loof, K. (1976) Phys. Stat. Sol. A, 37, 467.

/TAN07/ Tang, X., Xie, W., Li, H., Zhao, W., Zhang, Q. (2007) Appl. Phys. Lett., 90, 012102.

/TAN11/ Tang, M.Y. (2011) Doctoral Thesis, MIT, USA.

/TAN13/ Tan, G., Liu, W., Wang, S., Yan, Y., Li, H., Tang, X., Uher, C. (2013) J. Mat. Chem. A, 1, 12657.

/TAY33/ Taylor, G. F. (1933) US Patent N° 1 896 854.

/TER02/ Terasaki, I., Murayama, N. (2002) Oxide Thermoelectrics. Trivandrum, India: Res. Signpost.

/TER97/ Terasaki, I., Sasago, Y., Uchinokura, K. (1997) Phys. Rev. B, 56, R12685.

/TES61/ Testardi, L. R., Wiese, J. R. (1961) Trans. Metall. Soc. AIME, 221, 647.

/THO07/ Thompson, K., Lawrence, D., Larson, D.J., Olson, J.D., Kelly, T.F., Gorman, B. (2007) Ultramicroscopy, 107, 131.

/THO51/ Thomson, W. (1851) Proc. Royal Soc. Edinburgh, 91.

/TOG70/ Togei, R., Miller, G.R. (1970) The Physics of Semimetals and Narrow-Gap Semiconductors, Carter D.L., Bate, R.T. (Eds), New York, Pergamon Press. pp 349-360.

/TOK93/ Tokida, J. (1993) Soc. Powder tech. Japon, 30, 790.

/TOK99/ Tokita, M. (1999) Mater. Sci. Forum 308-311, 83.

/TRI01/ Tritt, T.M. (2001) Semicond. Semimet., Academic Press, vols. 69, 70, 71.

/UHE99/ Uher, C., Yang, J., Hu, S., Morelli, D.T., Meisner, G.P. (1999) Phys. Rev. B, 59, 8615.

/URB06/ Urban, J.J., Talapin, D.V., Shevchenko, E.V., Murray, C.B. (2006) J. Amer. Chem. Soc., 128, 3248.

/URE61/ Ure, R.W., Heikes, R.R. (1961) Thermoelectricity: Science and Engineering, Interscience, New York.

/VAN58/ Van der Pauw, L.J. (1958) Philips Research Rep., 13, 1.

/VAQ10/ Vaqueiro, P., Powell, A.V. (2010) J. Mat. Chem., 20, 9577.

/VAS10/ Vasilevskiy, D., Dawood, M.S., Masse, J.-P., Turenne, S., Masut, R.A. (2010) J. Electr. Mater., 39, 9.

/VEN01/ Venkatasubramanian, R., Siivola, E., Colpitts, T., O'Quinn, B. (2001) Nature, 413, 597.

/VIN08/ Vineis, C.J., Harman, T.C., Calawa, S.D., Walsh, M.P., Reeder, R.E., Singh, R., Shakouri, A. (2008) Phys. Rev. B, 77, 235202.

/VIN10/ Vineis, C.J., Shakouri, A., Majumdar, A., Kanatzidis, M.G. (2010) Adv. Mater., 22, 3970.

/VIN91a/ Vining, C.B., Laskow, W., Hanson, J.O., Van der Beck, R.R., Gorsuch, P.D. (1991) J. Appl. Phys. 69, 4333-4340

/VIN91b/ Vining, C.B., Laskow, W., Hanson, J.O., Van der Beck, R.R., Gorsuch, P.D. (1991) Mat. Res. Soc. Symp. Proc., 234, 95.

/VOL74/ Volotskii, M.P. (1974) Fiz. Tech. Polupr., SSSR, 8, 1044.

/WAN00/ Wang, G.-X., Prasad, V. (2000) Ann. Rev. Heat Trans., 11, 207.

/WAN07/ Wang, G., Cagin, T. (2007) Phys. Rev. B, 76, 075201.

/WAN08/ Wang, X.W., Lee, H., Lan, Y.C., Zhu, G.H., Joshi, G., Wang, D.Z., Yang, J., Muto, A.J., Tang, M.Y., Klatsky, J., Song, S., Dresselhaus, M.S., Chen, G., Ren, Z.F. (2008) Appl. Phys. Lett., 93, 3.

/WAN09/ Wang, S., Mingo, N. (2009). Appl. Phys. Lett., 94, 1.

/WEB99/ Webster, J.G. (1999) The Measurement, Instrumentation, and Sensors Handbook. CRC Press LLC, New York, 43.

/WOL62/ Wolfe, R., Smith, G.E. (1962) Appl. Phys. Lett., 1, 5.

/WOO88/ Wood, C. (1988) Rep. Prog. Phys., 51, 459.

/XIA04/ Xiao, Y., Cui, X., Martin, D.C. (2004) J. Electroanal. Chem., 573, 43.

/XIE09a/ Xie, W., Tang, X., Yan, Y., Zhang, Q., Tritt, T.M. (2009) J. Appl. Phys., 105, 113713.

/XIE09b/ Xie, W., Tang, X., Yan, Y., Zhang, Q., Tritt, T.M. (2009) Appl. Phys. Lett., 94, 102111.

/XIE10a/ Xie, W., He ; J., Kang, H.J., Tang, X., Zhu, S., Laver, M., Wang, S., Copley, J.R.D., Brown, C.M., Zhang, Q., Tritt, T.M. (2010) Nano Lett., 10, 3283.

/XIE10b/ Xie, W.J., He, J., Zhu, S., Su, X. L., Wang, S.Y., Holgate, T., Graff, J.W., Ponnambalam, V., Poon, S.J., Tang, X.F., Zhang, Q.J., T., Tritt, T.M. (2010) Acta Materialia, 58, 4705.

/XIE11/ Xie, W., He, J., Zhu, S., Holgate, T., Wang, Sh., Tang, X., Zhang, Q., Tritt, T.M. (2011) J. Mater. Res., 26, 15.

/XIE13/ Xie, W., Wang, S., Zhu, S., He, J., Tang, X., Zhang, Q., Tritt, T. M. (2013) J. Mater. Sci., 48, 2745.

/YAM03/ Yamashita, O., Tomiyoshi, S., Makita, K. (2003) J. Appl. Phys., 93, 368.

/YAN01/ Yang, J., Aizawa, T., Yamamoto, A., Ohta, T. (2001) Mater. Chem. Phys., 70, 90.

/YAN05/ Yang, R., Chen G., Dresselhaus, M. (2005) Phys. Rev. B, 72, 125418.

/YAN06/ Yang, J.Y., Fan, X.A., Chen, R.G., Zhu,W., Bao, S.Q., Duan, X.K. (2006) J. All. Comp., 416, 270.

/YAN07/ Yang, J., Zhang, W., Bai, S.Q., Mei, Z., Chen, L.D. (2007) Appl. Phys. Lett., 90, 192111.

/YAN09/ Yang, J., Hao, Q., Wang, H., Lan, Y. C., He, Q. Y., Minnich, A., Wang, D.Z., Harriman, J.A., Varki, V.M., Dresselhaus, M.S., Chen, G., Ren, Z. F. (2009) Phys. Rev. B, 80, 115329.

/YAN10/ Yan, X., Poudel, B., Ma, Y., Liu, W.S., Joshi, G., Wang, H., Lan, Y., Wang, D., Chen, G., Ren, Z.F. (2010) Nano Lett., 10, 3373.

/YAN11a/ Yan, X., Joshi, G., Liu, W., Lan, Y., Wang, H., Lee, S., Simonson, J.W., Poon, S.J., Tritt, T.M., Chen, G., Ren, Z. F. (2011) Nano Lett., 11, 556.

/YAN11b/ Yang Y, Lee K, Mielczarek K, Hu W, Zakhidov A. (2011) Nanotechnology, 22, 485301.

/YIM72/ Yim, W.M., Amith, A. (1972) Solid-State Electron., 15, 1141.

/YOU01/ Youn, S.J., Freeman, A.J. (2001) Phys. Rev. B, 63, 085112.

/ZAI06/ Zaitsev, V.K., Fedorov, M.I., Gurieva, E.A., Eremin, I.S., Konstantinov, P.P., Samunin, A.Yu., Vedernikov, M.V. (2006) Phys. Rev. B, 74, 045207.

/ZHA04/ Zhang, J. X., Lu, Q. M., Liu, K. G., Zhang, L., Zhou, M. L. (2004) Mater. Lett., 58, 1981.

/ZHA06a/ Zhao, X .Y., Shi, X., Chen, L.D., Zhang, W.Q., Bai, S.Q., Pei, Y.Z., Li, X.Y., Goto, T. (2006) Appl. Phys. Lett., 89, 1.

/ZHA06b/ Zhao, X.Y., Shi, X., Chen, L.D., Zhang, W.Q., Zhang, W.B., Pei, Y.Z. (2006) J. Appl. Phys., 99, 053711.

/ZHA08a/ Zhang, Q., He, J., Zhao, X.B., Zhang, S.N., Zhu, T.J., Yin, H., Tritt, T.M. (2008) J. Phys. D, 41, 185103.

/ZHA08b/ Zhang, Q., He, J., Zhu, J., Zhang, S.N., Zhao, X.B., Tritt, T M. (2008) Appl. Phys. Lett., 93, 102109.

/ZHA10/ Zhao, L.D., Zhang, B.P., Liu, W.S., Zhang, H.L., Li, J.F. (2010) J. All. Comp., 467, 91.

/ZHA11/ Zhang, H., Borrmann, H., Oeschler, N., Candolfi, C., Schnelle, W., Schmidt, M., Burkhardt, U., Baitinger, M., Zhao, J.-T., Grin, Y. Inorg. Chemistry, 50, 1250-1257 (2011).

/ZHA14a/ Zhao, L.D., He, J., Berardan, D., Lin, Y., Li, J.F., Nan, C.W., Dragoe, N. (2014) Ener. Env. Sci., 7, 2900.

/ZHA14b/ Zhao, L.D., Lo, S.H., Zhang, Y., Sun, H., Tan, G., Uher, C., Wolverton, C., Vinayak, P.D., Kanatzidis, M.G. (2014) Nature, 508, 373.

Résumé (version française) :

Ce travail a été réalisé en collaboration avec EDF R&D, dans le cadre d'une convention CIFRE-ANRT, l'objectif étant d'améliorer le coefficient de performance de pompes à chaleur thermoélectriques (PACTEs) pour des "Bâtiments Basse Consommation". Les PACTEs présentent de nombreux avantages environnementaux, le désavantage étant leur faible performance. Ainsi l'objectif de ce travail a été d'examiner la possibilité d'améliorer, par nanostructuration les performances des semi-conducteurs utilisés dans les modules thermoélectriques des PACTEs. Nos travaux se sont concentrés sur les solutions solides à base de Sb2-xBixTe3, celles-ci étant, selon l'état-de-l'art, les plus performantes pour l'application visée. La nanostructuration a été réalisée par la technique de trempe sur roue (technique de refroidissement rapide de liquides) de matériaux synthétisés auparavent à l'état liquide dans des tubes en quartz. Les moyens de caractérisation (DRX, MEB, MET, METHR) ont permis de corréler les changements structurels avec la variation des propriétés thermiques et électriques (le pouvoir thermoélectrique, la résistivité électrique, l'effet de Hall, la conductivité thermique) mesurées sur de larges gammes de température (5-460 K). L'influence favorable de la nanostructuration par la diminution de conductivité thermique a été prouvée. Nous avons montré la forte dépendance des propriétés thermoélectriques des matériaux étudiés avec la concentration de défauts et la stœchiométrie. Le dopage avec du Te a été examiné comme une possibilité de contrôler le niveau de la concentration des porteurs de charge. L'idée de créer des niveaux d'impuretés résonantes par un dopage au Sn s'est montrée infructueuse, vraisemblablement en raison de la structure de bande complexe du composé ternaire. Néanmoins, des valeurs du facteur de mérite adimensionel ZT de près de 1,2 ont été obtenues pendant ce travail.

Abstract (English version):

This work results from the collaboration between IJL and EDF R&D performed under a CIFRE-ANRT convention, in order to improve the coefficient of performance of thermoelectric heat pumps (THPs). THPs attracted attention of EDF due to its numerous environmental advantages, but the main drawback remains its low performance. The objective of our work was thus to investigate the possibility to enhance the performance of the semiconductors used in the thermoelectric modules of the THPs, by nanostructuration. The research was concentrated on the Sb2-xBixTe3-based solid solutions, the most effective materials for the application sought. The nanostructuration was performed by applying the melt-spinning technique (rapid quenching from a melt on a water-cooled cupper wheel) to the material synthesised beforehand from liquid state in quartz tubes. The means of characterisation (XRD, SEM, TEM, HRTEM) gave the possibility to correlate the structural changes with the variation of the thermal and electrical properties (thermoelectric power, electrical resistivity, Hall effect, thermal conductivity) measured over a wide temperature range (5-460 K). The favourable influence of nanostructuration through the decreasing of thermal conductivity was proved. A high dependence of the thermoelectric efficiency of the studied materials on the concentration of defects and stoichiometry is shown. Doping with Te was investigated as a possibility to control the resulting level of the charge carrier concentration. The idea of creating resonant impurity levels by Sn-doping was shown to be non-conclusive presumably due to the complex band structure of the ternary compounds. Nevertheless, relatively high values of the dimensionless TE figure of merit, close to 1.2, were obtained during this work.